Spring 2015

Performance Based Earthquake Engineering of Concrete Dams

Mohammad Amin Hariri-Ardebili
University of Colorado at Boulder, mohammad.haririardebili@colorado.edu

Performance Based Earthquake Engineering of Concrete Dams

by

Mohammad Amin Hariri-Ardebili

B.Sc., K.N.Toosi University of Technology, Tehran, Iran, 2007

M.Sc., K.N.Toosi University of Technology, Tehran, Iran, 2010

M.Sc., University of Colorado, Boulder, USA, 2014

A thesis submitted to the

Faculty of the Graduate School of the

University of Colorado in partial fulfillment

of the requirements for the degree of

Doctor of Philosophy

Department of Civil, Environmental and Architectural Engineering

2015

This thesis entitled:
Performance Based Earthquake Engineering of Concrete Dams
written by Mohammad Amin Hariri-Ardebili
has been approved for the Department of Civil, Environmental and Architectural Engineering

Prof. Victor E. Saouma

Prof. Shideh Dashti

Prof. Abbie B. Liel

Mr. Larry K. Nuss

Prof. Keith A. Porter

Date

The final copy of this thesis has been examined by the signatories, and we find that both the content and the form meet acceptable presentation standards of scholarly work in the above mentioned discipline.

Hariri-Ardebili, Mohammad Amin (Ph.D. Civil Engineering)

Performance Based Earthquake Engineering of Concrete Dams

Thesis directed by Prof. Victor E. Saouma

The main objective of this thesis is to develop a framework for performance based earthquake engineering (PBEE) of concrete dams. To pursue this goal, this study first develops an extended and quantitative version of potential failure mode analysis (PFMA) for concrete dams. Different failure modes are investigated for all types of concrete dams.

A Matlab-based code is developed for probabilistic performance assessment of concrete dams (PPACD). This code is used for assessment of concrete dams within the context of PBEE. A probabilistic seismic demand model (PSDM) is proposed for concrete dams based on cloud analysis methodology. The outcome of PSDM is selection of optima intensity measure (IM) parameters for gravity dams. Then, the sensitivity and uncertainty of dam-foundation system is quantified under the mixed-mode fracture of zero-thickness interface joint element. Capacity and fragility curves are derived for most sensitive random variables.

This research also examined the performance of the dam under incremental dynamic analysis (IDA). First, the anatomy of a single-record IDA is studied and contrasted by framed structures. Then, the collapse fragility curves are derived for single and multiple-component ground motions. The impact of epistemic uncertainty is investigated in addition to the aleatoric one.

Finally, a multi-scale damage index (DI) is proposed for gravity dams which is a function of crest displacement, crack ratio, and dissipated energy. Using this hybrid DI, a computationally simple but effective methodology is proposed for progressive failure analysis of dams. In all cases, first the methodology is discussed and then, a numerical example illustrates the details.

Dedication

This thesis is dedicated to my parents Mohammad Reza and Yekta who have supported me all the way since the beginning of my studies.

Acknowledgements

I would like to thank my advisor, Professor Victor E. Saouma, for his support/advising/guidance through this PhD research. He has been a tremendous mentor for me. His guidance helped me in all the time of research and writing of this thesis. He was always accessible to my numerous questions even on weekends. Undoubtedly, he is my academic father.

I also would like to thank Professor K.A. Porter, Professor B.R. Ellingwood, Professor S. Dashti, Professor A.B. Liel, Professor P. Sideris, and Mr. L.K. Nuss for serving as my (comprehensive exam and final defense) committee members even at hardship. Thanks for all the brilliant comments and suggestions.

Contents

Chapter

Tables

Table

Figures

Figure

Chapter 1

Introduction

1.1 Motivation

Dams are critical components of a nation's infrastructure. They provide energy, flood protection, water storage for domestic, industrial, agricultural use and recreation. Yet, many dams are aging and most were designed at a time with limited seismic field data, or technical knowledge. Taking a simple binary approach Safe/Fail, as commonly done presently through a deterministic application of safety codes (FERC-PFMA, 2005; USACE, 2007; CDA, 2007) is not only unrealistic but could yield very expensive rehabilitation program. On the other hand, performance based earthquake engineering (PBEE) (Porter, 2003), by now widely embraced for buildings, does provide a new paradigm for dams, one where nonlinear time history analysis is performed and quantitative failure assessment is necessary.

PBEE offers a step-by-step methodology for assessing structural safety. It requires both a global probabilistic framework that integrates different steps of the methodology and detailed analysis for each one. The Pacific Earthquake Engineering Research (PEER) Center has developed a comprehensive framework for PBEE. During the past decade, many researchers developed and extended different steps of the PEER PBEE for buildings and bridges. Yet, there is no sign of such a research for concrete dams. Thus, each step of this methodology should be carefully executed.

1.2 Objectives

The objective of this research is to extend the PBEE in different aspects for concrete dams. For this purpose, some elements of conventional potential failure mode analysis is combined with some others from PBEE for probabilistically safety assessment if dams.

The major objectives of this research are: 1) Develop an extended and quantitative version of potential failure mode analysis for concrete dams, 2) Develop a Matlab-based computational tool for probabilistic performance assessment of concrete dams, 3) Develop a probabilistic seismic demand model for concrete dams considering the global failure, 4) Propose an optimal intensity measure parameter for concrete dams, 5) Perform the sensitivity analysis on dam-foundation system, quantify the material (epistemic) uncertainties, determine tornado diagram, capacity and fragility curves, 6) Perform different structural analysis techniques on concrete dams. In particular: cloud analysis, multiple strip analysis, incremental dynamic analysis, and endurance time analysis, 7) Determine the collapse fragility curves of concrete dams though multiple-record incremental dynamic analysis, 8) Propose a multi-scale damage index for gravity dams as a function of crest displacement, crack ratio, and dissipated energy, and 9) Propose a computationally simple but effective methodology for progressive failure analysis of dams though damage index and endurance time analysis.

1.3 Outline

This thesis is a based on a compilation of research papers and reports. Some of these papers/reports are co-authored, so the first part of each chapter shows all the authors and a journal in which the manuscript is submitted.

Chapter 2 will review the general steps in PFMA and PBEE. In particular for PBEE, first the basic definitions will be explained, then the PBEE predecessors will be reviewed. It will be followed by comparison of first and second generation of PBEE. Moreover, application of probabilistic methods in concrete dams will be categorized in different groups. Finally, the dam safety decision-making guidelines will be compared based on different agencies

recommendations.

Chapter 3 will review and revisit all the numerical methods for progressive failure analysis of concrete dams. We will propose the concept of capacity functions for concrete dams and will present a simple mathematical model for it.

Chapter 4 will present the computational tools developed and used during this research for probabilistic performance assessment of concrete dams (PPACD). This includes a group of Matlab-based scripts and functions which are used also Merlin finite element code for processing the models. The interaction of all these scripts and their application in PBEE will be explained.

Chapter 5 will explain a detailed nonlinear dynamic analysis for a gravity dam. First, the characteristics of the dam and the finite element model will be presented. Then, probabilistic seismic hazard analysis will be explained on this particular dam. The seismic hazard curves and deaggregation plots will be extracted. Finally, using only one ground motion, a detailed deterministic dynamic analysis will be performed. Both the smeared crack model and zero-thickness interface joint element between dam and foundation will be considered.

Chapter 6 will represent the potential failure mode analysis for all three types of concrete dams, i.e. gravity, arch, and buttress. First, the qualitative approach will be reviewed and then the extended quantitative version will be proposed for both the linear and nonlinear systems. Multiple strip analysis method will be used for assessment of a case study arch dam. A large set of simulated engineering demand parameters will be generated for the dam and the optimal scalar and vectorized intensity measure parameter will be quantified. Finally, the results of linear and nonlinear system will be correlated.

Chapter 7 will quantify the sensitivity and uncertainty in dam-foundation system. First, the theory of an advanced fracture mechanics based zero-thickness interface joint element will be studied. Then, it will be applied for analysis of three problems: mode I and II fracture

mechanics of idealized blocks subjected to displacement control pushover analysis, and mixed-mode fracture analysis of a real gravity dam-foundation system. For each case, the most sensitive random variables (RV) will be determined and the associated tornado diagram will be plotted. Monte Carlo simulation with Latin Hypercube Sampling will be used for uncertainty quantification of the sensitive RVs. The impact of correlation among the RVs will be studied also. Finally, the capacity curve will be plotted for each case and the associated fragility curve will be derived.

Chapter 8 will propose a probabilistic seismic demand model for gravity dams. First, all the existing intensity measure parameters for structural systems will be summarized in seven categories and a new one will be proposed for dams. Then, a cloud-based probabilistic seismic demand analysis will be performed using 100 un-scaled ground motions. Using these ground motions, an appropriate distributional model will be proposed for each intensity measure. The most optimal intensity measure parameter will be determined considering the parameters such as sufficiency, efficiency, proficiency, practicality, and hazard compatibility. Finally, the fragility curves will be derived for the dam and the impact of different intensity measure and engineering demand parameters will be investigated.

Chapter 9 will present collapse fragility curves for gravity dams. First, the background theory of collapse fragility curves and different methods for fitting a lognormal cumulative distribution function to the empirical data points will be reviewed. Transient analyses will be performed based on incremental dynamic analysis (IDA) methodology. The Anatomy of a single-record IDA will be studied in detail and contrasted with framed structures. The optimal intensity measure parameter will be selected based on the minimum dispersion of multiple-record IDA curves. Finally, the collapse fragility curves will be derived for the dam.

Chapter 10 will propose a multi-scale damage index (DI) for gravity dams. The new DI will be based on maximum crest displacement, energy dissipation in system and the ratio of the

cracked segments. Then, a computationally simple but effective method will be proposed for systematic progressive failure assessment of gravity dams based on endurance time analysis. This method provides continuous performance of the dam in terms of DI and the desired intensity measure parameter.

Chapter 11 will present the summary and conclusions of this research, as well as the future research needs.

Chapter 2

Literature Review and Background Theory

This chapter is based on the following two references:

Hariri-Ardebili, M.A. and Saouma, V.E., Performance Based Seismic Design Guidelines for Concrete Dams – Part 2: Background Information, Report prepared for Enerjisa, Turkey, Sep 2012.

Saouma, V.E., Porter, K., Nuss, L.K. and Hariri-Ardebili, M.A., Performance Based Seismic Design Guidelines for Concrete Dams – Part 1: Main Report, Report prepared for Enerjisa, Turkey, Sep 2012.

2.1 Introduction

Over the past years there have been two concomitant developments: 1) performance-based earthquake engineering (PBEE) which is a proposed new paradigm for the seismic safety investigation of building, and 2) potential failure mode analysis (PFMA) which is a generally accepted methodology to assess dam safety. Though similar, and written by different communities, much can be gained through an attempt to bring together those two paradigms. Figure 2.1 highlight the similarities between the two approaches in general. Each one will discuss later in detail.

In the following sections, the general steps in each of them are explained. Whenever it is required the differences between the dam safety assessment and the loss analysis in buildings are highlighted. Some of the steps are explained in the subsequent chapters (as part of a submitted paper) and thus, they will skipped in this chapter.

	Potential Failure Mode Analysis	Performance Based Earthquake Engineering
Step 1	Define the failure criteria (i.e. uncontrolled release of the water)	Perform seismic hazard analysis at the facility site, produce target response spectrum and select ground motions
Step 2	Define the initiator, and identify the potential failure modes (i.e. sliding due to an earthquake)	Perform a set of nonlinear dynamic structural analyses and determine the response of the facility
Step 3	Develop a sequence of events for a failure to transpire (event tree and if needed fault tree)	Perform damage analysis on the facility and determine the fragility curves in term of structural responses
Step 4	Select a path with the most likely chance to failure, perform the structural analysis, and quantify the uncertainties	Evaluate the repair efforts to determine repair costs, operability, repair duration, and the potential for casualities
Step 5	Quantify the risk and import the results on an f-N curve, and final decision making	Final decision making based on contribution of all the previous steps

Figure 2.1: Comparison of general methodologies in PFMA and PBEE

2.2 Performance Based Earthquake Engineering

2.2.1 Basic Definitions

2.2.1.1 Performance-Based Engineering (PBE)

PBE is defined as consisting of the selection of design criteria, appropriate structural systems, layout, proportioning, and detailing for a structure and its non-structural components and contents, and the assurance and control of construction quality and long-term maintenance, such that at specified levels of all the excitation and with defined levels of reliability, the structure or facility will not be damaged beyond certain limit states. PBE is a process that begins with the first concepts of a project and lasts throughout the life of the structure (Bertero and Bertero, 2002).

2.2.1.2 Performance-Based Earthquake Engineering (PBEE)

PBEE is defined as the application of PBE to the case that seismic hazard controls the design. Therefore, PBEE involves the complete design, construction and control (monitoring) of the maintenance and function of the structure to assure that the constructed structures will resist the effects of earthquake ground motions with different severity within specified limiting levels of damage (Bertero and V.V., 2000).

2.2.1.3 Performance-Based Seismic Design (PBSD)

PBSD is the subset of activities of PBEE that focus on the design process. Therefore, it includes identification of seismic hazards, selection of the performance levels and performance design objectives, determination of site suitability, conceptual design, numerical preliminary design, final design, acceptability checks during design, design review, specification of quality assurance during the construction and of monitoring of the maintenance and occupancy (function) during the life of the structure (Bertero and Bertero, 2002).

2.2.1.4 Performance-Based Assessment (PBA)

PBA is the implementation of the PBEE in quantitative evaluation of the performance of a given structure (even an existing structure or a completed design of a new structure). PBA provides stakeholders with information about the structure (usually expressed in probabilistic terms) that facilitates informed decision making for risk management (Zareian and Krawinkler, 2009).

2.2.2 PBEE Predecessors

In the US, interest in PBSD initiated in the 1980s among engineers engaged in seismic retrofit of existing buildings. Owners of existing buildings would not commit to investment in retrofit construction unless they had an understanding of the probable performance of their buildings in future earthquakes, decided that this performance was undesirable, and that acceptable performance could be obtained at reasonable cost. Engineers quickly found that evaluations of buildings to the current editions of the building code provided information on the building's conformance to current design practice but did not provide direct information on the way a building was likely to behave in an earthquake. Thus, engineers began to develop rudimentary procedures for assessing the likely earthquake performance of existing buildings so that they could evaluate whether collapse or other life-threatening damage was likely, and if not to assess the severity and likely consequences of damage that would occur (Hamburger et al., 2004).

Several documents were credited with laying the basis of PBE concepts. The following section

describes each of these codes and documents in detail. It should be mentioned that all these documents attempted to develop procedures that can be used as seismic provisions in building codes.

2.2.2.1 ATC-13 (1985) and ATC-14 (1987)

In the mid-1980s, the Applied Technology Council (ATC) published several documents. The ATC-13 report provided statistical data on the probable repair costs for buildings of different types, based on the opinions of earthquake engineering experts (ATC-13, 1985). The ATC-14 report provided a standardized methodology for evaluating life safety hazards in buildings (ATC-14, 1987).

2.2.2.2 SEAOC Vision 2000 (1995)

Based on Structural Engineers Association of California (SEAOC) Vision 2000 the first step in PBEE is the definition and selection of the performance objectives (PO). A PO is a coupling of expected performance levels with levels of seismic ground motions. A performance level represents a distinct band in the spectrum of damage to the structural and non-structural components and contents, and also considers the consequences of the damage to the occupants and functions of the facility (Bertero and Bertero, 2002). Four discrete performance levels in this document are: 1) fully operational, 2) operational, 3) life safety, and 4) near collapse in terms of damage to structural and non-structural components and consequences to the occupants and functions carried on within the facility as shown in figure 2.2 (SEAOC, 1995). Also SEAOC Vision 2000 describes various hazard levels as: 1) frequent intensity level with a 50% exceedance probability in 30 years hazard level, 2) the occasional intensity level with a 50% exceedance probability in 50 years, 3) the rare intensity level with a 10% exceedance probability in 50 years, and 4) the very rare intensity level with a 10% exceedance probability in 100 years. It should be noted that the earthquake design levels were shown as earthquake with specific return period in figure 2.2. The diagonal lines represent different *objectives* in this figure correspond to different facility types.

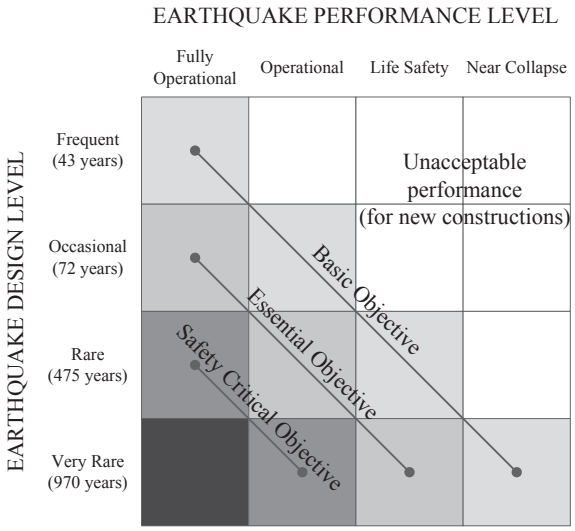

Figure 2.2: Recommended minimum seismic performance design objectives for buildings

2.2.2.3 ATC-40 (1996)

In 1996, the ATC published a document entitled: "*Seismic Evaluation and Retrofit of Concrete Buildings*". in which the performance-based design refers to the methodology that structural criteria are expressed in terms of achieving a performance objective. The document is limited to concrete buildings and emphasizes the use of the capacity spectrum method (ATC-40, 1996).

2.2.2.4 FEMA 273 (1997) and FEMA 274 (1997)

In 1997, the Federal Emergency Management Agency (FEMA) published the National Earthquake Hazards Reduction Program (NEHRP) guidelines for the seismic rehabilitation of buildings (FEMA, 1997b) and associated commentary documents (FEMA, 1997a). FEMA 273 document presents a variety of performance objectives with associated probabilistic ground motions. Analysis and design methods for the multiple-level performance range from linear static to inelastic time history analysis. The document defines performance levels for non-structural elements and systems and proposes drift limits for various lateral-load-resisting structural systems at different performance levels.

2.2.2.5 FEMA 356 (2000)

FEMA 365 is one of the most comprehensive guidelines for PBEE entitled: "*Prestandard and Commentary for the Seismic Rehabilitation of Buildings*". FEMA 356 was written to provide professional engineers nationwide a tool for designing seismic rehabilitation measures for existing structures (FEMA, 2000). The document defines various target building performance levels and earthquake hazard levels similar to those presented in SEAOC Vision 2000. The performance levels and descriptions of corresponding physical damage are shown in Table 2.1.

Table 2.1: The range of damage of structural and non-structural components for various target building performance levels (Table C1-2) (FEMA, 2000)

Performance levels	Collapse prevention	Life safety	Immediate occupancy	Operational
Overall damage	Severe	Moderate	Light	Very light
Structural components	Little residual stiffness and strength, but load-bearing columns and walls function. Large permanent drifts. Some exits blocked. Infills and unbraced parapets failed or at incipient failure. Building is near collapse.	Some residual strength and stiffness left in all stories. Gravity-load-bearing elements function. No out-of plane failure of walls or tipping of parapets. Some permanent drift. Damage to partitions. Building may be beyond economical repair.	No permanent drift. Structure substantially retains original strength and stiffness. Minor cracking of facades, partitions, and ceilings as well as structural elements. Elevators can be restarted. Fire protection operable.	No permanent drift. Structure substantially retains original strength and stiffness. Minor cracking of facades, partitions, and ceilings as well as structural elements. All systems important to normal operation are functional.
Non-structural components	Extensive damage.	Falling hazards mitigated but many architectural, mechanical, and electrical systems are damaged.	Equipment and contents are generally secure, but may not operate due to mechanical failure or lack of utilities.	Negligible damage occurs. Power and other utilities are available, possibly from standby sources.

2.2.2.6 Global Framework for PBEE

As mentioned before there are several conceptual frameworks for PBEE (SEAOC Vision 2000, FEMA 273, ATC-40) which differ in details but not in concepts (Ghobarah, 2001). Figure 2.3 is proposed by Krawinkler (1999) as a global framework which identifies processes, concepts, and major issues that need to be addressed. The issues include seismological, geotechnical, structural,

architectural, and socio-economic considerations.

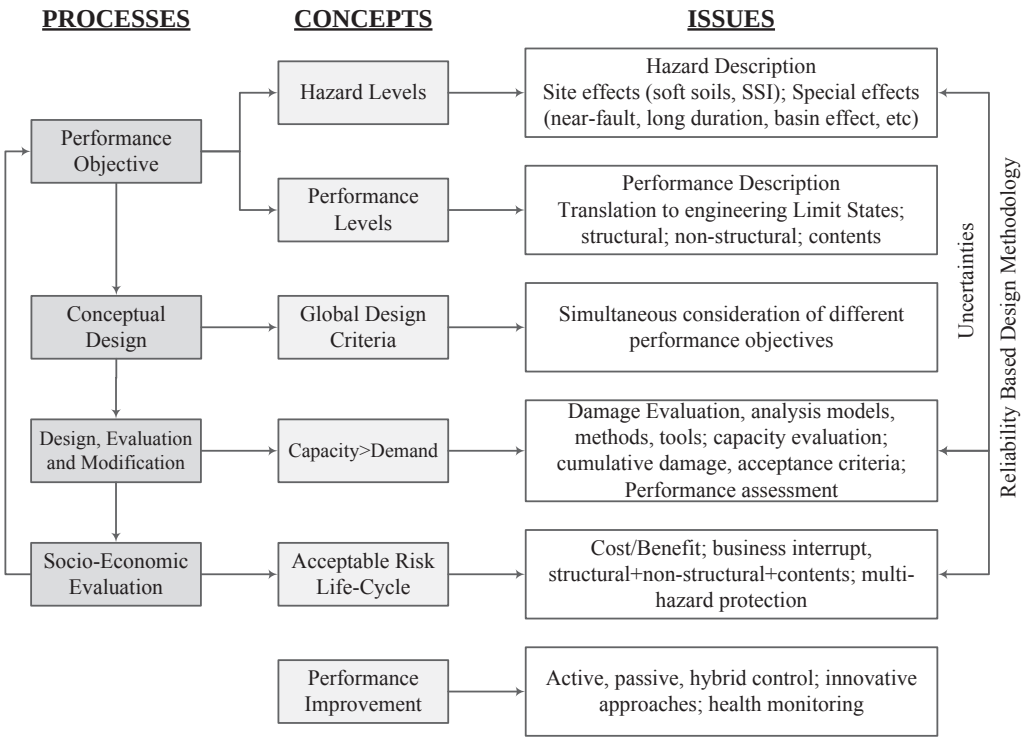

Figure 2.3: Global framework for performance-based earthquake engineering

Some other authors were more emphasized on developing a deep understanding and appreciation of the multi-disciplinary aspects of PBEE. They proposed that any new conceptual developments in existing researches (downstream nodal point at the figure 2.4) should be accompanied by updating the upstream nodal point accordingly (Chandler and Lam, 2001).

2.2.3 First Generation of PBEE

All the documents discussed in previous section are categorized as part of the first generation of PBEE which presents assessment and design procedures for buildings (Moehle and Deierlein, 2004). This procedure is also shown in figure 2.5 conceptually (Whittaker et al., 2003) and it is assumed that a structure is loaded by earthquake-induced lateral forces that produce nonlinear response in structural components. Relations were established between structural responses

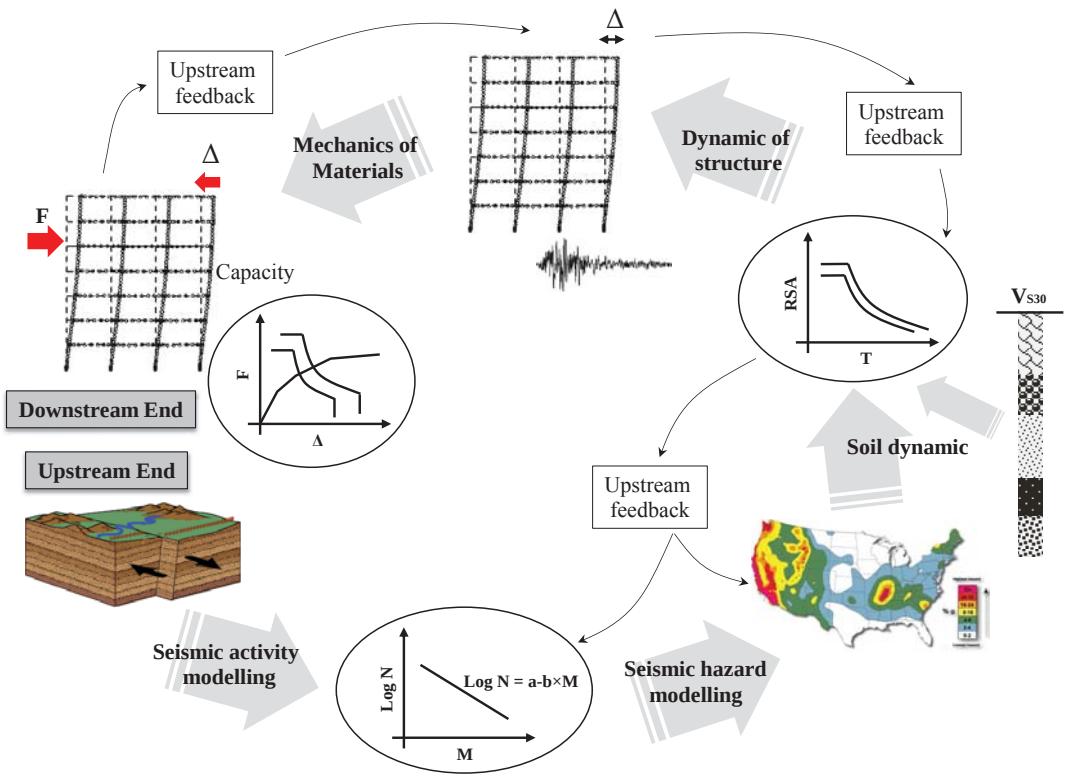

Figure 2.4: The disciplines contribute in global framework of performance-based earthquake engineering

(inter-story drift ratio, inelastic member deformation, and member force) and performance-oriented descriptions (such as immediate occupancy, life safety and collapse prevention, Table 2.1).

The first-generation of PBEE (also called as PBEE-1) represents a significant improvement over past practice. It includes standard methods of defining performance in terms of quantified performance levels that relate to calculated seismic response parameters and incorporate a formal methodology for simulating building response to earthquake motions and assessing performance capability based on the predicted magnitude of a series of structural response parameters (Hamburger et al., 2004). Considering all these developments also they had shortcomings which need to be improved:

- PBEE-1 has evaluated performance on the basis of the demands and capacities of individual

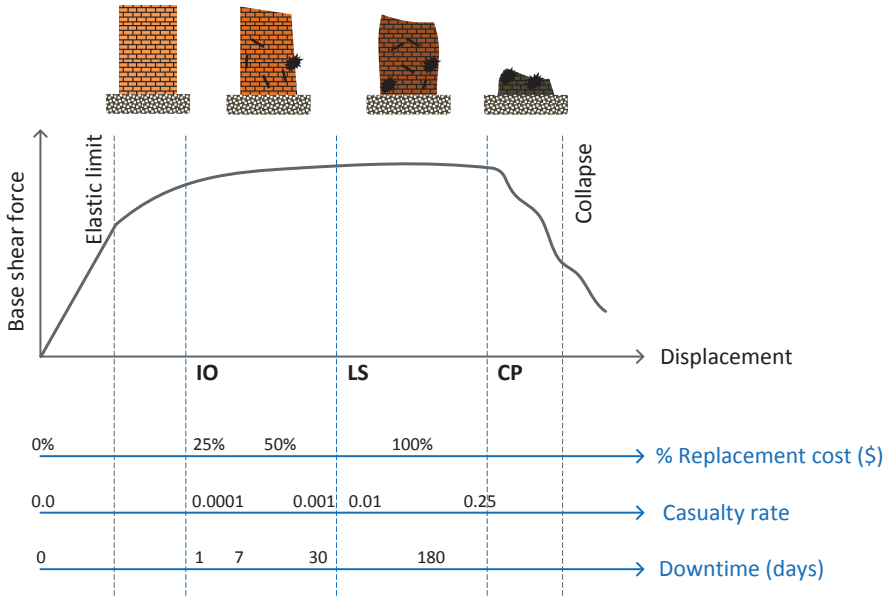

Figure 2.5: Conceptually description of first generation of PBEE

components, rather than global building behavior. So the weakest or the least ductile elements in a structure were controlled the estimation of overall structural performance (even if these elements had relatively little significance to the structure's overall seismic resistance).

- The reliability of PBEE-1 is questionable because many of the acceptance criteria contained in the documents are based on the judgment of those who developed the method, rather than laboratory data or other direct substantiating evidence.

- Considering that much of the losses experienced by structures in past earthquakes can be attributed to the performance of non-structural components and systems, the procedures that evaluate these elements in PBEE-1 are limited almost entirely to consideration of the ability of them to remain structurally stable and do not address well either the damageability or post-earthquake functionality of these components and systems comprised of these components.

- The reliability of the procedures in PBEE-1 and their ability to achieve the desired performance has never been established and many engineers believe that the procedures are excessively conservative and may not result in adequate performance capability. The standard performance levels do not directly address some primary stakeholder concerns, that is probable repair costs and time of occupancy loss in the building, due to earthquake induced damage.

- The basic process of performance-based engineering carries with it significant potential liability as many building owners may perceive that the design professional has provided a warranty on the design's performance capability.

2.2.4 Second Generation of PBEE

2.2.4.1 PBEE Historical Development: Review

Although there are many research about the different aspects of PBEE (theoretical models and case studies), only the fundamental ones are reviewed in this section. A detailed literature review will provide for each specific topic in the next chapters.

- Czarnecki (1973): To the best of the author knowledge, this is the first analytical procedure to estimate the seismic vulnerability of structures which is similar to the modern PBEE. The work is mainly component based which begins with structural analysis of system to estimate forces and deformations under a particular level of shaking. It follows with damage and loss assessment of system. In this method, damage is estimated by ratio of the absorbed energy in the building components to the maximum energy absorption capacity of that component. This method is similar to the concept of "damage index". The proposed methodology is then applied to several tall buildings damaged by the 1971 San Fernando earthquake. It is concluded that the method predicts the general trend of damage but might come with considerable error for other specific case.

- Kustu et al. (1982): They provided component damage function from laboratory tests to calculate total damage to tall buildings. They used a component-based deterministic approach which does not account for the record-to-record variability, structural response (mostly story drift), component damageability, or repair costs. In this research, there is no distinguish between the repair cost and replacement one.

- Porter (2000): He proposed a methodology to evaluate the assembly-based seismic vulnerability of buildings on a building-specific basis. In this method, the building is assumed as a unique collection of standard assemblies with probabilistic fragility, repair costs, and repair durations. This procedure relies on Monte Carlo approach to simulate ground motion, structural response, assembly damage, repair costs and duration. Moreover, he presented a decision-analysis approach within the context of assembly-based vulnerability methodology. Finally, he presented different techniques to derive the empirical and theoretical assembly fragilities (which are illustrated through the creation of structural and non-structural fragility functions).

- Aslani and Miranda (2005): They proposed a component-based approach via using the economic (annual) losses as a measure for seismic performance of the framed structures. This procedure aims at computing the probability of exceedance of different types of engineering demand parameters. The peak interstory drift ratio provides a way to estimate the damage to (mainly) structural components, while the peak floor acceleration is (mainly) suitable for estimating damage to acceleration-sensitive (non-structural) components. Epistemic uncertainties are considered explicitly and propagated. They proposed loss disaggregation as a way to identify the ground motion intensities, level of structural response and components that primary contribute to damage and direct economic losses. Moreover, the probability of collapse at different intensity levels is taken into account in loss estimation. It is noteworthy that both collapse mechanisms are studied, i.e. 1) resulting from dynamic instability, and 2) progressive collapse due to loss of vertical carrying capacity of critical

members.

- Mitrani-Reiser (2007): She developed an analytical approach for PBEE and used to evaluate the performance of a new RC building. The method is capable of propagating the uncertainties within the shaking intensity, the mechanical properties of the facility, and the damageability and unit repair costs of the facility. This methodology estimates the direct economic losses due to repair costs as well as indirect economic losses (due to building downtime and human fatalities).

- Yang et al. (2009b): Within the context of PBEE, he proposed a procedure in order to generate additional engineering demand parameters for a system that originally has limited number of nonlinear transient analyses (numerical or experimental). In this method, first a joint lognormal distribution is fitted to the structural response matrix. Then, the correlated EDP vectors are generated using a computationally inexpensive procedure. This procedure enables a Monte-Carlo type implementation of the PBEE framework.

- Lin (2012): She focused on ground motion selection and scaling that connects the first two elements of PBEE (hazard and structural analyses). Any change in ground motion intensity level changes the target distribution of ground motion parameters (e.g., magnitude and distance). Subsequently, the target response spectrum can be computed using a single or multiple ground motion prediction models. She used the concept of conditional spectrum (CS) to address properly the contributing uncertainties in ground motion selection process. The CS estimates the distribution (with mean and standard deviation) of the response spectrum, conditioned on the occurrence of a target S_a value at the period of interest. Utilizing the correlation of S_a across periods, the CS methodology eliminates the conservatism from the Uniform Hazard Spectrum.

2.2.4.2 PEER PBEE Framework

PBEE implies design, evaluation, and construction of engineered facilities whose performance under common and extreme loads responds to the diverse needs and objectives of owners-users and society. In 1997 the Pacific Earthquake Engineering Research Center (PEER) decided to develop a more robust methodology for performance-based earthquake engineering, called as next generation PBEE (also called as PBEE-2 or PEER PBEE). The PEER PBEE framework developed by PEER facilitates direct calculation of the effects of uncertainty and randomness on each step in the performance based procedure (Porter, 2003).

The general framework for PEER PBEE is shown in figure 2.6. It breaks the seismic performance assessment into four primary steps: 1) ground motion hazard characterization, 2) structural response analysis, 3) damage analysis, and 4) loss assessment (Haselton et al., 2008). The results of each of these steps are represented as generalized variables, Intensity Measure (IM), Engineering Demand Parameter (EDP), Damage Measure (DM), and Decision Variable (DV). This process can be expressed in terms of a triple integral that is an application of the total probability theorem (Porter, 2003):

$$g\,[\mathrm{DV}|\mathrm{D}] = \int\int\int p\,[\mathrm{DV}|\mathrm{DM,D}]\,p\,[\mathrm{DM}|\mathrm{EDP,D}]\,p\,[\mathrm{EDP}|\mathrm{IM,D}]\,g\,[\mathrm{IM}|\mathrm{D}]\,d\mathrm{IM}.d\mathrm{EDP}.d\mathrm{DM} \qquad (2.1)$$

where $p\,[\mathrm{X}|\mathrm{Y}]$ denotes the complementary cumulative distribution function of X conditioned on Y, $g\,[\mathrm{X}|\mathrm{Y}]$ denotes the mean annual occurrence rate of X given Y, and D denotes facility location, structural, non-structural, and other features. Note that in future we omit conditioning on D for simplicity.

IM: describes the characteristics of the earthquake ground motion quantitatively. This parameter is expressed typically as a function of mean annual probability of exceedance, $g\,[\mathrm{IM}]$.

EDP: describes the response of the structural and the non-structural components and contents to earthquake shaking. The products of this step are conditional probabilities, $p\,[\mathrm{EDP}|\mathrm{IM}]$.

DM: describes the physical condition of structural and non-structural components. DMs include

effective descriptions of damage to characterize the functionality, occupancy-ready, life safety and necessary repairs of the building. The products of this step are conditional probabilities, $p\,[\mathrm{DM}|\mathrm{EDP}]$.

DV: serves to translate damage estimates into quantities that are useful to those tasked with making risk-related decisions. Currently used DVs which are identified as decision metrics are direct dollar losses, downtime (or restoration time) and deaths (casualties). The products of this step are conditional probabilities, $p\,[\mathrm{DV}|\mathrm{DM}]$.

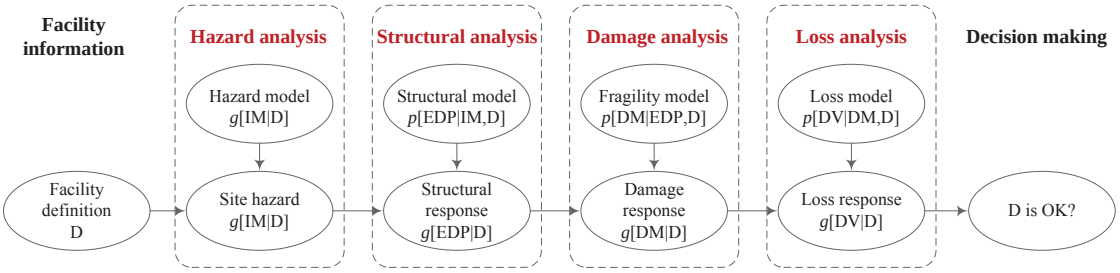

Figure 2.6: General framework of PEER PBEE methodology (Porter, 2003)

As mentioned before direct dollar losses, downtime and casualties are used as decision variables in PBEE-2 methodology for performance assessment of structures. ATC-58 (2012) uses three types of performance assessments, i.e. 1) intensity-based, 2) scenario-based, and 3) time-based.

2.2.4.3 Intensity-Based Performance Assessments (IBPA)

This method evaluates a structure's performance assuming that it is subjected to a specific intensity of shaking. In the case of frame structures, shaking intensity is defined by 5% damped elastic acceleration response spectra. This assessment usually is used when the structure is subjected to the earthquake shaking with specific response spectrum (such as design response spectrum) (ATC-58, 2012).

2.2.4.4 Scenario-Based Performance Assessments (SBPA)

This method evaluate a structure's performance assuming that it is subjected to the effects of a specific magnitude earthquake occurring at a specific location relative to the structure site. Scenario assessments may be useful for decision makers with structures located close to one or more known active faults. Scenario-based assessments are very similar to intensity-based assessments except that uncertainty in the earthquake intensity, given the scenario, is considered (ATC-58, 2012).

2.2.4.5 Time-Based Performance Assessments (TBPA)

This method evaluates a structure's performance over a period of time considering all earthquakes that may occur in that period of time, and the probability that each will occur. Time-based assessments consider uncertainty in the magnitude and location of future earthquakes as well as the intensity of motion resulting from these earthquakes. Assessments based on a single year are useful for cost-benefit evaluations used to decide between alternative performance criteria (ATC-58, 2012).

Figure 2.7 compares the step-by-step procedure for ground motion selection and scaling based on the three above mentioned methods. It is noteworthy that in TBPA, the recommended values for the parameters introduced in figure 2.7 are as follows: $(S_a)_{min} = 0.05$ g and $(S_a)_{max}$ is associated with annual frequency of exceedance of $0.00002/yr$ (that is, 1 occurrence in 50,000 years). Number of intervals m usually is recommended to be 8.

2.3 Potential Failure Mode Analysis

A dam potential failure mode (PFM) is a chain of events leading to unsatisfactory performance of the dam which could lead to uncontrolled release of the reservoir water (FERC-PFMA, 2005).

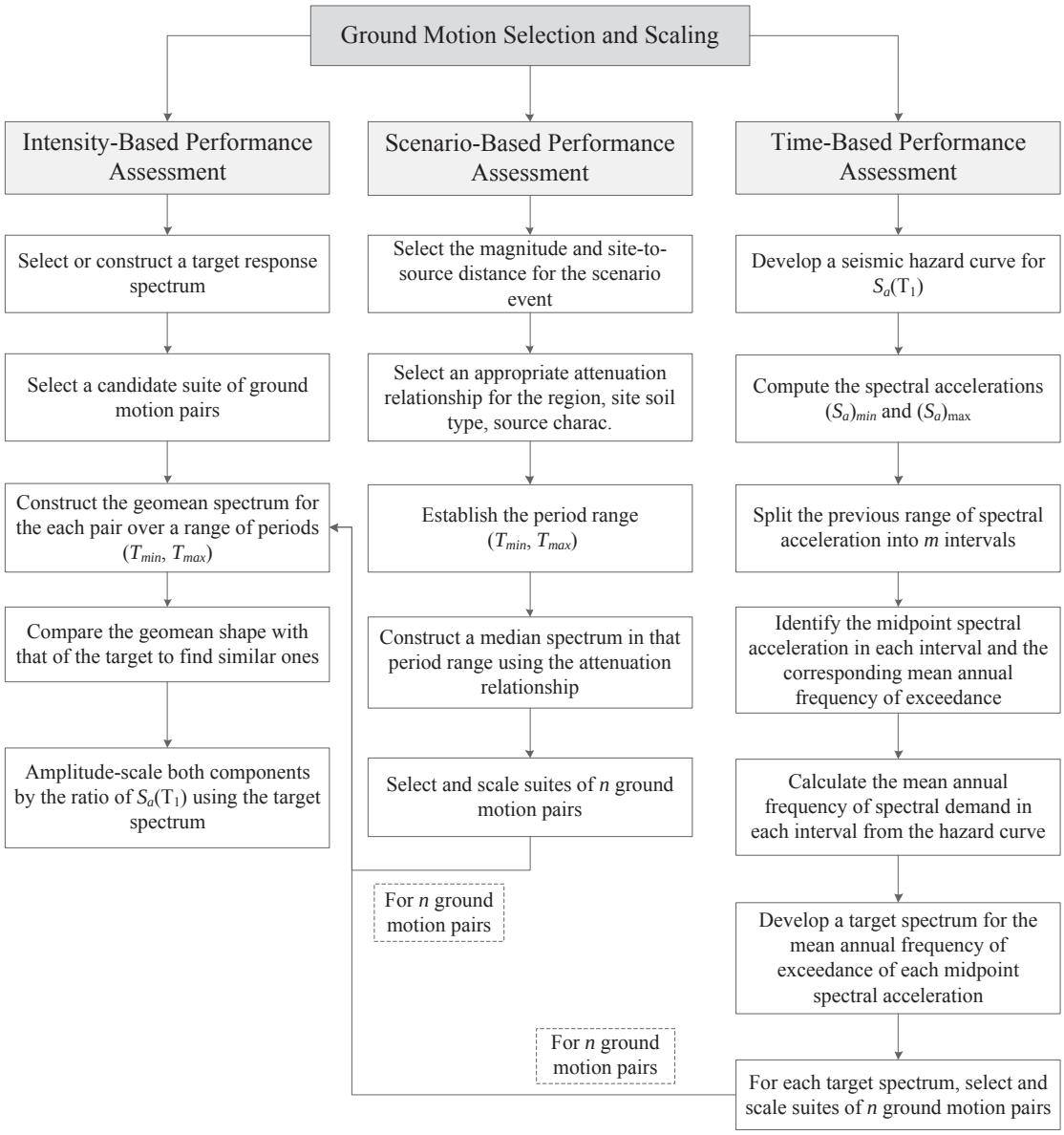

Figure 2.7: Comparison of ground motion selection and scaling for IBPA, SBPA and TBPA

2.3.1 Initiating events

Failures of dams start with some initiating event that causes an adverse change in the structure. This thesis focuses on seismic events, but initiating events can occur from loads or changing conditions during normal loading conditions such as flooding, human interaction, or landslides.

During an earthquake, inertial forces on the structure might lead to overstressing and cracking of the dam or concrete members in an appurtenant structure, or displacement of the foundation under the dam could cause overstressing or misalignment of the dam, finally a long-duration seismic event might cause a sliding instability.

Safety is assessed in terms of the probability of deaths due to uncontrolled release of water. Since it is impossible to completely assure life safety, some low probability of deaths is deemed to be tolerable, and since more deaths are generally less tolerable than fewer deaths, we offer acceptance criteria that tolerate more earthquake-related deaths albeit with lower probability.

2.3.2 Potential Failure Modes

Identifying, fully describing, and evaluating site-specific potential failure modes and sequences leading to failure are arguably the most important initial steps in conducting a structural analysis of a dam, assessing the dam safety assessment, developing an instrumentation plan, budgeting funds for modifications, and scheduling maintenance (FEMA-PFM, 2011). The process can clearly show why certain activities are undertaken or why certain decisions are made. This process lays out potential problems with a facility, develops the sequence of events required to adversely affect the facility, and finally helps all involved to better understand the facility.

A facilitated multi-discipline team (rather than individual person) is best for developing potential failure modes for a concrete dam since concrete dams are complex structures and synergy develops within a group. A complete understanding of the structure would involve team members with specialties in seismology, concrete construction, concrete materials, structural stability, foundation materials, rock mechanics, foundation stability, and dam operations.

There are two basic methods of developing potential failure modes. The first method starts with initiating events and then determines possible adverse effects. The second method identifies potentially adverse effects and then determines possible mechanisms that could lead to it. Both should be used to make sure all modes are captured.

After the potential failure modes are identified, they should be developed further by describing

the sequence of events leading to failure that occur from an initiating event.

2.3.3 Categorize Identified PFMs

The identified PFMs should be categorized based on their importance. The importance of the PFM is a function of what types of issues are deemed important to management, the client, to society, etc. This could include statements concerning the potential loss of life, economic, environmental, political, etc. The present thesis focus mainly on life safety, though they could be extended using PBEE principles to repair costs and environment impacts.

After a PFM has been identified, described and screened, each one is categorized according to the classification system shown in Table 2.2. This table gives definitions for categories to rank potential failure mode analysis by FERC-PFMA (2005) and USBR-manual (2011). It does not provide quantitative likelihood estimates for the identified PFMs.

2.4 Probabilistic Seismic Assessment of Concrete Dams

Although the application probabilistic methods in seismic safety and risk assessment of framed structures (Rosenblueth, 1956), (Cornell, 1968), (Vanmarcke, 1977) and nuclear power plants (Kennedy et al., 1980) has a half century history; however, it is relatively new in concrete dam engineering and to the best of the author knowledge, deArajo and Awruch (1998) is the first solid research on this area (will be explained subsequently).

Different researchers adopted/used/improved part of probabilistic assessment methodologies for concrete dam. Application of the probabilistic methods in concrete dam engineering can be categorized into the following groups:

- Advanced failure mode analysis
- Advanced structural analysis
- Seismic fragility analysis
- Seismic damage correlation

Table 2.2: Categories used to rank PFMs based on USBR-manual (2011) and FERC-PFMA (2005)

ID	Code	Identifier	Definition
I	USBR-USACE	*Failure is in progress or imminent*	The PFM has initiated and is in progress, in which case emergency actions may be warranted, or the situation appears to be so dangerous, that increased monitoring or other interim risk reduction actions may be warranted while risk estimates and documentation are being completed.
	FERC	*Highlighted PFM*	Those PFMs of greatest significance considering need for awareness, potential for occurrence, magnitude of consequence and likelihood of adverse response are highlighted.
II	USBR-USACE	*Failure mode is credible*	These PFMs are significant enough that they should be carried forward into a risk analysis, but do not appear to require immediate action based on the available information. Monitoring may be an appropriate risk management activity.
	FERC	*PFM considered but not highlighted*	These are judged to be of lesser significance considering need for awareness, potential for occurrence, magnitude of consequence and likelihood of adverse response. They are still described and included with reasons for and against the occurrence of the PFM.
III	USBR-USACE	*Insufficient information to determine credibility of failure mode*	There is insufficient information to make a judgment on whether these PFMs should be carried forward for risk analysis. Increased monitoring may be an appropriate interim risk management activity while information is being collected.
	FERC	*More information or analyses are needed in order to classify*	These PFMs to some degree lacked information to allow a confident judgment of significance and thus a dam safety investigative action or analyses can be recommended. Because action is required before resolution the need for this action may also be highlighted.
IV	USBR-USACE	*Failure mode is not credible*	These PFMs are clearly so remote that the likelihood of failure is negligible, and hence do not need to be carried forward for risk estimates. However, they still need to be documented along with the reasons they are considered to be negligible risk contributors. Monitoring is likely not warranted for these PFMs.
	FERC	*Failure mode ruled out or is considered not viable*	The candidate PFM is ruled out as a PFM because the team discovers that the physical possibility for the failure mode does not exist. Or the candidate PFM is considered as not a viable one because it is found to clearly be so remote as to be non-credible or not reasonable to postulate based on information available at this time.

- Seismic reliability analysis
- Quantitative risk analysis

2.4.1 Advanced failure mode analysis

- deArajo and Awruch (1998): They proposed a methodology for probabilistic finite element analysis of gravity dams. Both the concrete properties and seismic excitation were assumed to be random variables. The seismic excitation was artificially generated using a non-stationary stochastic process. On the other hand, the random concrete properties are function of mean properties and the position vector on the structural domain. The position vector itself is related to distance between each two point (usually center of elements), a scale factor, and coefficient of variation of material property. They computed the safety factors against sliding, concrete crushing at the toe and concrete cracking at the heel of the dam for 50 simulations (Monte Carlo method). They also determined the cumulative distribution of the safety factor against cracking at the heel and compared with the cumulative distribution corresponding to a Gaussian variable. They reported that a good agreement between two cumulative probabilities.

- Su et al. (2013): They proposed a probabilistic method to assess the lifetime performance of the dams under deterioration. They determined the potential failure modes of the dam and the influences of the correlations among them on series, parallel, or series-parallel structure were discussed. The limit state functions for failure modes derived. The progressive deterioration of various random variables (describe the aging) was quantified. Finally, a prediction model for remaining service life of the dam was proposed.

2.4.2 Advanced structural analysis

- Pan et al. (2015): They used an approximate incremental dynamic analysis (IDA) method for seismic performance assessment of an arch dam. The used average response spectra of

over 50 ground motions which already scaled to the target spectrum. Then, generated a three-component artificial ground motion to match the target one. The generated signal is used for single-record IDA of the dam-foundation system in different levels and the results were presented in terms of displacement, concrete cracking and joint opening. They did not verified this approximate IDA method with the conventional multiple-record IDA.

- Alembagheri and Ghaemian (2013b) and Alembagheri and Ghaemian (2013a): They performed multiple-record IDA on both the gravity and arch dams. The system nonlinearity was originated from concrete cracking and the effect of arch dam contraction joints was neglected. They also applied the monotonic and cyclic pushover analysis on dam in order to determine different limit states (e.g. yielding and ultimate points). Finally, they proposed an energy-based damage index for capacity estimation of concrete dams.

- Hariri-Ardebili and Mirzabozorg (2014): They applied endurance time analysis (ETA) method for seismic performance assessment of an arch dam. ETA provides a continuous performance curve for the dam under different seismic excitation levels. They analyses were performed for both the linear and nonlinear models and the results were correlated. Furthermore, the results of ETA method verified with conventional time history analysis (THA) at some discrete seismic excitation levels. They found that ETA and THA are in good agreement and ETA can be used as an alternative method for IDA with less computational efforts.

2.4.3 Seismic fragility analysis

- Tekie and Ellingwood (2003) and Tekie and Ellingwood (2002): Finite element method is used for modeling the dam and foundation, while the Darbe's approach (nodal masses in series with dampers) is used for water simulation. Dam-foundation interface is modeled by a Mohr-Coulomb friction law. The coupled system is analyzed using recorded ground motions and a Monte Carlo method with Latin Hypercube sampling is used to reduce the

computational efforts. The randomness in material property is originated from concrete compressive strength, friction angle, cohesion and dilation angle of foundation rock. In addition, the efficiency of vertical drains, the grout curtains and the effective uplift area are also considered as random variables. They used a normal distribution for the concrete compressive strength and a uniform distribution for all the other input variables.

Spectral accelerations of 0.3g, 0.5g, 0.7g, 0.9g, 1.0g, and 1.2g are used for the finite element analyses. Twelve finite element analyses are performed for each spectral acceleration using the selected ground motion records. They originally considered seven limit states, while they used only four of them (LS4 to LS7) for developing the seismic fragility curves:

  * LS1: Resultant outside the kern (rigid body analysis) or tension at the heel
  * LS2: Resultant outside of middle half of base of dam
  * LS3: Concrete material compressive failure (at the toe)
  * LS4: Concrete material tensile failure (at the neck of the dam)
  * LS5: Foundation material compressive failure (at the toe)
  * LS6: Sliding at the dam-foundation interface
  * LS7: Deflection of the top of the dam relative to the heel

- Lupoi and Callari (2011) and Lupoi and Callari (2012): They developed a probabilistically-based methodology for seismic performance assessment of existing concrete gravity dams. The procedure is capable of accounting for uncertainties both in material properties and in external actions (ground motion and reservoir level) and also for multiple failure mechanisms. The dynamic interaction among the dam, foundation and reservoir is considered. For the operational limit state, the following failure mechanisms are used:

  * Excessive deformation of the dam body inducing service limitation for equipment and installations.
  * Cracking or sliding at dam base.

  - Cracking at the dam neck.
  - Cracking at the upstream face.

  Four basic (material/structural) random variables are considered (as follows) and other material properties and capacity models are developed based on them.

  - Characteristic strength of concrete.
  - Geological strength index of the rock mass.
  - Error term in the drift capacity model.
  - Error term in the capacity model for tensile strength at concrete-rock interface.

  The transient analyses are performed for the combination of the ten selected ground motions (all at PGA = 0.1g) and three different reservoir levels (leading to a total of 30 simulations). Then, assuming a linear behavior, the dam response at higher seismic levels are obtained by scaling up the results calculated for PGA = 0.1g. To evaluate the response gradients, other sets of 30 analyses are required (for each basic random variable).

- Ghanaat et al. (2011), Ghanaat et al. (2012) and Ghanaat et al. (2015): They performed a comprehensive analysis on different case studies of gravity dams (overflow and non-overflow sections). Both the 2D and 3D models were investigated. The approach they employed is similar to that used by Tekie and Ellingwood (2003). They mainly focused on sliding of the dams either in based or at the neck area. They developed the fragility curves based on the probability of the sliding failure. Both the lognormal and Weibull models are used. They also compared the impact of epistemic plus aleatory uncertainties on the fragility curves with respect to only epistemic one.

2.4.4 Seismic damage correlation

- Zhang et al. (2013b), Zhang et al. (2013a) and Zhang and Wang (2013): For a same case study (2D model of a gravity dam), the authors investigated the correlation between the

different characteristics of the input ground motions and the resulted damage. The concrete damaged plasticity model including the strain hardening or softening behavior is applied in nonlinear analysis. Westergaard added mass approach is used to apply the hydrodynamic pressure in Zhang et al. (2013b), Zhang et al. (2013a), while the Lagrangian fluid-structure model is used in Zhang and Wang (2013). They mainly focused on three features:

  * Impact of mainshock-aftershock seismic sequences: Thirty mainshock-aftershock events are used. They found that as-recorded sequences of ground motions have a significant effect on the accumulated damage. Damage to the upper zone of the dam is more sensitive to the aftershock. Moreover, the global damage index of the dam for seismic sequences is 1.7 times than that for the first seismic event, on average.
  * Impact of strong motion duration: Two sets of strong motion duration are used: 70% and 90% of the Arias intensity. The originally selected 20 ground motions are truncated based on these criteria and applied to the finite element model. The results show that strong motion duration is positively correlated to the accumulated damage for events with similar response spectrum, and has significant influence on the cumulative damage.
  * Impact of near-fault and far-fault ground motions: They applied 10 near-fault and 10 far-fault ground motions to the numerical model. They reported that the nonlinear displacement time history of the dam crest under near-fault ground motions is substantially different from that obtained from far-fault ground motions. Near-fault ground motion has the potential to cause more severe damage to the dam. The upper zone of dam is more vulnerable to near-fault ground motions.

- Hariri-Ardebili and Kianoush (2015): They analyzed an arch dam including massed foundation with viscous boundary model and pressure-based fluid finite elements. A large set of artificial ground motions are generated with different intensity levels and duration. Finally, 16 representative ground motions are selected and applied to the coupled system.

The nonlinear response of the dam is correlated with the ground motion intensity level and duration using over 12 intensity measure (IM) parameter. They found that increasing the significant duration and the intensity level both lead to increasing the demand parameter. In general, crest displacement has higher correlation with IM parameter than the joint response and overstressed area ratio.

2.5 Dam Safety Decision-Making: Code Review

Risk management encompasses activities related to making risk-informed decisions, prioritizing evaluations of risk, prioritizing risk reduction activities, and making program decisions associated with managing a portfolio of facilities. Risk management includes evaluating the environmental, social, cultural, ethical, political, and legal considerations of all parts of the decision process (USBR-manual, 2011), figure 2.8.

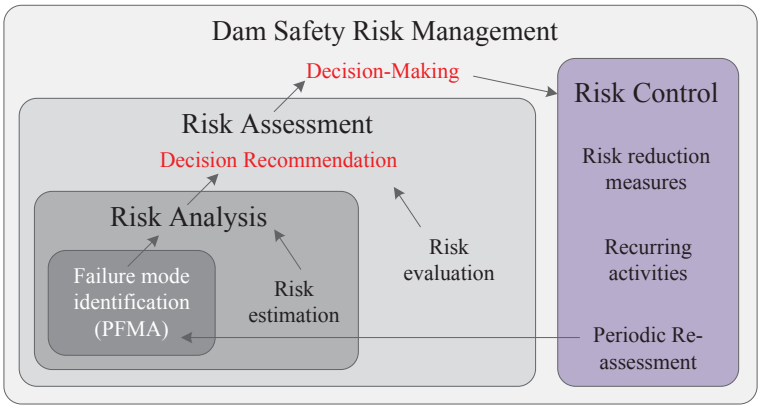

Figure 2.8: Dam safety risk management

Risk assessment is "the process of deciding whether existing risks are tolerable and present risk control measures are adequate and if not, whether alternative risk control measures are justified or will be implemented. Risk assessment incorporates the risk analysis and risk evaluation phases" (ANCOLD, 2003). Risk assessment encompasses activities including risk analyses and the decisions resulting from individual risk analyses. This typically involves developing and evaluating poten-

tial failure modes, coordinating supporting engineering studies, developing structural loads, risk analysis, consequence analysis, and recommendations to support decisions. There is some overlap between risk assessment and risk management as they are both integral in decision-making.

Several water resources-related regulators and government entities have developed tolerable risk guidelines of various origins. These ranges from fairly broad qualitative guidelines like those used by the UK Health and Safety Executive (HSE) to strict quantitative criteria, such as those developed by Australian National Committee on Large Dams (ANCOLD) to be used by regulatory agencies and dam owners. Tolerable risk means different things to different people and organizations. Some focus on economic risks to their company or organization (insurance, chemical, offshore oil and gas, etc.) while others focus on loss of life (USBR-manual, 2011).

In order to evaluate tolerable risks using quantitative risk estimates, numeric tolerable risk thresholds or guidelines have been developed by several agencies. Specifically related to dams, four entities have extensive information that relate directly to tolerable risks for water resources facilities - HSE, ANCOLD, and the New South Wales Dam Safety Committee (NSW DSC). In addition, the Canadian Dam Association (CDA) and the U.S. Bureau of Reclamation (USBR) have developed tolerable risk guidelines, which are similar.

First, the methodology used by USBR is reviewed in detail (Sec. 2.5.1). Recommendations by other agencies will briefly reviewed later.

2.5.1 U.S. Bureau of Reclamation

Reclamation uses two guidelines to assess dam safety risk, 1) "Annualized Failure Probability", which serves to fulfill the public trust responsibility associated with agency exposure as a result of dam failures, and 2) "Annualized Life Loss", where multiple fatalities are possible as the result of dam failure (USBR-manual, 2011).

- Annualized Failure Probability: There is no such thing as a dam with zero chance of failure. However, the probability of dam failure must be very low. Reclamation terms this measure of risk Annualized Failure Probability, and uses a guideline of 1 in 10,000 per year for

the accumulation of failure likelihoods from all PFMs that would result in life-threatening unintentional release of the reservoir.

- Annualized Life Loss: Reclamation defines the risk as Annualized Life Loss, and uses a guideline of 0.001 fatalities per year to address it. When the mean estimate is above the guideline of 0.001 fatalities per year, there is generally greater need to take action to reduce or better understand the risks. There is generally decreasing need to reduce or better understand the risks when they are below this guideline value. The primary means to portray risks is a risk curve that relates frequency f (mean number of events per year) of N or more fatalities, as a function of N (f-N chart). Figure 2.9 illustrates the USBR's f-N risk chart.

It is important to notice the differences between the f-N and F-N charts:

- An f-N "event" chart is composed of individual f-N pairs. Each pair typically represents one failure mode or the summation of selected failure modes. f represents the "annualized failure probability" and N represents the expected life loss or number of fatalities.

- F-N chart is, in fact, a complementary cumulative distribution function to portray risk. Horizontal axis shows the number of fatalities, N, and the vertical axis represents the annual exceedance probability of causing "N" lives or greater.

2.5.2 UK Health and Safety Executive (UK-HSE)

The HSE proposes that F-N curves can be helpful for decision-making; however, it does not specifically promote one for water resources structures. Instead it proposes figures 2.10 and 2.11 for individual and societal risk, respectively. They are inverted triangular in which the shape indicates the amount of attention and risk limit on a particular situation (HSE, 2001). Except in extraordinary circumstances, unacceptable risks must be reduced regardless of the cost of the risk reduction measures.

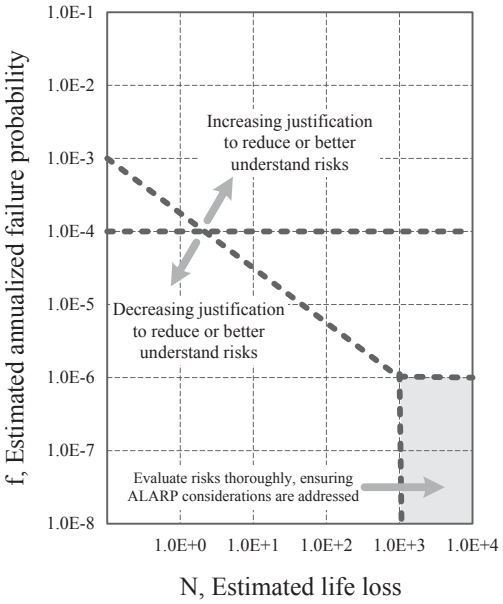

Figure 2.9: USBR risk guidelines (USBR-manual, 2011)

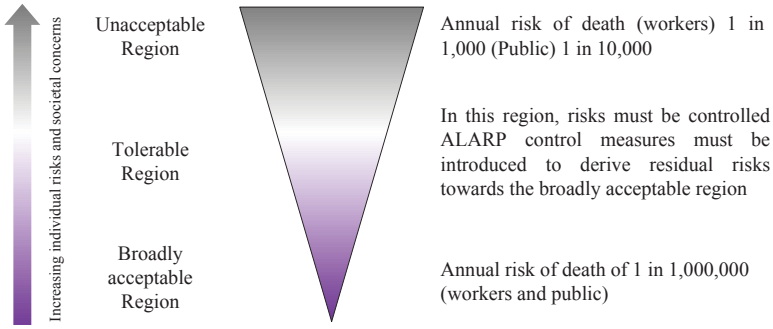

Figure 2.10: HSE individual risk limits (HSE, 2001)

2.5.3 Australian National Committee on Large Dams (ANCOLD)

For individual risk, ANCOLD sets tolerable risk limits as: "*For existing dams, an individual risk to the person or group, which is most at risk, that is higher than 10^{-4} per annum is unacceptable, except in exceptional circumstances; for new dams of major augmentations of existing dams, an individual risk to the person or group, which is most at risk, that is higher than 10^{-5} per annum is unacceptable, except in exceptional circumstances (ANCOLD, 2003).*" In addition, ANCOLD sets

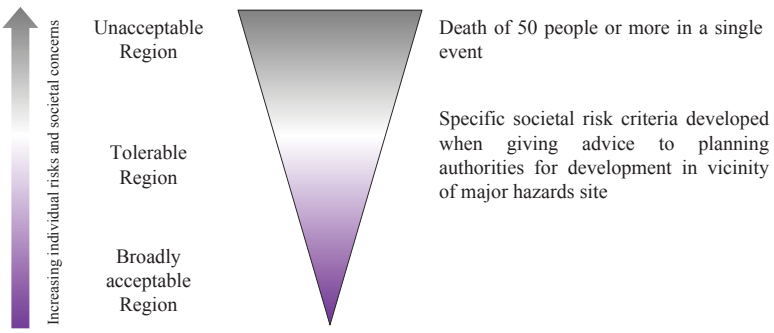

Figure 2.11: HSE societal risk limits (HSE, 2001)

tolerable risk limits for societal risk based on figure 2.12.

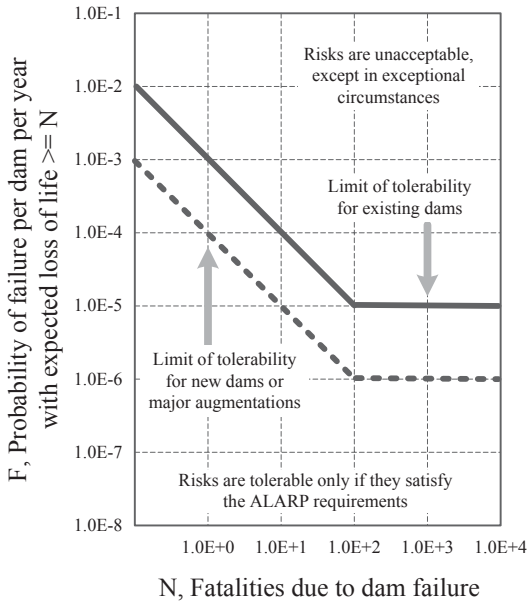

Figure 2.12: ANCOLD societal risk guidelines (ANCOLD, 2003)

2.5.4 New South Wales Dam Safety Committee (NSW DSC)

The NSW DSC guidelines are similar to that of ANCOLD with some differences. The first is that they treat dams with the potential to cause more than 1000 fatalities differently. NSW DSC social risk guidelines are shown in figure 2.13. The second exception is that they ignore the lower

bound horizontal truncation of the societal risk limit of 10^{-5} used by ANCOLD and instead adopt a more rigorous 10^{-6} limit for existing structures (NSW, 2006).

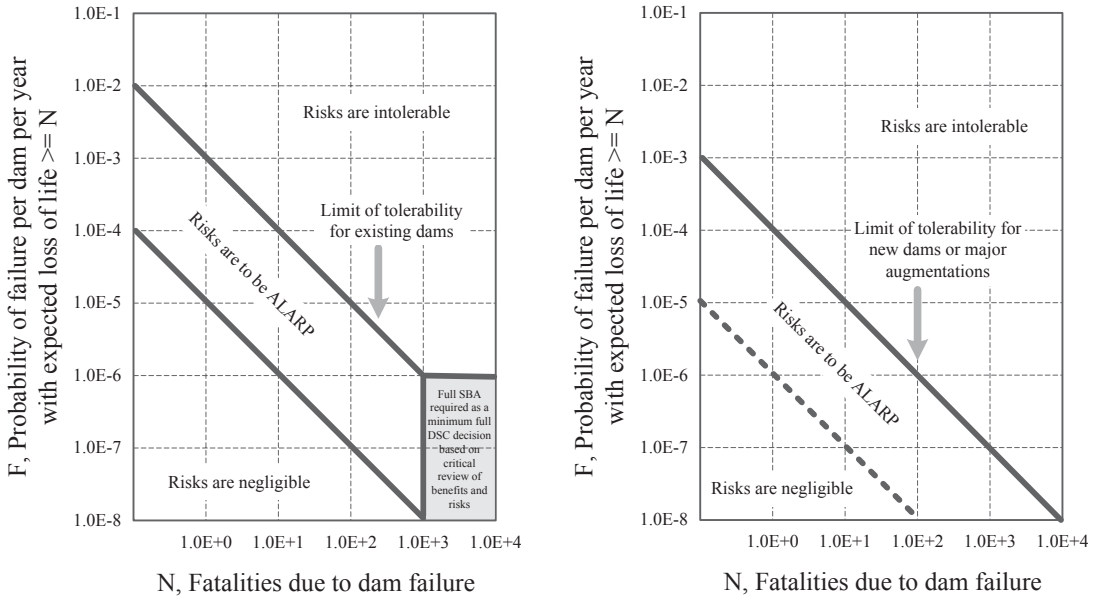

Figure 2.13: NSW DCS societal risk guidelines (NSW, 2006)

2.5.5 Canadian Dam Association (CDA)

The CDA uses similar terminology and definitions to ANCOLD, HSE, and NSW DSC. This guideline states: *Individual risk relates to concerns of how individuals see the risk from a particular hazard affecting them and their property. It is usually defined as the risk to a hypothetical member of the public living in the zone that can be affected in the event that a hazard occurs. The criteria for individual risk depend on such factors as whether or not the exposure is voluntary, whether the individual derives benefits from accepting the risk, whether the individual has some control over the risk, and whether the risk engenders particular dread (CDA, 2007).*" CDA societal risk guidelines are shown in figure 2.14.

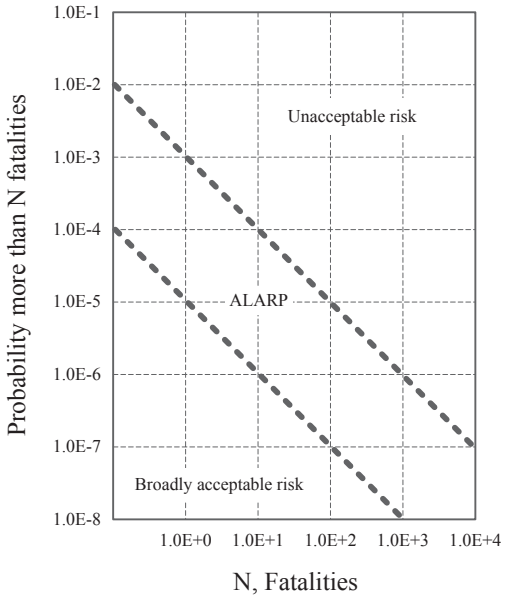

Figure 2.14: CDA societal risk guidelines (CDA, 2007)

Chapter 3

Capacity Function for Concrete Dams

This chapter is based on:

Hariri-Ardebili, M.A. and Saouma, V.E., (2015), Capacity Functions for Concrete Dams: Review and Revisit (under preparation for Bulletin of Earthquake Engineering)

3.1 Introduction

Safety of infrastructures (concrete dams in this paper) is affected by many events. A comprehensive safety evaluation methodology should takes into account all the possible ones. The final decision making can be based on either the critical one or resultant of all events with their contributions. Safety assessment can be performed within the concept of performance-based engineering (PBE). This is a process that begins with the first concepts of a project and lasts throughout the life of the structure Bertero and Bertero (2002).

PBE of buildings and infrastructure has been indirectly undertaken since the introduction of strength for concrete structures design in the 1960s Whittaker et al. (2003). It was included force-based analysis and design checking of components using:

$$\sum \alpha_i \, L_i \leq \phi \, C \tag{3.1}$$

where α_i is load factor, L_i load effects (dead load, live load, ...), ϕ a capacity reduction factor and C the component capacity.

In concrete dams, "failure" refers to the uncontrolled release of the reservoir water. This may or may not always be the case, and any other definitions are acceptable for failure based on the purpose of the project (FERC-PFMA, 2005). The initiating events leads to failure of dam are (Hariri-Ardebili et al., 2015): 1) hydrologic events such as flood and increasing flow through the spillway; 2) static events such as reservoir water load, ice load, and equipment failure; 3) material deterioration such as erosion, and alkali-aggregate reaction (AAR) in the concrete; 4) increased seepage, clogging of drains, degradation of the grout curtain; 5) seismic events such as earthquake load; and 6) other initiators such as human operating errors, fire, landslides into the reservoir, vehicular impact, underwater explosion, sabotage, vandalism.

Considering only the most probable events, i.e. seismic, hydrologic, and material degradation, the capacity of the dam should be evaluated within the context of PBE. This concept is already developed for different events, e.g. performance-based earthquake engineering (PBEE) (Porter, 2003), performance-based fire engineering (PBFE) (Wang et al., 2012), performance-based hurricane engineering (PBHE) (Barbato et al., 2013), performance-based blast engineering (PBBE) (Whittaker et al., 2003), and performance-based wind engineering (PBWE) (Ciampoli et al., 2011). One of the common points among all of them is to evaluate the capacity of the structure subjected to that specific event with varying amplitude. This helps to have the response of the system in different structural levels (i.e. linear, nonlinear, collapse).

In this paper, the concept of "capacity function" is introduced for concrete dams and is combined with the existing structural analysis techniques. Figure 3.1 shows the position of capacity function inside the global framework for performance-based assessment of concrete dams.

First the general concept and the mathematical model is presented for capacity function. Then different mechanics-, hydraulic- and earthquake-based structural analysis methodologies are reviewed in detail. Finally, their application is concrete dam engineering is studied.

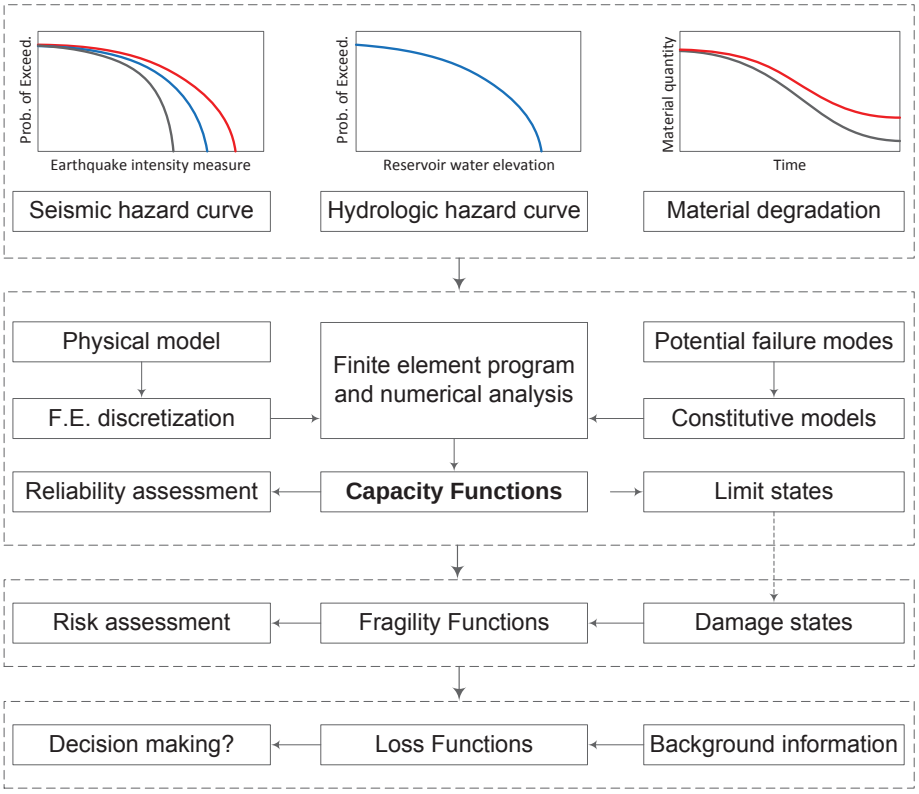

Figure 3.1: Global framework for PBE of concrete dams

3.2 Capacity Functions

3.2.1 Fundamental Definitions

First, let us distinguish different terms related to the "capacity" of the structural system.

Capacity Curve : In its original definition, this refers to a nonlinear force-displacement curve (Freeman, 1978). It is determined by statically loading the structure to calculate the roof displacement *vs.* base shear. This curve also refers to *pushover curve* (Freeman, 1998). In the lab, the load-displacement curve may be captures by set up either load control or displacement control protocols, depending on the availability of the facilities. However, using displacement control test, the post-failure can be captured. The conventional capacity curve can also be plotted in term of dissipated energy, referred to *energy-based capacity*

curve (DAmbrisi and Mezzi, 2014).

Capacity Diagram : This refers to the pseudo-acceleration *vs.* deformation spectrum ordinate (Chopra and Goel, 1999). This is computed dividing the base shear by the effective modal mass at the fundamental vibration mode and the top displacement by the mass participation factor. It is also called *capacity spectrum*.

Capacity Function : This is defined as a relationship between an external (or internal) parameter affects the capacity of the structure, referred as "stressor" (S), and "response" (R) of the system in the macro level. In spite of the conventional capacity curve, the capacity function is a more general concept and can generated by any of the initiators explained in introduction and is not limited to only seismic action.

Stressor: can be 1) incrementally increasing monotonic, cyclic or time-dependent load (or displacement, acceleration, pressure); 2) incrementally decreasing the resistance parameter or degradation of the strength properties; and 3) discrete increasing/decreasing critical parameter in a system leads to failure. In PBEE, S is usually called intensity measure (IM) parameter (Porter, 2003). However, in the present paper, S has a more general definition and refers to any quantity that its variation (continuous or discrete) may leads to progressive failure in the system and its final collapse.

Response: is a representative of the system behavior under the varying stressor. It is represented either in an absolute sense or relative one. R can be 1) single damage variable (DV) such as drift and energy dissipation, 2) combination of several DVs in term of damage index (DI); and 3) any safety monitoring index (Wang et al., 2013a). In the field of earthquake engineering, R is usually called engineering demand parameter (EDP) (Vamvatsikos and Cornell, 2004).

3.2.2 Mathematical model

Figure 3.2(a) shows a sample capacity function normalized in both axes for simplicity. Three parts are detectable in this curve 1) linear, 2) nonlinear, and 3) asymptotic to horizon. The linear part refers to the elastic behavior of the structure; the nonlinear part refers to a transient from elastic to plastic (or any other nonlinear model); and the horizontal part represents the failure/collapse of the system. Also, figure 3.2(b) shows the derivation of the vertical axis with respect to the horizontal one $\frac{\partial S}{\partial R}$. In the first part the slope is constant, in the last part it is zero, and in the transient part the slope decreases regularly or in an irregular pattern. There are three important assumptions/key-points in the ideal capacity functions:

(1) Some of the capacity estimation methods are capable of capturing the post-failure behavior as will be discussed in section 3.3.5. It means that there is another part (forth part) in capacity function which has a decreasing nature (linear or nonlinear pattern). However, in the present study, we only consider the concrete dam behavior up to failure.

(2) Depends on the progressive failure methodology (section 3.3) used to derive the capacity function, we may have only one, two or all three parts. Mathematically, the absence of each part is modeled by considering very small variation for that part ($R_i \longrightarrow 0$).

(3) The capacity function shown in figure 3.2(a) and the subsequent mathematical representation in this section are idealized (and smoothed) one. In reality, single capacity curve has not uniform trend (especially in nonlinear phase) mainly due to specific characteristics of the model and analysis. However, it is a common practice to quantify the epistemic and aleatory uncertainties and use the mean or median curve, which are smoother (Vamvatsikos and Fragiadakis, 2010).

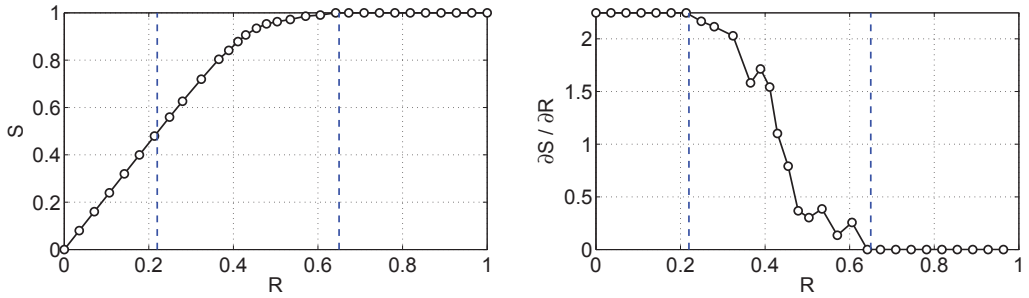

(a) Capacity function (b) Derivative of capacity function

Figure 3.2: A sample idealized capacity function (normalized form)

One can express the capacity function though analytical models. The analytical solution may have the following general form in its simplest format:

$$\begin{cases} \mathrm{S}_1 = a.\mathrm{R} + b & \text{for} \quad 0 \le \mathrm{R} < \mathrm{R}_e \\ \mathrm{S}_2 = f_N(\mathrm{R}) & \text{for} \quad \mathrm{R}_e \le \mathrm{R} < \mathrm{R}_u \\ \mathrm{S}_3 = c & \text{for} \quad \mathrm{R} \ge \mathrm{R}_u \end{cases} \tag{3.2}$$

where a, b and c are constants; f_N is a nonlinear function which represents the transition part; R_e and R_u are the limits for the elastic and ultimate responses. The following boundary conditions also should be satisfied when the three parts are connected to form an unified function:

$$\begin{cases} f_N(\mathrm{R}_e) - a.\mathrm{R}_e - b = 0 & \text{for} \quad \mathrm{R} = \mathrm{R}_e \\ f_N(\mathrm{R}_u) - c = 0 & \text{for} \quad \mathrm{R} = \mathrm{R}_u \\ \frac{\partial}{\partial \mathrm{S}} f_N(\mathrm{R}_e) - a = 0 & \text{for} \quad \mathrm{R} = \mathrm{R}_e \\ \frac{\partial}{\partial \mathrm{S}} f_N(\mathrm{R}_u) = 0 & \text{for} \quad \mathrm{R} = \mathrm{R}_u \end{cases} \tag{3.3}$$

It is possible to find a closed-form solution for the nonlinear function, f_N, by curve fitting to data obtained from numerical analyses or experimental test. Figure 3.3(a) shows an attempt to fit a three-part function to the original data points. The nonlinear least-square method is used for curve fitting (MATLAB, 2013). The residuals of the fitting also is shown in figure 3.3(b). As seen, the residuals are limited to 1% in this case. Also, all the residuals come from the second part of the curve (nonlinear transient part). For this specific example, the following function is selected:

$$f_N(\mathrm{R}) = \alpha_1 + \alpha_2.\frac{1 - e^{\alpha_3.\mathrm{R}+\alpha_4}}{1 + e^{\alpha_5.\mathrm{R}+\alpha_6}}, \qquad \mathrm{R}_e < \mathrm{R} < \mathrm{R}_u \tag{3.4}$$

where α_i (i=1, 2, ..., 6) are the constants of the model obtained from nonlinear least-square curve fitting.

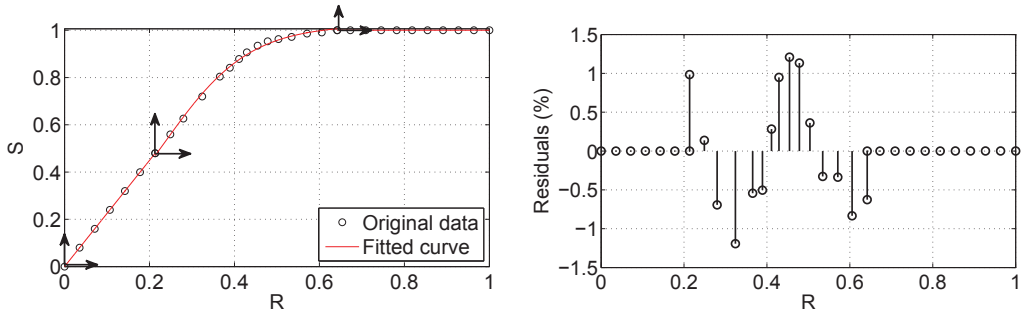

(a) Curve fitting (b) Residual assessment

Figure 3.3: Fitting an analytical capacity function

Figure 3.4 shows some of the probable form of the Eq. 3.4. All have the increasing nature. The first two ones have Concavity down and up, respectively; and the third one has an inflection point. It should be noticed that f_N is not limited to a specific form and can be represented in other forms also. Recently, Pujades et al. (2014) showed that the nonlinear part of a conventional capacity curve can be simulated by either cumulative lognormal or Beta functions.

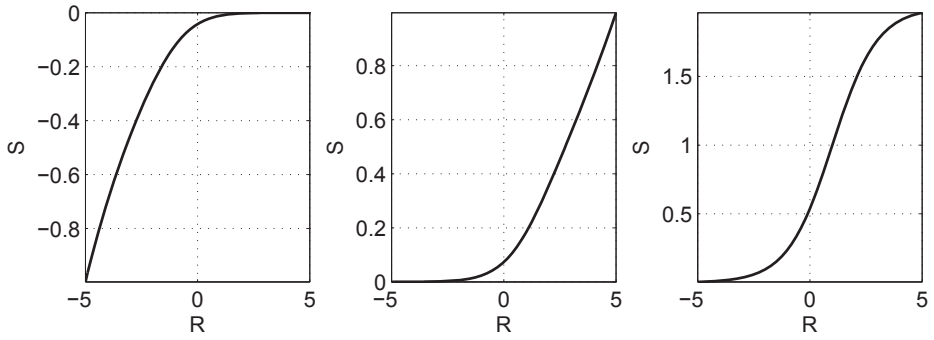

Figure 3.4: Different forms of the nonlinear function f_N based on Eq. 3.4

As discussed above, the capacity functions are used to determine the capacity of the concrete dam from linear phase to nonlinear and failure. Knowing the anatomy and general form of the capacity functions, it is important to discuss on different failure analysis methodologies that the capacity functions can be obtained.

3.3 Numerical Modeling of Progressive Failure in Concrete Dams

In general, static mechanics-based, hydraulic-based, Quasi-static, pseudo-dynamic and dynamic methods can be used for capacity estimation. Selection of the appropriate method depends on the application and desired level of accuracy. The methods for failure analysis and capacity function derivation are summarized in this section.

3.3.1 Strength Reserve Factor (SRF)

This method is usually used to study the ultimate bearing resistance (capacity) of the dam and its foundation. It is capable to emphasize the uncertainty and possible weakening effect of material strength so as to study the strength reserve degree of a structure (Wei et al., 2008).

Let κ_{SRF} is the strength reserve factor ($\kappa_{SRF} > 1.0$), and M_O is the original material property of the dam with the capability of deterioration (tensile strength of concrete, modulus of elasticity, cohesion, and ...). Then, strength reduction can be calculated as M_O/κ_{SRF}. Then, in an iterative procedure, the new properties are replaced with the previous ones. It is noteworthy that the loading condition (static loads) is kept unchanged and the system is analyzed for the new conditions. Gradually increasing κ_{SRF} leads to progressive failure from local to global scale and final failure of the system. Consequently, R can be recorded for each of the analyses up to failure. κ_{SRF} *vs.* R plot can be derived which is the capacity function indeed. Figure 3.5(a) shows this procedure schematically.

3.3.2 Time-dependent Strength Degradation (TSD)

This method is usually deals with uncertainty in time-dependent problems. This phenomenon is usually observed under special environmental conditions. Examples are alkali-aggregate reaction (AAR), alkali-silica reaction (ASR) (Saouma et al., 2015), and creep (Bazant, Z.P., 1988). AAR, creep and shrinkage are usually connected to each other. External manifestation (expansion) of AAR may be hidden by creep and shrinkage (contraction). Figure 3.6 shows a strain variation in a

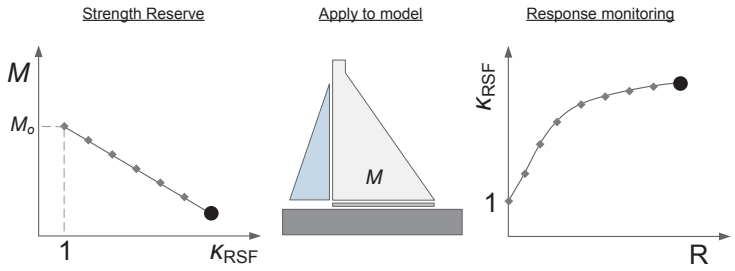

(a) Strength reserve factor

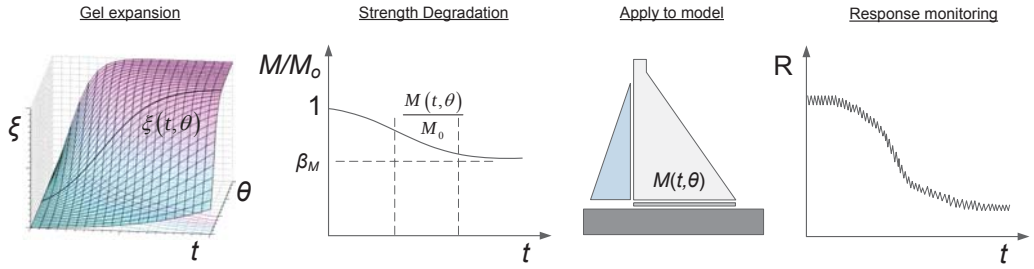

(b) Time-dependent strength degradation; AAR

Figure 3.5: Capacity estimation by mechanics-based methods

dam assuming that the elastic strain is $\varepsilon_{el} = 0.0003$, creep strain is $\varepsilon_{crp} = 0.001$ and AAR strain is $\varepsilon^{\infty}_{AAR} = 0.005$. It is apparent that the external manifestation of AAR has been substantially delayed by shrinkage/creep, and great care should be exercised in discerning shrinkage/creep contraction strains from AAR expansion ones.

AAR is a chemical reaction leads to expansion of the gel, reduction in strength and stiffness of the material, generating some micro-cracks and consequently, reducing the bearing capacity of the dam concrete (Saouma et al., 2007).

TSD-AAR is used for assessing the capacity of the concrete dams affected by ARR during its life time and define the remaining strength against the existing loads. The second author developed a comprehensive uncoupled model for the incremental free volumetric AAR strain:

$$\dot{\varepsilon}_V^{AAR}(t,\theta) = \underbrace{\Gamma_t\left(f_t'|w_c,\ \sigma_I|COD_{max}\right)\Gamma_c\left(\bar{\sigma},\ f_c'\right)}_{\text{Retardation}}\ \underbrace{g(h)}_{\text{Humidity}}\ \underbrace{\dot{\xi}\,(t,\theta)}_{\text{Kinetics}}\ \underbrace{\varepsilon^{\infty}|_{\theta=\theta_0}}_{\text{Strain}} \tag{3.5}$$

- Retardation: Γ_t and Γ_c account for AAR reduction due to tensile cracking and the AAR

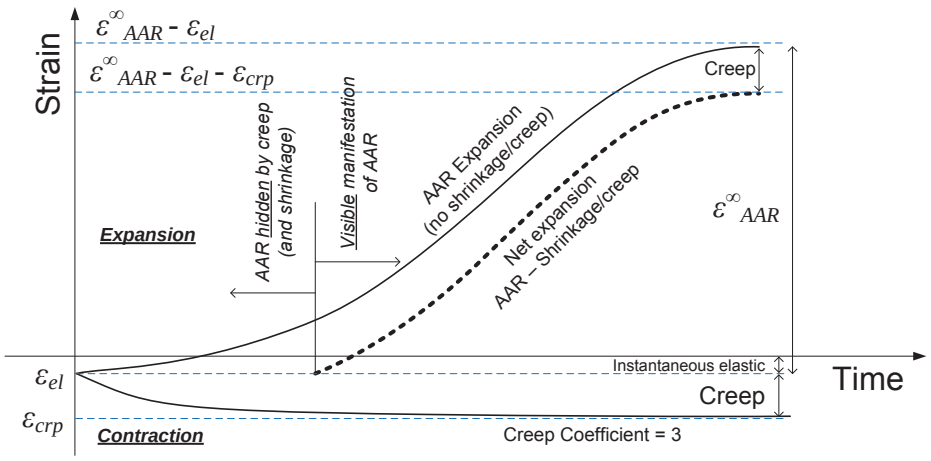

Figure 3.6: AAR and creep interaction (Saouma, V., 2014)

volumetric expansion reduction under compressive stresses. $f_t{}'$ and $f_c{}'$ are the tensile and compressive strength, respectively. σ_I is the first invariant of the stress tensor, $\bar{\sigma}$ is the combination of principal stresses. COD_{max} is the maximum crack opening displacement at the Gauss point, and w_c the maximum crack opening displacement on the tensile softening curve.

- Humidity: $g(h)$ is function of relative humidity, h. For most of the practical cases, $g(h) \longrightarrow 1$.

- Kinetics: In the present paper, the AAR expansion evolution is modeled using thermodynamical-based Larive (1997) model:

$$\xi\left(t,\theta\right) = \frac{1 - e^{-\frac{t}{\tau_c(\theta)}}}{1 + e^{-\frac{t-\tau_l(\theta)}{\tau_c(\theta)}}} \tag{3.6}$$

  where $\tau_l(\theta)$ and $\tau_c(\theta)$ are the temperature-dependent latency and characteristic times, respectively.

- AAR strain: ε^{∞} is the maximum free volumetric expansion at the reference temperature θ_0.

This AAR process results in time-dependent material deterioration:

$$\frac{M(t,\theta)}{M_0} = 1 - (1 - \beta_M)\,\xi(t,\theta) \tag{3.7}$$

where M is either modulus of elasticity, E, or tensile strength, $f_t{}'$, M_0 is the original material property and β_M is residual fractional value when strain tends to $\varepsilon^{\infty}_{AAR}$.

The numerical formulation of AAR expansion and material degradation/cracking is already applied in the finite element code "Merlin" by the second author. A sample application of the proposed model on two concrete dams and a RC frame structure is discussed in Saouma et al. (2007). Once the time-dependent material degradation is applied in the numerical model, the system is analyzed under the current load condition in order to determine the capacity function. Time history of the desired R is recorded. This procedure is shown in figure 3.5(b).

3.3.3 Hydro-pressure Overload Factor (HPOF)

This method mainly deals with the uncertainty of the applied load to determine the bearing capability of the structure. It is also called triangle overloading method through a progressive overloading of the upstream water pressure, which is assumed equivalent to the increase of water density. Meantime, all other properties of the dam and foundation are kept unchanged (Li and Ren, 2013).

Let κ_{HPOF} is the overload factor ($\kappa_{HPOF} > 1.0$), and P_0 denotes the total hydrostatic load at the normal reservoir level. Then, overloading can be calculated as $\kappa_{HPOF} \times P_0$ (Liu et al., 2003). In this method, the shape of the loading vector is the same for all increments. Therefore, the finite element model can be overloaded by multiplying the mass density of water in overload factor, i.e. $\kappa_{HPOF} \times \rho_w$.

Hydro-pressure overload factor method is a suitable way to calibrate the the structural physical-model experiments (Zhu et al., 2010) where the hydrostatic pressure is applied by servo-controlled hydraulic jacks on the upstream face. This method usually needs a large κ_{HPOF} to leads collapse of the system. Consequently, κ_{HPOF} *vs.* R plot can be derived for the system as shown in

figure 3.7(a).

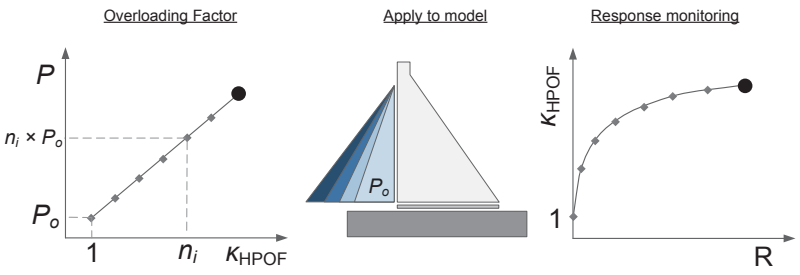

(a) Hydro-pressure overload factor

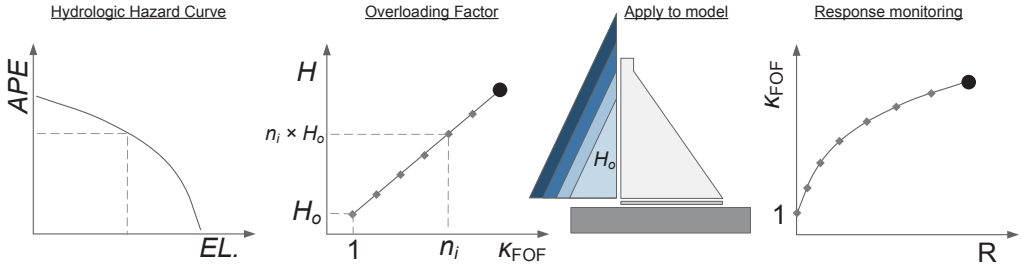

(b) Flood overload factor

Figure 3.7: Capacity estimation by hydraulic-based methods

3.3.4 Flood Overload Factor (FOF)

This method mainly deals with the uncertainty in potential flood on dam and the resultant applied pressure to determine the capability of the structure. In this method, the dam is overloaded by increasing the water head continuously. A sample application explained in (Comi et al., 2009). This method is similar to HPOF; however, technically in FOF the applied load is more uniform in height, while in HPOF, the main overloading is handled by the base of the dam. In 2D gravity dams, both the HPOF and FOF methods may end up to a similar capacity functions, because the gravity dam is only stands on its base. In 3D arch dams, the structure is supported both in base and the abutments (support along the height). Thus, HPOF and FOF may lead to different failure modes and consequently, different capacity functions.

First, a hydrologic hazard curve should be derived for the reservoir (Swain et al., 2004). It is

a graph of peak flow (or volume or maximum reservoir elevation - El.) versus annual probability of exceedance (APE). Then, the head of the water is increased based on a linear protocol. Let κ_{FOF} is the flood overload factor ($\kappa_{FOF} > 1.0$), and H_0 denotes the normal reservoir level. Then, flood overloading is calculated for new water level as $\kappa_{FOF} \times H_0$. The shape of the loading vector in FOF is different than HPOF. Figure 3.7(b) shows the step-by-step procedure.

3.3.5 Pushover-based Analysis (POA)

This method is mainly used to determine the load-displacement curve in the structural systems. In this method, the magnitude of applied load (or displacement) is increased incrementally according to a predefined protocols up to the failure. Extracting the capacity curve is usually one of the steps in POA. Different versions of the full POA for the frame structures investigated already by Freeman (1978), Chopra and Goel (1999), Fajfar (2000), Chopra and Goel (2002), Antoniou and Pinho (2004b), Casarotti and Pinho (2007) and Giorgi and Scotta (2013). These are different classifications for POA. Classification based on the type of the load vector (varying quantity):

- Forced-based Pushover Analysis (FPA): In this method, a scaled force vector is applied along the structure. In each step, the index point displacement is plotted *vs.* base shear.
- Displacement-based Pushover Analysis (DPA): In this method, a displacement vector is applied incrementally to the structure and the corresponding base shear is recorded. Subsequently, the base shear *vs.* max displacement is plotted for the structure (Antoniou and Pinho, 2004b).
- Energy-based Pushover Analysis (EPA): In this method, the displacement is applied based on the energy (area under the force-displacement curve) increments (Hernandez-Montes et al., 2004). Figure 3.8(a) compares three above-mentioned POA methods for a sample frame.

In the another classification, the POA is categorized based on the applied load distribution pattern:

- Conventional POA (CPOA): CPOA is the nonlinear incremental-iterative solution of the equilibrium equation $\mathbf{KU} = \mathbf{P}$ in a finite element formulation, where $\mathbf{K}$, $\mathbf{U}$ and $\mathbf{P}$ are nonlinear stiffness matrix, displacement and applied load vectors, respectively. In this method, the lateral load can be a set of forces or displacements that have a necessarily constant ratio throughout the analysis (fixed pattern) (Papanikolaou and Elnashai, 2005). The critical parameters in CPOA are: 1) the lateral load nature, 2) load distribution pattern along the height, 3) load magnitude, 4) number of applied load steps, 5) iterative strategy, and 6) the convergence criteria.

- Adaptive POA (APOA): In APOA, the analysis starts by assuming an initial lateral load distribution whereas the additional loads imposed in subsequent increments are calculated from the previous load step (Antoniou and Pinho, 2004a). The applied load is updated based on the instantaneous dynamic characteristics of the structure and a site-specific spectrum. Figure 3.8(b) shows two capacity functions for CPOA and APOA and also the load distributions in different levels of elastic, yielding, and collapse.

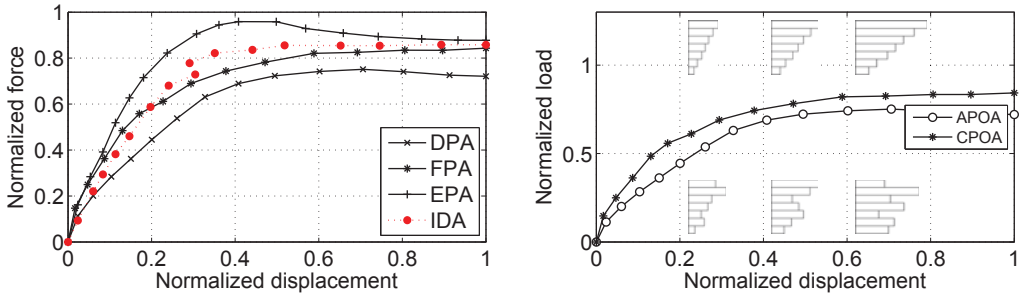

(a) Based on applied quantity (b) Based on conventional and adaptive

Figure 3.8: Classification of the pushover-based capacity functions

The following subsections classify the POA based on the lateral load pattern distribution on the concrete dams:

3.3.5.1 Invariant single load vectors

This method which is recommended by FEMA (2000) includes two sets of lateral load distributions:

(1) Load vector consists of a vertical distribution proportional to:

- Pseudo lateral load which is governed by $f_i^* = m_i(h_i)^k$ at the height of the structure, where, f_i^* is the lateral force, m_i is the mass of the i^{th} lumped mass, h_i is the height of the i^{th} lumped mass above the datum and the exponent k=1 is used for the structures with $T_1 \leq 0.5$ s (which is the case for most of the concrete gravity dams).
- Elastic first mode shape which is governed by $f_i^* = m_i\phi_{i1}$ at the height of the structure. In this load vector, ϕ_{i1} is the fundamental mode shape component at the i^{th} lumped mass.
- Story shear distribution computed by response spectrum analysis in which f^* is defined by the lateral force back-calculated from the story shears determined by linear response spectrum analysis of the structural system including at least 90% of the total mass. For the gravity dams, the story shear is computed along the lift joints.

(2) Load vector consists of mass proportional uniform load pattern, $f_i^* = m_i$, or adaptive load patterns that changes as the structure is displaced. This distribution should be modified from the original distribution by considering properties of the yielded structure.

3.3.5.2 Invariant multi-mode vectors

(1) Modal Pushover Analysis (MPOA): In MPOA, the seismic demand due to individual terms in the modal expansion of the effective earthquake forces is determined by a POA using the inertia force distribution for each mode. Combining these modal demands provides an estimate of the total seismic demand on inelastic systems (Chopra and Goel, 2002). In

MPOA, the lateral force distribution for the in each mode is expressed as:

$$f_n^{\mathrm{MPOA}} = \underbrace{\frac{\{\phi_n\}^T [m] \{i\}}{\{\phi_n\}^T [m] \{\phi_n\}}}_{\Gamma_n} [m] \{\phi_n\} \underbrace{\omega_n^2 D_n}_{A_n} \tag{3.8}$$

where f_n^{MPOA} is the lateral force distribution in each mode, $[m]$ is the mass matrix of the structure, $\{\phi_n\}$ the corresponding mode shape, ω_n the frequency and D_n the modal displacement. Γ_n is the modal participation factor of the nth mode and $\{i\}$ is the unit vector.

(2) Modified Modal Pushover Analysis (MMPOA): The MMPOA is an extension of MPOA, combines the elastic influence of higher modes with the inelastic response of a first mode pushover analysis using modal combination rules. The procedure involves conducting a nonlinear time history analysis of the first-mode SDOF system unless an inelastic response spectrum is available for the target (design) ground motion (Chopra and Goel, 2002).

(3) Upper-bound Pushover Analysis (UBPOA): The UBPOA is based on utilizing a single load vector obtained as the combination of the first mode shape and a factored second mode shape. The spectral displacements corresponding to elastic first and second mode periods are estimated from the elastic spectrum of the considered ground motion and the upper-bound contribution of the second mode is established using modal participation factors (Chopra and Goel, 2002).

3.3.5.3 Hybrid load vector

As it was mentioned already, the lateral load vector should be applied to the structural system with the same (or as close as possible) pattern of the imposed seismic lateral loads in an earthquake event. Despite of the conventional frame structures in which the load vector is mainly composes by the inertia loads due to the frame self-weight, concrete dams experience one another load vector due to the reservoir water pressure which is the hydrodynamic load. Thus, a hybrid load vector is required to be applied incrementally.

For concrete gravity dams, obviously there is a non-uniform mass distribution along the height. Gravity dams usually have small vibration period and are known as first-mode predominant structures. Figure 3.9 shows the variation of the natural period of a typical gravity dam as well as some of the selected mode shapes based on finite element technique. Thus, assuming that dynamic behavior of the gravity dam is mainly originated from its first vibration mode, the inertia load vector can be represented as:

$$f_{inr}(z) \quad = \quad m_c(z)\, \phi_1(z) \tag{3.9}$$

where $f_{inr}(z)$ is the lateral load vector due to inertia loads, $m_c(z)$ represents the mass distribution along the height of the dam, $\phi_1(z)$ is the normalized fundamental model shape of the dam, and z is measured from the dam base. Considering the homogeneous concrete in dam body, the mass distribution is proportional to the width of the dam along its height. Thus, for the equal increments of the dam height $m_c(z) = \rho_c b(z)$, where ρ_c is the concrete mass density and $b(z)$ is the height-dependent dam width.

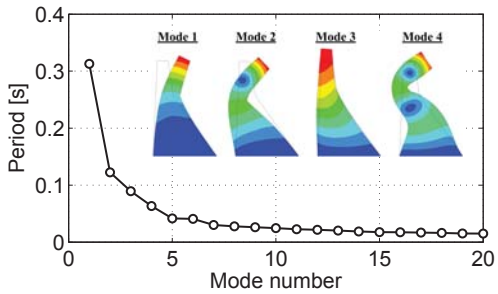

Figure 3.9: Modal analysis of a typical gravity dam including major mode shapes

Subsequently, the hydrostatic pressure and total force are function of the water height and represent as:

$$p_{hst}(z) = \rho_w\, g\, (H_w - z), \quad f_{hst}(z) = \frac{1}{2}\rho_w\, g\, (H_w - z)^2 \tag{3.10}$$

where ρ_w is the water mass density and H_w is the reservoir water height.

During an earthquake, the interaction between the dam and the reservoir creates additional pressures on the upstream face of the dam. These hydrodynamic pressures may be approximated

either by the Westergaard (1933) formula or Zangar (1953).

- Westergaard (1933) uses a parabolic approximation for the additional pressures due to earthquake motion as:

$$p^{w}_{hdy}(z) = \frac{7.99\,\alpha_{GM}\,K_{\theta}}{\sqrt{1-7.75\left(\frac{H_w}{1000T}\right)^2}}\sqrt{H_w(H_w-z)} \tag{3.11}$$

  where α_{GM} measures the intensity of the ground motion by the relation $a_g = \alpha_{GM} g$, where a_g is the maximum horizontal acceleration. For the sloped upstream face, a correction factor K_θ should be applied. For an angle of slope θ from the vertical, the correction factor is $K_\theta = \cos^2\theta$, and T is the period to characterize the ground seismic acceleration imposed on the dam. In this relation units are in kilo-newton, meter, and seconds.

- Using an electric analog Zangar (1953) determined experimentally the hydrodynamic effect of horizontal earthquake action on dams having upstream faces with either constant or compound slopes. The pressure is given by:

$$p^{z}_{hyd} = \underbrace{\frac{C_m}{2}\left[\frac{z}{H_w}\left(2-\frac{z}{H_w}\right)+\sqrt{\frac{z}{H_w}\left(2-\frac{z}{H_w}\right)}\right]}_{C_z}\alpha_{GM}\rho_w H_w \tag{3.12}$$

  where all the parameters are similar to Westergaard model and C_z is a coefficient with the maximum value of C_m. Figure 3.10(a) shows the variation of C_m and C_z at the dam base for different slopes of the upstream face. As seen, almost for all angles, the C_z is not maximum at the base. Also, figure 3.10(b) represents the values of the empirical pressure coefficient, C_z, with respect to the normalized height.

All the inertia, hydrostatic and hydrodynamic forces should be combined to form the final lateral load vector on the dam. The total lateral load vector can be composes as:

$$f_{hybrid}(z) \;=\; \delta_1 f_{inr}(z) + \delta_2 f_{hst}(z) + \delta_3 f_{hdy}(z) \tag{3.13}$$

where δ_i (i=1, 2, 3) is the weight proportional factors among the load vectors and should be obtained for the considered dam by comparison of the total base shear of the dam for the full and

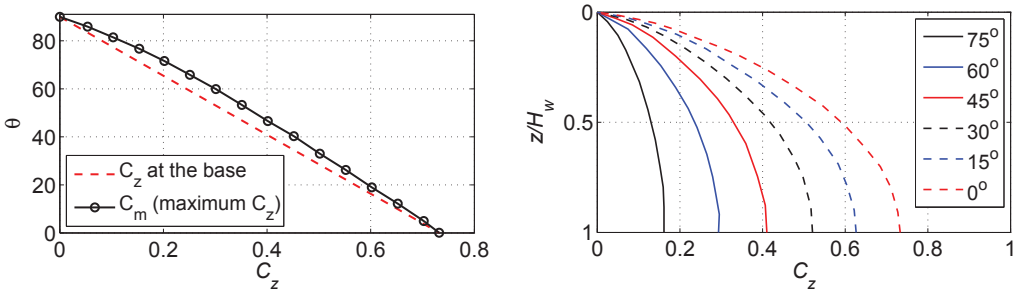

(a) Comparison of C_z at the base and C_m (b) Variation of C_z for different θ

Figure 3.10: Zangar (1953) pressure coefficient

empty reservoirs. There are some preliminary recommendations by Alembagheri and Ghaemian (2013b) for a specific gravity dam (Pine-Flat dam).

It should be noticed that the hydrostatic force is independent of earthquake and is kept unchanged during incrementally increasing the inertia and hydrodynamic loads. Another important point in correct derivation of a capacity function for a dam-reservoir-foundation system based on POA is to account for the uplift pressure at the dam-foundation interface. Uplift pressure decrease the capacity of the dam. Note that the uplift is not affected by earthquake (its depends on the head water and the crack length, l_{cr}, at the dam-foundation interface). Figure 3.11 shows a flowchart for applying a hybrid load vector on the coupled dam-reservoir-foundation system.

It is noteworthy that due to un-biased nature of the concrete dams, the computed lateral load should be applied twice monotonically and in separate analyses, i.e. on the upstream face towards the downstream direction, and on the downstream face towards the upstream direction. The final function is the one with less capacity.

3.3.6 Cyclic Pushover Procedure (CPP)

In the POA, the loads are applied statically to the structure and thus strain rate is negligible. However, when a concrete structure is subjected to cyclic loading, cumulative damage occurs under repeated loads resulting in stiffness degradation and strength deterioration (Panyakapo, 2014). A research shows that the monotonic loading provides greater strength than the cyclic loading for

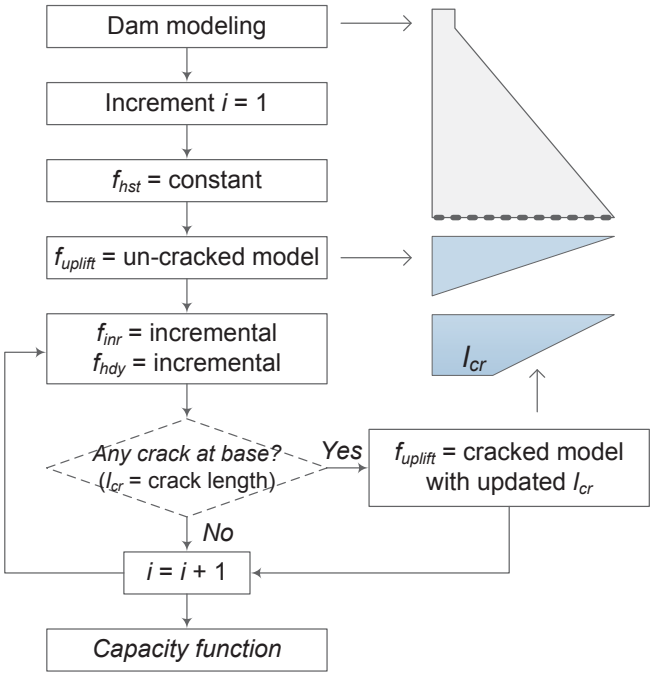

Figure 3.11: Algorithm for derivation of capacity function using hybrid load vector

RC frame structures (Koutromanos et al., 2011). Considering that the mass concrete structures (concrete dams in general as brittle structures) follow the same rules, it is more appropriate to apply a cyclic load to capture the capacity function. Similar to Eq. 3.8, a lateral force vector can be derived for a CPP as suggested in (Panyakapo, 2014):

$$f_n^{\mathrm{CPP}} = \lambda_j \Gamma_n [m] \{\phi_n\} A_n \tag{3.14}$$

where f_n^{CPP} is the lateral force distribution for cyclic pushover in each mode. j defines the sequence numbers of peak displacement for the specified displacement history, and $\lambda_j = (-1)^{j+1}$ is a factor defines the direction of force.

Key point in successful implementation of CPP is to use the appropriate displacement time history. Different displacement time histories were proposed for experimental studies which can be distinguished in: 1) total number of cycles, 2) number of initiation cycles, 3) number of primary cycles, 4) inclusion of trailing cycles, 5) inclusion of repeating cycles, 6) sequence of amplitudes of

primary cycles, 7) reference parameter, and 8) loading symmetry (Filiatrault et al., 2008).

To the best of the authors knowledge, there is no specific recommendation for appropriate selection of the cyclic loading protocol on the concrete dams; however there are some applications as explained in Ghobarah and Ghaemian (1998) and Alembagheri and Ghaemian (2013b). In the present paper, the following protocols are recommended for concrete dams:

Experimental Cyclic Test Protocol : Displacement histories can be categorized based on the type of the structure as:

- Concrete structures: New Zealand protocol (Cheung et al., 1991)
- Steel structures: ATC-24 protocol (Council, 1992), SAC protocol (Clark et al., 1997).
- Wood structures: FCC protocol (Karacabeyli, 1998), ASTM E72 protocol (1995), ASTM E564 protocols (1995), CEN protocol (1995), ISO protocol (1998), CUREE-Caltech protocol (2000)
- Masonry structures: Sequential Phase Displacement (SPD) protocol

New Zealand protocol (Cheung et al., 1991) which is basically developed for concrete structures can be a good choose for concrete dams. Also, SPD can be used considering that the cracking pattern of the masonry material is similar to mass concrete.

New Zealand protocol is based on a yield displacement, Δ_y, obtained by extrapolating the displacement of the test specimen at 75% of the theoretical strength, V_i, measured during the third cycle of the loading sequence ($\Delta_y = 1.33\Delta_{0.75V_i}$). Although this protocol does not need to preliminary monotonic test, theoretical strength of the test specimen should be defined first. Displacement history for this protocol is shown in figure 3.12(a). The first three cycles are load controlled. The first two cycles impose a lateral force corresponding to 50% of V_i. The first yield displacement is determined in the third cycle. The other cycles are displacement controlled based on displacement ductility ratio ($\mu_\Delta = \Delta/\Delta_y$).

It is clear that the capacity function will have a cyclic nature in this method. The envelope

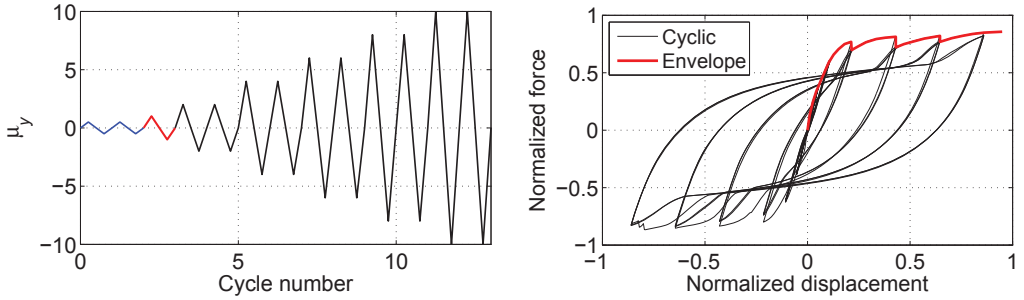

(a) Displacement history (b) Cyclic and envelope capacity functions

Figure 3.12: Cyclic pushover procedure for New Zealand protocol

of this loop should be determined to obtain a capacity function similar to monotonic loading. For this purpose, ASCE/SEI4106 (2007) criterion can be used which takes into account the strength and stiffness deterioration. The capacity function is obtained using the points given by the intersection of an unloading branch and the loading curve of the next load cycle that goes to a higher level of displacement. Figure 3.12(b) shows the cyclic pushover function and its envelope (capacity function) for a sample frame. The envelope curve may be smoothed further to be used in conjunction with the analytical solution provided in section 3.2.2.

Numerical Cyclic Loading Protocol : Filiatrault et al. (2008) proposed a numerical cyclic protocol which was resulted taking into account the general properties of all the experimental protocols. This is two-step process including both the monotonic and cyclic analyses:

(1) Monotonic POA: Perform a preliminary POA and derive the capacity curve. Identify the failure displacement, Δ_y. The expected failure displacement corresponds to a fraction, α_y, of the maximum base shear. α_y is either calibrated based on the results of IDA or approximately is 0.80 (Filiatrault et al., 2008).

(2) Cyclic POA: Perform a CPP as discussed in the previous case. The only difference is a new displacement history. The new protocol includes 7 cycle groups and 3 cycles in each one (totally 21 cycles). The amplitude for 7 groups are: $\mu_\Delta = \Delta/\Delta_y = 0.1$, 0.2,

0.3, 0.4, 0.6, 0.8 and 1.0.

The control point (target point) for a frame structures is usually located at the center of mass at the roof level. Due to special shape of the concrete dams (specially 3D model of arch dams), the displacement distribution pattern is usually non-uniform both in height and in cross-stream directions. The control point for concrete dams may highly affected by local failure modes or partially failure of dam while it does not a representation of the global failure mode. So the control point should be selected considering the global failure mode of the dam. It is possible to track the capacity curve for more than one control point at the start of the assessment process, while the final capacity curve should be chosen based on overall failure of the dam. For 2D model of gravity dams with a standard body topology, the target point can be selected as the crest node on upstream face, while the node located at the point of slope discontinuity on the downstream face can be also candidate as target point. For 3D model of arch dam, further invitations are required to reveal the location of the target point both in height and in cross-stream directions in the case of symmetry ans un-symmetry typologies.

3.3.7 Equivalent Static Lateral Force (ESLF)

Response spectrum analysis (RSA) estimates the peak responses directly from the earthquake design spectrum and usually is used for preliminary design and safety evaluation of concrete gravity dams. In a series of publication, Fenves and Chopra (1984), Fenves and Chopra (1987), Løkke and Chopra (2013) and Løkke and Chopra (2014) developed an analytical solution for RSA of gravity dam-foundation-reservoir system using the ESLF. It is possible to adopt this equivalent lateral force vector and apply it incrementally to the dam.

Considering only the fundamental vibration mode and neglecting the vertical component of the ground motion, the dam alone can be subjected to ESLF acting on the upstream face as (Løkke and Chopra, 2013):

$$f^{\mathrm{ESLF}}(z) = \frac{\widetilde{L_1}}{\widetilde{M_1}} \frac{A\left(\widetilde{T_1}, \widetilde{\zeta_1}\right)}{g} \left[w_s(z)\phi_1(z) + g\, p(z, \widetilde{T_r}) \right] \tag{3.15}$$

where $\phi_1(z)$ is the horizontal component of displacement at the upstream face of the dam in the fundamental mode supported on a rigid foundation with empty reservoir; $w_s(z)$ is weight per unit height of the dam; g is the ground acceleration. The generalized mass, $\widetilde{L_1}$, and generalized earthquake force coefficient, $\widetilde{M_1}$ are:

$$\begin{aligned} \widetilde{M_1} &= (R_r)^2 \frac{1}{g} \int_0^{H_s} w_s(z)\, \phi_1^2(z)\, dz \\ \widetilde{L_1} &= \frac{1}{g} \left(\frac{w_r H_w^2}{2} \right) \left(\frac{H_w}{H_s} \right)^2 A_p + \frac{1}{g} \int_0^{H_s} w_s(z)\, \phi_1(z)\, dz \end{aligned} \tag{3.16}$$

where H_w and H_s are the height of water and dam in meter, respectively; w_r is the unit weight of the reservoir, R_r is the period lengthening ratio and depends on the wave reflection coefficient, α_w, H_w/H_s, and mass concrete modulus of elasticity in MPa, E_s. A_p is the hydrodynamic force coefficient corresponding to period ratio, $R_w = \frac{4H_w}{C_w} \frac{1}{\widetilde{T_r}}$ and α_w (Figure 3.13). C_w is the velocity of the pressure wave in the water.

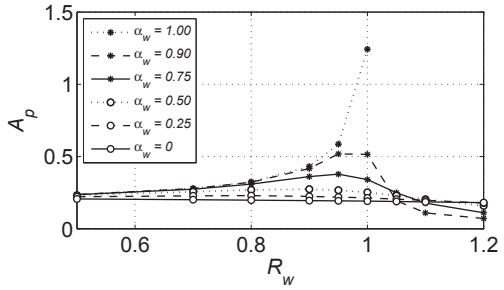

Figure 3.13: Standard values for A_p (Løkke and Chopra, 2013)

The fundamental period of the dam-reservoir, $\widetilde{T_r}$, dam-reservoir-foundation, $\widetilde{T_1}$, and the damping ratio of the equivalent SDOF system of dam-reservoir-foundation, $\widetilde{\zeta_1}$ are(Løkke and Chopra, 2013):

$$\begin{aligned} \widetilde{T_r} &= R_r T_1\,, \quad T_1 = 0.38 \frac{H_s}{\sqrt{E_s}} \\ \widetilde{T_1} &= R_r R_f T_1 \\ \widetilde{\zeta_1} &= \frac{1}{R_r} \frac{1}{(R_f)^3}\, \zeta_1 + \zeta_r + \zeta_f \end{aligned} \tag{3.17}$$

where T_1 is the fundamental period of the dam body itself on rigid foundation, R_f is the the period-lengthening ratio which depends on E_f/E_s where E_f is the foundation modulus of elasticity, ζ_1 is

the viscous damping ratio of the dam body itself, ζ_r is the added damping due to dam-reservoir interaction and reservoir bottom absorption, ζ_f is the added radiation and material damping due to dam-foundation interaction, and the constant hysteretic damping factor for the foundation rock, η_f. Figures 3.14 and 3.15 shows the standard values of R_r, ζ_r, R_f and ζ_f for concrete gravity dams.

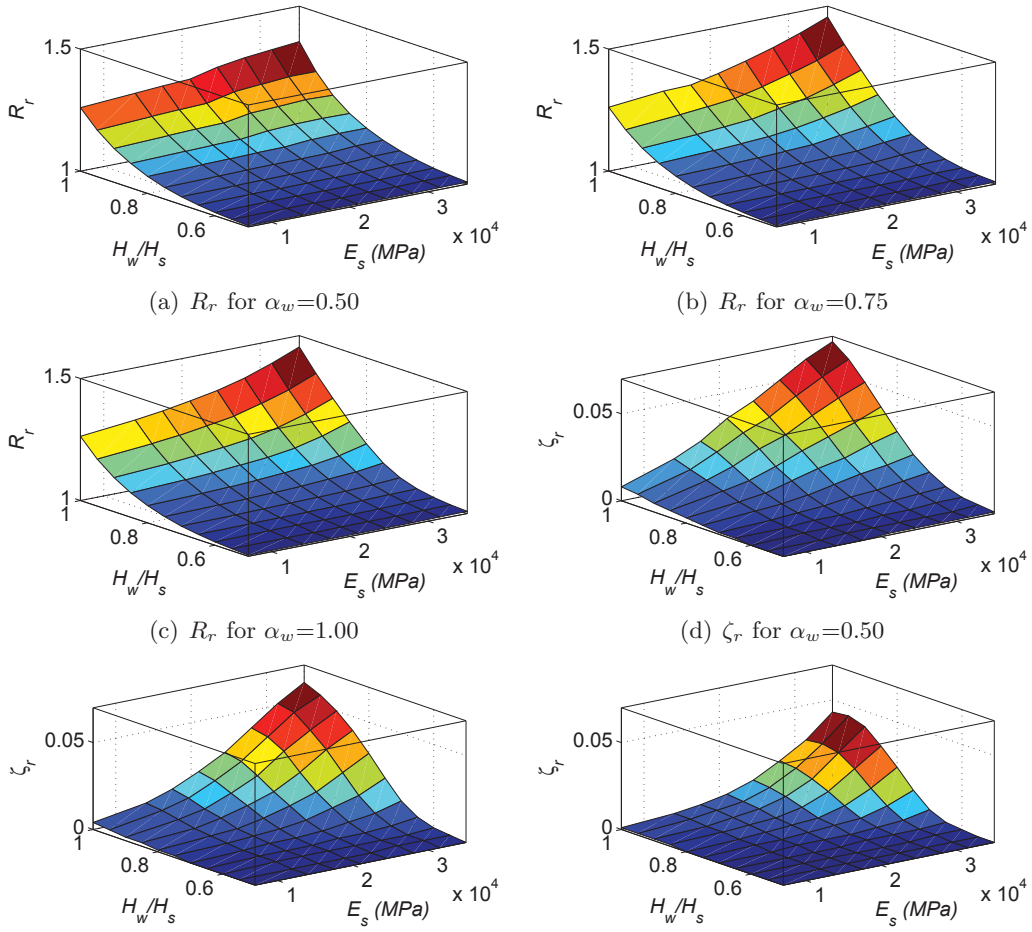

(a) R_r for α_w=0.50

(b) R_r for α_w=0.75

(c) R_r for α_w=1.00

(d) ζ_r for α_w=0.50

(e) ζ_r for α_w=0.75

(f) ζ_r for α_w=0.90

Figure 3.14: Standard contribution factors for dam-reservoir interaction (Løkke and Chopra, 2013)

$A\left(\widetilde{T_1}, \widetilde{\zeta_1}\right)$ is the pseudo-acceleration ordinate of the earthquake design spectrum, evaluated at vibration period $\widetilde{T_1}$ and damping ratio $\widetilde{\zeta_1}$ of the equivalent SDOF system representing the dam-reservoir-foundation system. Note that in the incremental format of the ESLF, $A\left(\widetilde{T_1}, \widetilde{\zeta_1}\right)$ should be increased incrementally.

The function $p(z, \widetilde{T_r})$ is the real valued component of the complex valued function representing

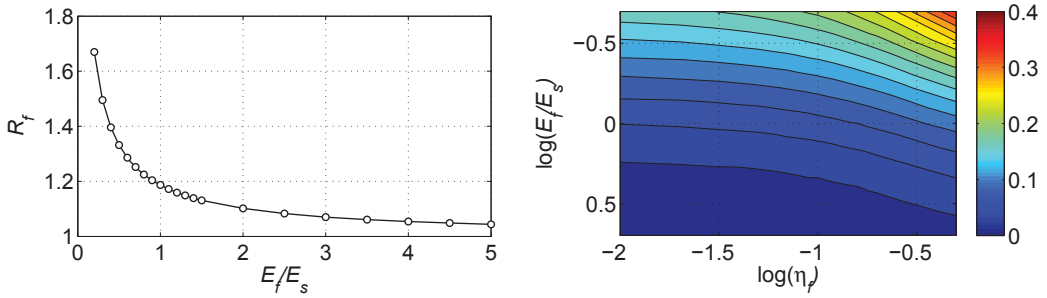

(a) R_f (b) ζ_f

Figure 3.15: Standard contribution factors for dam-foundation interaction (Løkke and Chopra, 2013)

the hydrodynamic pressure on the upstream face. $g\,p(z, \widetilde{T_r})$ can be computed based on figure 3.16 corresponding to the value of R_w, α_w, and assumed $H_w/H_s = 1$. Finally, the result is multiplied by $(H/H_s)^2$.

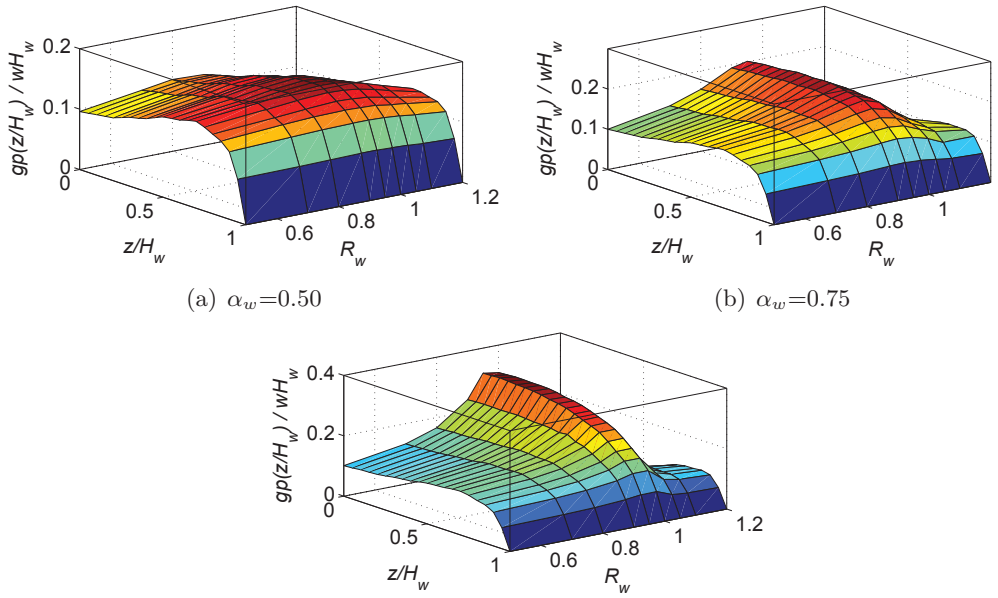

(a) α_w=0.50 (b) α_w=0.75

(c) α_w=0.90

Figure 3.16: Standard values of the hydrodynamic pressure for full reservoir (Løkke and Chopra, 2013)

3.3.8 Incremental Dynamic Analysis (IDA)

3.3.8.1 Single-Record IDA (SR-IDA)

The seismic capacity function can be obtained using a real ground motion. In the SR-IDA, single ground motion is used for nonlinear time history analysis of the coupled system. The ground motion can be obtained from hazard analysis. However, this method is mainly used for the structures (or their small scales models in lab) already damaged by a certain ground motion. The examples are: 1967 Koynanagar earthquake for analysis of Koyna gravity dam (Hariri-Ardebili and Saouma, 2014) and 1990 Manjil earthquake for analysis of Sefidrud buttress dam (Ghaemmaghami and Ghaemian, 2008). An especial format of SR-IDA using the artificial accelerogram is reported by Pan et al. (2015) for concrete arch dams.

Let $\ddot{\mathbf{x}}_g$ be the "as-recorded" (un-scaled) acceleration time history (it may already filtered, rotated, or baseline corrected). The elements of the vector are $\ddot{x}_g(t_i)$, $t_i = 0, t_1, t_{n-1}$. In order to consider the stronger and weaker scenarios, the ground motion can be scaled uniformaly using a scale factor $\lambda_{SF} \in [0, +\infty)$ (Vamvatsikos and Cornel, 2002). The scaled ground motion will be $\ddot{\mathbf{x}}_g^{\lambda} = \lambda_{SF}\ddot{\mathbf{x}}_g$. Note that one of the following three methods (at least) may be used for scaling: 1) time domain direct scaling of the acceleration time history, 2) scaling the elastic acceleration response spectrum, and 3) frequency domain scaling by applying λ_{SF} to the all Fourier amplitudes while keeping the phase unchanged. The scaled ground motion should be represented by a monotonic scalable intensity measure (usually referred as Intensity Measure - IM) in the form of Eq. 3.18. Note that IM in SR-IDA corresponds to load vector (Sec. 3.3.5) in POA and engineering quantity, EQ, (Sec. 3.2.1) in general definition of capacity function.

$$\text{IM} = \Xi(\ddot{\mathbf{x}}_g^{\lambda}) \ , \quad \text{IM} \in [0, +\infty) \tag{3.18}$$

where Ξ is the any scalar monotonic representation of the scaled ground motion such as peak ground acceleration (PGA), the 5% damped Spectral Acceleration at the first-mode period ($S_a(T_1, \xi = 5\%)$). A comprehensive list of ground motion IMs are summarized in (Riddell, 2007). The application of optimal IMs in dam engineering can has already studied by Hariri-Ardebili and Kianoush

(2015) and Hariri-Ardebili et al. (2015).

Having the scaled ground motions, the nonlinear time history analysis should perform in each case. Let's assume that the response of the nonlinear system to the scaled signal is $\mathbf{rp}^{\lambda}$ where the elements of the response vector are $rp^{\lambda}(t_i)$, $t_i = 0, t_1, t_{n-1}$. The response parameter, RP, can be any general monitoring item in dams such as deformation, stress, uplift; or even DIs. It is usually of interest to record the maximum absolute value of $\mathbf{rp}^{\lambda}$ for each scaled ground motion, Eq. 3.19. In the earthquake engineering language, the RP is refereed to engineering demand parameter (EDP).

$$\text{EDP} = \Omega(\mathbf{rp}^{\lambda}) = \max\left\{\text{Abs}\left(rp^{\lambda}(\tau) : \tau \in [0, t_{n-1}]\right)\right\} \quad , \quad \text{EDP} \in [0, +\infty) \tag{3.19}$$

where Ω is the maximum absolute function.

Single-IM SR-IDA (SIM-SR-IDA) : This is a plot of different pairs of (IM, EDP) from linear elastic to nonlinear phase and the failure of the system. The m discrete points (which means there are m nonlinear time history analyses) are then connected to each other using either 1) piecewise linear interpolation, 2) spline interpolation, or 3) Ramberg-Osgood equation to form the capacity function.

Spline interpolation : The spline comes in m cubic polynomial pieces, m is the number of convergent runs plus one for $(0, 0)$ point, and is parameterized on a single non-negative parameter, $\tau \in [0, \tau_1] \cup ... \cup [\tau_{n-1}, \tau_n]$. For each value of the parameter τ, and depending on the interval $[\tau_{i-1}, \tau_i]$ where it lies, one polynomial for IM and one another for EDP can be derived (Vamvatsikos and Cornell, 2004):

$$\begin{cases} x_i(\tau) = (a_1)_{xi}\tau^3 + (a_2)_{xi}\tau^2 + (a_3)_{xi}\tau + (a_4)_{xi} \\ y_i(\tau) = (a_1)_{yi}\tau^3 + (a_2)_{yi}\tau^2 + (a_3)_{yi}\tau + (a_4)_{yi} \end{cases} \tag{3.20}$$

where $\tau \in [\tau_{i-1}, \tau_i], i = 1, 2, ..., n$.

Using above equation, it is possible to approximate EDP value at arbitrary level of

IM and vice versa:

$$\begin{aligned} \mathrm{EDP} &= y\left(x^{-1}\left(\mathrm{IM}\right)\right) \\ \mathrm{IM} &= x\left(y^{-1}\left(\mathrm{EDP}\right)\right) \end{aligned} \tag{3.21}$$

Ramberg-Osgood (R-O) equation : Considering that the spline interpolation is cumbersome in some cases, the R-O equation can be used (Mander et al., 2007):

$$\frac{\mathrm{EDP}}{\mathrm{EDP}_c} = \frac{\mathrm{IM}}{\mathrm{IM}_c} + \left(\frac{\mathrm{IM}}{\mathrm{IM}_c}\right)^r = \frac{\mathrm{IM}}{K.\mathrm{EDP}_c}\left(1 + \left|\frac{\mathrm{IM}}{\mathrm{IM}_c}\right|^{r-1}\right) \tag{3.22}$$

where K is the initial slope of the IDA curve in the proportional range; IM_c critical IM that occurs at the onset of large EDPs that subsequently lead to collapse; $\mathrm{EDP}_c = \mathrm{IM}_c/K$ is the critical value of EDP, and r is the constant parameter.

In order to use the R-O equation, first the median IDA curve should be derived by interpolation from the actual IDA data, and then the R-O equation should be fitted to the observed median IDA curve. The value of the r parameter may be fixed to a reasonable number and the other parameters K and IM_c can be estimated using least square analyses.

Anatomy of SIM-SR-IDA : For a simple frame structure four types of the capacity curves are distinguishable, i.e. 1) capacity curve with fully softening response, 2) capacity curve including some minor hardening, 3) capacity curve including severe hardening, and 4) capacity curve with fully wavy behavior. In concrete gravity dams, only the first three types can be observed, figure 9.5(b). Both the option (1) and (2) have the capability to be represented in the form of Eqs. 3.2 and 3.3 explained in Sec. 3.2.2. However, due to highly ground motion-dependent nature of the option (3), there is no analytical form for them.

Multi-IM SR-IDA (MIM-SR-IDA) : As mentioned previously, the capacity function based on SIM-SR-IDA is a planer curve of IM *vs.* EDP. Choose of an appropriate IM parameter is always challenging and differs by type of the structure. For the conventional frame structures $S_a(T_1, \xi = 5\%)$ usually is the best choice (Vamvatsikos and Cornel, 2005). For

the concrete arch dam, Acceleration Spectrum Intensity (ASI) and PGA are the most optimal ones (Hariri-Ardebili et al., 2015). Thus, it it helpful to have a three-dimensional curve where the vertical axis is EDP and the horizontal axes are two IMs. Note that similar to SIM-SR-IDA, in MIM-SR-IDA again one of the IMs is scaled and the other one is computed externally using simple calculations on the scaled ground motion. Figure 3.17(b) shows a 3D capacity function as EDP-IM_1-IM_2. The projections of this curve also are shown which represents the conventional SIM-SR-IDA as EDP-IM_1 and EDP-IM_2.

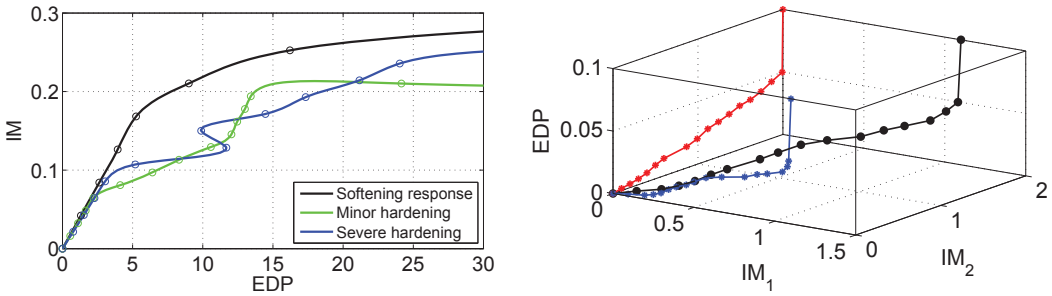

(a) SIM-SR-IDA (b) MIM-SR-IDA

Figure 3.17: Single-Record IDA capacity functions

3.3.8.2 Multi-Record IDA (MR-IDA)

MR-IDA is a collection of several, n, SR-IDA for a same structural system. The required ground motion records are usually obtained from Probabilistic Seismic Hazard Analysis (PSHA) of the site (McGuire, 1995). The number of required records usually varies considering the dispersion among them. The order of n for the frame structures (with less computational effort) is about 30 (Vamvatsikos and Cornel, 2005), while for the concrete dams (with high computational effort) is about 12 (Alembagheri and Ghaemian, 2013b). It is noteworthy that some approximate methods are proposed in order to reduce the number of the required records to estimate the median response of the structures (Azarbakht and Dolsek, 2007), (Azarbakht and Dolsek, 2011).

Single-IM MR-IDA (SIM-MR-IDA) : This is the most common format of IDA plot in the IM-EDP coordinate system. Figure shows the raw data obtained from MR-IDA. Also this

figure 3.18 shows the capacity functions resulted from n=40 ground motion based on piecewise linear interpolation and spline interpolation techniques discussed in Sec. 3.3.8.1 for SR-IDA.

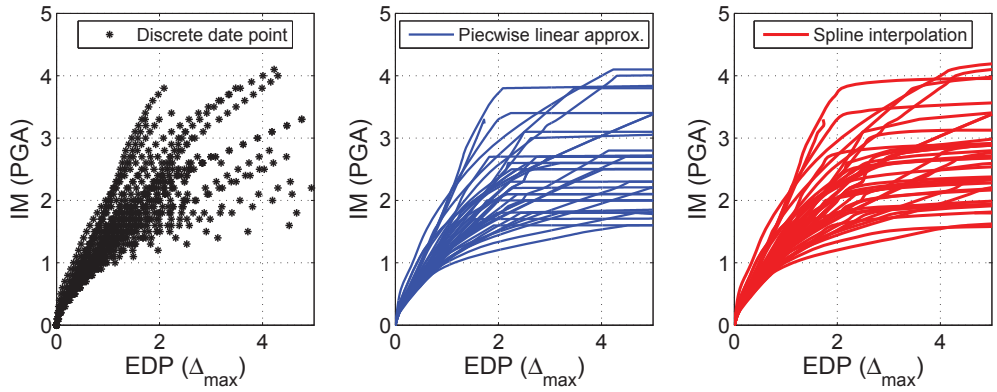

Figure 3.18: Multi-Record IDA capacity functions with different interpolation techniques

Considering the record-to-record variety of the capacity functions in SIM-MR-IDA, they should be summarized to some central values such as mean, median, 16% and 84% fractiles. Two methods can be used: 1) first, find the parametric model for each SIM-SR-IDA (using Eq. 3.2 or any other model), then find the statistics of the parameters; 2) use of the non-parametric methods such as running mean, running median, LOESS or the smoothing spline (Hastie, T.J. and Tibshirani, R.J., 1990), (Vamvatsikos and Cornel, 2002). The resulted summarized capacity curves are usually smoother than the SIM-SR-IDA curve (figure 9.5(b) and they can be easily fitted to the analytical model (Eq. 3.2).

Vector-IM MR-IDA (VIM-MR-IDA) : MR-IDA curves are plotted in $< \mathrm{IM}_{SC}, \mathrm{IM}_{NSC}, \mathrm{EDP} >$ coordinate, with one scalable and one non-scalable IM. The already proposed vector-valued IMs for frame structures are:

- Vamvatsikos and Cornel (2005) proposed $S_a(T_1)$ as scalable component, while the spectral ratio, $R_{sa}(\kappa, T_1)$, is the non-scalable one:

$$\langle S_a(T_1), R_{sa}(\kappa, T_1)\rangle = \left\langle S_a(T_1), \frac{S_a(\kappa T_1)}{S_a(T_1)} \right\rangle \tag{3.23}$$

where κ is a constant factor, usually 1.5.

- Baker and Cornell (2005) proposed $S_a(T_1)$ as scalable component and epsilon, ϵ as scaling-independent one. It is found that $\langle S_a(T_1), \epsilon \rangle$ is significantly superior to $S_a(T_1)$ alone. ϵ is defined as the number of standard deviations by which an observed logarithmic spectral acceleration, $\ln S_a(T)$, differs from the mean logarithmic spectral acceleration, $\overline{\ln S_a(T)}$, of a ground-motion prediction equation.

- Bojorquez et al. (2012) proposed the following two vector-valued IMs:

$$\begin{aligned} \langle S_a(T_1), R_{T_1,T_2} \rangle \ , \quad R_{T_1,T_2} &= \frac{S_a(T_2)}{S_a(T_1)} \\ \langle S_a(T_1), N_p \rangle \ , \quad N_p &= \frac{S_a\left(\left(\prod_{i=1}^{N_m} T_i\right)^{1/N_m}\right)}{S_a(T_1)} \end{aligned} \tag{3.24}$$

  where N_m is the number of contributed modes.

Figure 3.19(a) shows the MR-IDA for Pine Flat dam. The next step is to summarize the discrete 3D curve and generate a "surface" Vamvatsikos and Cornel (2005). The resulted so-called IDA surface can then be used for 16%, 50% and 84% capacity lines for a specific limit state.

Multi-IM MR-IDA (MIM-MR-IDA) : The IDA curves are plotted in $< \mathrm{IM}_{SC}, \mathrm{IM}_{SC}, \mathrm{EDP} >$ coordinate, with two scalable IMs. Bojorquez et al. (2012) used combination of $S_a(T_1)$ with other scalar IMs in order to determine the optimal vector IM. $\langle S_a(T_1), PGA \rangle$ and $\langle S_a(T_1), PGV \rangle$ were used as indicators of the peak responses of the structural system. $\langle S_a(T_1), t_{sig} \rangle$ and $\langle S_a(T_1), I_D \rangle$ were used as indicator of combination of peaks and cumulative damage potential of ground motions. Figure 3.19(b) shows 3D MR-IDA curves where $S_a(T_1)$ and ASI are two scalable IMs.

Multi-EDP MR-IDA (MEDP-MR-IDA) : The IDA curves are plotted in $< \mathrm{EDP}_1, \mathrm{EDP}_2, \mathrm{IM}_{SC} >$ coordinate, with two EDPs. This type of 3D plot is useful when the two EDPs have strong dependency, i.e. joint opening and sliding in mixed-mode fracture mechanics problems,

figure 3.19(c). The summarized curves can be shown in the format of "curved capacity surfaces" (not shown here).

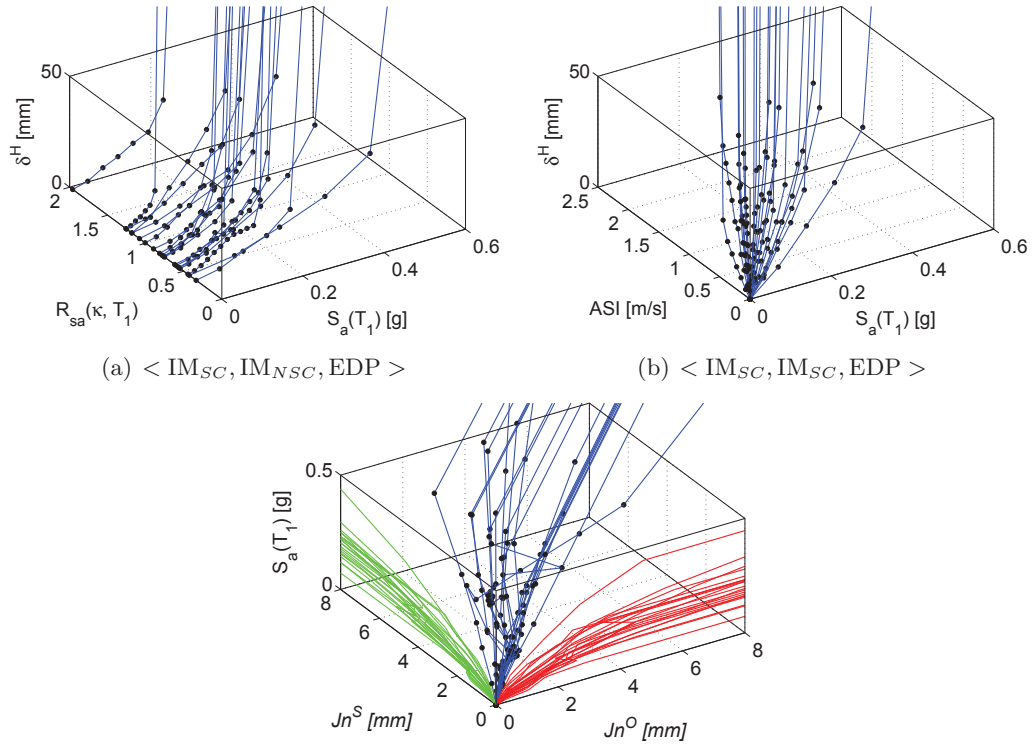

(a) $< \mathrm{IM}_{SC}, \mathrm{IM}_{NSC}, \mathrm{EDP} >$ (b) $< \mathrm{IM}_{SC}, \mathrm{IM}_{SC}, \mathrm{EDP} >$

(c) $< \mathrm{EDP}_1, \mathrm{EDP}_2, \mathrm{IM}_{SC} >$

Figure 3.19: Comparison of different 3D MR-IDA capacity functions

3.3.9 Cloud Analysis (CLA)

CLA is a numerical procedure in which first a structure is subjected to a set of (un-scaled or as-recorded) ground motions and is analyzed numerically. If the ground motion records are taken from a bin, they can represent an earthquake scenario defined by (M_{bin}, R_{bin}), the magnitude and distance representative of the bin (Jalayer, 2003). Then from the results, EDP *vs.* IM are determined and form the so-called cloud response. CLA method usually is used in conjunction with probabilistic seismic demand analysis (PSDA) Shome (1999). It is well-accepted that the discrete data points resulted from CLA have linear trend in the logarithmic scale implying a power curve in the arithmetic scale (Padgett et al., 2008), (Jankovic and Stojadinovic, 2004), (Ramamoorthy

et al., 2006).

$$\begin{aligned} \eta_{\mathrm{EDP|IM}}(\mathrm{IM}) = & \quad a.(\mathrm{IM})^b \\ \ln\left(\eta_{\mathrm{EDP|IM}}(\mathrm{IM})\right) = & \quad b.\ln(\mathrm{IM}) + \ln(a) \end{aligned} \tag{3.25}$$

where $\ln(a)$ and b are the linear regression constants and $\eta_{\mathrm{EDP|IM}}$ is the median value of EDP given IM.

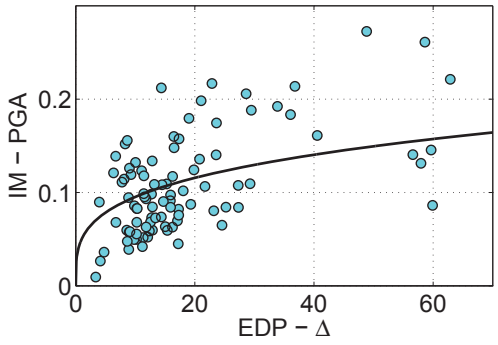

Figure 3.20: Cloud-based data power-form capacity function

3.3.10 Endurance Time Analysis (ETA)

ETA is a dynamic pushover procedure which is used to estimate the seismic performance of structures when subjected to pre-designed intensifying excitation (Estekanchi et al., 2004). The simulated acceleration functions are aimed to shake the structure from a low excitation level with a structural response in the elastic range to a medium excitation level where the structure experiences some nonlinearity and finally to a high excitation level, which causes the failure. All these responses ranges are experienced in a single time history analysis.

The challenging part of this method is generation of endurance time acceleration functions (ETAF). Different versions of ETAFs have been generated by (Nozari and Estekanchi, 2011) and further optimized by (Mashayekhi and Estekanchi, 2013). The major steps for producing ETAFs are:

- Generate a stationary random acceleration function, $Z(t)$ (using $\delta t = 0.01$, $N_{pnt} = 2^{11}$ node, and PGA= 1.0 g). Note that N_{pnt} is optional.

- Transfer the function to frequency domain, $Z(i\omega) = \mathcal{F}(Z(t))$, where i is imaginary unit and ω is frequency.

- Apply an appropriate filter function in order to resemble real ground motions Clough, R.W. and Penzien, J. (1993):

$$A(i\omega) = \frac{1 + 2i\xi_1 \frac{\omega}{\omega_1}}{1 - \left(\frac{\omega}{\omega_1}\right)^2 + 2i\xi_1 \frac{\omega}{\omega_1}} \frac{\left(\frac{\omega}{\omega_2}\right)^2}{1 - \left(\frac{\omega}{\omega_2}\right)^2 + 2i\xi_2 \frac{\omega}{\omega_2}} Z(i\omega) \tag{3.26}$$

  where the first and second terms are low-pass and high-pass filter function, ω_1 and ξ_1 are frequency and damping coefficients for the low-pass filter function, ω_2 and ξ_2 are frequency and damping coefficients for the high-pass filter function, respectively.

- Use several cycles of step-wise modification on frequency content of the filtered acceleration functions, $A(i\omega)$, in order to make the resulting response spectrum compatible with target one.

$$A^{new}(i\omega) = A^{old}(i\omega) \frac{S_a^{\text{trg}}(\omega)}{S_a^{\text{gen}}(\omega)} \tag{3.27}$$

  where $A^{new}(i\omega)$ is the modified frequency content which is replaced with the old one in each cycle of modification. $S_a^{\text{trg}}(\omega)$ is the target spectrum (code-base spectrum or from probabilistic seismic hazard analysis), $S_a^{\text{gen}}(\omega)$ is the generated response spectrum.

- Modify the acceleration time history by a linear profile function, $l(t) = t/t_{trg}$, that make resulting one intensifying at various time intervals. Note that t_{trg} is optional; however, usually is considered to be 10 s.

- Modify both the acceleration and displacement response spectra by applying a linear profile function. Unconstrained optimization technique in the time domain may be used as:

$$\min_{a_g} F(a_g) = \int_0^{T_{max}} \int_0^{t_{max}} \left\{ \left[S_a(T,t) - \frac{t}{t_{\text{trg}}} S_a^{\text{trg}}(T) \right]^2 + \chi_0 \left[S_d(T,t) - \frac{t}{t_{\text{trg}}} \left(\frac{T}{2\pi}\right)^2 S_a^{\text{trg}}(T) \right]^2 \right\} \tag{3.28}$$

  where a_g is ETAF being sought, χ_0 weight parameter, t_{max} and T_{max} are the maximum time and period in optimization process, respectively. Figure 3.21(a) shows a sample ETAF.

In order to retrieve a capacity function in the form of figure 3.2(a), first "ETA curve" should be derived, figure 3.21(b). It is a diagram, whose vertical axis refer to the maximum absolute values of EDP during the time interval from 0 to t, (see Eq. 3.29) and the horizontal axis is time.

$$\Omega\left(\mathrm{EDP}(t)\right) \equiv \max\left\{\mathrm{Abs}\left(\mathrm{EDP}(\tau) : \tau \in [0,t]\right)\right\} \tag{3.29}$$

Finally, the "time" parameter is converted to IM (this can be easily done as there is a direct relation between time and acceleration, figure 3.21(a)) and the EDP-IM coordinate is changed to IM-EDP. The resulted step-wise capacity function can be smoothed later, figure 3.21(c). Note that although this procedure is applicable only with single ETAF, in order to reduce the uncertainty (due to random nature) of ETAFs, usually the mean of three is used (Hariri-Ardebili and Mirzabozorg, 2014) (Hariri-Ardebili and Saouma, 2014).

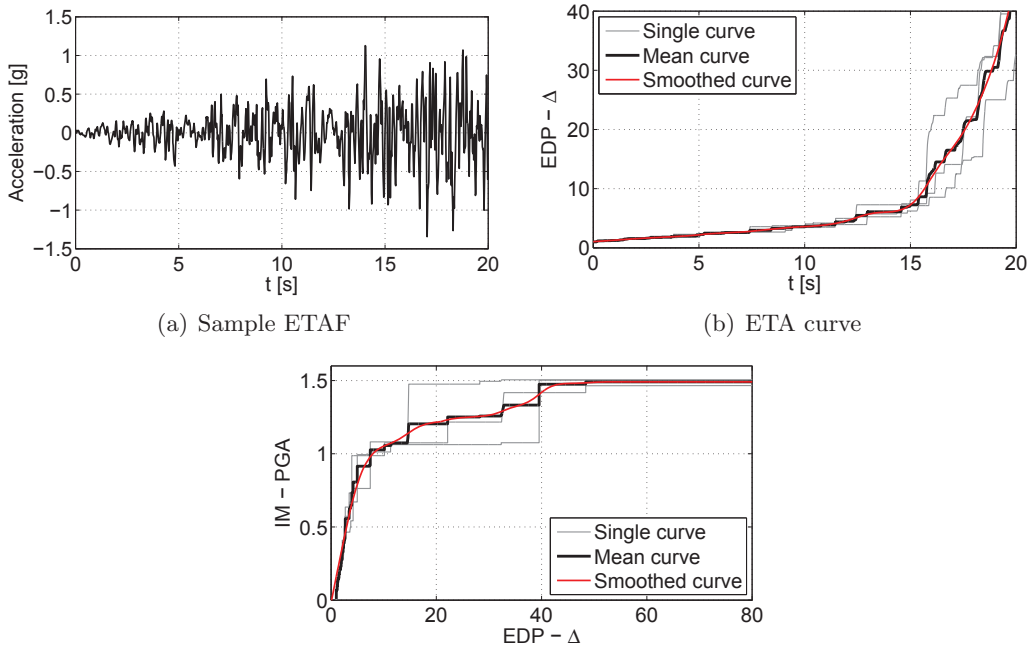

(a) Sample ETAF

(b) ETA curve

(c) Capacity function

Figure 3.21: ETA-based Capacity function generation

3.4 Extended/Combined Capacity Functions

As explained in Sec. 3.3 and also shown in figure 3.1; seismic, hydrologic, and time dependent material are three sources of uncertainties in capacity function derivation. One may either 1) extend the capacity function, or 2) combine two capacity functions.

3.4.1 Extended Capacity Function

Extended capacity function refers to those previously explained in Sec. 3.3 considering one more uncertainty source (which is usually material uncertainty). This procedure is explained for two events.

- Seismic + Material uncertainty: There are different approaches for considering both the material (epistemic) and seismic record-to-record (aleatory) uncertainties in analysis of structures (Padgett and DesRoches, 2007), (Liel et al., 2009), (Vamvatsikos and Fragiadakis, 2010), (Celik and Ellingwood, 2010), (Dolšek, 2012), (Celarec and Dolsek, 2013), and (Kazantzi et al., 2014). However, one of the low computationally demanding methods (with respect to Monte Carlo Simulation - MCS) is explained. This method accounts for epistemic uncertainty along with MR-IDA. The original method is explained in (Dolsek, 2009) (Dolsek, 2011) and is called extended-IDA. Thus we call the capacity curves resulted from this method as extended capacity functions.

  * Perform sensitivity analysis on N_{RV} random variable (RV) and select N_{Var} which are most sensitive.
  * Perform N_{Sim} sampling for each RV, where N_{Sim} is number of structural models.
  * Construct $\mathbf{X}_{N_{Sim}\times N_{Var}}$ which includes N_{Sim} realization for N_{Var} Rvs:

$$x_{j,i} = F_i^{-1}\left(\frac{\pi_i(j) - 0.5}{N_{Sim}}\right), \quad i = 1, ..., N_{Var},\ j = 1, ..., N_{Sim} \tag{3.30}$$

    where $\pi_i(1)$, ..., $\pi_i(N_{Sim})$ is a random permutation of 1,...,N_{Sim}; F_i^{-1} is the inverse of the cumulative distribution function of the i^{th} RV.

* Modify the correlation matrix of **X**, **C** with respect to the target correlation matrix, **T**. For this purpose, the Simulated Annealing method can be used (Voechovsk and Novk, 2009) to minimized the norm E, which is a measure for difference between the generated and the target correlation matrices.

* The optimized sample matrix $\mathbf{Y}_{N_{Sim} \times N_{Var}}$ has the arrays of **X** with the correlation matrix close to **T**.

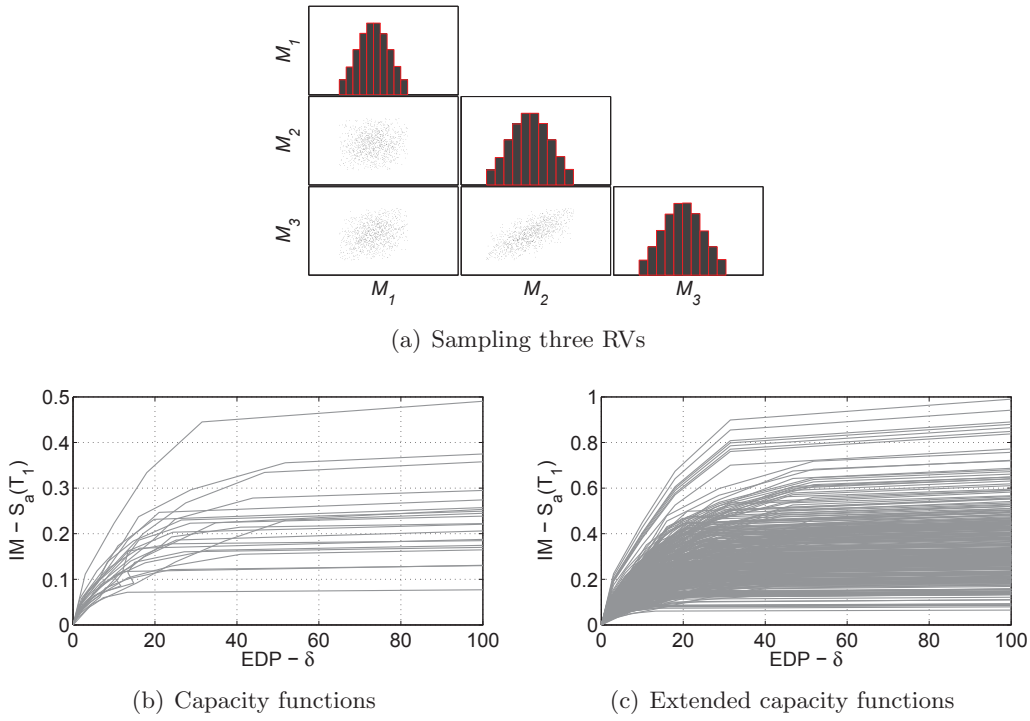

(a) Sampling three RVs

(b) Capacity functions

(c) Extended capacity functions

Figure 3.22: IDA-based extended capacity function generation

Figure 3.22(a) shows an example of system with three sensitive RVs, N_{Var}=3, (M_1, M_2 and M_3), where M_2 and M_3 are partially correlated. For each RV, N_{Sim}=100 realizations are sampled. Note that all RVs follow the normal distribution.

Figure 3.22(b) shows $N_{IDA} = 1 \times 20 = 20$ curve resulted from $N_{GM} = 20$ ground motions and $N_{Sim} = 1$ structural model. This set of capacity functions only account for the record-to-record variability and approximately this method respires $N_{Anlz} = 20 \times 10 = 200$ nonlinear transient analyses.

Figure 3.22(c) shows $N_{IDA} = 100 \times 20 = 2{,}000$ curve resulted from $N_{GM} = 20$ ground motions and $N_{Sim} = 100$ structural models. This set of capacity functions account for both the record-to-record variability and material uncertainty. This method approximately respires $N_{Anlz} = 2000 \times 10 = 20{,}000$ nonlinear transient analyses.

- AAR + Material uncertainty: In this condition the material uncertainty is considered along with material degradation (e.g. AAR). First, the time-dependent RV (material property) is sampled based on pre-defined distributional model, figure 3.23(a), at time t=0. Then, the material uncertainty is propagated in strength reduction functions using Eq. 3.7, figure 3.23(b). Finally, the finite element analyses are performed using the time-dependent uncertain material and the response are determined, figure 3.23(c). To be used within the concept of PBE, the median, 16% and 84% fractiles should be extracted.

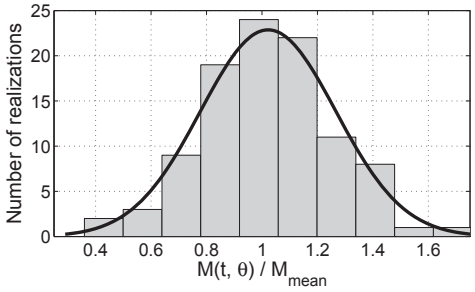

(a) Sampling RV

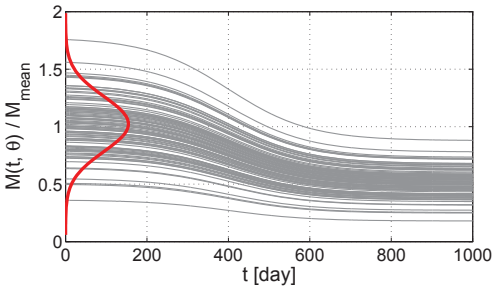

(b) Strength degradation functions

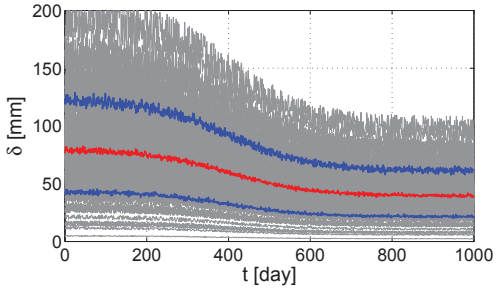

(c) Extended capacity functions

Figure 3.23: Time-dependent strength degradation with material uncertainty

3.4.2 Combined Capacity Function

Combined capacity functions deals with time-dependent seismic or hydrologic events. They mainly accounts for the aging and deterioration effects on the capacity function (and later on the fragility functions) of structures. Several studied showed the importance of the aging on the probability of failure of structures specially on the harsh environment. Among them Ghosh and Padgett (2010), Dong et al. (2013), Pitilakis et al. (2014), Guo et al. (2015).

Figure 3.24(a) shows a POA on a hypothetical system of dam with aging concrete. Original pushover curves along with the bi-linear idealizations are shown. Both the yield displacement and yield force reduce by increasing the time (again). Similar results were reported by Ghosh and Padgett (2010) on time-dependent corrosion of RC column. They found that due to corrosion and subsequent area loos of reinforcing steel, the load carrying capacity and yield curvature of the RC columns undergo a significant reduction (about 20% in 50 years).

Figure 3.24(b) shows the median IDA capacity function for a deteriorating system. Nearly identical conclusion can be drawn for the IDA-based capacity functions. Aging reduces both the load carrying capacity and the collapse displacement. It also reduces the dispersion of the SR-IDA curves. Thus the median and dispersion of the resulted fragility curves will reduce by aging.

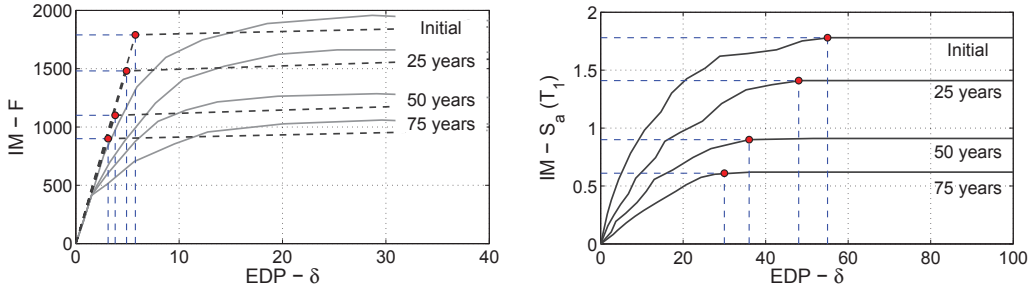

(a) POA (b) IDA

Figure 3.24: Combination of time-dependent and seismic capacity functions

Chapter 4

Computational Tools and Numerical Simulations

4.1 Introduction

Finite element (FE) method is used for nonlinear analysis of dam-foundation-reservoir system. The family of FE-based programs that are used in this study are:

- Pre-processor: The FE analysis requires the discretization of a structure into a mathematical representation. The discretized structure is then subjected to the governing differential equation with essential (displacement) and natural (traction) boundary conditions. KumoNoSu is a graphical front end to two programs, i.e. 1) T3D a mesh generator, and 2) T3D2Merlin which enables definition of material, boundary conditions and loads.

- Processor: The discritized structure subjected to the essential and natural boundary conditions is then transferred to the main processor (called Merlin) to be analyzed.

- Post-processor: Spider is a general purpose 3D post-processor for static and dynamic nonlinear FE analysis results. It is an OpenGL implementation under Windows.

Figure 4.1 shows the interaction among the three programs and the input/output file(s) for each one. They can be summarized as:

- KumoNoSu uses: 1) `.bd` (includes all geometric information of model), 2)`.t3d` (includes all meshing information), and 3) `.ctrl` (includes material property, boundary condition, loads, analysis information), and generates `.inp` (includes all the nodes, elements, material,

loads, boundary condition, analysis information) for processor (Merlin). The generated FE descritization can be saved in the form of `.eps`, `.jpeg`, and `.EMF`.

- Merlin uses `.inp` and generates: 1) `.out` (includes all the requested analysis results), 2) `.pst` (includes post-processing data for regular FE analysis), `.rtv` (includes post-processing data for Real Time View of a lengthy dynamic analysis), and 3) `.eig` (includes post-processing data to display the results of an eigenvalue analysis).

- Spider uses one of `.pst`, `.rtv`, or `.eig` and display the results. Results can be saved in the form of `.eps`, `.jpeg`, and `.EMF`.

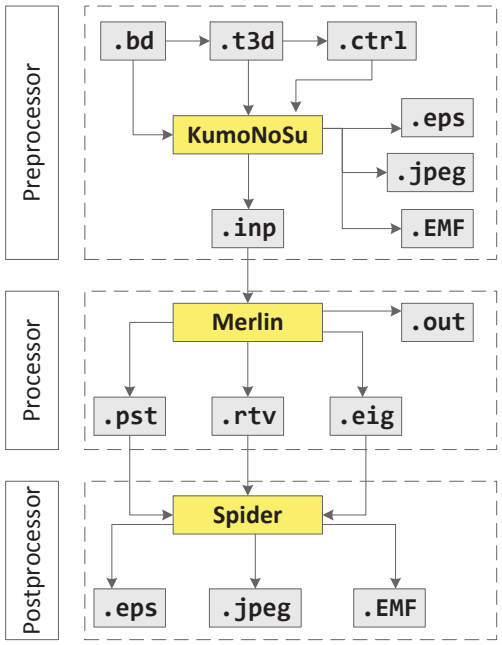

Figure 4.1: Interaction among KumoNoSu, Merlin and Spider

4.2 Probabilistic Performance Assessment of Concrete Dams (PPACD)

The group of programs in figure 4.1, are only able to perform a single deterministic analysis. To be used within the context of the present thesis, this should be expanded to the probabilistic

form. For this purpose, the Matlab-based algorithm called PPACD is developed which stands for "Probabilistic Performance Assessment of Concrete Dams". It includes many Matlab scripts and functions facilitates the probabilistic assessment of structures. Figure 4.2 shows the general algorithm of PPACD and interaction among different programs. This algorithm is applicable for any types of structures (not only dam) and any probabilistic model (load, material, time). This algorithm is briefly explained first. Next, its application in performance based earthquake engineering (PBEE) will explore.

Major steps and features of PPACD are:

- Use KumoNoSu to build a initial finite element model based on information from physical model. Hypothetical material property or load magnitude may be used in this step to develop a deterministic `test.inp`.

- The generated `test.inp` file is then broken to different sub-blocks, i.e. `Block-10.inp`, `Block-20.inp`, ...; each one includes a specific information about the FE model (e.g. analysis type, nodes, elements, material, loads, boundary condition).

- `P0.m` is used to determine the user-defined input parameters for FE model. This includes: ground motions for dynamic analysis, material property and its distributional model for uncertainty quantification, time-dependent aging and etc.

- `P1.m` uses all input blocks (i.e. `Block-10.inp`, ...) and input data from `P0.m` (`Material.mat`, `GroundMotion.mat`, ...) to generate N new input files, `test-N.inp` which have the desired probabilistic model.

- `P2.m` runs the Merlin N times and generates N `test-N.pst` and `test-N.out` (if requested `test-N.rtv` and `test-N.eig` also) files. Each of the N `test-N.pst` can be separately read by Spider and provide required graphical output.

- `P3.m` uses N `test-N.out` files (in the form of ASCII) and coverts them to `test-N.mat` files (in the form of Binary).

- `P4.m` further process the N `test-N.mat` files and generates N `ext-test-N.mat` files. This step includes process of the results for a specific structure, define the limit states and etc.

- `P5.m` uses the N `ext-test-N.mat` files and applies the probabilistic operations on them (e.g. different fractile, regression, probability of exceedance, ...). The final results can be either represented quantitatively (tabulated or central values) or graphically. Currently, PPACD uses one of the 1) Maltab, 2) ParaView, or 3) Ansys to show the contour plots on the FE model.

4.3 PPACD for PBEE

Each of the general scripts, i.e. `P0.m` to `P5.m` are explained in the context of PBEE for concrete dams.

4.3.1 `P0.m`

This script provides a set of appropriate ground motions to be used in dynamic analyses. The general steps and feature are:

- Select the type of the performance assessment: 1) intensity-based performance assessment (IBPA) assuming that the dam is subjected to a specific intensity of shaking (e.g. specific target response spectrum), 2) scenario-based performance assessment (SBPA) assuming that the dam is subjected to a specific $< R_{rup}, M_w >$ scenario (earthquake intensity is uncertain parameter), and 3) time-based performance assessment (TBPA) assuming the uncertainty in R_{rup}, M_w and the intensity of motion.

- Select between the real (recorded) ground motions and the synthetic one(which is suitable for dam sites that there is no enough recorded signals).

- In the case of real ground motions, either use the direct ground motion selection through PEER online tool, or use a set of Matlab codes developed by Baker research group. In

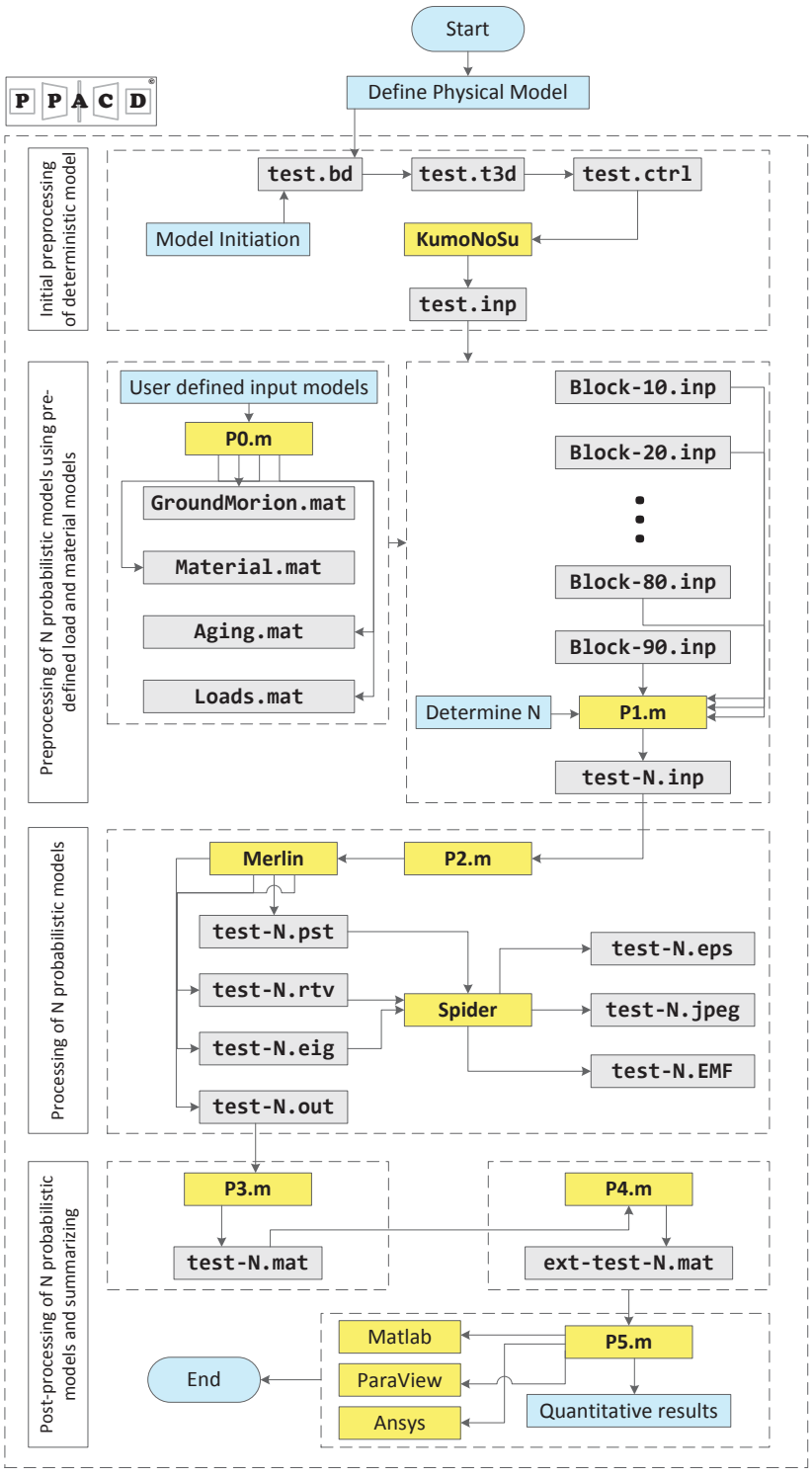

Figure 4.2: Interaction among different programs in PPACD

both cases, the selected ground motions are saved in the form of `GMList.xlsx`. The same procedure should be performed for synthetic ground motions.

- The selected ground motions can be truncated (e.g. [5%, 95%] A_I, or [5%, 75%] A_I) using `GM_Truncat.m`.

4.3.2 `P1.m`

Figure 4.4 shows different types of uncertainty analysis can be performed though PPACD. Four sources of uncertainty in performance assessment of concrete dams are:

- Mechanical (material): For an existing dam, this refers to uncertainty in determination of material property and also different random variables (RV) in the constitutive model.
- Hydrologic: Refers to uncertainty in pool elevation. Should be quantified based on hydrologic hazard curve.
- Seismic: Refers to record-to-record variability of the input ground motions. Should be quantified based on seismic hazard curve.
- Time: Refers to time-dependent degradation of the material, e.g. alkali-aggregate reaction and creep.

1st degree uncertainty refers to incorporating only one of the four sources. Subsequently, 2nd, 3rd and 4th degree uncertainty refer to simultaneous effect of two, three and four uncertainty source. In the present thesis only the shaded uncertainty types in figure 4.4 are used.

Seismic analysis is performed in two steps: 1) static analysis with all the body forces and hydrostatic one, and 2) through a "restart", a dynamic analysis is initiated form the preceding static one. Thus, two set of `.inp` and `.out` files will generate for each analysis. Hereafter, the static input file corresponds to N^{th} analysis refers to `test-N_dyn1.inp` and the dynamic one refers to `test-N_dyn2.inp`.

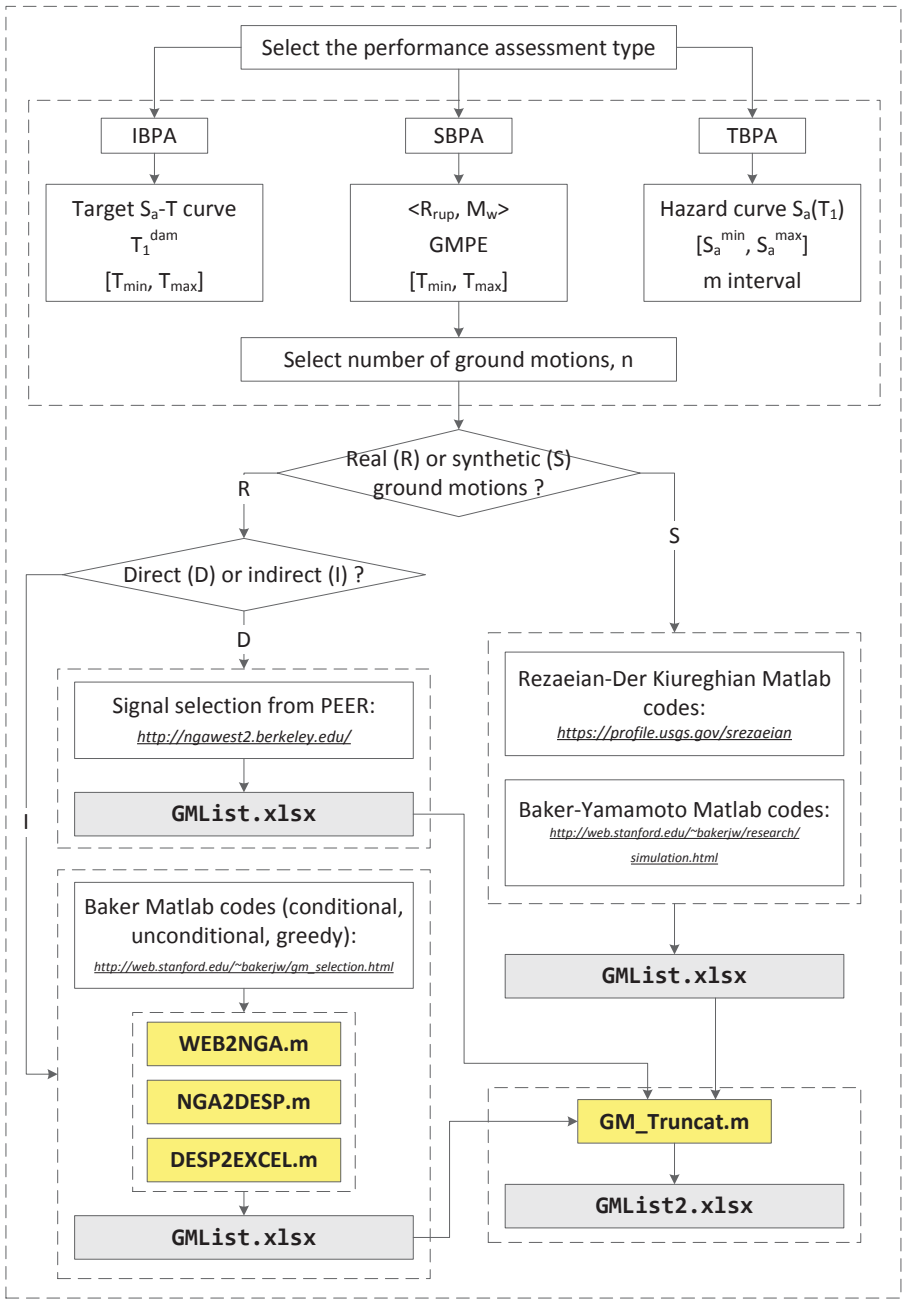

Figure 4.3: General algorithm in `P0.m`

Figure 4.5 shows the general algorithm to generate input files for static analysis. Based on figure 4.2, the initially generated input file should break into different sub-blocks as:

- `Block-Sta-10.inp`: title and definition

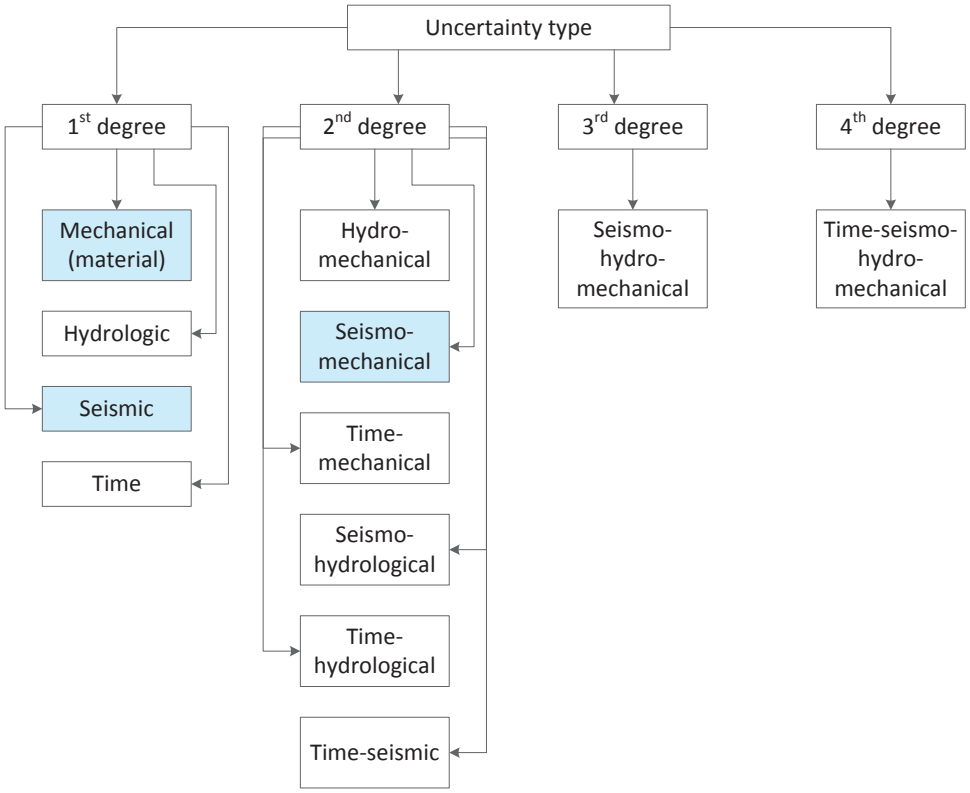

Figure 4.4: Different types of uncertainties in PPACD

- `Block-Sta-20.inp`: control block, includes number of increments, ...
- `Block-Sta-30.inp`: element group, includes element types and material property
- `Block-Sta-40.inp`: mesh group, includes nodal mass and damping, master/slave crack
- `Block-Sta-50.inp`: analysis control, includes iterations, error, ...
- `Block-Sta-60.inp`: body forces
- `Block-Sta-70.inp`: uplift model
- `Block-Sta-80.inp`: displacement boundary condition
- `Block-Sta-90.inp`: hydrostatic pressure

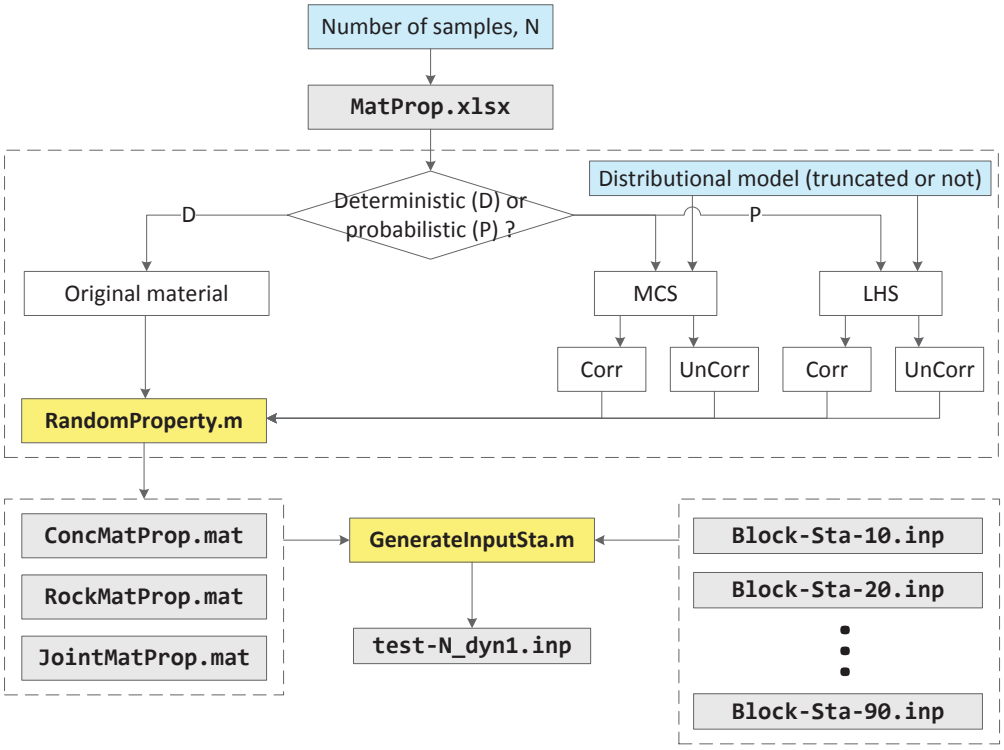

Figure 4.5: General algorithm in `P1Sta.m`

In figure 4.5, `RandomProperty.m` generates N samples based on either crude Monte Carlo Simulation (MCS) or Latin Hypercube Sampling (LHS). In both cases the correlated or uncorrelated modes are possible. Sampling is based on predefined distributional model (e.g. normal, lognormal, ...) by user for each RV. Moreover the upper and lower bounds can be defined to truncate the distributional model.

Figure 4.6(a) shows 500 samples for each of three RVs based on LHS. There is a weak correlation between Mat_1 and Mat_2 and also Mat_1 and Mat_3; however, the correlation is strong between Mat_2 and Mat_3. On the other hand, figure 7.3 shows an un-symmetry truncation of a normal distribution in the range [18, 38] GPa.

Figure 4.7 shows the general algorithm to generate input files for dynamic analysis. Similar to static analysis, figure 4.7, there are nine blocks define the `test-N_dyn2.inp`; however, some of them are empty in dynamic analysis (e.g. material, mesh) because they already defined though

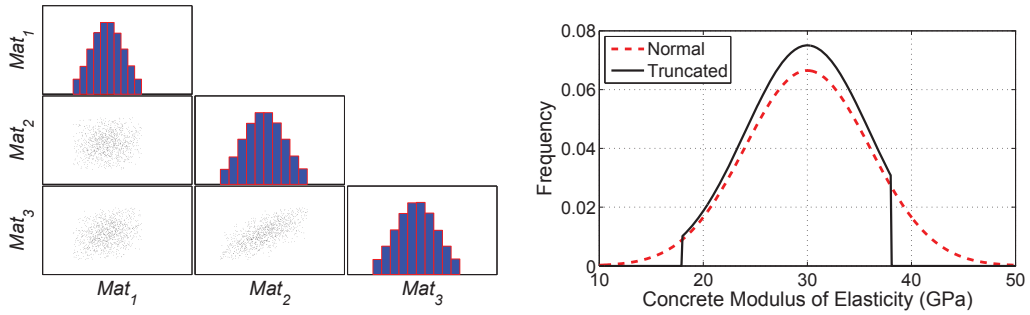

(a) Correlation among RVs

(b) Unsymmetry truncation of normal distribution

Figure 4.6: Sampling the material properties based on algorithm in figure 4.5

the static input file. User selects the type of dynamic analysis and a `Groundmotion.mat` file is generated includes all the required seismic input with their specifications. Five types of analysis in PPACD are:

- Single ground motion (SGM): only a single ground motion is used for the all N samples. If N = 1, this results to single deterministic analysis, and if N = "large number" this is either sensitivity or material uncertainty assessment.

- Cloud analysis (CLA), figure 4.8(a): N (un-scaled) ground motions are applied to N samples. If all the samples have same characteristics, this method only shows the record-to-record variability. However, if samples are different, it accounts for epistemic uncertainty also.

- Endurance time analysis (ETA), figure 4.8(b): Only three samples are required for three acceleration functions.

- Multiple stripe analysis (MSA), figure 4.8(c): N ground motions are applied in m level (n=N/m for each level).

- Incremental dynamic analysis (IDA), figure 4.8(d): n ground motions are incrementally scaled in N/n levels and applied to dam.

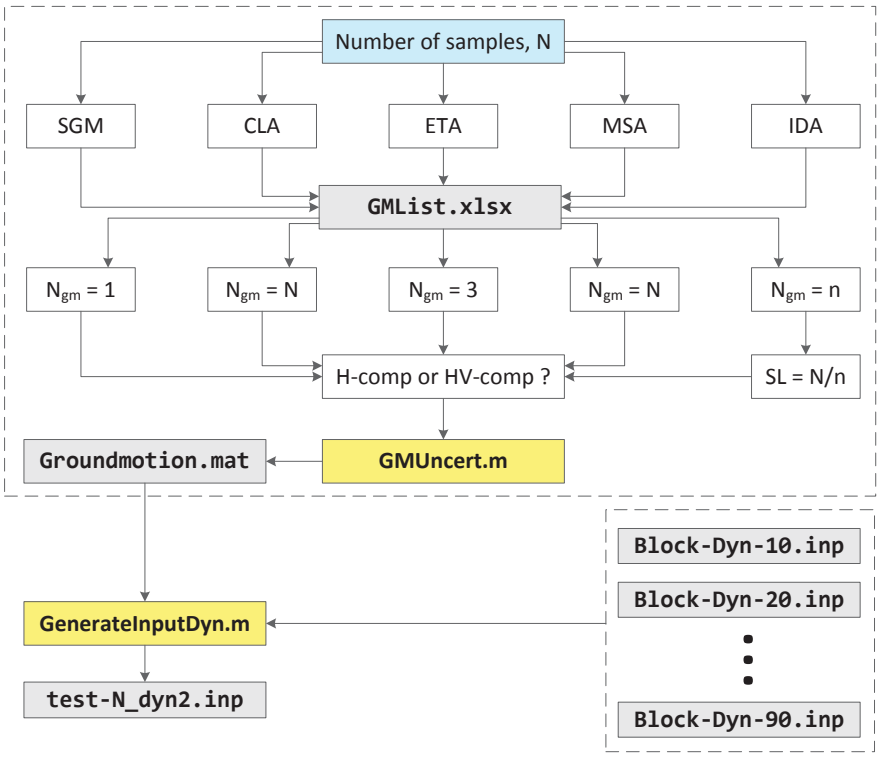

Figure 4.7: General algorithm in `P1Dyn.m`

At the end of this step, N input files are generated for dynamic analysis. Note that the vibration characteristics of dam are treated separately though a modal analysis which provides the period of the dam and effective mass in different directions. In the present research, the bounded Rayleigh damping method (with constant mass and stiffness proportional damping coefficients along with updated tangent stiffness matrix) is used. This procedure is summarized in figure 4.9. Dependency of the Rayleigh coefficients to natural frequency and R parameter simultaneously under a constant ξ is also show in this figure.

4.3.3 `P2.m`

Having the 2N input files (static + dynamic), `P2Sta.m` and `P2Dyn.m` are executed, sensationally. They run the Merlin (main processor) 2N times and generate `test-N_dyn1.out` and `test-N_dyn2.out`. Note that `test-N_dyn1.out` is used as part of input file for dynamic analysis.

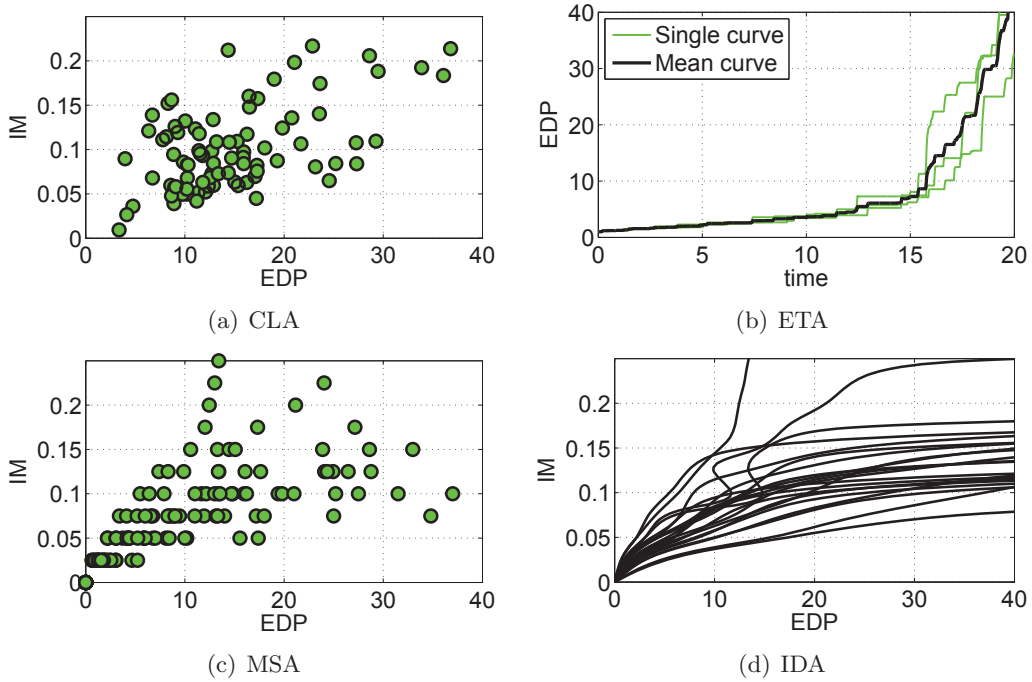

(a) CLA (b) ETA

(c) MSA (d) IDA

Figure 4.8: Different types of dynamic analysis methodologies in PPACD

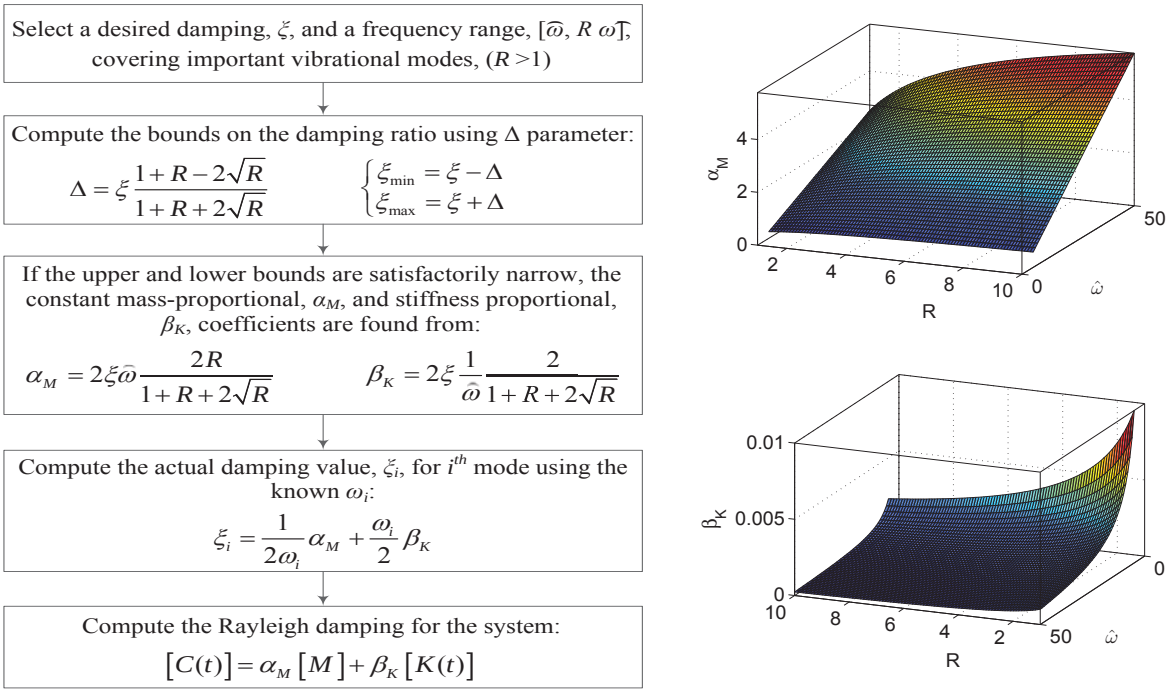

Figure 4.9: Bounded Rayleigh damping formulation using updated stiffness matrix

4.3.4 P3.m

P3Dyn.m converts N test-N_dyn2.out ASCII files to test-Dyn-N.mat Binary files. P3Dyn.m is computationally expensive especially for long duration ground motions with small time step. It can be run on both PC and supercomputer (CU's 184-teraflop Dell supercomputer called Janus is used for some of the analyses; it is currently ranked 164 among the world's top-500 supercomputer sites).

4.3.5 P4.m

P4Dyn.m processes the raw data from N test-Dyn-N.mat files and generates N ext-test-Dyn-N.mat files. In the context of PBEE, two major set of post-processing are required: 1) processing the ground motion intensity measures (IM), and 2) processing the dam engineering demand parameter (EDP). Figure 4.10 shows the seven category of IMs that are computed for any ground motion in P4Dyn.m. For each category, there are several individual IMs that will be explained later.

One of the most important parts in nonlinear transient analysis is determination of local and global failure. The function that decides on global safety/failure of cracked dam is GlobF.m. In the present study, the global failure criterion is defined based on the combination of cracked length ratio at the dam-foundation interface and the deformation of the index point (crest in gravity dams):

$$\text{GlobF} = f\left(\frac{L_{cr}}{L_T}, \frac{u_{max}}{u_{ult}}\right) = \begin{cases} 0 & \text{No through crack; No global failure} \\ 1 & \text{Through crack; No global failure} \\ 2 & \text{Through crack; Global failure} \end{cases} \tag{4.1}$$

where GlobF shows the global failure of the system. It depends on the cracked length, L_{cr}, total dam base, L_T, maximum absolute displacement, u_{max}, of the index point at the increment where $L_T = L_{cr}$, and finally the ultimate absolute displacement of the index point which is defined by the user (usually is a factor of u_{max}). u_{ult} represents the condition in which beyond that point the dam is assumed to be slides or overturns. In the present study this limit is considered to be $u_{ult} = 2\ u_{max}$. Figure 4.11 shows the three possible conditions for GlobF:

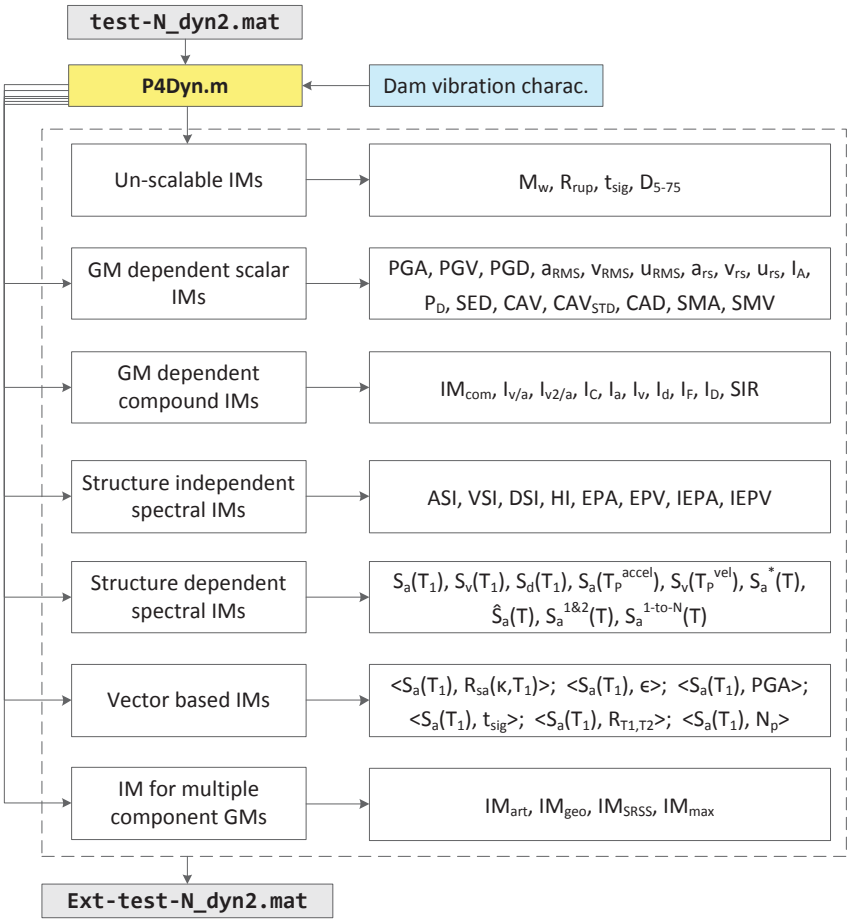

Figure 4.10: Treatment of IMs in `P4.m`

- GlobF = 0: The ratio of the $\frac{L_{cr}}{L_T}$ does not reach to 1.0. Displacement time history of the index point is not important in this case. The "cut off" time for the analysis in this case corresponds to "total time", $t_{\text{cutoff}} = t_{\text{tot}}$.

- GlobF = 1: In this case, $\frac{L_{cr}}{L_T} = 1.0$ at time t_{eff} which is less than the total time of the ground motion signal, t_{tot}. First, the maximum absolute value of the index point's displacement up to t_{eff} should be found:

$$u_{max} = \max\left(\text{abs}\left(u_{index}(t)\right)\right), t \in [0, t_{\text{eff}}] \tag{4.2}$$

The post-cracking displacement of the index point should be tracked again up to the end

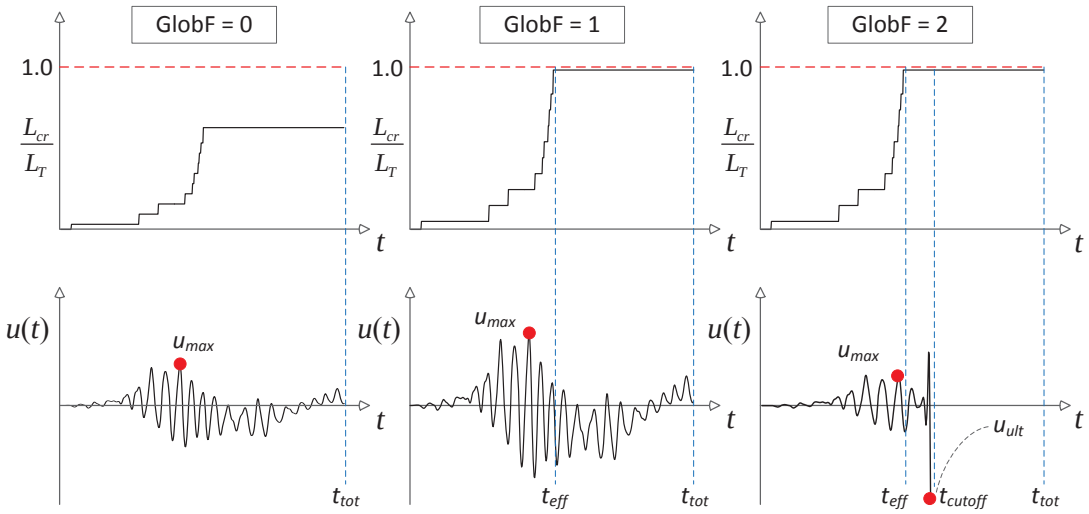

Figure 4.11: Global failure algorithm for nonlinear analysis with dam-foundation interface joint

of the analysis:

$$u_{post-cr} = \max\left(\text{abs}\left(u_{index}(t)\right)\right), t \in (t_{\text{eff}}, t_{\text{tot}}] \tag{4.3}$$

In this case, $u_{post-cr}$ is less than u_{ult} ($u_{post-cr} < u_{ult}$), the dam is judged to be not failed globally. The "cut off" time for the analysis in this case is the total time, $t_{\text{cutoff}} = t_{\text{tot}}$.

- GlobF = 2: In this case, $\frac{L_{cr}}{L_T} = 1.0$ at time t_{eff}. However, $u_{post-cr} \geq u_{ult}$. In this condition, the dam is assumed to be globally failed. The "cut off" time for the analysis is the first increment when $u_{post-cr} = u_{ult}$ and should be in $t_{\text{eff}} < t_{\text{cutoff}} \leq t_{\text{tot}}$

The above mentioned global failure is still valid for the cases that the dam is cracked in multiple locations as long as the base crack fails before the any other possible crack path within the dam body (base crack is governing). Otherwise, the local failure criterion is defined as:

$$\text{LoclF} = f\left(\left(\frac{L_{cr}}{L_T^{min}}\right)_{max}, \frac{u_{max}}{u_{ult}}\right) = \begin{cases} 0 & \text{No through crack; No local failure} \\ 1 & \text{Through crack; No local failure} \\ 2 & \text{Through crack; Local failure} \end{cases} \tag{4.4}$$

where LoclF shows the local failure of the system. Note that local failure means damage in dam body not the dam-foundation interface. It depends on the cracked length, L_{cr}, minimum probable

crack path, L_T^{min}, maximum absolute displacement, u_{max}, and the ultimate absolute displacement, u_{ult}. Note that among different crack paths the one should be selected which has the maximum $\frac{L_{cr}}{L_T^{min}}$.

4.3.6 `P5.m`

`P5.m` uses N `ext-test-Dyn-N.mat` files and applies the probabilistic operations which depends on the type of analysis:

- CLA:
  - Determination of histograms and best fit to IM parameters
  - Determination of optimal IM in terms of efficiency, sufficiency, proficiency, and practicality
  - Determination of optimal vector IM
  - Determination of fragility curves and surfaces
- IDA:
  - Determination of capacity curves
  - Summary of capacity curve into central values and fractiles
  - Determination of optimal IM parameter
  - Determination of fragility curves

Chapter 5

Deterministic Nonlinear Dynamic Assessment of a Gravity Dam

5.1 Introduction

Detained nonlinear seismic analysis of gravity dams is essential for performance-based earthquake engineering (PBEE). Whereas theory was described in the previous chapter, this one applies the presented methodology to Pine Flat gravity dam. This includes: geometry, load, seismic hazard analysis, modal and nonlinear structural analysis. Both the dam-foundation interface joint nonlinearity and the concrete cracking based on smeared crack approach are used. Failure modes in each case are extracted for different seismic intensity levels and compared with the theoretical ones.

5.2 Dam Description

Pine Flat Dam is a concrete gravity dam on the Kings River of central California in the United States. Situated about 32 km east of Fresno, at 36.8322N (Latitude) and -119.3261W (Longitude). Figure 5.1 shows the site location of dam and it's reservoir (Google, 2013). The height of the dam is 121.92 m (400 ft) and its length in cross-stream direction is 560.83 m (1840 ft). The thickness of the dam at the base and the crest level is 95.81 (314.4 ft) and 9.75 m (32 ft), respectively. Figure 8.4 shows the cross section of the tallest non-overflow monolith. The dam's primary purpose is flood control, with irrigation, power generation and recreation secondary in importance. The dam was built by the U.S. Army Corps of Engineers (USACE) after a six-year controversy between supporters of irrigation development and proponents of flood control. Construction began in 1947 and was completed in 1954 (wikipedia, 2015).

Figure 5.1: General site location of Pine Flat Dam (Google, 2013)

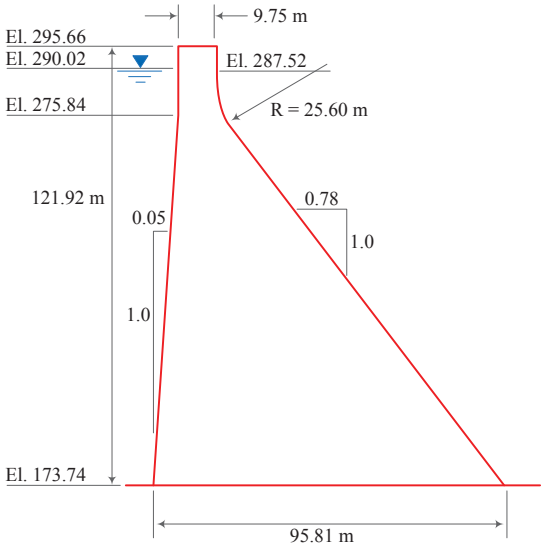

Figure 5.2: Tallest non-overflow monolith of Pine Flat Dam

5.3 Site Characteristics

The site conditions for Pine Flat Dam is estimated using the *opensha* application (Field et al., 2003). For this purpose CGS/Wills site classification map is used. Figure 5.3(a) shows the

estimated V_{S30} at the dam site. As seen, V_{S30} for the Pine Flat Dam is about 760 m/s. Moreover, the values of $Z1.0$ and $Z2.5$ are obtained as 0.008886 km/s and 0.015554 km/s, respectively, using USGS Bay area velocity model (Field et al., 2003).

Figure 5.3(b) shows the average shear wave velocity estimated by Allen and Wald (2007) simplified procedure. As seen, V_{S30} categorize as Class B of USGS for the considered location.

Pine Flat Dam is situated on hard metamorphic (meta-volcanic) rock consisting primarily of jointed amphibolite with scattered seams of calcite, quartz, and lesser occurrences of gypsum (MWH-Global, 2003). No significant through-going fault zones are known to exist within the area (California Division of Mines and Geology, 1966). Typically, rock at the dam site is hard, dark gray, fine-grained, and brittle. Thin seams of gypsum and deeply weathered joints were encountered on the right abutment during construction of Pine Flat Dam. Thus in overall, the dam site is considered as rock with V_{S30} to be at least 760 m/s.

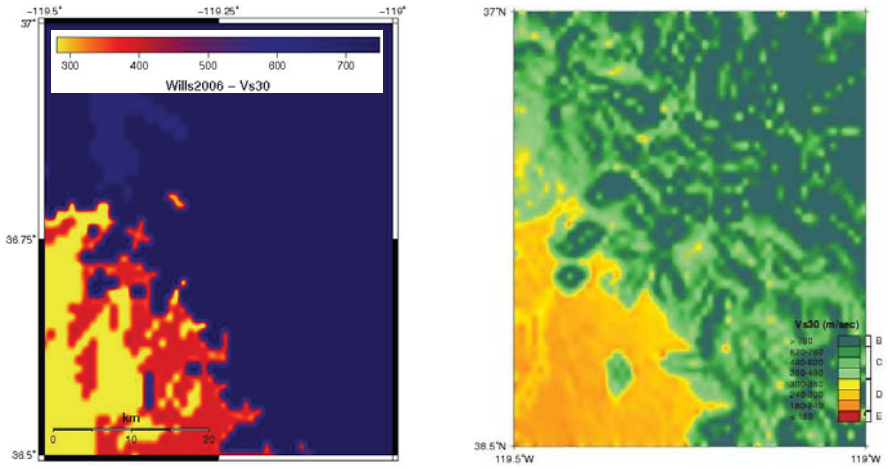

(a) *OpenSHA* online application

(b) Simplified Allen and Wald (2007) method

Figure 5.3: Estimated V_{S30} at the Pine Flat Dam site

5.4 Hazard Analysis

Seismic hazard analysis of Pine Flat Dam site is performed based on the probabilistic approach, i.e. probabilistic seismic hazard analysis (PSHA). For this purpose, the *OpenSHA Hazard Curve Calculator (local)* (www.opensha.org/apps) is used. Abrahamson and Silva (2008) attenuation relationship is used in this section. This model is capable to support the peak ground acceleration (PGA), peak ground velocity (PGV), and spectral acceleration (S_a) as earthquake intensity measures (IMs). The choice of this model is arbitrary here and any other well-establish model can be used also. Although there are some differences between the hazard curve's shape using different attenuation relations, it is negligible for the sake of the current research.

Working Group on California Earthquake Probabilities (WGCEP, 2007) Uniform California Earthquake Rupture Forecast (UCERF2) is used as earthquake rapture forecast model. Details on this model which was basically developed for California area can be found in (on California Earthquake Probabilities, 2008). Figure 5.4(a) shows the generated mean hazard curves for Pine Flat Dam site considering $S_a(T = 0.3s)$ as intensity measure and different forecast duration as labeled. Note that $T = 0.3$ s is the fundamental period of the dam (this is fundamental period based on numerical simulations without considering the reservoir and foundation interaction effects). As seen, the probability of exceedance increases with duration.

Assuming 50-year as earthquake rapture forecast duration (the time interval is typically set to 50 years because the hazard maps are usually represented in 50-year return period), the mean hazard curve for different period of vibration of the considered structure are calculated as shown in figure 5.4(b). As seen, the probability of exceedance increases vibration period up to $T = 0.25s$, then it decreases with any increases in period. Specifically, the mean hazard curve for period of $T = 0.20s$ and $T = 0.30s$ are the same. Also the differences of the mean hazard curves for period range [0.20 s, 0.30 s] is negligible.

The calculated hazard curves can be represented in terms of the annual probability of exceedance (or return period) as shown in figure 5.5 for two major intensity measures, PGA and S_a,

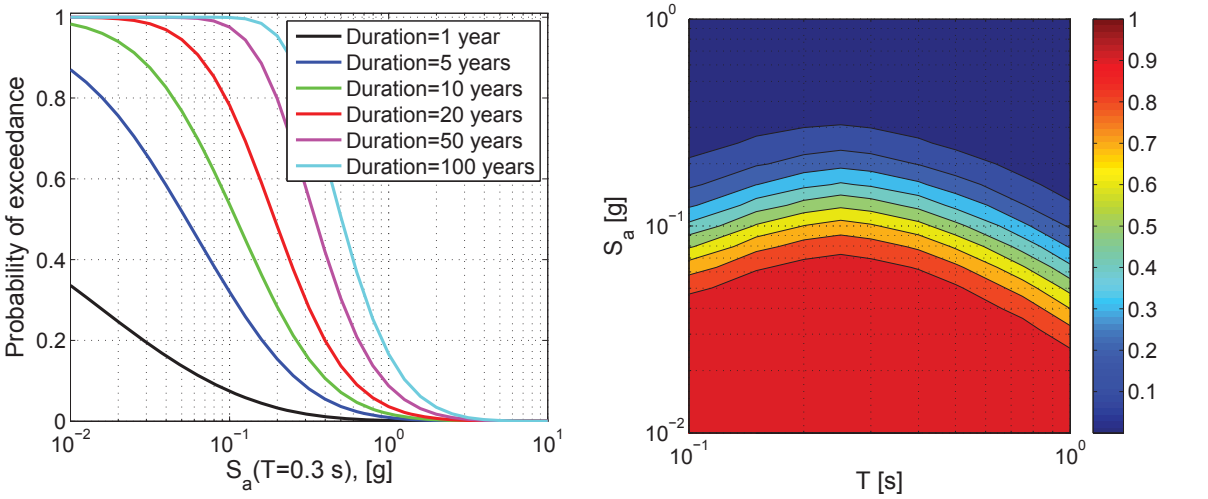

(a) Variation on forecast duration

(b) Variation on S_a and T

Figure 5.4: Mean hazard curves (probability of exceedance) for Pine Flat Dam

using the following relation (Cornell, 1968):

$$P\left[N \geq 1,\ Y \geq y^*\right] = 1 - e^{-\lambda_{y^*}.\Delta t} \tag{5.1}$$

where, $P\left[N \geq 1,\ Y \geq y^*\right]$ is the probability of having at least one earthquake with $Y \geq y^*$, λ_{y^*} is annual number of events that produce the ground motion parameter $Y \geq y^*$, and Δt is the earthquake rapture forecast duration. In addition, the return period, T_R, is $\frac{1}{\lambda_{y^*}}$.

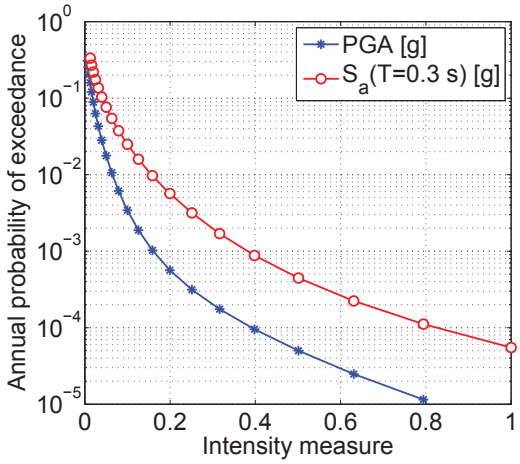

Figure 5.5: Comparison of mean hazard curves for Pine Flat Dam with different intensity measures

The next step is to develop the seismic hazard de-aggregation plots for the dam site to find

out the contribution of the various earthquake sources with different magnitudes, M_w, and distance, R, from the dam site. Figure 5.6 shows the seismic hazard de-aggregation plots for Pine Flat Dam (Deaggregation, 2003) using two intensity measures, i.e. PGA and $S_a(T = 0.3s)$. Also these plots are extended for different return periods. The modal distance, magnitude, and inter-event term can be found in each case. As seen, in overall, the dominant events at the site for both the PGA and $S_a(T)$ are in magnitude range of $5.5 < M_w < 7.0$ and in fault distance rage of $0 < R < 40$ km.

Also it is required to develop the target response spectrum for different seismic hazard intervals. In this section, the uniform hazard spectra (UHS) is used. Figure 5.7 shows the UHS for horizontal and vertical directions. It is noteworthy that the vertical component of response spectrum is estimated based on the horizontal component as discussed before.

5.5 Ground Motion Selection

Although PBEE requires probabilistic approach for ground motion selection and scaling, in this chapter, the nonlinear response of the dam is studied only under a specific ground motion. The detailed probabilistic seismic assessment is discussed in the future chapters.

The selected ground motion can be one of those obtained from PSHA or it can be the one which is known to have induced severe damages to other dams. It is noteworthy that concrete dams have for the most part performed well when subjected to earthquake. In a comprehensive paper, Nuss et al. (2012) categorized data from the concrete dams that subjected to significant shaking. Table 5.1 summarized the reported cases.

In this section the 1967 Koynanagar earthquake is used. This ground motion was led to damage to Koyna gravity dam. Figure 5.8 shows the detailed time history characteristics of the horizontal component. It is noteworthy that only horizontal component is used in this chapter (the effect of vertical component is studied in a separate chapter).

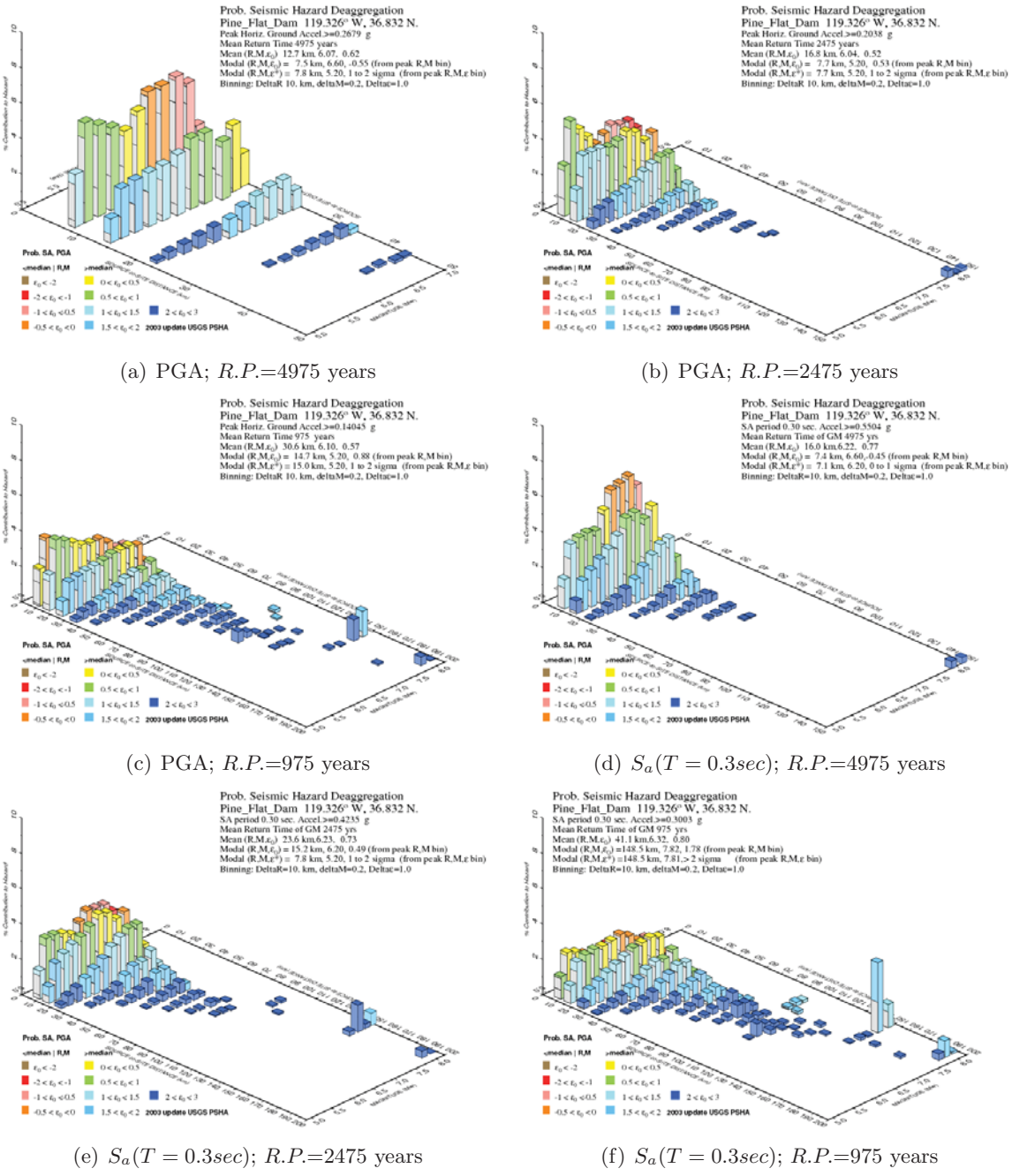

(a) PGA; $R.P.$=4975 years

(b) PGA; $R.P.$=2475 years

(c) PGA; $R.P.$=975 years

(d) $S_a(T = 0.3sec)$; $R.P.$=4975 years

(e) $S_a(T = 0.3sec)$; $R.P.$=2475 years

(f) $S_a(T = 0.3sec)$; $R.P.$=975 years

Figure 5.6: Seismic de-aggregation plots for Pine Flat Dam based on different intensity measure parameters and return periods

5.6 Finite Element Model

The finite element code Merlin (Saouma et al., 2010) is used for analysis. The geometric model is illustrated by figure 5.9. Different types of meshing is used for different types of analyses,

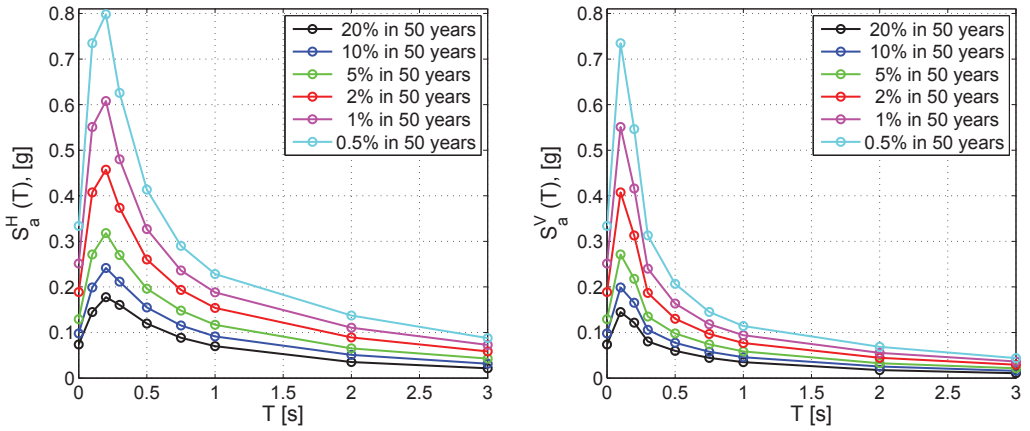

(a) Horizontal component (b) Vertical component

Figure 5.7: Uniform seismic hazard spectra for Pine Flat Dam

Table 5.1: Concrete dams shaken by significant earthquake, adapted from Nuss et al. (2012)

ID	Dam (completed)	Type	Height (m)	Crest (m)	Earthquake (date)	R (km)	Mag.	PHGA (g)	Notes
1	Lower Crystal Springs (1890)	Gravity	47	183	San Francisco (Apr 18, 1906)	0.4	8.3	0.52-0.68 (Est.)	Not the slightest crack
2	Koyna (1963)	Gravity	103	807	Koynanagar (Dec 11, 1967)	3.0	6.5	0.5	Cracks in both faces
3	Williams (1895)	Gravity	21	27	Loma Prieta (Oct 17, 1989)	9.7	7.1	0.60 (Est.)	No damage
4	Bear Valley (1912, 1988)	Gravity	28	110	Big Bear (Jun 29, 1992)	14.5	6.6	0.57	No structural damage
5	Shih Kang (1977)	Gravity	21.4	357	Chi Chi (Sep 21, 1999)	0	7.6	0.51	Vertical displ. of 9m, concrete rapture
6	Mingtan (1990)	Gravity	82	-	Chi Chi (Sep 21, 1999)	12	7.6	0.4-0.5 (Est.)	No damage
7	Kasho (1989)	Gravity	46.4	174	Western Tottori (Oct 6, 2000)	3-8	7.3	0.54	Cracks in control building
8	Takou (2007)	Gravity	77	322	Tohoku (Mar 11, 2011)	109	9.0	0.38	Cracking of gate-house
9	Miyatoko (1993)	Gravity	157	-	Tohoku (Mar 11, 2011)	135	9.0	0.32	No damage
10	Gibraltar (1920)	Arch	52	183	Santa Barbara (Jun 29, 1925)	-	6.3	¿0.3 (Est.)	No damage
11	Pacoima (1929)	Arch	113	180	San Fernando (Feb 9, 1971)	5	6.6	0.6-0.8 (Est.)	Joint opening near thrust block
					Northridge (Jan 17, 1994)	18	6.8	0.53	2” Joint opening between arch and thrust block
12	Ambiesta (1956)	Arch	59	145	Gemona-Friuli (May 6, 1976)	20	6.5	0.36 (abutment)	No damage
13	Rapel (1968)	Arch	111	270	Santiago (Mar 3, 1985)	45	7.8	0.31	Damage to spillway and intake tower, cracked pavement
					Maule (Feb 27, 2010)	232	8.8	0.302	
14	Techi (1974)	Arch	185	290	Chi-Chi (Sep 21, 1999)	85	7.6	0.5	Local cracking of curb at crest
15	Shapai RCC (2003)	Arch	132	250	Wenchuan (May 12, 2008)	32	8.0	0.25-0.5 (Est.)	No damage
16	Hsinfengkiang (1959)	Buttress	105	440	Reservoir (May 19, 1962)	1.1	6.1	0.54	Horiz. cracks in top of dam
17	Sefidrud (1962)	Buttress	106	414	Manjil (Jun 21, 1990)	-	7.7	0.71 (Est.)	Horiz. cracks near crest, minor displ. of blocks

i.e. linear and nonlinear. 4-node and 3-node plain strain 2D elements are used for modeling the dam body and the foundation. 2-node joint elements are used for modeling the discrete joints.

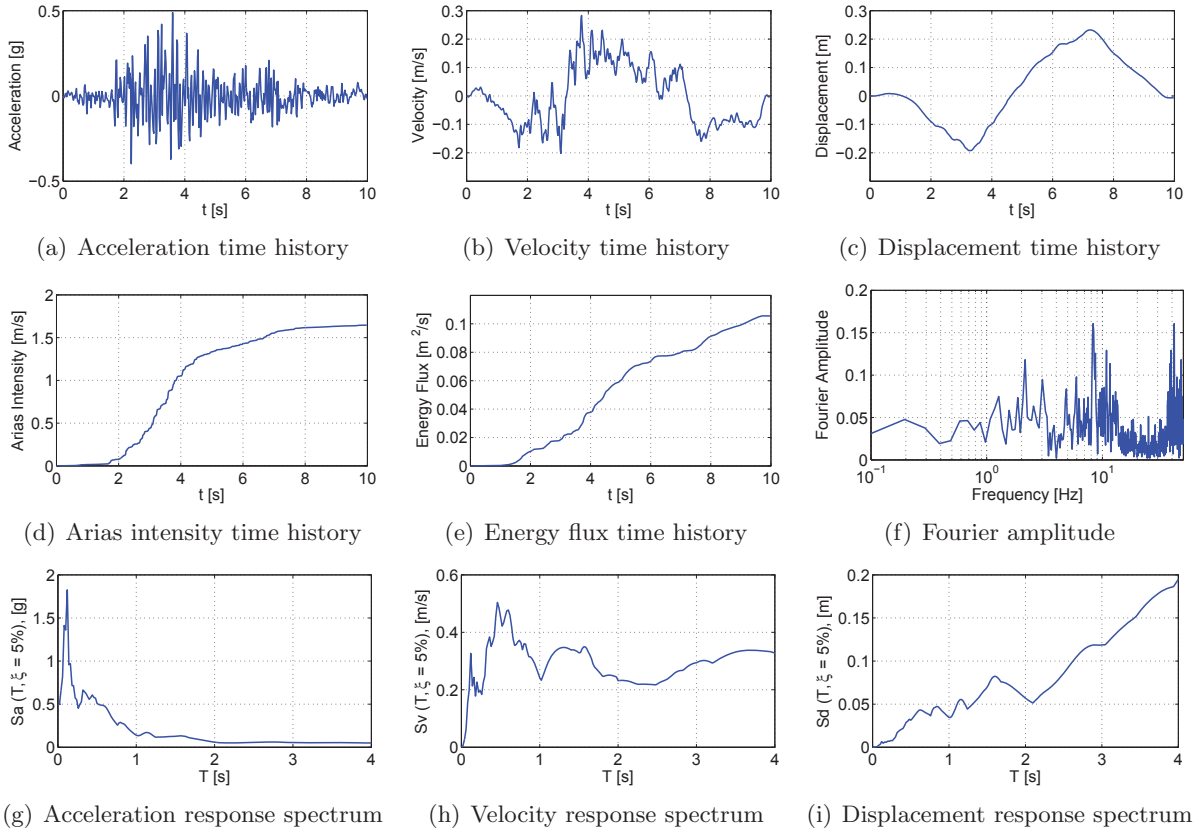

(a) Acceleration time history (b) Velocity time history (c) Displacement time history

(d) Arias intensity time history (e) Energy flux time history (f) Fourier amplitude

(g) Acceleration response spectrum (h) Velocity response spectrum (i) Displacement response spectrum

Figure 5.8: Detailed time history characteristics of the Koyna ground motion

Applied loads to the system are: 1) self-weight, 2) hydrostatic pressure, 3) uplift, 4) seismic loads. Hydrodynamic pressure is modeled based on Westergaard (Westergaard, 1933) added mass approach on both the dam upstream face and the foundation. Nonlinear material properties for the concrete (Cervenka and Papanikolaou, 2008), rock and joint elements (Cervenka et al., 1998) are summarized in Tables 5.2, 5.3 and 5.4.

5.7 Modal Analysis

Finite element modal analysis is a critical preliminary component prior to nonlinear transient analysis. This will assess the mesh by ensuring that the computed natural frequencies are consistent with the ones measured in-situ or determined by other analyses.

As a reference model, the gravity dam is analyzed without the foundation support nor added

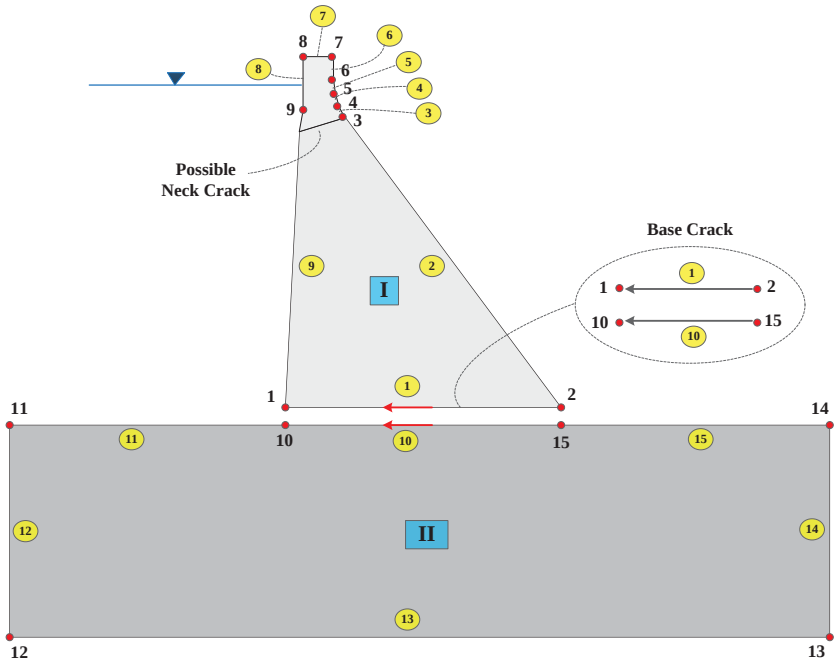

Figure 5.9: Geometric model of dam and foundation in `kumonosu`

Table 5.2: Characteristics of mass concrete

Characteristics	Symbol	Unit	Quantity
Mass density	ρ	kg/m^3	2,250
Coefficient of thermal expansion	α_T	$1/^o$C	9.5E-6
Modulus of elasticity	E	MPa	22,410
Poisson's ratio	ν	-	0.20
Tensile strength	f'_t	MPa	2.241
Compressive strength	f'_c	MPa	-22.41
Specific mode I fracture energy	G_F^I	N/m	252
Compressive critical displacement	w_d	m	-0.0005
Return direction in Haig-Westergaard space	β_{HW}	-	0
Factor for shape of Menetrey-Willam surface	e	-	0.55
Onset of nonlinearity in compression	f_{c0}	MPa	-13.5
Plastic strain at compressive strength	ε_{cp}	-	-0.001

Table 5.3: Characteristics of foundation rock

Characteristics	Symbol	Unit	Quantity
Mass density	ρ	kg/m^3	2,600
Modulus of elasticity	E	MPa	24,000
Poisson's ratio	ν	-	0.25

Table 5.4: Characteristics of dam-foundation joint

Characteristics	Symbol	Unit	Quantity
Tangential (shear) stiffness	K_t	GPa	224.1
Normal stiffness	K_n	GPa	224.1
Tensile strength	σ_{t0}	MPa	2.241
Cohesion	c	MPa	1.90
Friction angle	Φ_F	Degree	38
Dilatancy angle	Φ_D	Degree	20
Maximum aggregate size	G_{max}	m	0.08
Specific mode I fracture energy	G_F^I	N/m	252
Specific mode II fracture energy	G_F^{II}	N/m	2520
Relative irreversible deformation	γ_s	-	0.3
Maximum displacement for dilatancy	u_D^{max}	m	0.01
Tensile stress at break point (bilinear)	s_1	MPa	0.56
Crack opening displacement (COD) at break point (bilinear)	sw_1	m	1.12E-4
Cohesion at break point (bilinear)	c_1	MPa	0.375
Crack sliding displacement (CSD) at break point (bilinear)	cw_1	m	1.26E-3

mass due to hydrodynamic pressure. Table 5.5 shows the natural periods and also the effective mass in each direction. As seen, considering only the first four modes covers about 95% of the total mass in x direction. Also the most effective mode in y direction is the third one. The first period, fundamental period, is 0.309 s. This is the exact value reported also by Løkke and Chopra (2013) for the Pine Flat Dam without foundation and reservoir.

Table 5.5: Vibration characteristics of Pine Flat Dam

Mode	Period [s]	m_x^{eff} %	m_y^{eff} %	$\mathrm{m}_{rot_z}^{eff}$ %
1	0.309	42.1	2.0	54.2
2	0.151	30.1	0.6	7.9
3	0.113	8.2	69.0	25.2
4	0.088	14.3	8.2	0.6
5	0.058	0.0	0.0	0.0
6	0.052	0.1	16.5	8.0
7	0.042	3.7	1.3	0.6
8	0.041	0.0	0.0	1.5
9	0.038	1.3	1.8	1.4
10	0.035	0.3	0.5	0.6

Finally, it is important to account for the foundation and reservoir effect in overall vibration behavior of dams. In the present study, foundation is model as massless medium and the water is

modeled by Westergaard added mass approach. Six models are prepared for the system:

- Model 1: Dam alone on rigid base
- Model 2: Dam on rigid base + water added mass
- Model 3: Dam + massless foundation (fixed B.C. for foundation)
- Model 4: Dam + massless foundation (fixed B.C. for foundation) + water added mass
- Model 5: Dam + massless foundation (roller B.C. for foundation)
- Model 6: Dam + massless foundation (roller B.C. for foundation) + water added mass

Figure 5.10 compares the vibration period of dam at different conditions. In general, reservoir added mass increases the vibration period. Also considering the massless foundation increases the period as it decreases the total stiffness of the system. In addition, assuming the roller support for the foundation boundaries increases the vibration period almost in all modes.

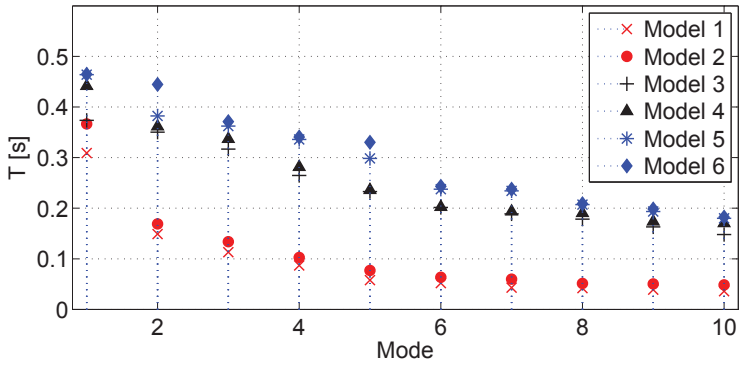

Figure 5.10: Comparison of the vibration period for different models of the Pine Flat Dam

5.8 Seismic Failure Modes

The major potential failure modes in gravity dams are due to overstressing, sliding along cracked surfaces in the dam or planes of weakness within the foundation, and sliding accompanied by rotation in the downstream direction (Ghanaat, 2004). All these failure modes can be resulted due

to cracking and consequently detaching whole or a part of the dam. Under severe ground shaking a typical gravity dam section may suffer tensile cracks at the base and/or near the downstream slope change discontinuity. The upper cracks usually initiate from the upstream or downstream face of the dam and propagate horizontally or at an angle toward the opposite face. The consequence of cracking, if extended through the dam section, may lead to sliding or rotational instability of the separated block (Ghanaat, 2004). Based on an extensive literature survey, the following limit state (LS) parameters which could lead to partial failure (in the sense that they are likely to result in uncontrollable release of water, or major economic losses) are identified, figure 5.11:

- LS-1: Concrete cracking at the neck
- LS-2: Concrete or rock cracking at the dam-foundation interface
- LS-3: Damage cracking at the key points (slope discontinuity)
- LS-4: Deflection of the crest point beyond the ultimate displacement
- LS-5: Overturning of the dam around the heel
- LS-6: Sliding along dam-rock interface due to joint breaking
- LS-7: Sliding along lift joints (weak planes)
- LS-8: Damage cracking due to fault movement in the foundation

5.9 Structural Analysis; Joint Nonlinearity

This section nonlinearity stems only from the rock concrete joint, whereaas the concrete is assumed to be linear elastic. This corresponds to LS-2, LS-5 and LS-6 as discussed already. The concrete and rock are assumed to be linear elastic. Hydrodynamic pressure is modeled by Westergaard added mass and the dynamic uplift is modeled inside the opened joints.

Koyna ground motion (figure 5.8) is used for the seismic analyses. The PGA of the horizontal component is $\sim$ 0.5g. However, in order to capture the seismic potential failure modes in detail,

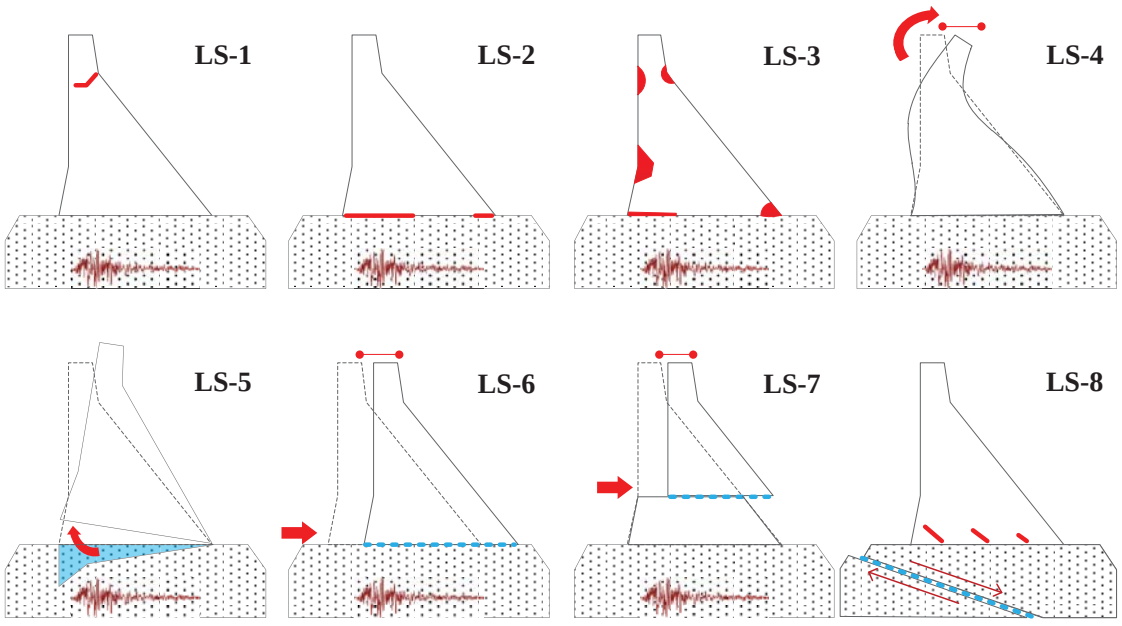

Figure 5.11: Seismic potential failure modes of a typical gravity dam in term of limit states

the ground motion is scaled for lower and higher intensities also. Two linear scale factors are: 0.7 and 1.4. Consequently, we have three ground motion records and the PGA are: 0.3g, 0.5g and 0.7g. The ground motion signal is applied at the foundation base (curve 13 in figure 5.9).

The results are reported for all three cases; however, it should be noted that in the case that the dam is failed before ending the ground motion, the results are shown up to the failure time.

5.9.1 Acceleration

Figure 5.12(a) shows the applied horizontal acceleration at the base of the foundation. In addition, figure 5.12(b) shows the recorded horizontal acceleration at the dam crest. As seen, in all cases the acceleration is amplified at the crest and has a different pattern than the base one. The amplification factor is ∼3 for the safe model (PGA = 0.3g) and ∼6 for a damaged modeled before failure (PGA = 0.5g, 0.7g).

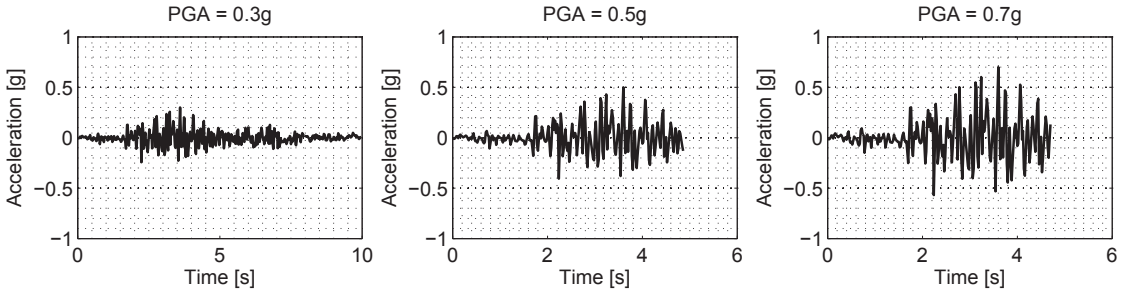

(a) Applied at the base of foundation

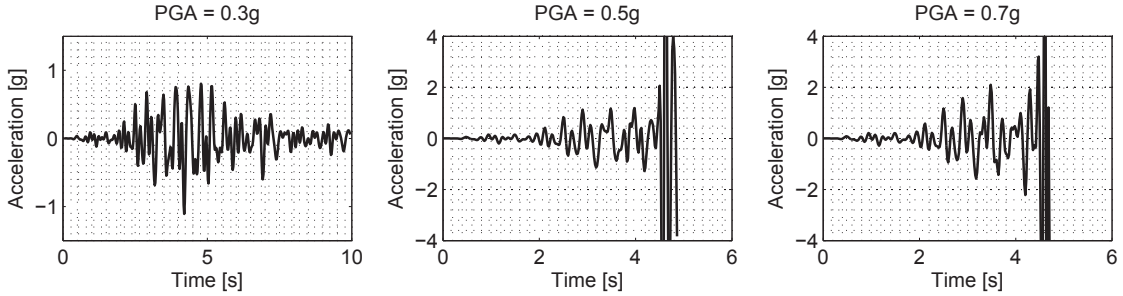

(b) Amplified at the dam crest

Figure 5.12: Acceleration response; horizontal component only

5.9.2 Displacement in Dam

Figure 5.13 Shows the displacement time history of the dam crest. Although only the horizontal acceleration is applied in these cases, both the horizontal and vertical displacement time histories are generated. For the ground motion with PGA = 0.3g, the maximum displacement in horizontal direction is almost twice of the vertical one. Both the cases with PGA = 0.5g and 0.7g are failed at 4.41 and 4.28 s, respectively. These curves show that the dam slides (or overturns) at the base more than the ultimate displacement.

In the seismic safety evaluation of concrete dam, not only the displacement time history of the index point should be checked, but also the non-concurrent displacement envelope should be evaluate for whole the dam body. Figure 5.14 shows the displacement envelope for the case with PGA = 0.3g. Horizontal displacement has uniform distribution in height. On the other hand, vertical displacement has almost uniform distribution along the base of the dam. This can be attributed to the joint opening at the heel, while there is no opening/sliding at the toe.

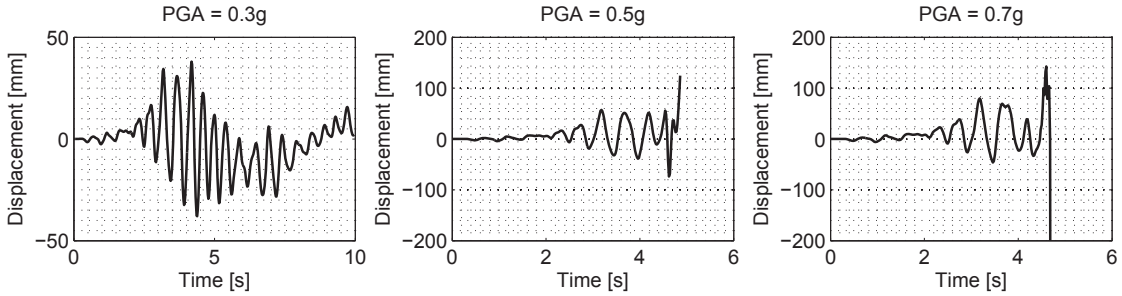

(a) Horizontal component

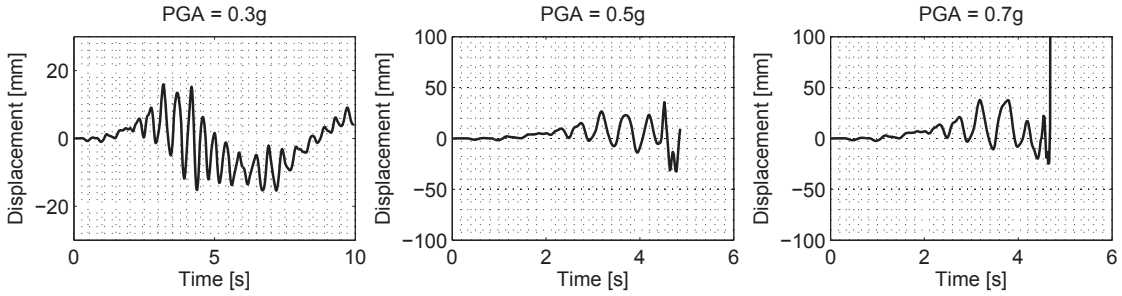

(b) Vertical component

Figure 5.13: Time history of crest displacement

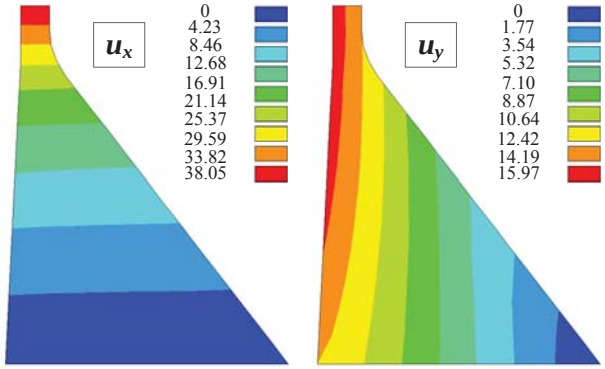

Figure 5.14: Non-concurrent displacement envelope of dam under the ground motion with PGA = 0.3g

5.9.3 Stress in Dam

Time history of the first principal stress is shown in figure 5.15 for three critical points, i.e. crest, heel, toe. Before failure (PGA = 0.3g), the crest point experiences mainly the tension, while the toe is under compression. Heel experiences both the tensile and compressive stresses. When the major part of the dam-foundation interface is cracked, most of the stresses are in the form of

tension.

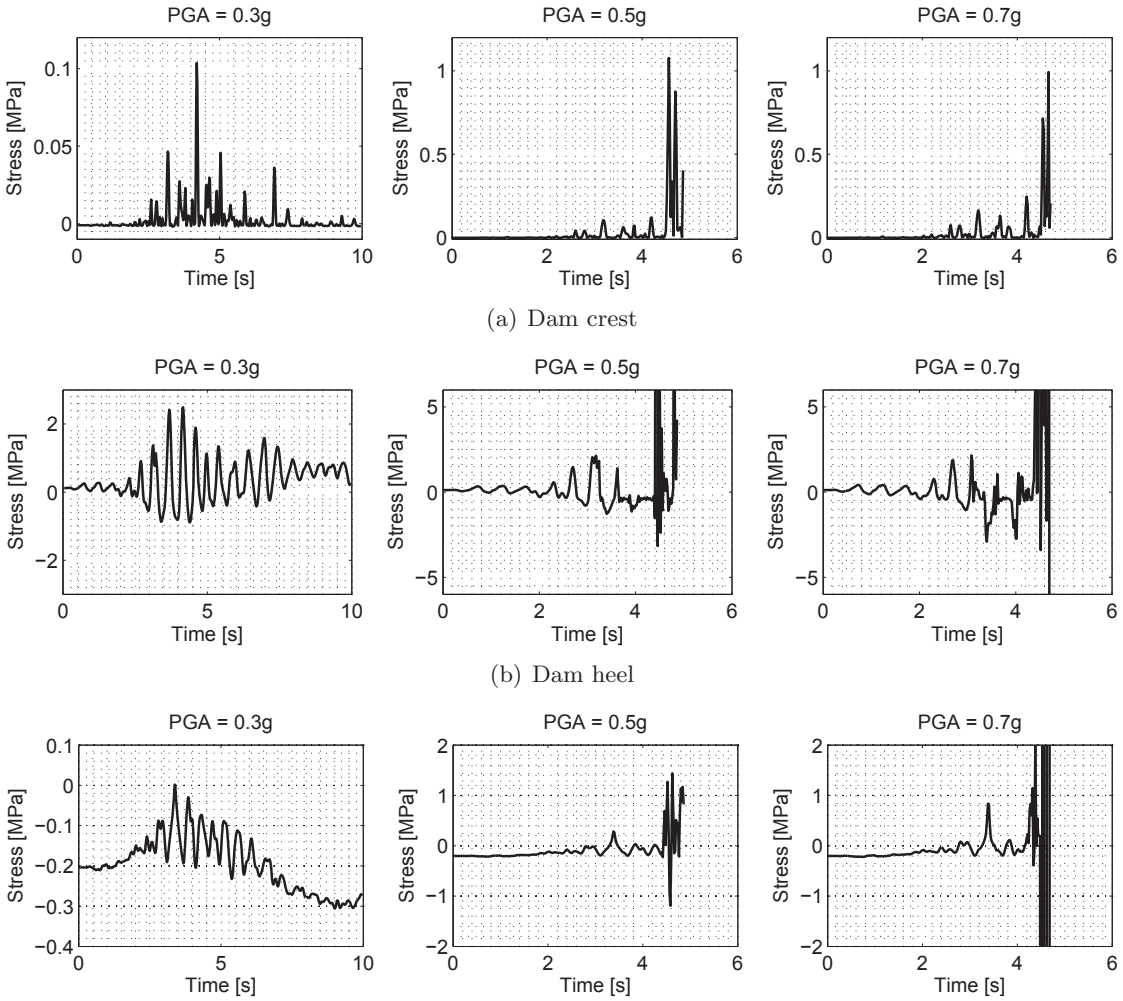

(a) Dam crest

(b) Dam heel

(c) Dam toe

Figure 5.15: Time history of first principal stress

Figure 5.16 shows the non-concurrent stress envelope for the case with PGA = 0.3g. Maximum of first principal stress (S11), minimum of third principal stress (S33) and maximum of shear stress (S31) are shown. As see, the most critical point is dam heel in term of tension and dam toe in term of compression.

When the concrete is modeled based on linear elastic assumption, two simple criteria can be used for estimation of the intensity of damage, i.e. uniaxial failure criterion and biaxial failure

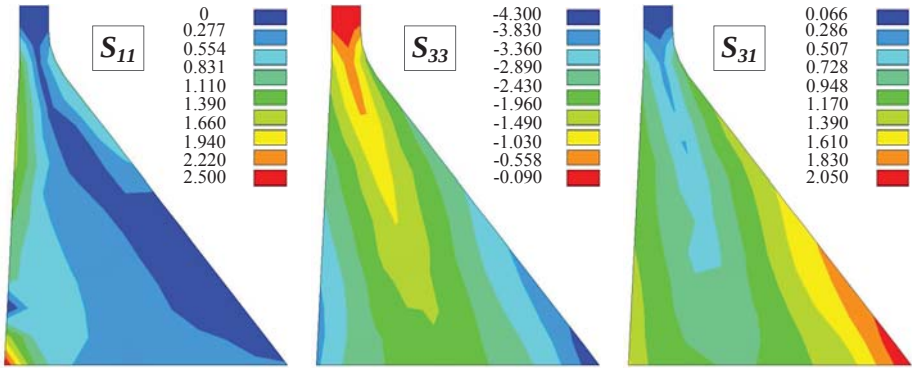

Figure 5.16: Non-concurrent principal stresses envelope of dam under the ground motion with PGA = 0.3g

criterion. The uniaxial failure criterion can be represented as:

$$S11 \geq f'_t \quad \text{or} \quad S33 \leq f'_c \tag{5.2}$$

The concrete biaxial failure envelope has been improved from that given originally by Kupfer et al. (1969), also described in Wang and Hsu (2001). In addition, the linear variation of concrete strength in the compression-tension zone is substituted by a quadratic curve as proposed by Chen W.F. (1982). Different zones of performance as well as their mathematical relations are summarized in figure 5.17. In the current example (for PGA = 0.3g), the heel of the dam violates both the uniaxial and biaxial failure criteria.

5.9.4 Strain in Dam

Figure 5.18 shows the time history of the first principal strain only for the crest point. As seen, the trend of strain variation matches well with that reported for the stress in figure 5.15(a). However, many of the concrete failure criteria are originally developed based on principal stress state, it should be noted that the actual cracking of a concrete element is based on the strain exceedance from the critical value. Moreover, figure 5.19 shows the non-concurrent strain envelope on the dam body for the case with PGA = 0.3g. In this case, not only the heel but also the toe of the dam experience some tensile strains (E11).

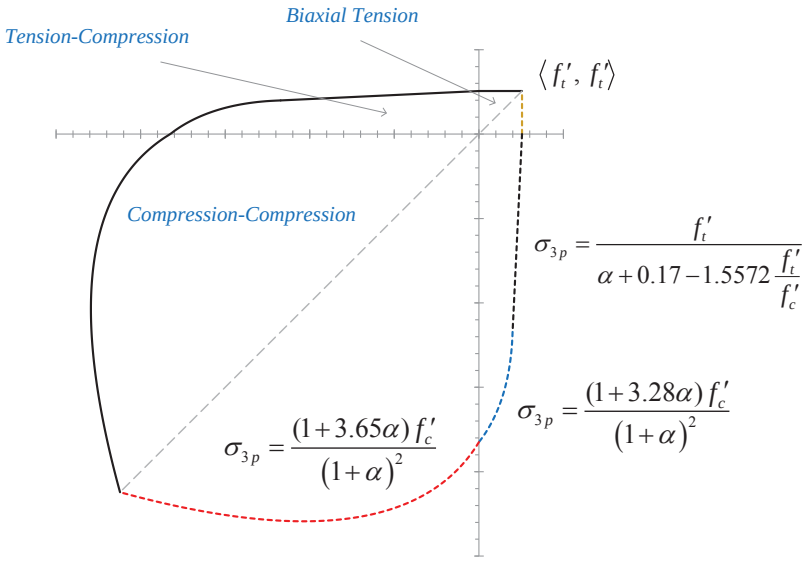

Figure 5.17: Biaxial failure envelope of the concrete

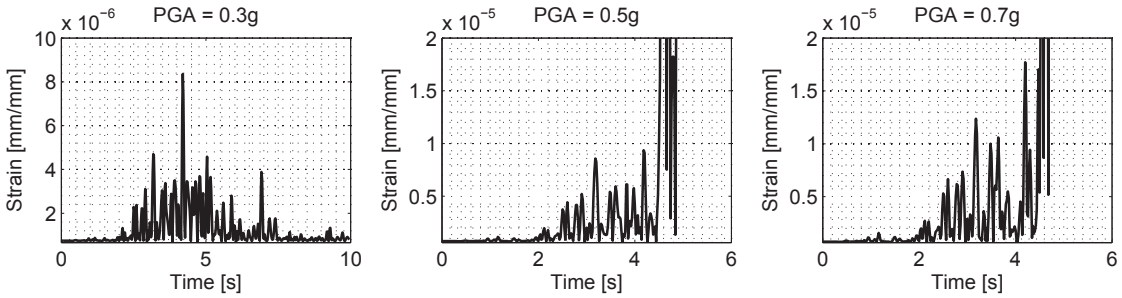

Figure 5.18: Time history of first principal strain at the crest point

5.9.5 Joint Response

Considering that in the present example the nonlinearity of the system is originated from dam-foundation interface joint, the seismic response of the joint is investigated in detail.

Figure 5.20(a) shows the time history for ratio of the cracked length to the dam base. Based on this figure, only 15% of the base is cracked at the end of the seismic analysis with ground motion PGA = 0.3g. Under the both PGA = 0.5g and 0.7g the dam fully cracked; however, more intense ground motion leads to early failure. As mention before, this curve can be used as a single variable

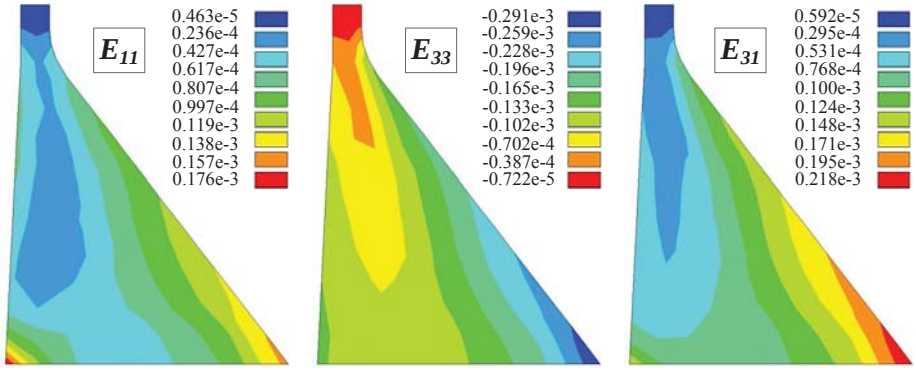

Figure 5.19: Non-concurrent principal strains envelope of dam under the ground motion with PGA = 0.3g

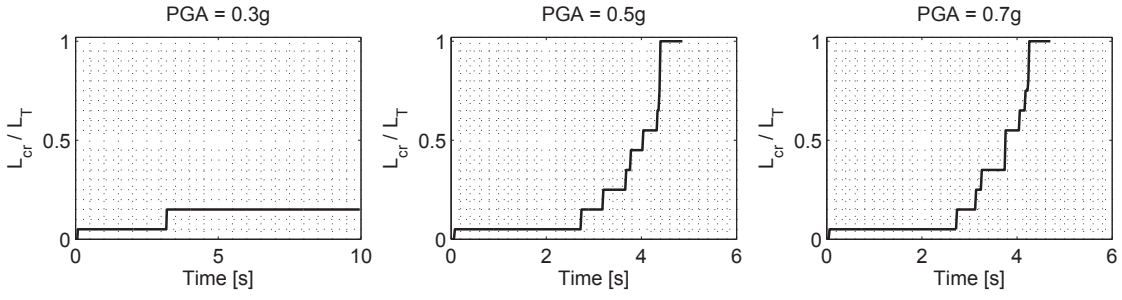

(a) Joint cracking

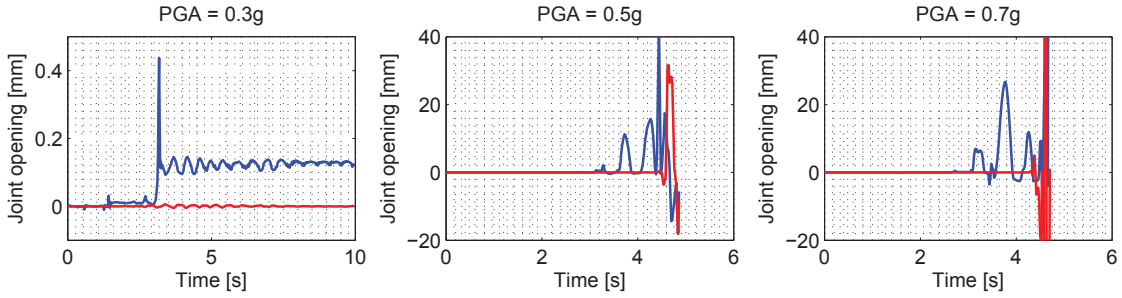

(b) Joint opening in heel (blue line) and toe (red line)

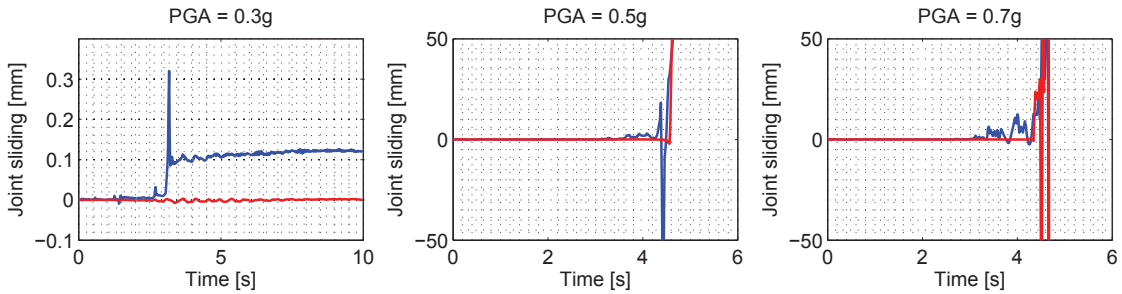

(c) Joint sliding in heel (blue line) and toe (red line)

Figure 5.20: Time history of joint displacement

damage index for quantification of the damage in dam.

Figures 5.20(b) and 5.20(c) shows the time history of the crack opening and crack sliding for two critical point, i.e. heel and toe. Based on this figure, for the case with PGA = 0.3g, there is no joint opening and sliding at the toe; however, dam experiences 0.4 mm joint opening and 0.3 mm joint sliding at the heel. For the case with PGA = 0.5g, the heel experiences some large joint openings (about 10 mm) about one second before failure; however the value of the joint sliding is not considerable until failure. For the case with PGA = 0.7g, the heel has joint opening about 25 mm one second before failure. Consequently, it has up to 10 mm sliding half second before failure. Note that the toe does not have any considerable joint opening and sliding before failure. For the current example, any relatively large values in joint opening/sliding of the toe corresponds to failure of the system.

Figure 5.21 shows the normal and tangential stresses on the interface joint at the heel and toe. For the case with PGA = 0.3g, the normal stress at the heel fluctuates between 0 and -4 MPa (with some exceptions). The joint at this point is not capable of enduring any tensile stresses after fracturing. This point can be tracked also based on figure 5.20(a). On the other hand, the value of normal stress at the toe fluctuates around -2 MPa. Figure 5.21(b) shows the variation of tangential stresses. For the case with PGA = 0.3g, the shear stress drops to zero after fracturing; however, there are still some positive stress up to end of the analysis. For the cases with PGA = 0.5g and 0.7g, the joint experiences some very high stresses (normal or shear) about one second before failure.

Figure 5.22 shows the time history of the joint safety factor. Global safety factor against sliding for the joint is determined as:

$$\mathrm{SFFS}_{\mathrm{glob}} = \frac{F_C + \sum F_N \tan\Phi}{\sum F_T} \tag{5.3}$$

where, F_C, F_N and F_T are total cohesive, normal and shear forces, respectively. Φ is the friction angle. In addition, the average safety factor, $\mathrm{SFFS}_{\mathrm{ave}}$, for the joint is computed from those determined at each Gauss point.

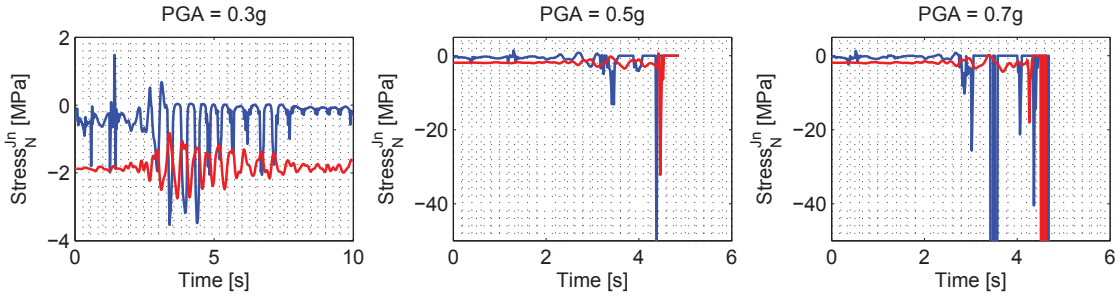

(a) Normal stress in heel (blue line) and toe (red line)

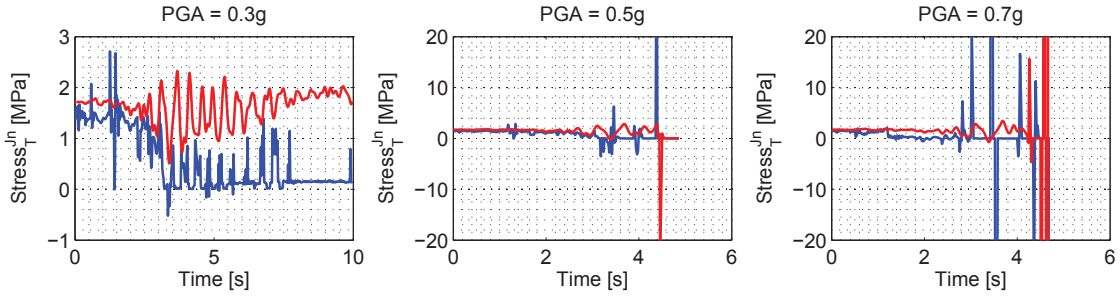

(b) Tangential stress in heel (blue line) and toe (red line)

Figure 5.21: Time history of joint stress

As seen, for the case with PGA = 0.3g, both the $SFFS_{glob}$ and $SFFS_{ave}$ fluctuates around 5. For the cases with PGA = 0.5g and 0.7g, the $SFFS_{ave}$ decreases by cracking of the joint and finally approaches to zero at the failure time.

5.10 Structural Analysis; Joint and Material Nonlinearity

Based on figure 5.11, the failure modes and limit states of the system is not limited to only dam-foundation interface joint. Any other set of cracks specially at the neck area and also the concrete of the heel and toe can be considered as failure mode.

For this purpose, the simultaneous effects of joint nonlinearity (due to pre-defined zero thickness dam-foundation interface joint) and material nonlinearity (due to concrete cracking under the smeared crack approach) are considered. This corresponds to LS-1, LS-2, LS-3, LS-5 and LS-6 as discussed already. The foundation rock is still assumed to be linear elastic. Hydrodynamic pressure is modeled by Westergaard added mass and the dynamic uplift is modeled inside the opened

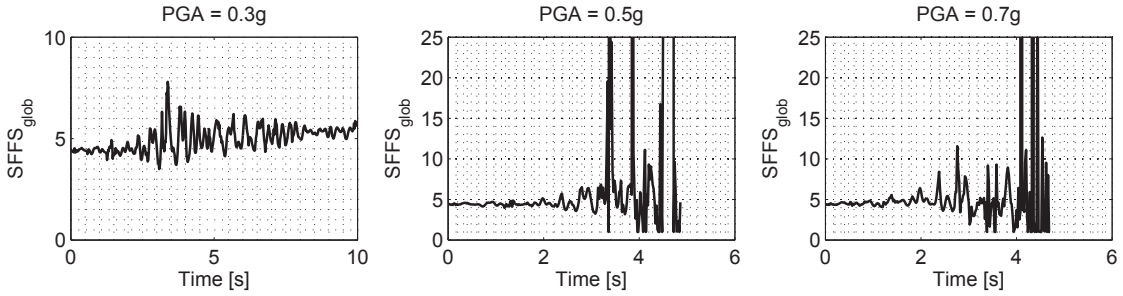

(a) Global safety factor

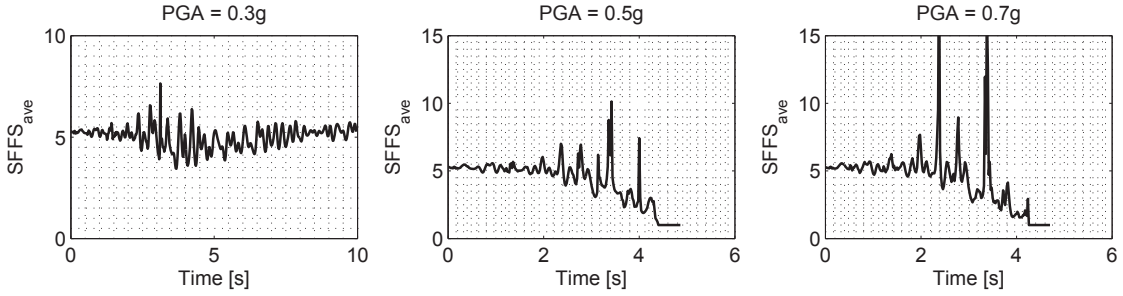

(b) Average safety factor

Figure 5.22: Time history of the safety factor in joint

joints/cracks.

Considering that the seismic response of the concrete dam including smeared crack model is highly sensitive to the intensity of the applied ground motion, the previously selected ground motion is scaled to six intensity levels, i.e. 0.2g, 0.3g, 0.4g, 0.5g, 0.6g and 0.7g. This method corresponds to the incremental dynamic analysis (IDA) (Vamvatsikos and Cornel, 2002); however, in the present chapter only the nonlinear dynamic analyses are performed and there is no specific post processing on the results.

5.10.1 Displacement Response History

Figure 5.23 Shows the displacement time history of the dam crest. Only the horizontal component is shown. The dam is survived for the cases with PGA = 0.2g, 0.3g and 0.4g; however, it fails in the other cases. For the safe modeled, the maximum absolute crest displacement is proportional to the seismic intensity. For the failed cases, increasing the intensity of the ground motion, reduced the final failure time.

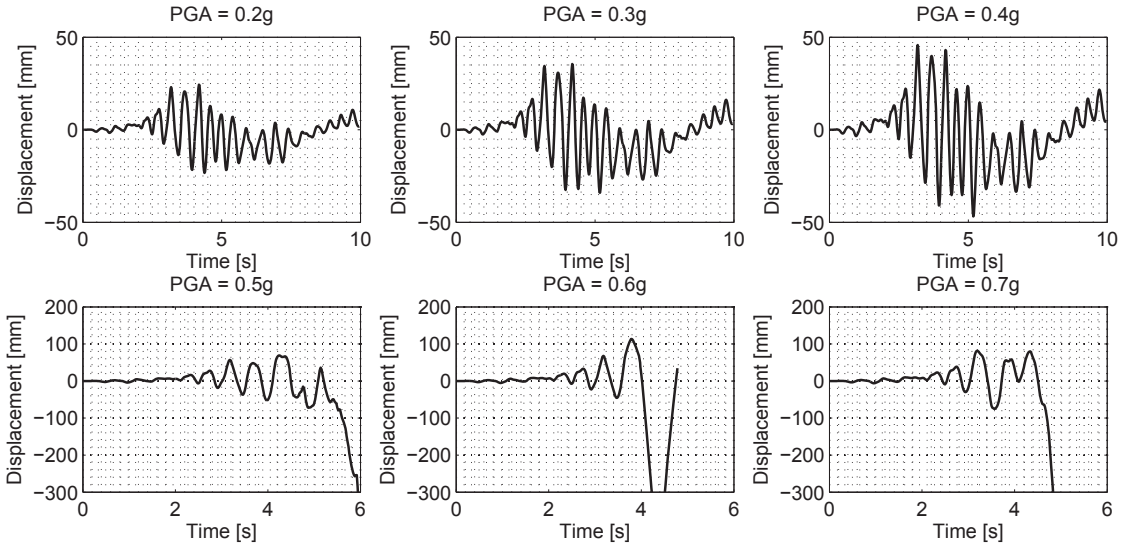

Figure 5.23: Time history of crest horizontal displacement for the model with interface joint and smeared crack

5.10.2 Joint Response History

Based on figure 5.24, in none of the cases the dam-foundation interface is fully cracked. However, for the high intensity ground motions, i.e. PGA = 0.5g, 0.6g and 0.7g, another failure mechanism (cracking of concrete based on smeared crack approach) leads to termination of the analysis before ending the ground motion. Almost in all cases, increasing the seismic intensity level, increases the base crack ratio.

Figures 5.25 and 5.26, shows the time history of the joint opening and joint sliding for the two critical points, i.e. heel and toe. Based on these figure, the joint at the toe is always safe (there is no opening and sliding in this point). The case with PGA = 0.3g shows higher opening/sliding that the case with PGA = 0.4g. This may attributed to the different cracking mechanism of concrete in these two cases. In all the cases with PGA = 0.5g, 0.6g and 0.7g, the heel experiences very high opening and sliding responses.

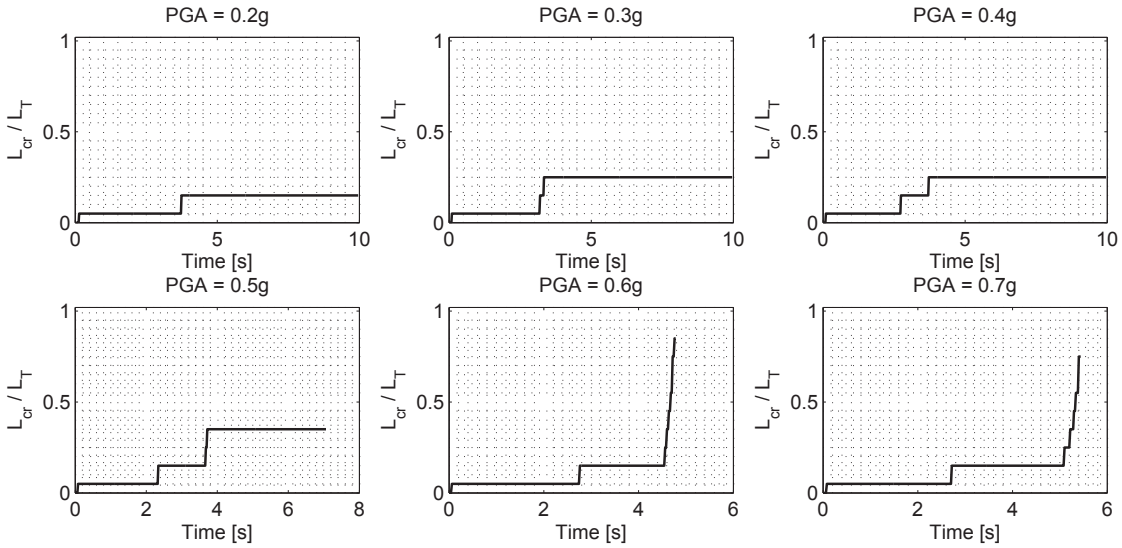

Figure 5.24: Time history of joint cracking

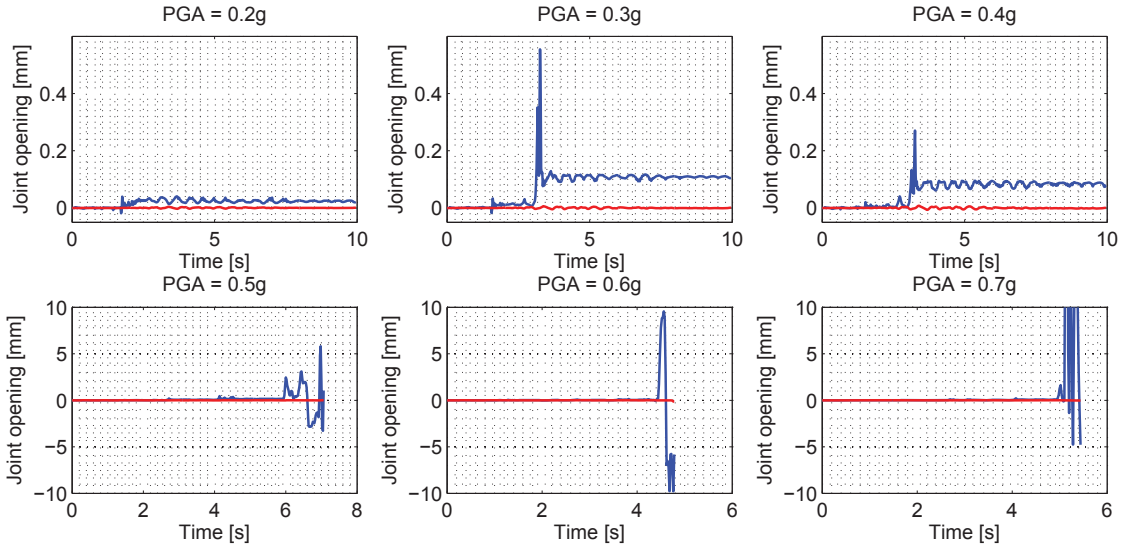

Figure 5.25: Time history of joint opening in heel (blue line) and toe (red line)

5.10.3 Cracking of Concrete

This section studies the crack profile of the dam for different intensity scenarios. Figure 5.27 shows the initiation of the cracking and the final crack profile for the cases which remain safe, i.e. PGA = 0.2g, 0.3g and 0.4g. As seen, in all cases cracking starts at the heel. This is the most critical point of the dam and in all the previous cases, the interface joint opening first occurs in

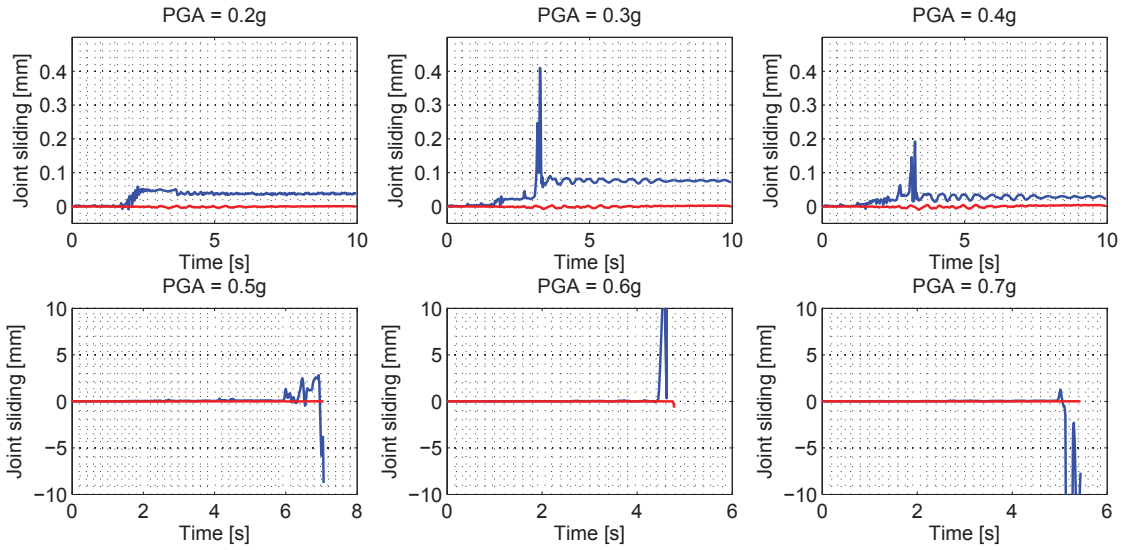

Figure 5.26: Time history of joint sliding in heel (blue line) and toe (red line)

this point. Then, cracking propagates at the dam base toward down stream. This is the crack path which is also followed by the interface joint.

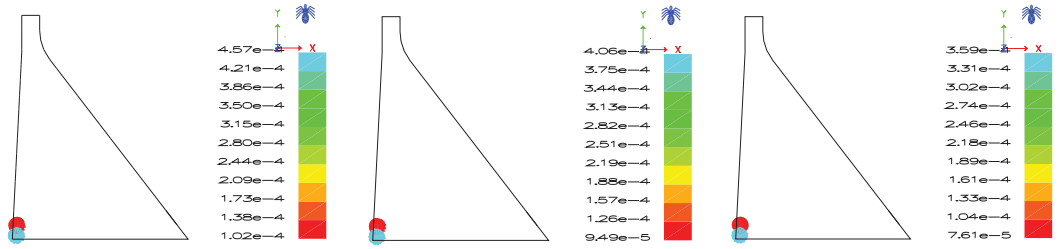

(a) PGA = 0.2g, Initiation t = 3.74 s (b) PGA = 0.3g, Initiation t = 3.70 s (c) PGA = 0.4g, Initiation t = 3.16 s

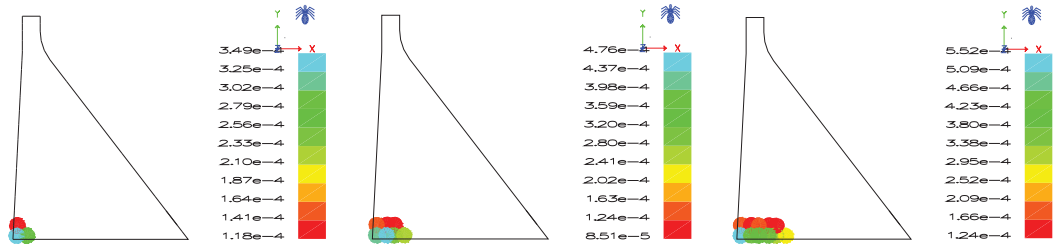

(d) PGA = 0.2g, Final t = 10.0 s (e) PGA = 0.3g, Final t = 10.0 s (f) PGA = 0.4g, Final t = 10.0 s

Figure 5.27: Concrete dynamic cracking for the safe models

The ratio of the crack length to the base of the dam is 0.15, 0.25 and 0.30 for the cases with PGA = 0.2g, 0.3g and 0.4g, respectively. Moreover, increasing the intensity of the ground motion,

decreases the time of first crack in body. The contour plot in figure 5.27 shows the crack opening at the considered time.

Figures 5.28, 5.29 and 5.30 shows the crack profiles at different times (from crack initiation to termination of the analysis) for different seismic intensities. Again, in all cases the crack starts at the heel of the dam and propagates toward downstream. Another set of crack starts at the neck near the slope discontinuity and propagates toward upstream face. In all of these cases, the failure occurs when at least one crack path generates near the neck area. Thus, the failure mode of the dam with both interface joint and smeared crack model is cracking of the neck. These limit states are already shown in figure 5.11 as LS-1, LS-2 and LS-3.

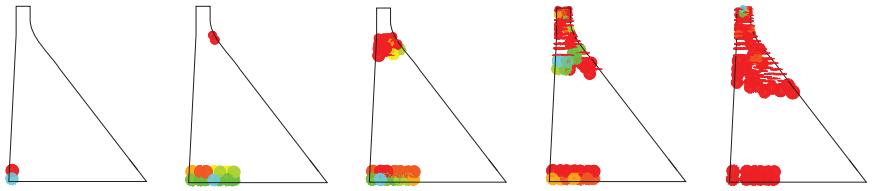

(a) t = 3.14 s (b) t = 3.98 s (c) t = 4.20 s (d) t = 5.48 s (e) t = 7.10 s

Figure 5.28: Concrete dynamic cracking for the case with PGA = 0.5g

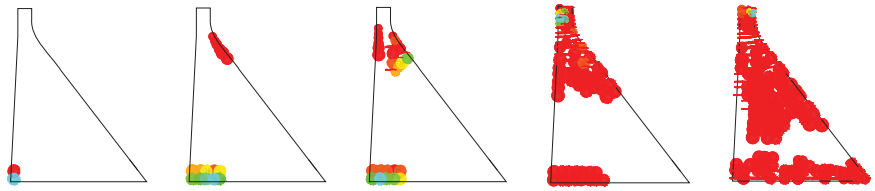

(a) t = 2.74 s (b) t = 3.50 s (c) t = 3.68 s (d) t = 4.54 s (e) t = 4.84 s

Figure 5.29: Concrete dynamic cracking for the case with PGA = 0.6g

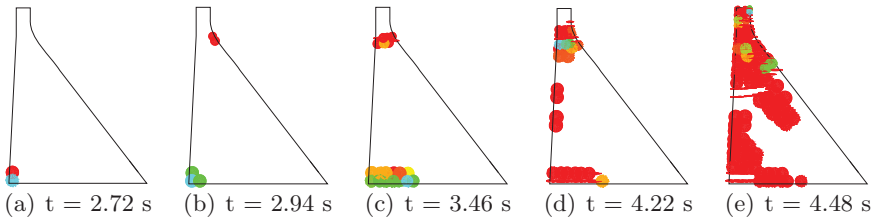

(a) t = 2.72 s (b) t = 2.94 s (c) t = 3.46 s (d) t = 4.22 s (e) t = 4.48 s

Figure 5.30: Concrete dynamic cracking for the case with PGA = 0.7g

Chapter 6

Quantified Potential Failure Mode Analysis of Concrete Dams

This chapter is based on the following two references:

Hariri-Ardebili, M.A., Saouma, V.E. and Porter, K.A., (2015), Quantification of Seismic Potential Failure Modes in Concrete Dams (submitted to Earthquake Engineering and Structural Dynamics)

6.1 Introduction

In its quadrennial report, American Society of Civil Engineers (2013) reports that the average age of the 84,000 dams in the US is 52 years, that the nation's dams are aging and the number of high-hazard dams is on the rise. It is further reported that overall number of high-hazard dams continues to increase, to nearly 14,000 in 2012, while those those considered deficient is estimated at more than 4,000 (which includes 2,000 deficient high-hazard dams). As a result ASCE gave a D+ assessment for the dam national infrastructure. Thus, it is not surprising that ASDSO (2011) estimates that it will require an investment of $21 billion to repair these aging, yet critical, high-hazard dams. Given the limited budget for repair and maintenance, national codes require a quantitative assessment of a dam safety for prioritization purposes (FERC-Arch, 1999) (USBR-manual, 2011) (ANCOLD, 2003) (CDA, 2007).

A potential failure mode (PFM) of a dam, in its general definition, is a chain of events leading to unsatisfactory performance and uncontrolled release of reservoir water (FERC-PFMA, 2005).

Correspondingly, a potential failure mode analysis (PFMA) is the exercise required to identify all PFMs under all possible loading conditions (USBR-manual, 2011) and not only structural. This is accomplished through multiple meetings of all those involved (closely or remotely) with the dam operation.

Broadly speaking, one may perform a potential failure mode analysis either qualitatively (based on site observations) or quantitatively (based on accompanying finite element analyses). The former approach is the one advocated by both (FERC-PFMA, 2005) and (USBR-manual, 2011). On the other hand, there have been very few attempts to quantify the method, and to the best of the authors' knowledge this was done exclusively for linear elastic analysis by Ghanaat (2004). The author of Ghanaat (2004) proposed a systematic approach to PFM identification in terms of demand capacity ratios, cumulative inelastic duration, and percentage of over-stressed area in dam body.

Other researchers have studied the failure modes of concrete dams without utilizing a systematic procedure. Instead a hybrid approach based on the specificity of the nonlinear model, the analysis technique and post-processing of the data is used. Amongst those researchers, it is worth mentioning a few. Tekie and Ellingwood (2003) developed fragility curves with several limit states; Wei et al. (2008) proposed a strength reserve factor method; Feng et al. (2011) adopted a set of innovative safety factors; Pan et al. (2014) relied on different fracture modeling approaches; Wang et al. (2013a) used a safety monitoring index; Dewals et al. (2011) proposed a failure mode based on malfunctions in a complex or a series of dams; Su et al. (2013) used correlated (sequential or parallel) failure modes.

The present contribution is a natural extension of the previous work by the first two authors (Hariri-Ardebili and Saouma, 2014) who proposed a multi-scale based damage index model for concrete dams. It provides an essential link with the second generation of performance based earthquake engineering (PBEE-2) offered in Porter (2003) and Applied Technology Council (2012). Proposed is a hybrid model based on PFMA and PBEE-2 for the seismic and probabilistic performance assessment of dams.

First an extensive review of the PFM in concrete dams (along with case studies) is presented. Then the proposed quantification of the PFM is addressed for both linear and nonlinear analysis. In both cases multiple strip analysis (MSA) approach is used. This approach leads to some interesting by-products: the probabilistic relationship between the linear and nonlinear analyses, and the selection of most efficient intensity measure parameter. A detailed numerical example is presented later.

6.2 State-of-the-Art Review on PFM

6.2.1 Fundamentals of PFMA

PFMA is characterized by three sequential steps: a) identification, b) description and c) screening of PFMs (FEMA-PFM, 2011). Identification of PFMs is usually done in a team setting with a diverse group of qualified people who collect and review all relevant background information (such as geology, design, analysis, construction, concrete material, flood and seismic loading, operation, safety evaluations and monitoring documentations). The second step fully describes the identified PFM from initiation, to failure progress, and possibly leading to breach and uncontrolled reservoir release. Typically, failure starts with some initiating event that causes an adverse change in the structure. The initiator could be: a) hydrologic, b) seismic; c) aging; and d) human. The final step (screening) defines the mechanism and magnitude of the breach and its impact. This approach (with minor variations) is the one currently adopted by Reclamation and Corps of Engineers (USBR-manual, 2011, joint manual), and by the Federal Energy Regulatory Commission (FERC) (FERC-PFMA, 2005).

6.2.2 Historical Seismic Damage in Concrete Dams

Since there have been few reported earthquake-induced failures or major damages in concrete dams, this section will review some of the most important cases reported in the literature. They can assist in the identification of PFM below.

Koyna Dam (India) was a rubble concrete gravity dam of 853 m length and 103 m height. The 1967 Koyna earthquake induced horizontal cracks on both faces of the tallest non-overflow blocks at the elevation of the downstream change of slope. However, the dam did not breach and no flooding occurred. Subsequently, the dam was strengthened by the addition of buttresses on the downstream face of the non-overflow blocks (Chopra and Chakrabarti, 1973). This observed performance clearly points to the type of overstressing failure that could occur in a gravity dam.

Shih Kang Dam (Taiwan) was 21.4 m gravity dam and 357 m long. The dam was located directly over a branch of the fault caused by the M7.6 Chi Chi earthquake on September 1999. The fault rupture extended both upstream and downstream of the dam and caused extensive damage to bays 16 to 18. The ground movement led to a vertical differential movement of about 9 m in these bays. There was also a diagonal horizontal offset through the dam of about 7 m, and the dam collapsed with uncontrolled release of water (Nuss et al., 2012).

Uh Dam (Japan) is a 14 m high concrete gravity dam. The dam is located about 1.0 km from the epicenter of the 2,000 Western Tottori Earthquake (M7.3). The only damage to the dam was cracking 10 mm to 30 mm wide on the spillway channel near the base of the downstream face and there was no uncontrolled release of water (Nuss et al., 2012).

Pacoima Dam (USA) is a 111 m high arch dam with a crest length of 180 m. Abutment rock movements and contraction joint opening were observed following the 1971 San Fernando earthquake and the 1994 Northridge earthquake. In 1994, the contraction joint between the arch dam and thrust block on the left abutment opened 5 cm at the crest level. The opening continued downward, tapering to 0.64 cm 18.3 m below the crest level. Also a crack diagonally crossed two lift joints and reached the abutment rock. Other contraction joints did also moderately open (Ghanaat, 2004).

Hsinfengkiang Dam (China) is a 105 m buttress dam with 440 m crest length. The dam has 19

diamond-head buttresses in the central portion with gravity section located on either side. In 1962, the dam was shaken by a M6.1 earthquake located very close to the dam (it is widely believed that it may have been triggered by the infill of the reservoir) resulting in horizontal cracks (Shen et al., 1974).

Sefid-rud Dam (Iran) is a 106 m gravity buttress dam with 7 gravity monoliths and 23 massive head buttress units. In 1990 it was damaged by M7.3 Manjil earthquake with the epicenter at about 32 km however the fault rupture was much closer. The main damage to the central monoliths was cracks at lift joints extending from the dam face through the buttress face and web. These occurred close to the change in slope near the crest and resulted in a 2 cm shear displacement. Although no catastrophic release of the reservoir did occur, the overall stability of the dam was not perceived to be of major concern. Subsequently the dam was repaired using epoxy-grouting for water tightness with post tensioning strands to restore shear strength in the cracked sections (Ahmadi et al., 1992).

6.3 Critical Assessment of Existing Qualitative Approach

As earlier stated, current regulations are mainly qualitative. This approach starts with a failure initiator and then determines its impact on the structure. Table 6.1 summarizes some of most important initiator events as well as their impacts on concrete dams. Furthermore, figures 6.1(a) and 6.1(b) illustrate the initiators for gravity and arch dams respectively. Once all PFMs have been determined, they must be ranked to identify the the most critical one which should be described in great details.

The PFMs should be categorized in terms of the adverse factors that are likely to induce failure modes. Each PFM is classified/categorized according to the classification system shown in Table 6.2. Finally, figure 6.2 illustrates the key steps of a PFMA. It should be noted that it is purely qualitative.

The next section will first introduce the tools used for the categorization of the above refer-

Table 6.1: Summary of the important initiators and the resultant impacts, based on (USBR-manual, 2011)

Initiator	**Resulting Impacts**
Increasing reservoir level	Increases stress, causes cracks and sliding Overtops the dam, causes to erosion and sliding
Increasing uplift pressure	Reduces the frictional resistance and increases sliding
Seismic load	Increases stress, causes cracks and sliding
Alkali-aggregate reaction	Reduces the strength and load-carrying capacity of concrete Expands the concrete and binds equipment
Human interaction	Fails in spillway gate operation, causing the reservoir to rise
Landslide	Causes a large rock mass to move into the reservoir, causing large waves, causing overtoping
Leaching of foundation	Reduces the bearing capacity, causes the dam settles

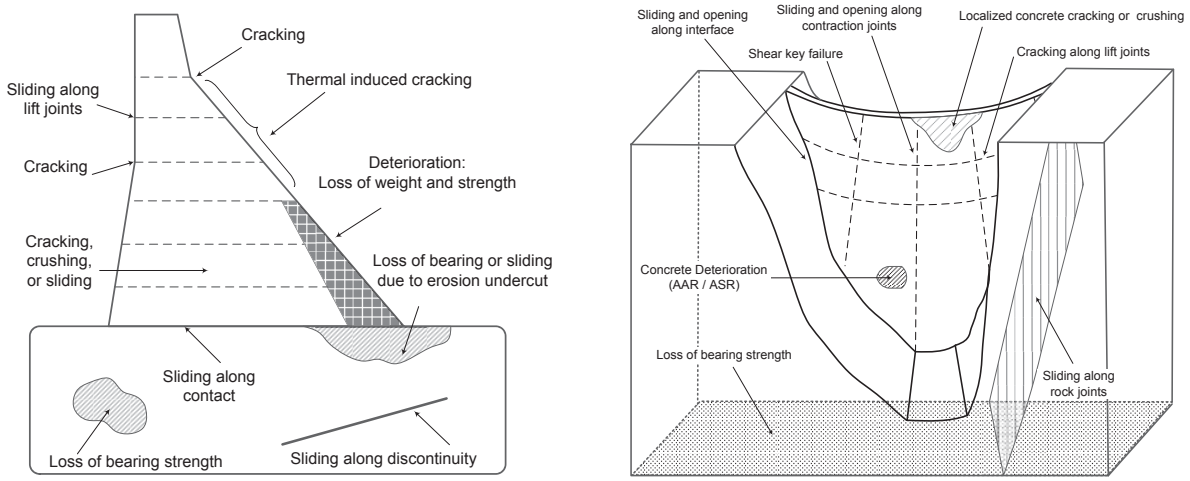

(a) Gravity dam, 2D, adopted from FEMA-PFM (2011)

(b) Arch dam, 3D

Figure 6.1: PFMs as initiators in concrete dams

enced PFMs and then their applicability to both dams and foundations.

Table 6.2: Categories of the identified PFMs adapted from USBR-manual (2011) and FERC-PFMA (2005)

ID	Code	Identifier	Definition
I	USBR-USACE	*Failure is in progress or imminent*	PFM initiated and in progress; emergency actions warranted; increased monitoring or other interim risk reduction actions may be warranted; risk estimates and documentation should be completed.
	FERC	*Highlighted PFM*	Some PFMs are of of great significance with high potential for occurrence; consequence and likelihood of adverse response highlighted.
II	USBR-USACE	*Failure mode is credible*	PFMs consequential; additional risk analysis required, no immediate action needed; monitoring recommended.
	FERC	*PFM considered but not highlighted*	PFM of some significance present; Arguments for retaining or ignoring must be made.
III	USBR-USACE	*Insufficient information to determine credibility of failure mode*	Insufficient information; PFMs must be carried; Increased monitoring recommended.
	FERC	*More information or analyses are needed in order to classify*	Additional information required.
IV	USBR-USACE	*Failure mode is not credible*	Likelihood of failure negligible; no additional studies required; additional documentation needed; additional monitoring not required.
	FERC	*Failure mode ruled out or is considered not viable*	No viable PFM.

6.3.1 Tools

6.3.1.1 Event Tree

An event-tree analysis is a technique used to identify possible outcomes given the occurrence of an initiating event. It is a commonly-used approach for understanding, analyzing and communicating dam safety risk and for supporting decision making, (Hartford and Baecher, 2004) and (Bowles and McClelland, 2000).

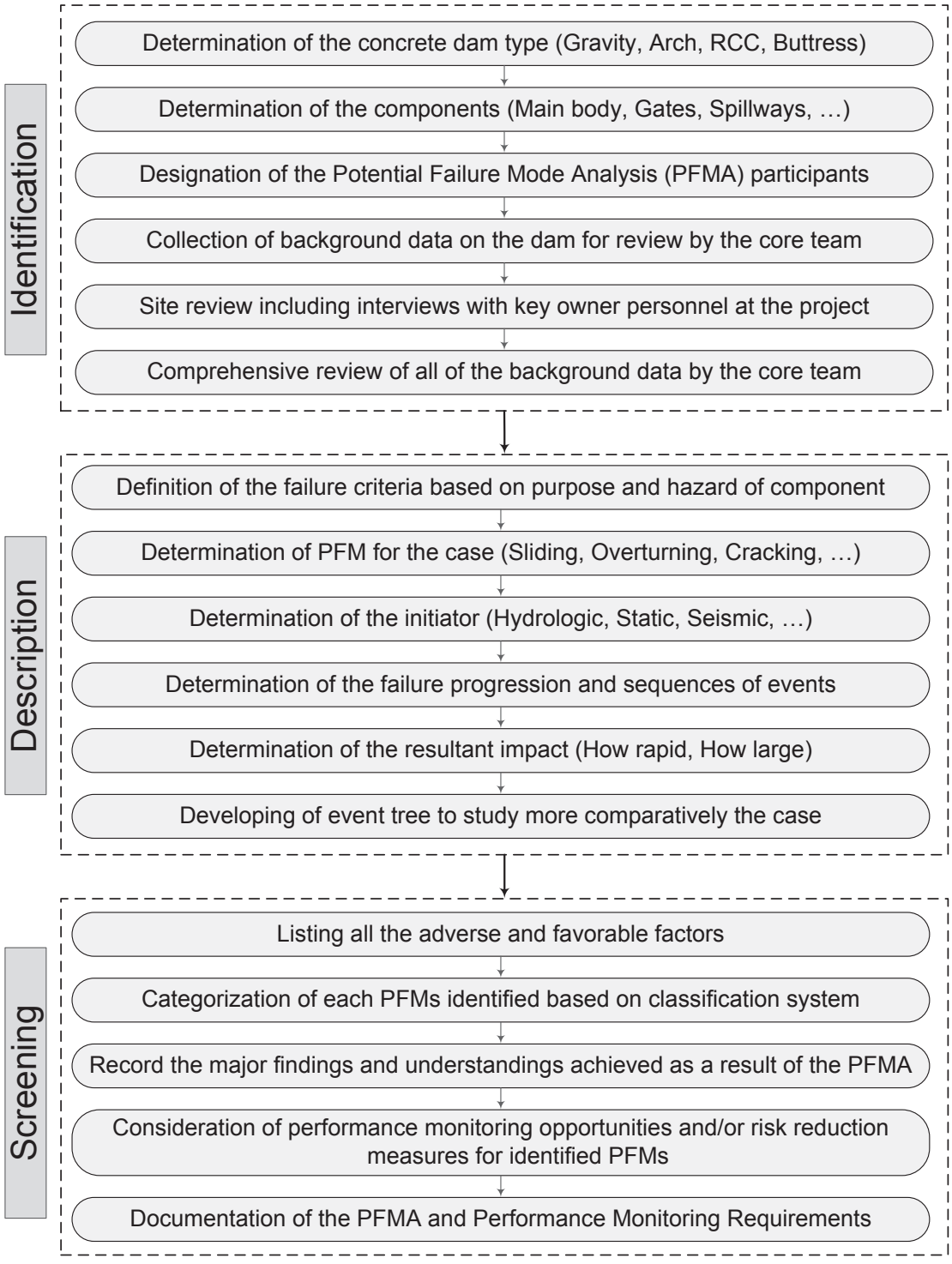

Figure 6.2: Steps towards PFMA of concrete dams based on qualitative approach; adapted from FERC-PFMA (2005) and USBR-manual (2011)

In the event-tree analysis, each identified potential failure mode is decomposed into a sequence of component events and conditions, and all must occur for the specified failure to occur. It depicts the sequence or progression of events and conditions through a branching fashion, with one or more paths leading to failure. Event trees consist of a set of linked nodes and branches with nodes representing an uncertain event or condition while branches represent a possible outcome with an assigned probability of occurrence. Event trees must start with an initiator and then proceed through potential failure mode development. Probabilities of occurrence are assigned through qualified judgment of experts who may have to rely on mechanics, numerical modeling, statistical analysis, case histories, or judgment (FEMA-PFM, 2011).

A typical event tree for a dam is shown in figure 6.3. Since the structure is in essence a system of inter-related components, each one of them with one or multiple failure modes, it is modeled as either a series, parallel, or series-parallel one. Failure modes may be independent or correlated. Assuming independent k modes, the total reliability probability of the dam in series (P_R^s) and parallel (P_R^p) is given by (Huaizhi et al., 2013):

$$P_R^s = \prod_{i=1}^{k} P_R\left(X_i\right) \tag{6.1}$$

$$P_R^p = 1 - \prod_{i=1}^{k} \left(1 - P_R\left(X_i\right)\right) \tag{6.2}$$

where $P_R\left(X_i\right)$ is the reliability probability of the ith failure mode.

Considering each component failure mode independently is not appropriate, one should consider the interaction of two or more components through correlation factors. For instance the failure of a shear key may be precipitated by the failure of water stop which resulted in additional uplift pressure along the joint. Those two component failure will thus be correlated. For a fully correlated system, the failure probability in a series system (P_F^s) is equal to its weakest component, while for a parallel one (P_F^p) it corresponds to the safest mode (Huaizhi et al., 2013). It is noteworthy that $P_R + P_F = 1$.

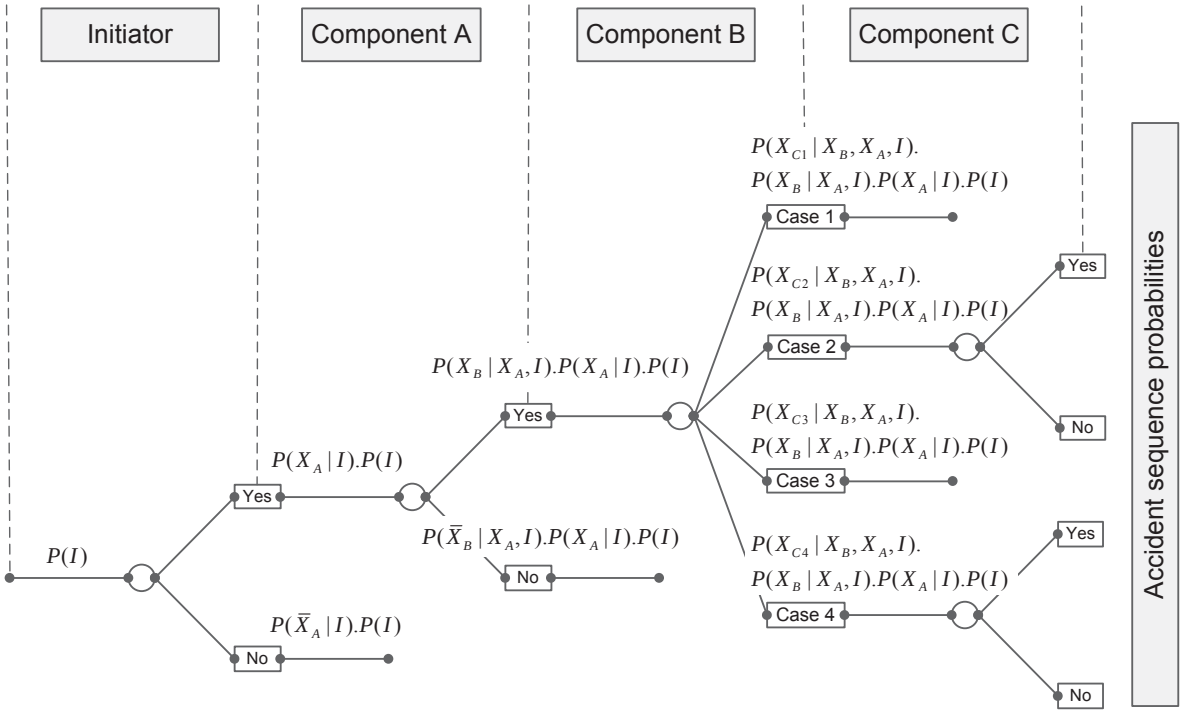

Figure 6.3: Event-tree for an independent three-component system indicating accident sequences; $P(X_A|I) = P(X_A)$, $P(X_B|X_A, I) = P(X_B)$, and $P(X_{Ci}|X_B, X_A, I) = P(X_{Ci})$

6.3.1.2 Fault Tree

A fault tree analysis on the other hand is a technique by which conditions that contribute to a specific undesired event are identified and organized in a logical manner with a pictorial representation. Hartford and Baecher (2004) used it as a quantitative or qualitative technique to deductively identify the conditions and factors that contribute to a specified undesired event. Fault tree analysis can also be defined as a top-down approach to failure analysis starting with an undesirable event called a top event, such as a failure or malfunction and then determining all the ways it can happen. Figure 6.4 illustrates some of the failure modes of a gravity dam system using a fault tree approach.

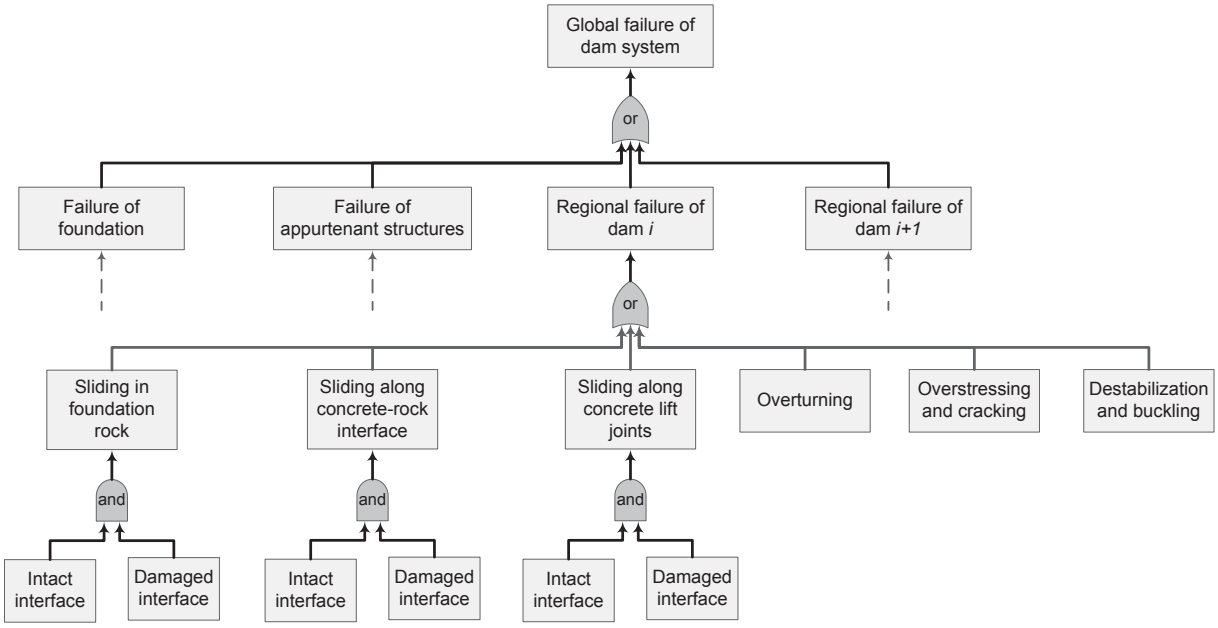

Figure 6.4: Failure modes of a gravity dam using fault tree approach

6.3.2 Application to Dams

Having preciously described the necessary tools to perform a PFM study, this section will address the detailed failure models of different types of concrete dams and foundations (Mills-Bria et al., 2006).

6.3.2.1 Gravity Dams

Ghanaat (2004) reported three major potential failure modes in gravity dams, i.e. overstressing, sliding (either along cracked surfaces in dam body or along the weak planes in dam-foundation interface), and sliding accompanied by rotation in the downstream direction. The damage response of a typical gravity dam due to earthquake ground motions is shown in figure 6.5(a). Different damages will result from the cyclic excitation. Under upstream direction acceleration cracking may occur at the heel of the dam, and for downstream acceleration, it is most likely to affect the slope discontinuity specially when the pool level is low (USACE, 2007).

When a crack nucleates at the slope discontinuity it is subjected to a mixed mode loading

condition (shear and normal stresses) that will cause the crack to propagate along an inclined direction toward the heel; this was indeed observed in Koyna dam (Chopra and Chakrabarti, 1973). As a result of this cracking, sliding, rotational instability, or both may occur (Malla and Wieland, 1999), as illustrated in figure 6.5(b).

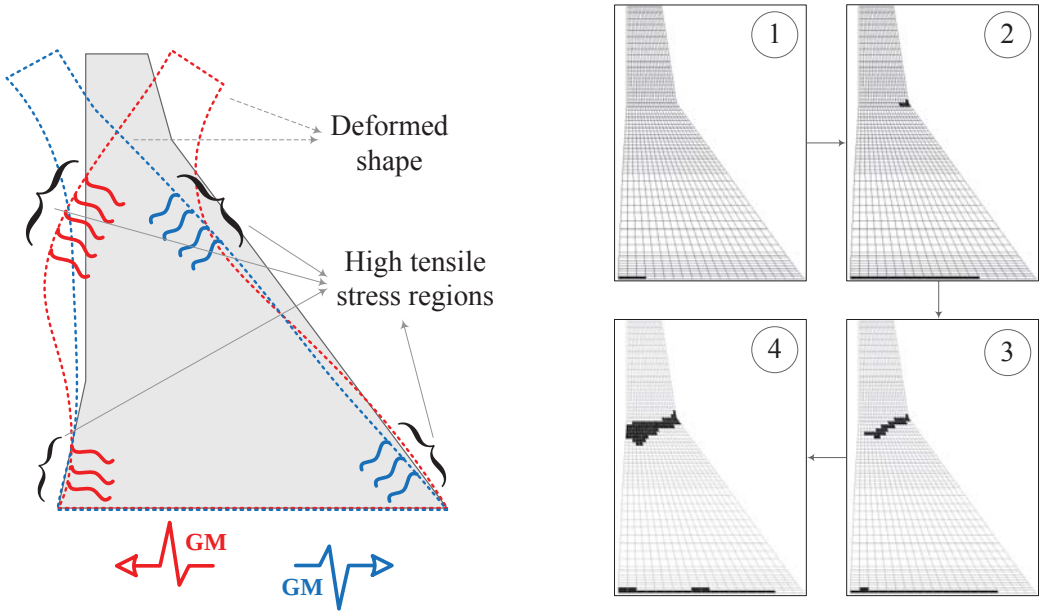

(a) Typical crack pattern under cyclic motion

(b) Crack propagation process

Figure 6.5: Damage response of gravity dam under earthquake ground motion

6.3.2.2 Arch Dams

Though, by design, arch dams are thin walled hyperstatic structures composed of intersecting arches and cantilevers, this added strength does not completely eliminate the likelihood of failure. Those are: 1) excessive contraction joint opening combined with tensile cracking of the cantilevers (and not in arches), 2) buckling, 3) crushing of concrete, and 4) global instability (Ghanaat, 2004). Since contraction joints have practically no tensile resistance; henceforth, repeated cyclic loads are likely to break the weak bond between the grout and the concrete. This, in turn, will relieve arch tensile stresses but drastically increase those in the cantilevers (USACE, 2007), which may

ultimately crack (possibly at the lift joints). Finally, the breakdown of the dam integrity may lead to failure, as shown in figure 6.6(a). This process is illustrated by the progressive chain of localized failures in Dez dam (subject of the subsequent case study in this paper), figure 6.6(b). However, it should be noted that most of these effects can be mitigated by the presence of shear keys.

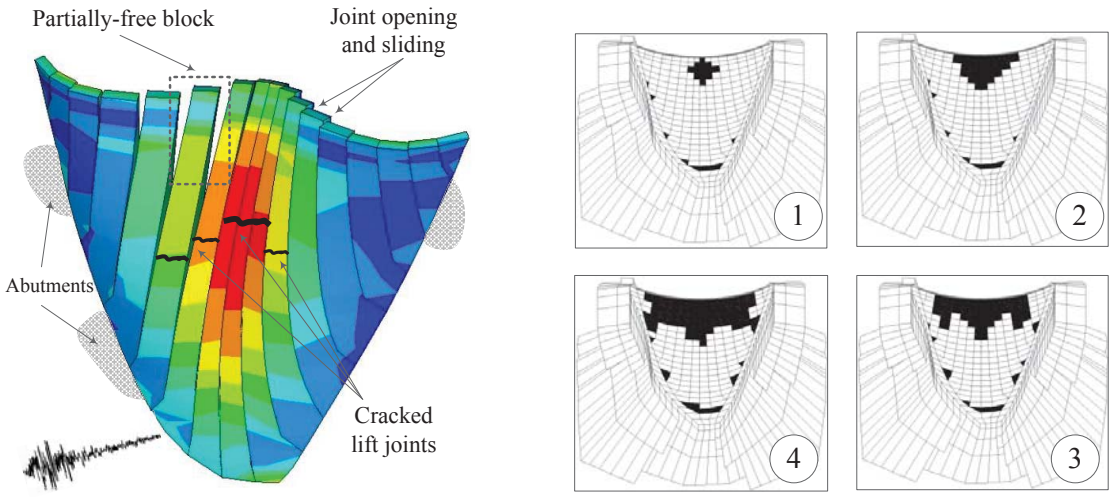

(a) Typical joint openings and cracking under cyclic motion

(b) Crack propagation process

Figure 6.6: Damage response of arch dam under earthquake ground motion

In some cases, it is found more convenient to analyze the cantilever by itself. In this case one can assume to have the adjacent contraction joints to be a) fully opened, or b) partially opened. In the first case, a stability analysis could be performed to assess its integrity (FERC-Arch, 1999). A numerical procedure for such a simplified analysis was recently undertaken by (Malla, 2013) and (Hariri-Ardebili and Kianoush, 2014).

6.3.2.3 Buttress Dams

Buttress dams are reinforced concrete structures composed of an upstream water barrier (flat slab, large domes, cylindrical arches, massive heads), and buttresses. Whereas hydrostatic pressure is transferred to the foundation through the slab and buttresses (analogous to gravity dams), resistance to lateral seismic forces (stream direction) is more akin to arch dams; it is a

three-dimensional hyperstatic problem. On the other hand, buttress dams are very sensitive to cross stream excitation.

Failure modes for such a dam include: 1) sliding of the weak planes (stream and cross stream), 2) racking (resulting from inelastic accumulated displacements) in cross-stream cases, 3) slab or buttress localized failures (cracking or crushing), 4) buckling of buttress, as illustrated in figure 6.7.

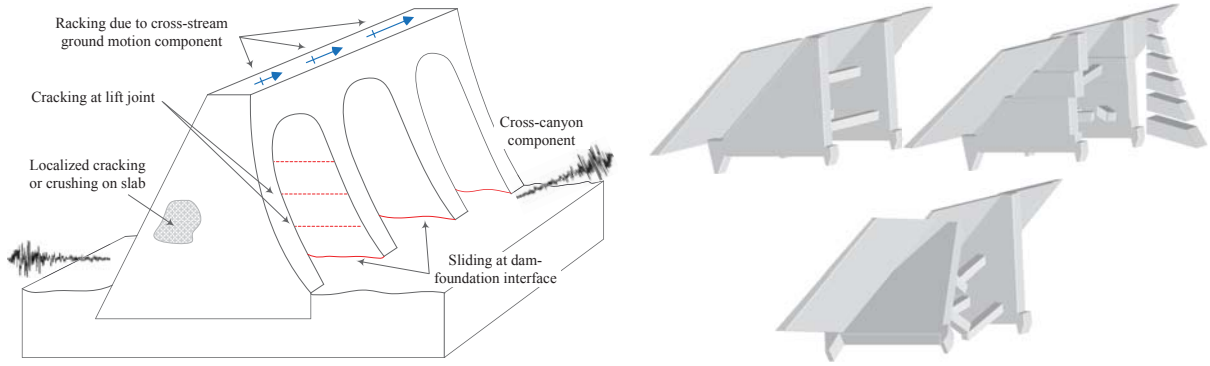

(a) Damage under two-component in-plane cyclic excitation (b) Progressive failure

Figure 6.7: Damage response of buttress dam under earthquake ground motion

6.3.2.4 Foundation-related PFMs

It is reported that about 70% of the concrete dam failures can be attributed to dam foundation issues, (geological or geotechnical) (ICOLD, 1974). Whereas dams have generic PFM, foundation failures modes are very specific to a dam. The major ones are tabulated in Table 6.3 (Boyer, 2006).

6.4 Proposed Quantitative Extensions

Finite element analysis of dams is either linear or nonlinear. It is suggested that the former be undertaken for small dam heights in low seismicity regions. Nonlinear analysis on the other hand should be undertaken for: a) high dams (> 100 m), b) those with large reservoir capacity ($> 1,000$ Mm^3), 3) thin arch and buttressed dams. In either case, one needs a quantification of the PFM (the previous section having addressed PFM in a qualitative manner) for the PBEE-2.

In the linear case quantification of the PFM have already been addressed by some and will

Table 6.3: Common foundation-related PFMs for concrete dams

Initiator	Foundation-related PFM
Static	Piping of foundation materials
	Sliding stability of foundation materials
	Sliding stability of reservoir rim materials
	Irregular settlement/deformation of foundation materials
	Dissolution of foundation materials
	Landslide-induced waves
Hydrologic	Overtopping of dam leading to erosion of the foundation
	Sliding stability of foundation/reservoir rim materials
	Landslide-induced waves
Seismic	Deformation of foundation materials
	Sliding stability of foundation/reservoir rim materials
	Landslide-induced waves

be revisited next. Subsequently, this paper presents a quantification of the PFM for nonlinear analysis.

6.4.1 Linear System

Quantification of PFM in linear analysis can be addressed through indices and corresponding criteria. The indices are dam type independent whereas the criteria are not.

6.4.1.1 Indices

Indices are essentially metrics for damage, and the recommended ones are an extension of those proposed by Ghanaat (2004) and later adopted by USACE (2007). Among the three original criteria, two are extended and a fourth proposed as follows:

Demand capacity ratio (DCR): Originally formulated in terms of stresses it is hereby argued that a more appropriate criteria would be a strain based one.

$$\begin{cases} \text{Stress} & DCR^{\sigma} = \frac{\sigma}{f_t'} \\ \text{Strain} & DCR^{\varepsilon} = \frac{\varepsilon}{\varepsilon_{cr}} \end{cases} \tag{6.3}$$

In either case, the compared stress or strain should correspond to the major principal one for gravity dams ($\varepsilon_{(1)}$), and the arch (ε_{arch}) or cantilever (ε_{cant}) quantities for arch dams.

Cumulative inelastic duration (CID): refers to the total duration of stress or strain excursions above a stress (or strain) level associated with a certain DCR. In the context of a linear elastic analysis, with dynamic elastic properties (Raphael, 1984), it is not surprising that stress or strain based criteria are being violated. However, since stress redistribution (known to occur in hyperstatic structures) is not accounted for (as they would be in a nonlinear analysis), a single exceedance does not inevitably lead to failure. Accordingly, this criterion establishes a heuristic rule simply counts the exceedance (stress or strain) duration during the seismic excitation at two levels ($1.0 \leq \text{DCR} \leq 2$), as shown in figures 6.8.

Cumulative inelastic area (CIA): The previous index does not account for the magnitude of the exceedance. This one seeks to account for it by measuring the sum of shaded areas in figure 6.8. If a stress based index is adopted, then the CIA has units of FT/L^2, which actually corresponds to a dynamic viscosity.

Damage spatial distribution ratio (DSDR): Whereas previous criteria were evaluated point-wise, this one seeks to measure the topological extent of computed damage (which may not match the one stemming from a nonlinear analysis). Hence, the ratio of the overstressed (or as stated above, overstrained) region to total dam area (cross-section area in gravity dams and upstream or downstream faces in the case of arch dam) at the specific DCR is the DSDR.

6.4.1.2 Criteria

To each of the preceding indices, one must specify limiting individual criteria. Those will be addressed first. Then criteria for coupled indices will be presented. For individual criteria, those shown in Table 6.4 are based on the authors' judgment (Hariri-Ardebili et al., 2013) and the

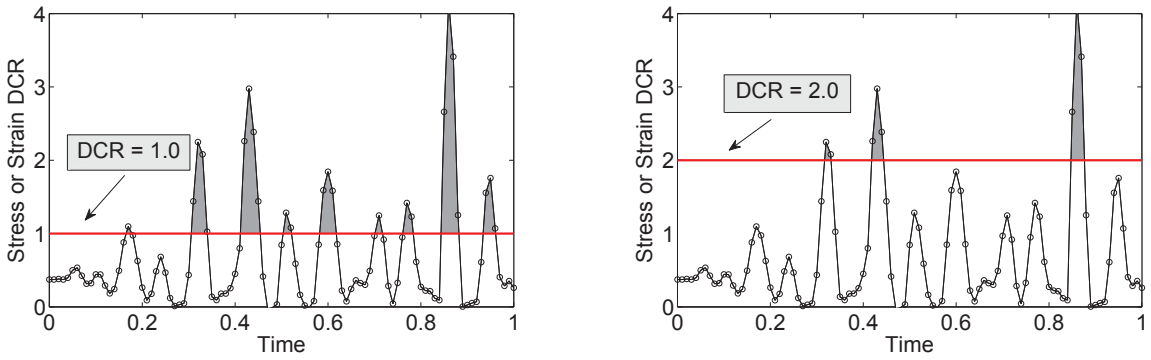

(a) Lower bound, DCR=1.0

(b) Upper bound, DCR=2.0

Figure 6.8: Calculation of the cumulative inelastic duration and area using stress/strain time histories

proposed ones in the literature (USACE, 2007). As to CIA_{cr}, it was derived from an assumption of a hypothetical harmonic excitation with a DCR of 2.0, oscillation period of 0.25 s and limited to 5 cycles. This would give 0.275 and given the approximate nature of the derivation is bracketed by 0.2 and 0.4.

A more comprehensive approach must account for the combined criteria and their possible coupling. This is accomplished by pairing the following indices: DCR-CID and DCR-DSDR, figure 6.9. In zone "A", stresses or strains are below their critical values, the structure is safe, and there is no need for further evaluation. Stresses or strains exceed their acceptable values in "B" and "C". Assessment through DSDR and CID is performed through "B" and "C" respectively. Finally, "D" is unacceptable, as it is outside the failure surface. Linear analysis in zone "A" is enough, in "B" and "C" is acceptable and in "D" is unacceptable.

6.4.2 Nonlinear System

Should a linear analysis of the dam indicate potential severe damage, as shown in figure 6.9, one should perform a nonlinear structural analysis. Furthermore, should there be initial cracks (thermal cracks, poor construction, previous earthquake, etc) a nonlinear analysis is always warranted. There are a number of factors that should be considered in nonlinear structural analysis of

Table 6.4: Proposed Index criteria

Index	**Quantity**			**Note**
	Arch	Gravity	Buttressed	
DCR_{cr}		[1, 2]		(Hariri-Ardebili et al., 2013)
CID_{cr}	0.4	0.3	0.4	(USACE, 2007)
CIA_{cr}		[0.2, 0.4]		Explanation in text
$DSDR_{cr}$	20%	15%	15%	(USACE, 2007)

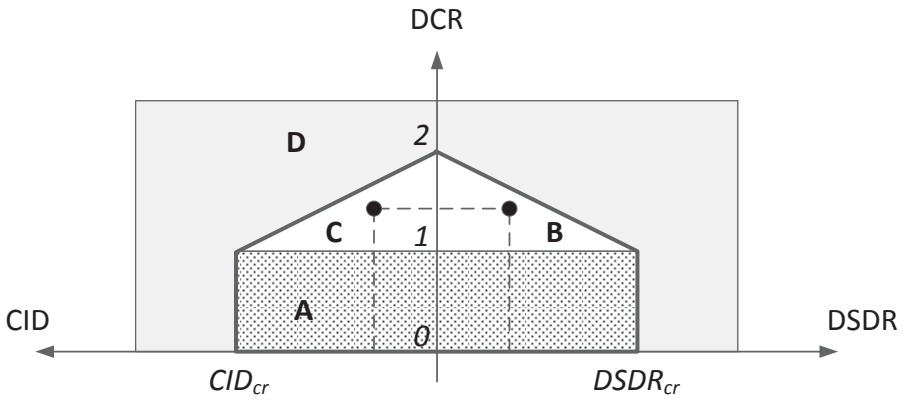

Figure 6.9: Failure surface for concrete dams under linear analysis

concrete dams:

- Staged construction process (de Arajo and Awruch, 1998)
- Fluid structure interaction (Ghaemian and Ghobarah, 1998), (Bouaanani and Lu, 2009)
- Soil structure interaction (Saouma et al., 2011), (Hariri-Ardebili and Mirzabozorg, 2013),
- Fluid fracture interaction (Slowik and Saouma, 2000a) (Barpi and Valente, 2008)
- Environmental effects such as thermal loads (Mirzabozorg et al., 2014) and ice loads (Bouaanani et al., 2009).
- Aging of concrete (Valliappan, S. and Chee, C., 2009), alkali-aggregate reaction (Saouma et al., 2007), and creep (Serra et al., 2012)
- Concrete fracture and joint modeling (concrete-concrete and concrete-rock)(Puntel et al., 2006)

- Concrete cracking and crushing (Lee and Fenves, 1998)
- Spatial variation of the ground motion (Chopra and Wang, 2010),(Mirzabozorg et al., 2012)

Whereas sensitivity analyses should be performed to assess the relevance of the aforementioned sources of nonlinearities, the first two authors personal experience indicates that dam-reservoir interaction, joints, and concrete cracking are predominant.

Because a nonlinear analysis attempts, in as much as possible, to capture the real response of a dam, failure can not be as explicitly assessed as in the linear analysis (such as with reference to figure 6.9). As such, the authors have introduced the notion of damage index (DI) in (Hariri-Ardebili and Saouma, 2014), which will be used below.

6.4.2.1 Methodology

In the context of a nonlinear analysis, the structural capacity is captured by any of the methods described below. Except for the first one (static analysis) the other three rely on a nonlinear dynamic one. For those analyses, one must start with the identification of location (with respect to a fault), geotechnical conditions (shear wave velocity) and structure type. From these data, one selects (or generates) a set of ground motion acceleration time histories. From the corresponding analysis one plots the intensity measure (IM) versus the engineering demand parameter (EDP) (which corresponds to the demand parameter, DP defined in (Applied Technology Council, 2012)). IM is a measure of the ground motion characteristic, typically the (peak or spectral) ground acceleration. EDP corresponds to any force or deformation calculated during the structural analysis that is relevant to the safety assessment, such as base shear or drift.

Pushover Analysis (POA): is a nonlinear static procedure that applies incrementally load or displacement and has been extensively used in the structural analysis of buildings to estimate structural response in lieu of the more expensive transient nonlinear analysis (Mwafy and Elnashai, 2001). The underlying assumption behind POA is that it is capable of mobilizing principal nonlinear modes of structural behavior up to collapse. The only reported

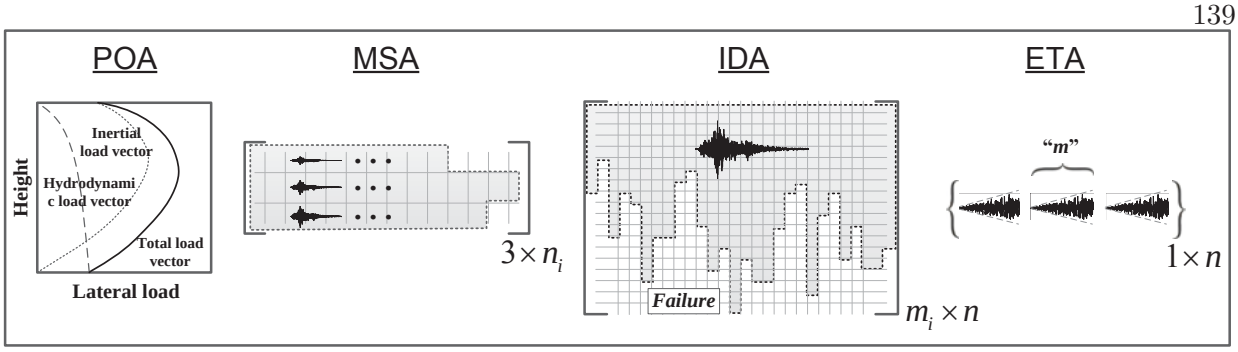

(a) Different possible input types for nonlinear transient (except POA) analyses

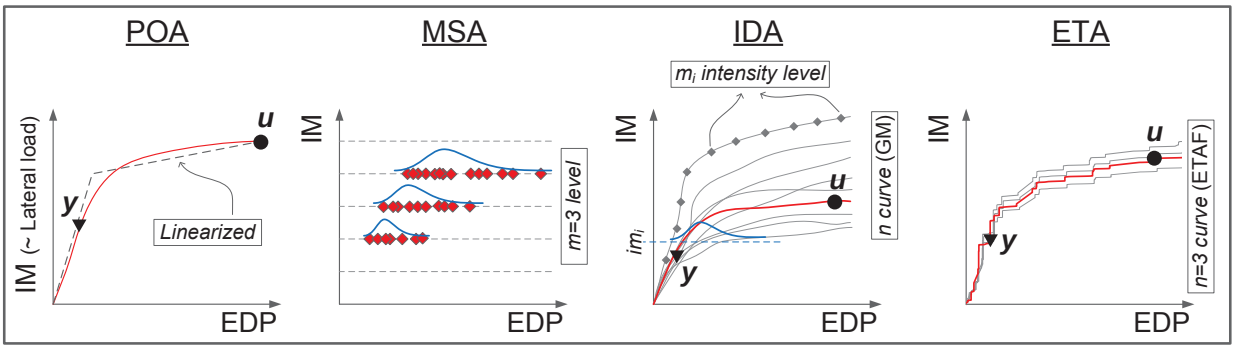

(b) Analysis outcome for assessment

Figure 6.10: Structural analysis based on four nonlinear methodologies

application of the POA to concrete dams is by Alembagheri and Ghaemian (2013b) where the horizontal force is composed of hydrostatic and inertia ones. Figure 6.10(a) shows the load vectors, and the corresponding intensity measure (in this case load vector magnitude). Following the analysis, figure 6.10(b) shows the IM (load amplitude in this case) versus EDP as well as the yield (triangle solid point) and ultimate (circle solid point) capacities for the EDP.

Multiple-Strip Analysis (MSA): hinges on a deterministic number of ground motion intensity levels m (or strips) (Cornell and Jalayer, 2002). Typically $m = 3$ corresponding to the exceedance probabilities of 10% in 50-year, 5% in 50-year, and 2% in 50-year (Mackie and Stojadinovic, 2005) and to each strip correspond n ground motions. In figure 6.10(a) the MSA analysis has $m = 3$. There are two possibilities: a) selection of n different ground motions scaled at m different levels; or b) selection of n_i ground motions for each of the

intensity levels with no scaling. Following the analysis, and for each m the usual IM versus EDP results are first plotted. Then for each IM histograms are generated and the most suitable probability distribution function (normal or log-normal) is selected, figure 6.10(b). Subsequently, fragility curves could be derived (Baker, 2014).

Incremental Dynamic Analysis (IDA): considers n ground motions which will all be incrementally scaled m times until failure occurs. *a priori* m is unknown and each ground motion n will result in a corresponding failure at a different intensity level m_i (Vamvatsikos and Cornel, 2002), figure 6.10(a). Following the analysis, the IDA curve (figure 6.10(b)) connects the resulting m demand parameters for each of the n ground motions. Each one of those curve will be asymptotic to the corresponding failure. Capture of the overall response by a single measurable quantity at a given IM (IM $= im_i$) can be determined through the corresponding probability distribution. Those curves can be used for the determination of the fragility plots (Porter et al., 2007).

Endurance Time Analysis (ETA): The preceding two methods started with actual recorded ground motion and required up to $m \times n$ analysis. This is computationally expensive and thus may force the analysis to make greatly simplified assumption in their model. Such assumptions may lead to erroneous conclusions. The ETA method starts with a synthetic ground motion (Naeim and Lew, 1995) whose amplitude increases over time, as shown in figure 6.10(a) (Estekanchi et al., 2007). The increasing amplitude in a single motion substitutes for suites of ground motion times histories where each subsequent suite has a higher amplitude. As before, n endurance time acceleration functions (ETAF) are used, figure 6.10(a). The outcome of the analysis, figure 6.10(b), is n capacity curves in terms of IM versus EDPs and their average which is used to reduce the uncertainty due to the random nature of ETAFs (Hariri-Ardebili et al., 2014b). The resulting average curve is analogous to the one of the POA or 50% fractile of IDA. This method was used by (Hariri-Ardebili and Saouma, 2014) for gravity dams.

6.4.2.2 Indices

DI for concrete dams include:

Deformation-based damage index (DI^{def}) in which the stability of the dam is judged based on the maximum absolute displacement of the index point (usually crest), $|\Delta_{max}|$ (Powell and Allahabadi, 1988):

$$DI^{\text{def}} = \frac{|\Delta_{max}| - \Delta_y}{\Delta_u - \Delta_y}, \qquad \Delta_y \leq |\Delta_{max}| \leq \Delta_u \tag{6.4}$$

where Δ_y and Δ_u are the maximum displacement at the yield point and ultimate point, respectively. $DI^{\text{def}} \in [0 \quad 1]$ corresponding to $[\Delta_y \quad \Delta_u]$.

Crack-based damage index (DI^{cracking}), in which the stability of the dam is judged based on the length (for 2D models) or area (for 3D models) of the cracked region. For concrete dams the DI is simply

$$\begin{cases} \text{Gravity dam} & DI^{\text{cracking}} = \frac{L_C}{L_T} \\ \text{Arch dam} & DI^{\text{cracking}} = \frac{A_C}{A_T} \end{cases} \tag{6.5}$$

where the numerator corresponds to cracked length or surface area, and the denominator to the total potential crack length in gravity dams and upstream/ downstream face in arch dams.

Energy-based damage index (DI^{energy}) in which the stability of the dam is evaluated as the ratio of the sum of the individual energies dissipated by the s cracks/joints, over the the one measured at collapse $(E_H)_u$, (Bhattacharjee and Leger, 1993):

$$DI^{\text{energy}} = \frac{\sum_{i=1}^{s} (E_H)_i}{(E_H)_u} \tag{6.6}$$

Joint damage index (DI^{joint}) will simply refer to the joint opening (DI^{opening}) and sliding (DI^{sliding}) along construction joints.

Hybrid damage index (DI^{hybrid}) in which the stability of the dam is judged based on a weighted average of DI^{cracking} and DI^{energy} and the index point displacement, u_{max}, (Hariri-Ardebili and Saouma, 2014).

$$DI^{\text{hybrid}} = f\left(L_C, E_H, u_{max}\right) \tag{6.7}$$

In summary, whereas for linear analysis the one starts by examining indices and then the corresponding criteria, the nonlinear analysis will start with methodology followed by indices.

6.5 Dam Description and Modeling

As a numerical example a high arch dam is selected, analyzed linearly and non linearly, and corresponding seismic PFMs quantitatively evaluated.

Dez (located in southwest Iran and commissioned in 1963), a double curvature (203.5 m high and 240 m crest length) arch dam is considered. Its Lombardi slenderness coefficient (Fanelli and Lombardi, 1997) is $C_l = 12.28$ corresponding $C_l \times H$ is 2,500, and the full reservoir capacity is 3,350 Mm^3. The dam thus meets all three criteria for an above-average susceptibility to damage as described in Hariri-Ardebili et al. (2015). The dam has sixteen contraction joints and a peripheral joint separating the main body from the concrete saddle (Pulvino).

The finite element mesh composed of 792 and 3,770 solid elements for the dam and foundation respectively, 956 joint elements and more than 30,000 nodes as shown in figure 6.11. Analysis included dynamic fluid-structure interaction using an Eulerian-Lagrangian approach, and massless foundation extending twice of the dam height (thus no need to include silent boundary conditions). All analyses were performed with the finite element code ANSYS (2007) and more details can be found in (Hariri-Ardebili and Kianoush, 2014). The material properties are summarized in Table 6.5.

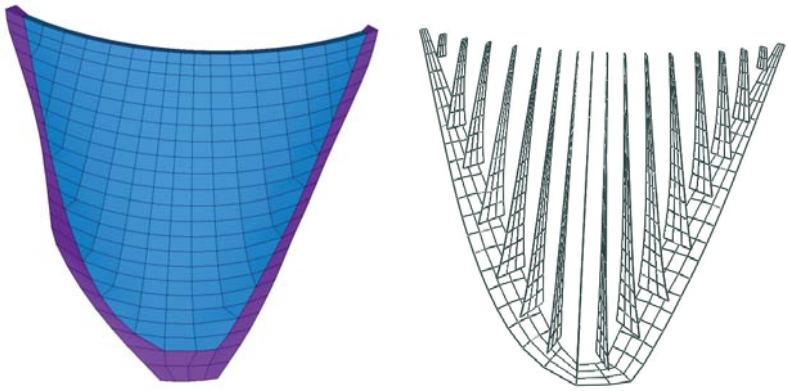

(a) Dam body (b) Joint Modeling

Figure 6.11: Finite element model of Dez dam

Table 6.5: Material characteristics in Dez dam (Hariri-Ardebili and Kianoush, 2015)

Material/element	**Property**	**Symbol (unit)**	**Value**
Concrete (dam element)	Isotropic elasticity	E_C (GPa)	40
	Mass density	ρ_C (kg/m^3)	2,400
	Poisson's ratio	υ_C	0.2
	Uniaxial tensile strength	f'_t (MPa)	3.4
	Uniaxial compressive strength	f'_c (MPa)	35.0
Rock (foundation element)	Saturated deformation modulus	E_R^{sat} (GPa)	13
	Unsaturated deformation modulus	E_R^{uns} (GPa)	15
	Mass density	ρ_R (kg/m^3)	2,450
	Poisson's ratio	υ_R	0.25
Water (fluid element)	Mass density	ρ_F (kg/m^3)	1,000
	Sound speed in fluid	C_0 (m/s)	1,440
	Wave reflection coefficient	α_0	0.70
Joint (contact element)	Normal stiffness of vertical joint	K_n^{ver} (GPa/m)	240
	Tangential stiffness of vertical joint	K_t^{ver} (GPa/m)	24
	Normal stiffness of peripheral joint	K_n^{per} (GPa/m)	210
	Tangential stiffness of peripheral joint	K_t^{per} (GPa/m)	16.8

6.6 Hazard Analysis

The previously discussed MSA approach is adopted with three seismic intensity levels (SIL), $m = 3$, and nine ground motion for each ($n = 9$). SIL refers to qualitative representation of the intensity against the quantitative representation using IM. It is common practice to select the ground motions for two or three SILs (ICOLD, 2010) (del Consiglio dei Ministri, 2001) (Gosschalk et al., 1994) (FERC-Arch, 1999). In the present paper, three SIL correspond to: design base level

(DBL), maximum design level (MDL) and an intermediary one between the two. Those will be labeled as 1, 3 and 2 for subsequent reference.

The annual rate of exceedance of the ground motion amplitude, λ, (inverse of return period T_R) for DBL and MDL are determined from a Poisson probability model (Cornell, 1968):

$$\lambda = -\frac{\mathrm{Ln}\,(1 - P_E)}{t} \tag{6.8}$$

where P_E is the occurrence (at least one) probability during life time t (generally assumed to be 100 years for dams). P_E for ground motion is usually assumed to be in the ranges [20%, 64%] for DBL and [10%, 20%] for MDL, (ICOLD, 1989). Consequently, the corresponding λ are 450 and 1,000 years for DBL and MDL, respectively (Eq. 6.8).

A probabilistic seismic hazard analysis (PSHA) leads to determination of: 1) Site characteristics including shear wave velocity, magnitude of previously recorded earthquakes, size of the rupture area, type of of fault, crustal rock damping characteristics, and rock properties; 2) Seismic hazard curves showing the annual rate of exceedance in terms of intensity measure parameter (McGuire, 1995), figure 6.12(a); and 3) Acceleration response spectra *vs.* period, figure 6.12(b).

For this site, the shear wave velocity exceeds 760 m/s, a threshold value in (Council, 2003) for ground motion selection on rock sites. A critical damping ratio, ξ=5% is assumed for both components of the ground motion.

6.7 Linear Structural Analysis

A linear elastic analysis is first conducted for each of the selected nine ground motions. By observation, it is noted that GM03 is the most critical one (highest tensile stresses). For illustrative purpose the CID for stress and strain is plotted in terms of both the DCR and SIL (figure 6.12(b)) in figure 6.14. Note that intermediary values for the SIL and DCR are interpolated. Figure 6.13(c) shows the threshold value for both stress and strain interpretations.

From these figures, one concludes that for all DCR values, the corresponding CIDs are higher

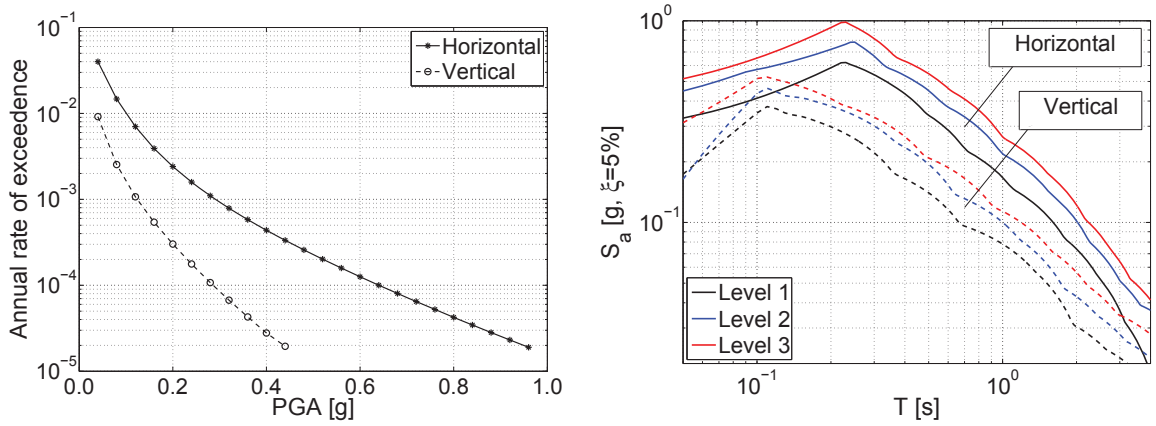

(a) Seismic hazard curves

(b) Acceleration response spectra

Figure 6.12: Quantification of site-specific seismic characteristics

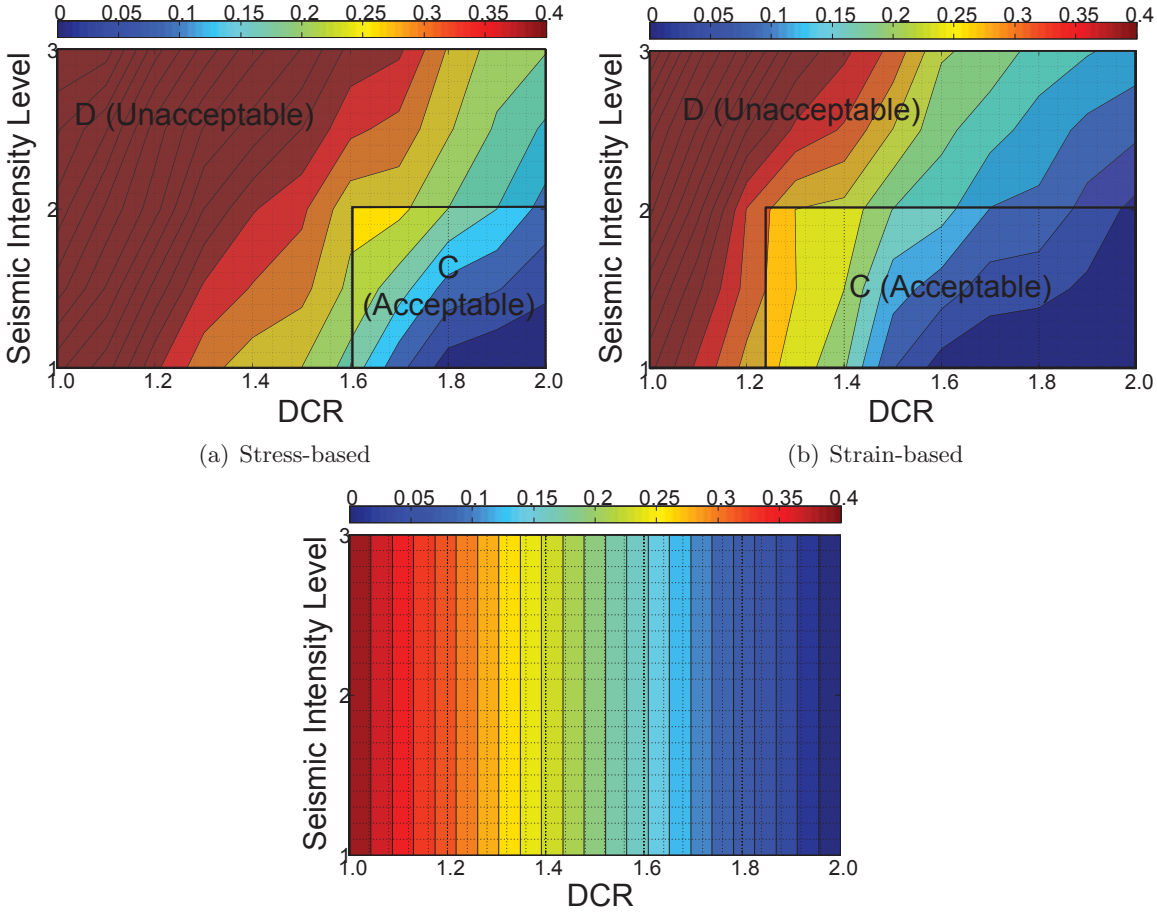

(a) Stress-based

(b) Strain-based

(c) Threshold

Figure 6.13: Contour plot of CID with respect to DCR and SIL for GM03 ground motion

for stresses than strain. Also shown are the two regions (acceptable or unacceptable) consistent with the failure surface diagram. Finally, since the unacceptable region is non-negligible, a nonlinear analysis is likely to be needed.

Whereas the previous observations were based on GM03 only, a detailed analysis of the complete set of the nine ground motions is now addressed. Shown in figure 6.14 are the mean values of the CID and DSDR *vs* DCR. Based on this figure:

(1) In all cases a stressed-based interpretation leads to higher mean CID than for strain-based one. This difference is reduced for higher DCR values.

(2) The mean CIDs remain in the acceptable region for level 1 and most of level 2; However clearly level 3 is in the unacceptable region.

(3) For level 2, the mean CIDs corresponding to stresses are in the unacceptable zone, whereas the strains are not.

(4) For mean DSDR it is clear that all three levels are in the acceptable region. However, as will be shown later some of the individual ground motions do indeed puncture the dam failure surface.

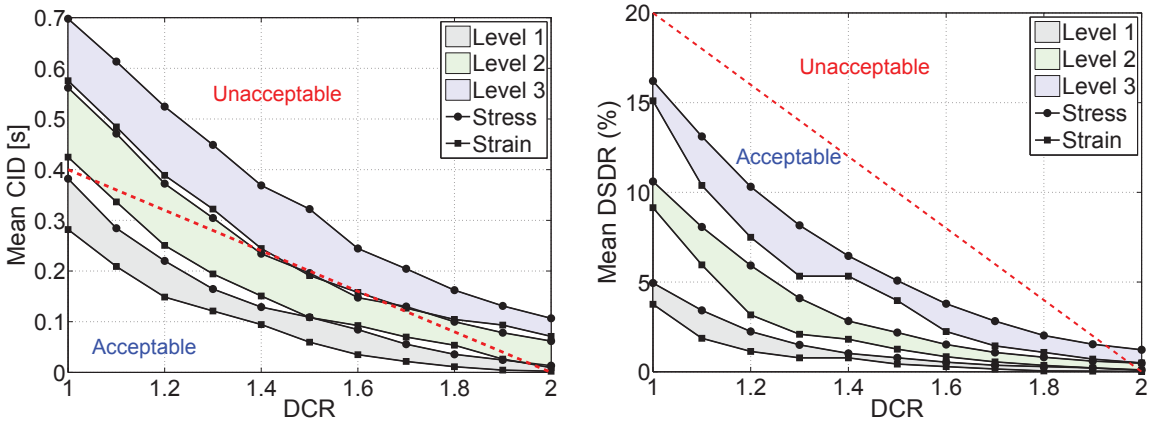

(a) CID-DCR relationship

(b) DSDR-DCR relationship

Figure 6.14: Mean performance curves for the dam using linear elastic analysis

6.8 Identification of Optimal IM Parameter

The outcome of WDM, i.e. MSA, IDA, and ETA should be plotted in IM-EDP coordinate system. For the EDP, DSDR is perceived as being the most representative for dams as it captures its global response. As to the IM, the options are many, the nearly optimal one will be identified.

6.8.1 Possible IM

In dam engineering the IM considered is in terms of the SIL's (such as DBL and MDL) (ICOLD, 2010) (del Consiglio dei Ministri, 2001) (Gosschalk et al., 1994) (FERC-Arch, 1999). On the other hand, in PBEE-2 approach the IM can be one of the parameters listed in Eq. 6.9 and can be directly computed from the ground motion acceleration time history.

$$\text{IM} = \begin{cases} \text{Peak ground acceleration} & \text{PGA} = max\left(|a\left(t\right)|\right) \\ \text{Peak ground velocity} & \text{PGV} = max\left(|v\left(t\right)|\right) \\ \text{Root-mean-square of acceleration} & \text{a}_{RMS} = (\frac{1}{t_{tot}}\int_0^{t_{tot}} a^2\big(t\big)dt)^{1/2} \\ \text{Root-mean-square of velocity} & \text{v}_{RMS} = (\frac{1}{t_{tot}}\int_0^{t_{tot}} v^2\big(t\big)dt)^{1/2} \\ \text{Arias intensity} & \text{I}_A = \frac{\pi}{2g}\int_0^{t_{tot}} a^2\big(t\big)dt \\ \text{Specific energy density} & \text{SED} = \int_0^{t_{tot}} v^2\big(t\big)dt \\ \text{Cumulative absolute velocity} & \text{CAV} = \int_0^{t_{tot}} |a\big(t\big)|dt \\ \text{Acceleration spectrum intensity} & \text{ASI} = \int_{0.1}^{0.5} S_a\left(T,\xi\right)dT \\ \text{Velocity spectrum intensity} & \text{VSI} = \int_{0.1}^{2.5} S_v\left(T,\xi\right)dT \end{cases} \tag{6.9}$$

where $a\left(t\right)$, $v\left(t\right)$ are acceleration and velocity time histories; t_{tot} total duration of ground motion, $S_a\left(T\right)$ and $S_v\left(T\right)$ spectral acceleration and velocity at the period T, and ξ the damping ratio.

Figure 6.15 shows the histograms for each of the aforementioned IM parameters for m=3 seismic levels and n=9 ground motions listed in Table **??**. In each case, data are fitted through one of the following distributions: 1) normal, 2) lognormal, 3) exponential, and 4) Weibull and the one with the best one selected. The Anderson-Darling (AD) test method (Anderson and Darling,

1954) is favored over the better known Chi-square goodness of fit or the Kolmogorov-Smirnov (KS) test because data came from a population with a specific distribution (Stephens, 1974).

The application of the AD method requires the conversion of the resulting statistic to a uniform variable, p-value $\in$ [0,1) (Marsaglia and Marsaglia, 2004). Hence, the larger p values for a given distribution, the better the fit. Figure 6.15 shows the best distribution for each of the selected IM and the corresponding p-values. One notes that in practically all cases, the lognormal distribution is best (except for a_{RMS} which is normal).

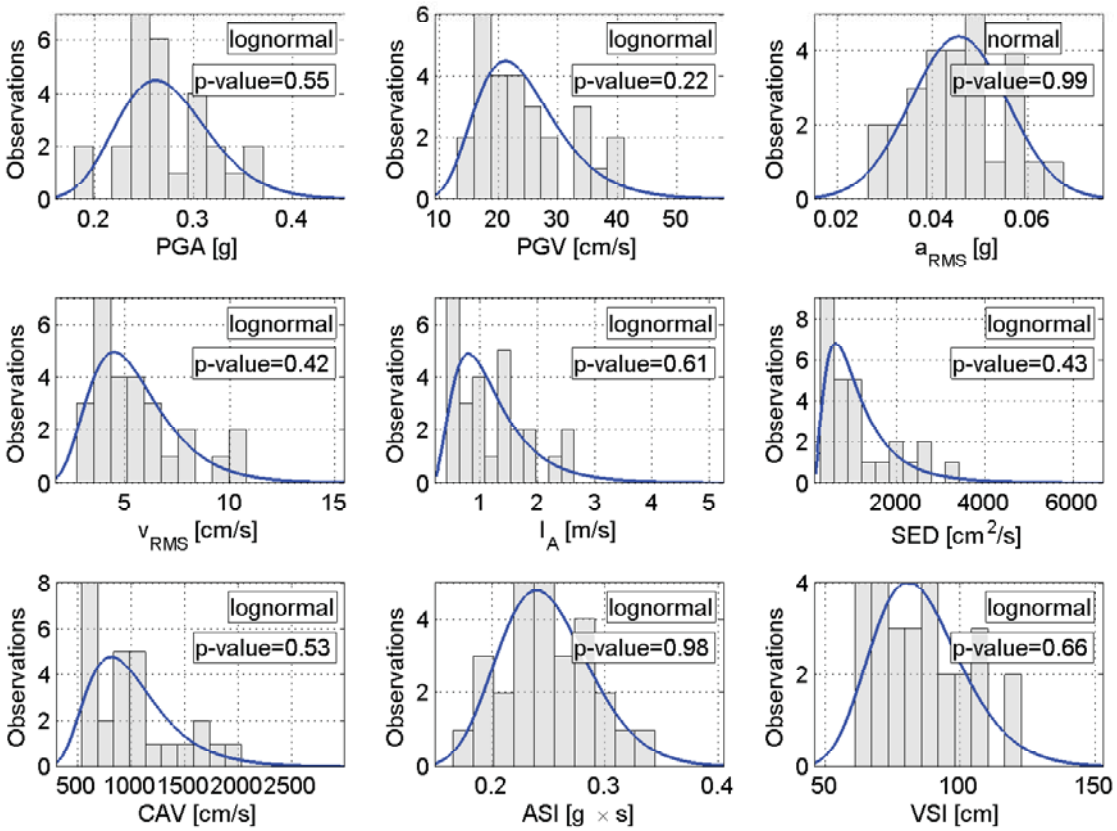

Figure 6.15: Distribution of IM parameter for selected ground motions

6.8.2 Selection of the Best IM

Using results from the linear analysis reported in section 6.7 regression analyses are performed to identify the best IM(s). Regression analysis, with the same objective, have been previously

addressed for framed structures in the context of PBEE-2. (Giovenale et al., 2004) emphasized the importance of limiting the variation of the EDP for a given IM, i.e. results should fit in an as narrow band as possible. On the other hand, Tothong and Luco (2007) emphasized the role of efficiency, practicality, sufficiency, hazard compatibility, and proficiency.

Linear regression model describes a relationship between a dependent variable, EDP, and independent (explanatory) variable, IM. Linear format of trend-line is chosen in this research because the data are obtained from linear analysis, $\text{EDP} = \hat{a}.\text{IM} + \hat{b}$. This assumption is controlled later in this section based on Akaike information criterion (AIC). Distribution of the residuals ($\text{EDP}_{original}$-EDP_{fitted}) over the IM values also should be checked. Residuals are useful for detecting outlying EDPs and checking the linear regression assumptions with respect to the error term in the regression model. High-leverage data have smaller residuals because they shift the regression line/surface closer to them. Finally, a 50% confidence interval for the fitted line (shaded area) is also provided.

Results of the regression analysis for each of the parameters identified in Eq. 6.9 are shown in figure 6.16 along with the 50% confidence limit for the regression and the GOF is evaluated based on R-squared and RMSE Eq. 6.10.

$$\begin{cases} \text{R-squared} &= \dfrac{\sum_{i=1}^{n} \beta_i \left(\hat{R}_i - \bar{R}\right)^2}{\sum_{i=1}^{n} \beta_i \left(R_i - \bar{R}\right)^2} \\ \text{RMSE} &= \sqrt{\dfrac{\sum_{i=1}^{n} \beta_i \left(R_i - \hat{R}_i\right)^2}{\delta}} \end{cases} \tag{6.10}$$

where R_i, $\hat{R}_i$ and $\bar{R}$ are original, fitted and mean response values, and δ is the residual degrees of freedom (differences between the number of response values and the number of fitted coefficients). Obviously, a large value for R-squared (near to unity) and a small value for RMSE are indicator of well-fitting.

Comparing all nine plots in figure 6.16 it is evident that for this particular dam the two best IMs are the PGA and ASI as they have the largest R-squared value. Furthermore, the PGA is essentially a differential quantity that capture a single peak value, and the ASI is essentially an integrative one which captures the area under the acceleration response spectrum. Henceforth, the cross correlation between those two IMs and their corresponding linear fit is shown in figure 6.17(a)

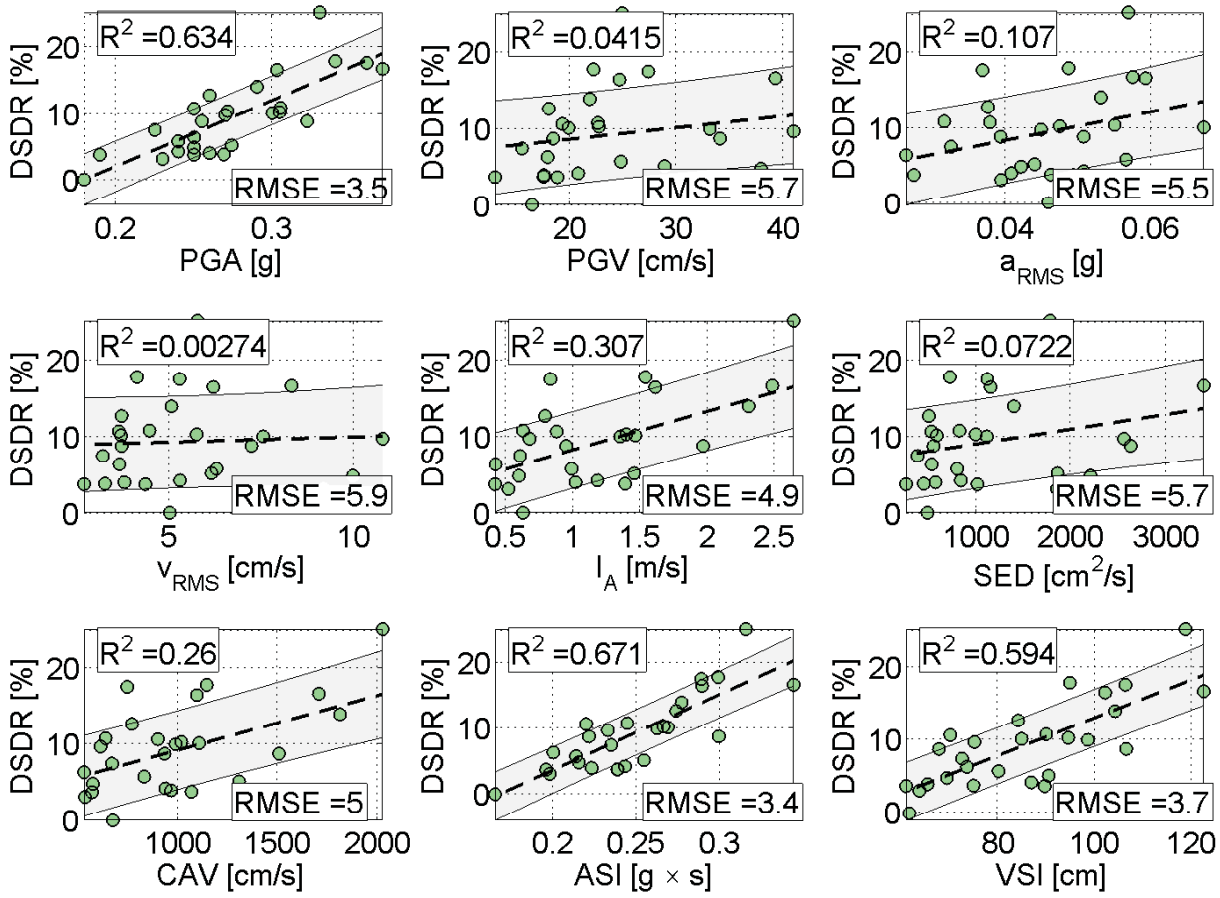

Figure 6.16: Impact of IM parameter on the responses of linear system, DSDR = overstrain area

as a bi-variate surface. Using a vectorized IM did slightly improve the R-squared value to from a previous maximum of 0.67 (ASI) to 0.69 and decreased the RMSE from 3.4 (ASI) to 3.33. Figure 6.17(b) shows the variation of the residuals (algebraic difference between actual data points and the fitted surface).

One can also examine competing scalar and vector IMs as predictors of an EDP or damage measure (such as DSDR) in light of the Akaike Information Criterion. For the reader unfamiliar with AIC, for any statistical model, the AIC value is

$$AIC = 2K - 2Ln(L) \tag{6.11}$$

where K is the number of parameters in the model and L is the maximized value of the likelihood

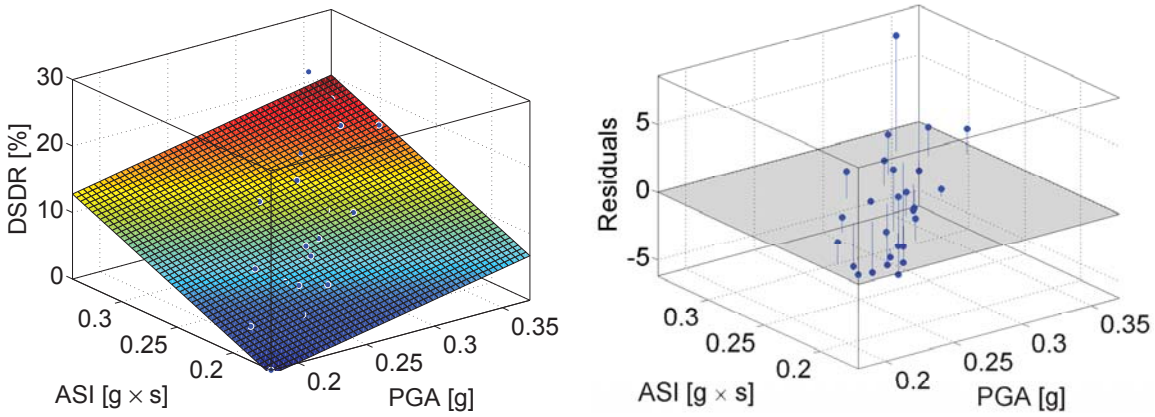

(a) Fitted surface (b) Residual assessment

Figure 6.17: Bi-variate surface fitting on the responses of linear system, DSDR = overstrain area

function for the model. When the sample size is finite, there is an alternative equation that corrects AIC for sample size. The AIC_C value is given by

$$AIC_C = AIC + \frac{2K(K+1)}{N-K-1} \tag{6.12}$$

where N denotes the sample size.

Especially when the sample size N is small or the number of parameters K is large, the analyst considering two or more competing models should prefer the one with the minimum AIC_C value. As Wikipedia says, "AIC (and by extension AIC_C) not only rewards GOF (measured here by $L0$, but also includes a penalty that is an increasing function of the number of estimated parameters (K)." Measuring the predictive power of a model by L or R-squared alone does not penalize the model for overfitting with more parameters. AIC_C is therefore a more rigorous measure of the information value of a model. Table 6.6 recaps AIC_C values of several IMs for their relationship to DSDR. It suggests that the best among them for predicting DSDR is the 4th-order polynomial on ASI. The advantage over the linear relationship between ASI and DSDR is slight though, and there appears to be slight disadvantage in using the vector [PGA, ASI] intensity measure, which has a higher AIC than ASI alone.

The foregoing does not consider any differences in uncertainty when one estimates ASI or

Table 6.6: AIC_C values for competing IMs and the example dam

IM(s)	Functional form	AIC_C
ASI	Linear	144.14
	2^{nd} order polynomial	145.99
	3^{rd} order polynomial	147.40
	4^{th} order polynomial	143.27
	5^{th} order polynomial	144.38
PGA	Linear	147.52
[PGA, ASI] vector	1^{st} order (planar)	145.71

PGA using a ground motion prediction equation. That is, if one fixes magnitude and distance, estimates ASI or PGA using a ground motion prediction equation, then estimates DSDR as a function of ASI or PGA, the uncertainty in DSDR will be greater, the R-squared and L values lower, and the AIC_C higher because of the added uncertainty in ASI or PGA. If the uncertainty in ASI given magnitude and distance differs from the uncertainty in PGA given the same magnitude and distance information, then the two IMs cannot be directly compared based solely on the value of AIC_C conditioned on known, fixed values of ASI and PGA.

We found that AIC_C for a linear relationship between DSDR is slightly lower for ASI than for PGA. However, uncertainty in ASI given magnitude and distance is slightly higher (0.6 according to (Bradley, 2010)) than uncertainty in PGA given magnitude and distance (about 0.53 using (Campbell and Bozorgnia, 2008)). The advantage in AIC_C of ASI versus PGA is thus offset at least somewhat by the better ground motion prediction equations for PGA than for ASI. ASI has not been the subject of as intense study through ground motion prediction equations as has PGA, so it may be that better ground motion prediction equations for ASI will in the future reduce the uncertainty in ASI given magnitude and distance.

The reader should bear in mind that these findings relate to this example dam only, not to dams in general, so one cannot make a general conclusion about the best IM based on this analysis. We can only say that for this dam, ASI, PGA, and a vector measure of the two are all approximately equally good IMs. The differences are small enough that the analyst can be excused for choosing among these IMs for other reasons than AIC_C or R-squared. We will be interested to see in future

studies whether the vector proves generally superior for the reasons we have discussed.

6.9 Nonlinear Structural Analysis

From figure 6.14 it is clear that a nonlinear analysis of the dam for Level 3 and possibly 2 is warranted. Results from such an analysis will be reported next.

Whereas lift joints were not modeled, contraction and peripheral ones were considered through simple node-to-node contact elements. Material nonlinearity are modeled through the smeared crack approach (Bazant and Lin, 1988). All other details are identical to the linear analysis case.

6.9.1 Joint Displacements Demand and Capacity

Results from the nonlinear analysis will be evaluated through the joint damage index (DI^{joint}). From each of the $n = 9$ analyses, the maximum joint opening and sliding displacement is recorded in terms of height. The mean and standard deviation of these values are shown in figure 6.18. The discontinuity in joint opening can be explained by the softening of the adjacent concrete as shown in figure 6.20(b).

These joint displacements (demand parameter) should be examined with reference to the specific dam design and its ability to accommodate them without water leakage (capacity parameter).

6.9.2 Simulated EDP Correlation

The nonlinear analysis of a dam is a very complex and CPU intensive operation. Henceforth, in the context of a PBEE-2 analysis one can either reduce the complexity of the model while increasing the number of analyses (n), or vice-versa model as accurately the structure albeit with a reduced n. In the present study $n = 9$. This dilemma can be circumvented by a palliative (Yang et al., 2009c) that generates additional correlated EDPs. This procedure was recently adopted by Applied Technology Council (2012, Appendix G) and can be summarized as:

(1) Select a specific SIL and perform n transient analysis.

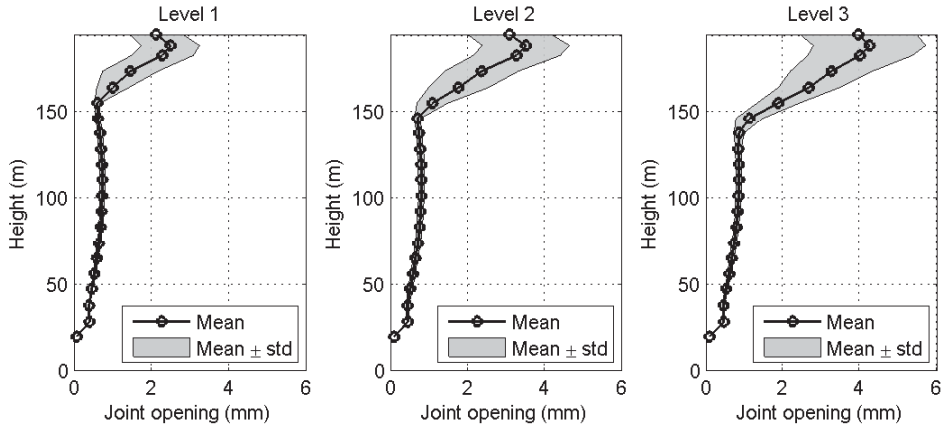

(a) Joint opening

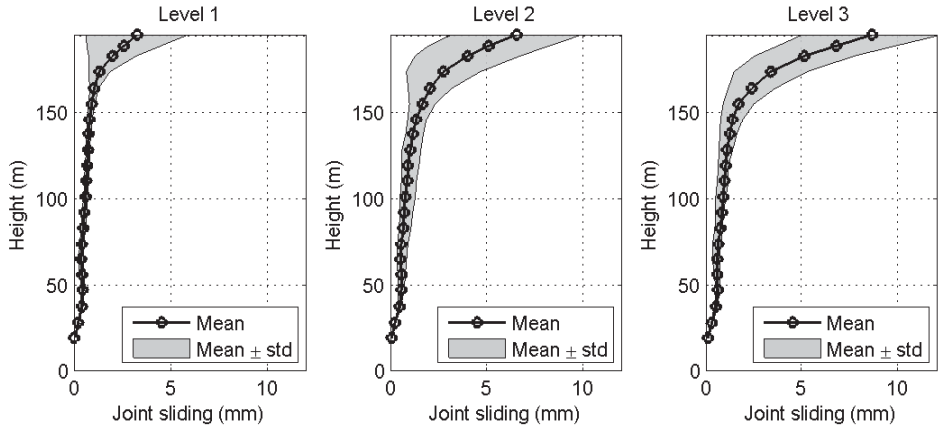

(b) Joint sliding

Figure 6.18: Nonlinear behavior of dam in terms of joint movement

(2) Save the extreme EDPs in the $\mathbf{X}_{n\times k}$ matrix, where k is the number of different EDPs.

(3) Compute $\mathbf{Y}_{n\times k} = \ln \mathbf{X}_{n\times k}$, which has the joint normal distribution.

(4) Compute the mean vector $\mathbf{M_Y} = (\text{mean}\,(\mathbf{Y}))^t$.

(5) Compute the diagonal standard deviation matrix $\mathbf{D_Y} = \text{diag}\,(\text{std}\,(\mathbf{Y}))$.

(6) Compute the correlation coefficient matrix $\mathbf{R_{YY}} = \text{corrcoef}\,(\mathbf{Y})$.

(7) Compute the covariance matrix $\Sigma_{\mathbf{YY}} = \mathbf{D_Y R_{YY} D_Y}$.

(8) Compute the lower-triangular decomposition $\mathbf{L_Y} = (\text{chol}\,(\mathbf{R_{YY}}))^t$.

(9) Generate a vector of uncorrelated standard normal random variables, $\mathbf{U}$ having zero mean

and unit standard deviation.

(10) Perform a linear transformation and translation from $\mathbf{U}$ to $\mathbf{Z}$ as $\mathbf{Z} = \mathbf{D_Y L_Y U} + \mathbf{M_Y}$.

(11) Transfer the generated joint normal logarithmic EDPs, $\mathbf{Z}$ to artificially generated EDPs as $\mathbf{W} = \exp(\mathbf{Z})$.

The three (k=3) EDP (joint opening, sliding, and cracking DI) associated with the n analysis are first assembled in $\mathbf{X}_{n\times k}$. Then using the previously mentioned procedure, N_{sim} synthetic set of k values are generated assuming that the components of $\mathbf{X}$ are correlated as in the n analyses and that they are jointly lognormal (Cornell and Krawinkler, 2000).

Given the simplicity of the algorithm, a large value of N_{sim} was used as it would facilitate data interpretation. Figure 6.19(a) shows the matrix plot of the simulated EDPs and the resulted histograms (shown along the diagonal). The off-diagonal plots show the correlations between all pairs of EDPs. The lognormal distribution results in a scatter of data within a cone which apex is at the origin. Among the three possible pairs, it is clear that DI^{cracking} *vs.* DI^{opening} and DI^{cracking} *vs.* DI^{sliding} have the smallest and largest dispersion respectively. This implies that as one would expect extensive cracking will result in commensurate opening, whereas cracking is not necessarily implied by shear sliding. As such, should one select a pair of EDPs to assess the probability of failure, the best pair candidates would be the last one. The normalized joint probability density function for DI^{cracking} *vs.* DI^{sliding} is shown in figure 6.19(b).

6.10 Linear and Nonlinear Analyses Correlation

Whereas a nonlinear analysis would ultimately best capture the response of a structure, computational cost and complexity often are an impediment for the practicing engineer. It is not uncommon to seek a correlation between the two which would ultimately allow the engineer to only perform a linear elastic analysis (Chopra and Goel, 2002). This section will attempt to seek such a relation for the considered dam.

In the current practice for seismic analysis of concrete dams, the IM is considered in terms

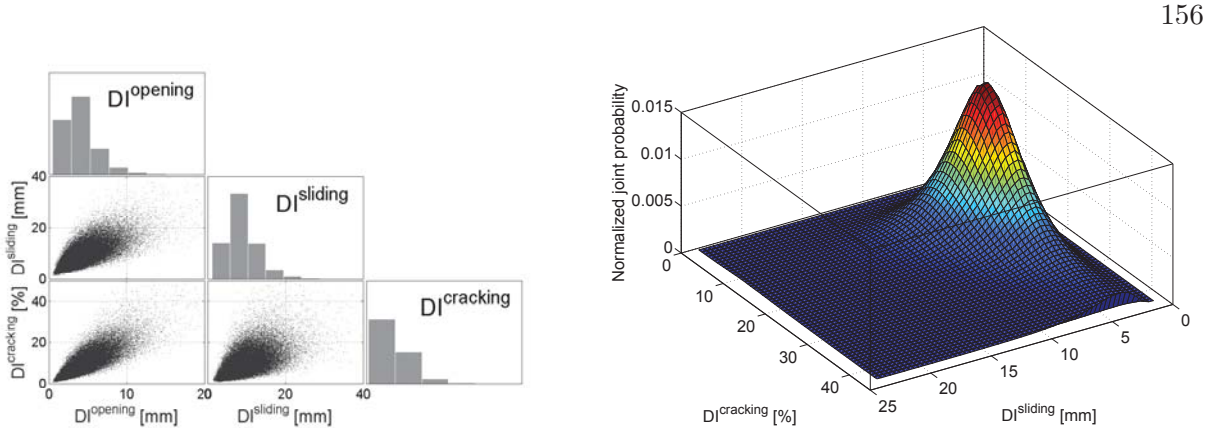

(a) Matrix plot of EDPs

(b) Joint distribution plot

Figure 6.19: Cross correlation between the simulated EDPs for nonlinear analysis at level 3

of the SILs (such as DBL and MDL) (ICOLD, 2010) (del Consiglio dei Ministri, 2001) (FERC-Arch, 1999). Thus, the primary goal should be selecting a set of ground motion signals $(x_i(t), i = 1, 2, ..., n)$ all scaled to the predefined response spectra $(\widetilde{x}_i(t), i = 1, 2, ..., n)$. These signals do not have the same IM parameter necessarily, except that all are scaled to a certain response spectrum. Let's assume that the response of the linear and nonlinear systems to the scaled signals are $r_i^{le}(t)$ and $r_i^{nl}(t), i = 1, 2, ..., n$. The response r can be any general monitoring item in dams such as deformation, stress, uplift; or even the predefined damage index (DI). The extreme value of the r for $t \subseteq [0, t_{tot}]$ is assumed to be R. Thus, the group of extreme responses under the applied signals will be R_i^{le} and $R_i^{nl}, i = 1, 2, ..., n$ for linear and nonlinear systems, respectively. From the preceding analyses, the extreme responses R_i are identified, and then a probability distribution (normal or lognormal) fitted for both the linear and nonlinear analyses. Then a relationship among these quantities is sought

$$(\mu_R^{le}, \sigma_R^{le}) = g_m(\mu_R^{nl}, \sigma_R^{nl}) \tag{6.13}$$

for a given hazard level m.

Figure 6.20 shows the selected R for linear and nonlinear analysis at level 3 where the shaded area in 6.20(a) corresponds to DSDR (overstressed area) and in 6.20(b) to DI^{cracking}. One notes the good correlation among the two sets. Given the limited number of analysis ($n = 9$) in figure 6.20,

the N_{sim} simulated ones (as previously mentioned) are used to generate figure 6.21 and a lognormal distribution is fitted. The mean and standard deviation for the linear case are equal to 16.5 and 4.6, respectively, whereas for the nonlinear one they are equal to 8.6 and 4.1. Those two curves have nearly the same standard deviation and are nearly parallel in the [0.1, 0.8] vertical range. Hence, one could simplistically assume that outcome of a nonlinear analysis may be predicted from a linear one by simply dividing the mean value of the overstressed area by ≈ 2. Alternatively, these curves indicate that a linear elastic analysis has a safety factor of nearly two.

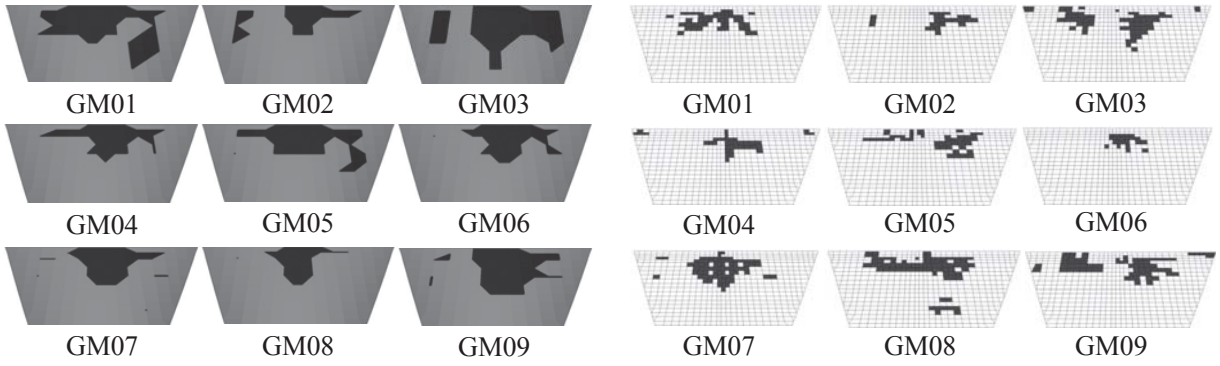

(a) Linear Analysis (b) Nonlinear Analysis

Figure 6.20: Correlation between linear and nonlinear analyses for level-3 seismic intensity

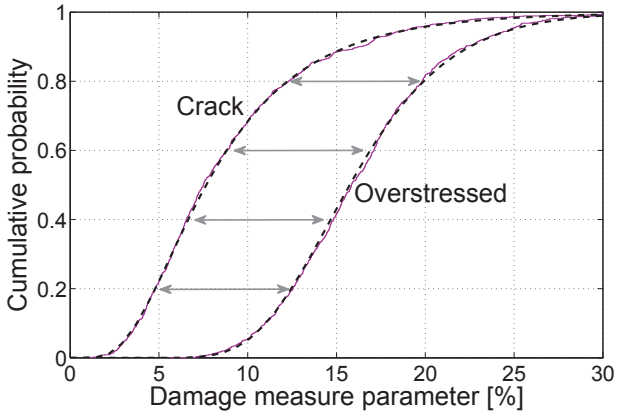

Figure 6.21: Cumulative probability distribution of damage measure parameters (dashed lines correspond to the simulated EDPs, solid ones to the fitted curve)

6.11 Summary and Conclusion

Heavily borrowing from the PBEE-2 (buildings) and PFMA (dams) safety assessment procedures, a new hybrid one is presented.

First, safety assessment of various dam types are addressed qualitatively and then quantitatively, figure 6.22. Then, a failure surface for concrete dams based on a linear elastic analysis are introduced. For the nonlinear analyses, a new set of damage indices specific to concrete dams are proposed. The newly proposed methodology is a radical departure of currently established ones for concrete dams, difference were duly highlighted, and the application is illustrated

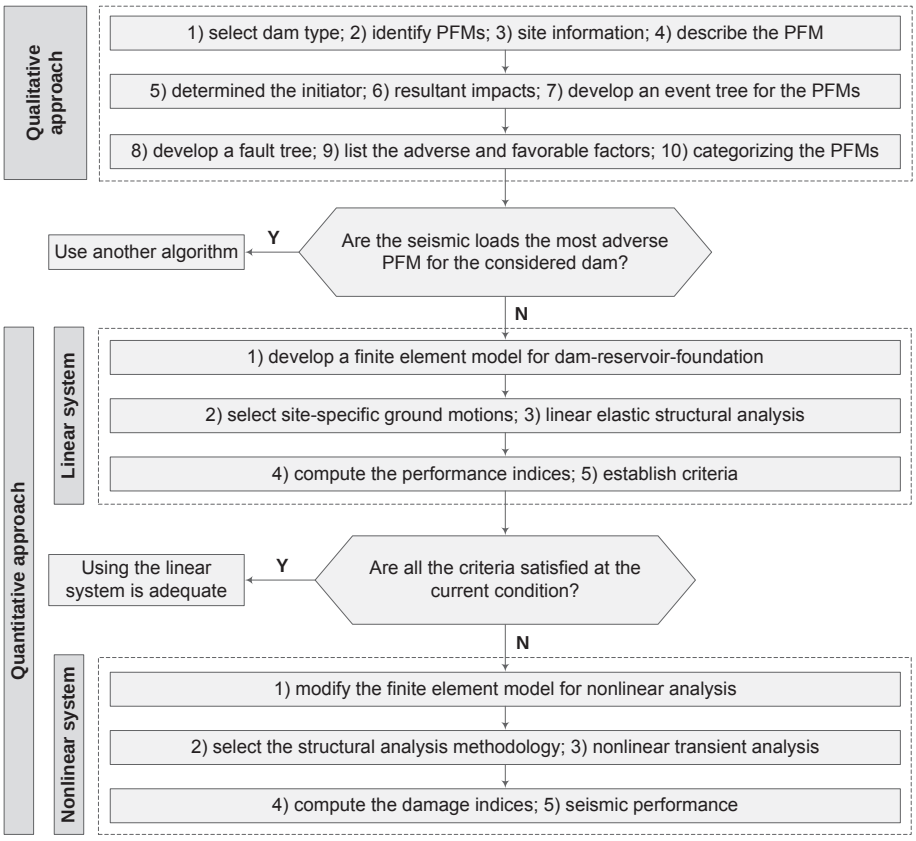

Figure 6.22: Summary of the proposed algorithm for quantitative PFMA

Chapter 7

Sensitivity and Uncertainty Quantification of Dam-Foundation System

This chapter is based on:

Hariri-Ardebili, M.A. and Saouma, V.E., (2015), Sensitivity and Uncertainty Quantification of the Cohesive Crack Model (submitted to Engineering Fracture Mechanics)

7.1 Introduction

Zero thickness interface elements were first developed in the context of rock mechanics Goodman, R.E. and Taylor, R.C. and Brekke, T.C. (1968). With the emergence of Hillerborg's cohesive crack model (Hillerborg et al., 1976) a new class of fracture mechanics-based interface elements appeared (Lotfi and Shing, 1994) (Carol et al., 1997) (Cervenka et al., 1998) and (Cocchetti et al., 2002). They are used in the context of the so-called discrete crack model (as opposed to smeared crack model) in the finite element simulation of cracking. These finite elements will be collectively referred to as cohesive crack models subsequently. Those elements were used in the context of numerous applications in quasi-brittle materials (primarily concrete, but also rock, ceramics, stiff soil) (Lopez et al., 2008) (Saouma, 2015), or through simplifications of these models in the context of blast such as Cirak et al. (2005).

The cohesive elements would typically be formulated in terms of well over 10 parameters (described below). A major challenge in their use is the selection of the parameters as only few can be measured experimentally, and the remaining must be estimated. Hence, a critical question is

how important is the accurate estimate of each of the model parameters. This can only be achieved through sensitivity and uncertainty analyses.

Sources of uncertainty can in be traced to one of eight groups (Der-Kiureghian and Ditlevsen, 2009). Chief among them is the basic random variables (RVs), $\mathbf{X} = (X_1, ..., X_n)$. The RVs in turn can be categorized as aleatoric or epistemic (Der-Kiureghian and Ditlevsen, 2009). An aleatoric uncertainty is presumed to be the intrinsic randomness of a phenomenon, while an epistemic one is due to lack of knowledge. The basic qualifier refers to directly observable quantities such as material properties (strength and stiffness), loads (earthquake magnitude and sea wave height), environmental phenomenons (temperature, alkali-aggregate reaction), and geometric dimensions (section size).

The focus of this paper is on the basic RVs, $\mathbf{X}$, describing cohesive crack model. It should be noted that for an existing structure, the RV's are epistemic as they can be measured. However for projected structures, they would be aleatoric.

This paper will perform a sensitivity analysis to assess the relative importance of each of the RVs (all epistemic) resulting in a tornado diagram. For the most sensitive ones, uncertainty quantification will be performed through Latin Hypercube Sampling (LHS) to determine capacity and fragility curves. Finally, impact of correlations among the parameters is assessed.

The study is conducted by performing pushover analysis of a simple interface element under mode I and II, and dynamic analysis of a dam with joint elements subjected to mixed-mode fracture. This investigation leads to a probabilistic-based safety assessment of structures which responses is primarily governed by cohesive cracking.

7.2 Background; Theory

7.2.1 Interface Joint Model

As mentioned earlier, there are a number of fracture mechanics based interface joint models; however for the context of this paper Cervenka et al. (1998) is used. It should be noted that most

of the existing models are essentially mere variation of the one used. For analysis purposes, the computer code Merlin Saouma et al. (2010) is used.

The element constitutive model is defined with respect to a general fracture, figure 7.1(a), and the corresponding failure surface, figure 7.1(b). The premises of the model are:

(1) Shear strength depends on the normal stress (Coulomb friction).

(2) Softening is present both in shear and tension, (Hillerborg extended).

(3) Residual shear strength due to the friction along the interface, which depends on the compressive normal stress, (Coulomb).

(4) Reduction in strength, i.e. softening, is caused by crack formation.

(5) Zero normal and shear stiffness when the interface is totally destroyed.

(6) Under compressive normal stresses neither the shear and nor the normal stiffness decrease to zero. In addition, should a compressive stress be introduced in the normal direction following a full crack opening, two faces of the interface come to contact, and both tangential and normal stiffness become nonzero (contact problem).

(7) Irreversible relative displacements are caused by broken segments of the interface material and by friction between the two crack surfaces, (permanent plastic damage).

(8) Roughness of the interface causes opening displacements (i.e. dilatancy) when subjected to sliding displacements.

(9) The dilatancy vanishes with increasing sliding or opening displacements.

The generalized failure surface is given by Carol et al. (1992)

$$F = (\tau_1^2 + \tau_2^2) - 2\,c\,\tan(\phi_f)(f_t - \sigma) - \tan^2(\phi_f)(\sigma^2 - f_t^2) = 0 \tag{7.1}$$

where c is the cohesion, ϕ_f is the angle of friction, f_t is the tensile strength of the interface, τ_1 and τ_2 are the two tangential components of the interface traction vector, and finally σ is the normal

traction component. The shape of the 2D failure function is shown in figure 7.1(b). The general 3D failure function is obtained by mere rotation around the σ-axis. Note that the residual shear strength can be obtained by setting both c and f_t equal to zero:

$$\tau_1^2 + \tau_2^2 \;=\; \tan^2(\phi_f)\;\sigma^2 \tag{7.2}$$

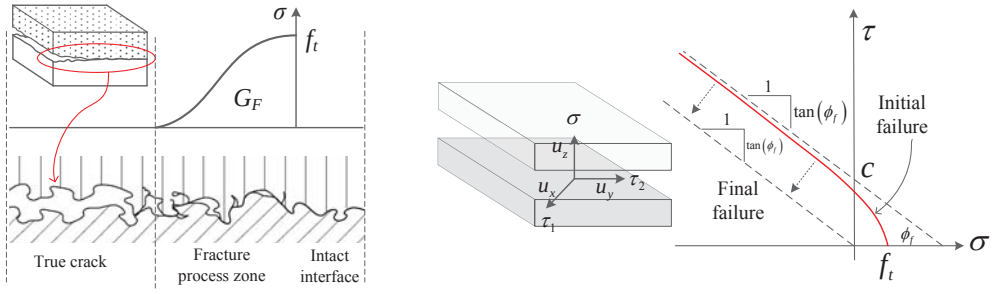

(a) 3D fracture process zone

(b) Failure function

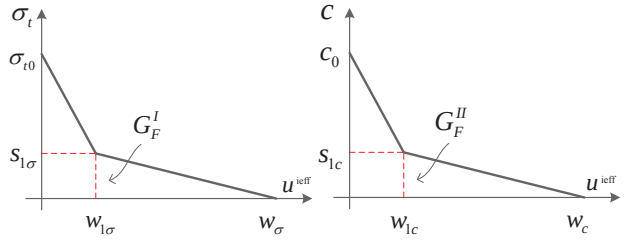

(c) Softening models

Figure 7.1: Zero-thickness interface joint element and corresponding failure surface

The evolution of the failure function is based on a softening parameter u^{ieff} which is the norm of the inelastic displacement vector u^i. The inelastic displacement vector is obtained by decomposition of the displacement vector u into an elastic part u^e and an inelastic part u^i. The inelastic part can subsequently be decomposed into plastic (irreversible) displacements u^p and fracturing displacements u^f. The plastic displacements are assumed to be caused by friction between crack surfaces and the fracturing displacements by the formation of micro-cracks.

In the present study a bi-linear relationship is used for $c(u^{\text{ieff}})$ and $\sigma_t(u^{\text{ieff}})$, figure 7.1(c) where G_F^I and G_F^{II} are mode I and II fracture energies. s_{1c}, w_{1c} and $s_{1\sigma}$, $w_{1\sigma}$ are the coordinates of

the break-point in the bi-linear softening laws for cohesion and tensile strength, respectively. The critical opening and sliding corresponding to zero cohesion and tensile strength are denoted by w_σ and w_c respectively, and they are determined from the condition that the area under the bi-linear softening law must be equal to G_F^I and G_F^{II} respectively.

$$\begin{aligned} u &= u^e + u^i \\ u^i &= u^p + u^f \\ u^{\text{ieff}} &= ||u^i|| = ({u_x^i}^2 + {u_y^i}^2 + {u_z^i}^2)^{1/2} \end{aligned} \tag{7.3}$$

Stiffness degradation is modeled through a damage parameter, $D \in \langle 0, 1 \rangle$, which is a relative measure of the fractured surface. Thus, D is related to the secant of the normal stiffness K_{ns} in the uni-axial case:

$$D = \frac{A_f}{A_o} = 1 - \frac{K_{ns}}{K_{no}} = 1 - \frac{\sigma_t(u^{\text{ieff}})}{\sigma_t(u^{\text{ieff}}) + (1-\gamma)u^{\text{ieff}}K_{no}} \tag{7.4}$$

where K_{no} is the initial normal stiffness of the interface, A_o and A_f are the total interface area and the fractured area respectively, γ is the ratio of irreversible inelastic normal displacement to the total value of inelastic displacement. For concrete, γ is usually assumed equal to 0.2 or 0.3 Dahlblom and Ottosen (1990).

7.2.2 Sensitivity and Uncertainty Quantification

7.2.2.1 Sensitivity Assessment

Sensitivity analysis determines the impact of a variation in an input parameter on output results. Mathematically, this corresponds to the partial derivative of the output function (the finite element model in this case) with respect to an input parameter at a given design point.

The procedure starts with the identification of the basic RVs, $\mathbf{X} = (X_1, \cdots, X_n)$, and their corresponding distributional model (e.g. normal, lognormal). Then $2n + 1$ analyses are performed Army Corps of Engineers (1992) using mean (X_i^{mean}), minimum ($X_i^{\min}$) and maximum ($X_i^{\max}$) values of the RVs. The response can be mathematically expressed in terms of

$$\Theta = f\left(X_1, X_2, \cdots, X_i, \cdots, X_n\right) \tag{7.5}$$

A reference response Θ^{Ref} is first computed in terms of the n RVs in $S = \{1, 2, ..., n\}$ equal to their mean values

$$\Theta^{\text{Ref}} = f\left(X_i^{\text{mean}}\right),\ \forall\, i \in S \tag{7.6}$$

Then $2n$ analyses are performed, each corresponding to a given maximum or minimum of an RV, while all others are set to their mean value:

$$\begin{aligned} \Theta_i^{\min} &= f\left(X_i^{\min}, X_j^{\text{mean}}\right),\ i = RV,\ \forall j \in S \wedge j \neq i \\ \Theta_i^{\max} &= f\left(X_i^{\max}, X_j^{\text{mean}}\right),\ i = RV,\ \forall j \in S \wedge j \neq i \end{aligned} \tag{7.7}$$

The swing for each of the n RVs is computed next

$$\Theta_i^{\text{swing}} = \left|\Theta_i^{\max} - \Theta_i^{\min}\right| \tag{7.8}$$

and are sorted in descending order to form the tornado diagram. Finally, the tornado diagram is plotted and one has to arbitrarily decide what are the most sensitive RVs, figure 7.2.

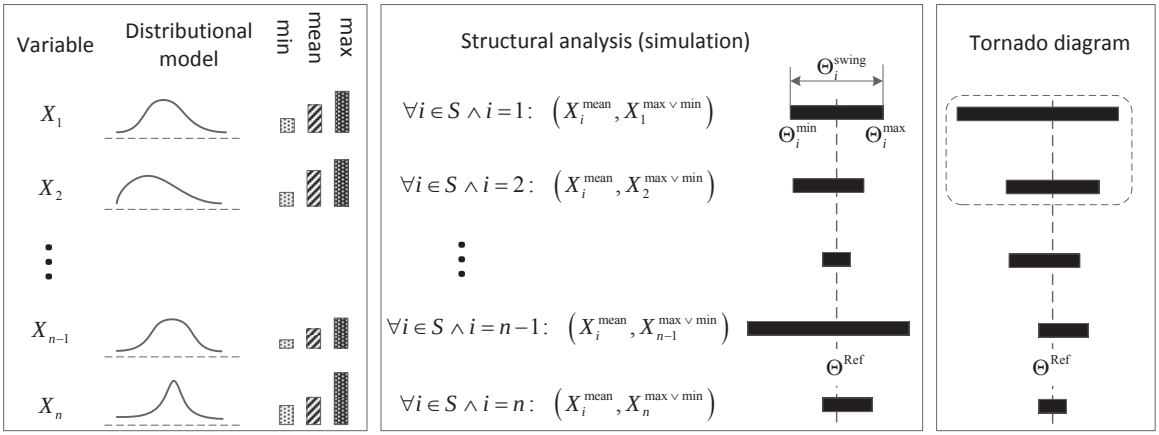

Figure 7.2: Sensitivity analysis using tornado diagram

7.2.2.2 Uncertainty Analysis

Uncertainty arises from the probabilistic nature of the input data resulting in a non-deterministic outcome. It should be noted that the area under a normal distribution function plus and minus

a standard deviation is 68% of the total area. Should one consider two standard deviations, then the area increases to 95%. Furthermore, the normal distribution function being bounded by $\pm\infty$, it is then desirable to truncate those limits into physically acceptable range when sampling occurs. Truncating the distributional model requires adjustment of the curve so that the area under the truncated one remains unchanged. For example, considering a normal distribution with mean of ten and a standard deviation of three, should it be truncated to be bounded by $[10 - \frac{10}{2}, 10 + \frac{10}{2}]$ then the original and truncated curves are shown in figure 7.3.

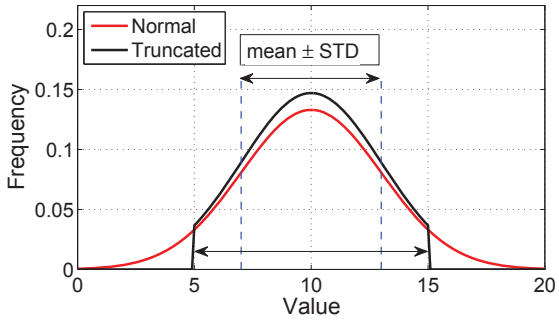

Figure 7.3: Comparison of the normal distribution and the truncated one

Sampling of the distributional model is indeed a key element of an uncertainty analysis. By far, the most widely used sampling method is the so-called Monte Carlo Simulation (MCS). Success of the method hinges on a very large number of analysis as limited sampling may not include values in the outer ranges of the distribution. As a palliative to this handicap, an improved sampling method is achieved through the so-called Latin Hypercube Sampling Iman and Conover (1982). LHS guarantees samples to be drawn over the whole range of the distribution and proceeds as follows. Given a system with basic RVs, $\mathbf{X} = (X_1, ..., X_n)$ and corresponding distributions D_1, ..., D_n, first the range of each variable is split into m non-overlapping intervals of equal marginal probability $1/m$. Then sampling starts with the random selection of an interval followed by another random selection of a point inside it. The procedure is repeated until all intervals have been accessed, and none of them more than once. This procedure is repeated for each of the n RVs. It should be noted that should there be a single RV, then one could evaluate each interval sequentially.

However should there be two or more RVs, then the random access of the combination of interval is essential. Figure 7.4 illustrated the LHS when two variables X_1 and X_2 are considered with D_1 D_2 being uniform and normal distribution respectively, and m is set to eight.

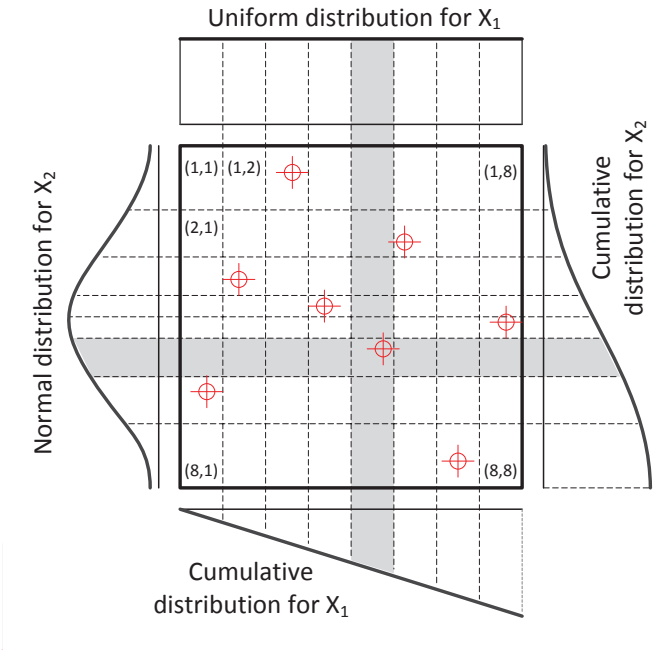

Figure 7.4: Illustrative example of Latin hypercube sampling for $\mathbf{X} = (X_1, X_2)$

So far, the RVs have been assumed to be uncorrelated. Yet at times they are, e.g. the compressive strength and elastic modulus of concrete are related by $E = 57,000\sqrt{f'_c}$. However, in the presence of correlated variables, the previously described algorithm for the LHS must be refined.

Given a random vector $\mathbf{X}$ originally uncorrelated, we seek a transformation of $\mathbf{X}$ which would have a correlation matrix $\mathbf{C}$. Since $\mathbf{C}$ is positive definite and symmetric, it can be expressed as $\mathbf{C} = \mathbf{P}\mathbf{P}^T$. Then the new row vector $\mathbf{Y} = \mathbf{X}\mathbf{P}^T$ should have a correlation matrix $\mathbf{M}$ close to the desired one $\mathbf{C}$ Iman and Conover (1982). The algorithm proceeds as follows:

(1) Construct an input matrix $\mathbf{R}_{m\times n}$ defined by m LHS for each of the n RVs.

(2) Define a target correlation matrix as $\mathbf{C}_{n\times n}$ where $0 < C_{ij} < 1$ which encapsulates the

relationships between variables. It is often a subjective indicator.

(3) Compute the sample correlation matrix $\mathbf{T}_{n\times n}$ of $\mathbf{R}_{m\times n}$ by populating each cell of an $n \times n$ matrix with a random number.

(4) Perform a Cholesky decomposition of the target correlation matrix $\mathbf{C}_{n\times n} = \mathbf{P}\mathbf{P}^T$.

(5) Similarly decompose the sample correlation matrix $\mathbf{T}_{n\times n} = \mathbf{Q}\mathbf{Q}^T$.

(6) Determine $\mathbf{S}_{n\times n}$ using either $\mathbf{C} = \mathbf{S}\mathbf{T}\mathbf{S}^T$ or $\mathbf{S} = \mathbf{P}\mathbf{Q}^{-1}$.

(7) Generate an $n \times m$ matrix $\mathbf{R}_{s1}$ whose columns represent n independent permutations of an arbitrary set $a(i)$, $i = 1, 2, ..., m$.

(8) Convert $\mathbf{R}_{s1}$ to van der Waerden scores, $\mathbf{R}_{s2}$ (Conover, W.J., 1980). The van der Waerden scores is defined as $\Phi^{-1}\left(\frac{i}{m+1}\right)$, $i = 1, 2, ..., m$, where Φ^{-1} is the inverse of the standard normal distribution.

(9) Re-construct the matrix $\mathbf{R}^*_{n\times n} = \mathbf{R}_{s2}\mathbf{S}^T$. Match up the rank pairing in $\mathbf{R}$ based on $\mathbf{R}^*$.

7.2.3 Capacity and Fragility Curves

Capacity Curve: Results of structural analyses under the monotonically increased force or displacement can be expressed in term of capacity curve. In he context of a static analysis, this is a pushover curve, and in a seismic one it can be an Endurance Time Analysis (ETA) Hariri-Ardebili et al. (2014b). The capacity curve has on its horizontal axis an engineering demand parameter (EDP) (e.g. displacement, crack length ratio, joint opening) and on the vertical one an intensity measure (IM) (e.g. PGA or $S_a(T)$ for dynamic analysis and applied force or displacement in a pushover analysis). Capacity curve covers the full range of response from linear to nonlinear and ultimately failure.

Fragility Curve: A fragility curve is the probability of failure (or other limit states - LS) of a system as a function of IM (Baker, 2014). It is called seismic fragility curve if it is obtained

from seismic analysis. A log-normal cumulative distribution function is usually used to define it:

$$P\left[\text{FRAC}|\text{IM}=im\right]=\Phi\left(\frac{\ln(im)-\ln(\eta_{\text{FRAC}|\text{IM}})}{\beta_{\text{FRAC}|\text{IM}}}\right) \tag{7.9}$$

where $\Phi(.)$ is the standard normal cumulative distribution function, $\eta_{\text{FRAC}|\text{IM}}$ median of the fragility function $\beta_{\text{FRAC}|\text{IM}}$ the logarithmic standard deviation (also called dispersion). The median and dispersion (logarithmic standard deviation) are given by

$$\begin{aligned}\ln\hat{\eta}_{\text{FRAC}|\text{IM}} &= \frac{1}{n}\sum_{i=1}^{n}\ln(\text{IM}_i)\\ \hat{\beta}_{\text{FRAC}|\text{IM}} &= \sqrt{\frac{1}{n-1}\sum_{i=1}^{n}\left(\ln\left(\frac{\text{IM}_i}{\hat{\eta}_{\text{FRAC}|\text{IM}}}\right)\right)^2}\end{aligned} \tag{7.10}$$

where n is the number of simulations.

7.3 Finite Element Simulations

7.3.1 Models

Three representative problems are selected to assess the sensitivity and uncertainty of the cohesive crack model previously described.

- Mode I fracture: The response of a crack in pure mode I fracture subjected to monotonically increased displacement (pushover analysis, POA).
- Mode II fracture: Similar to the preceding case, but the crack is subjected to a mode II crack sliding displacement.
- Mixed-mode fracture: The dynamic response of a concrete dam-foundation joint is assessed using ETA method.

The finite element models of the three case studies are shown in figure 7.5. The mode I fracture is subjected to an imposed vertical displacement, while the mode II one is subjected to an imposed shear displacement on the lower face of the upper block (while it is also subjected to imposed

compressive traction). The mixed-mode fracture is simulated through the seismic response of a rock-concrete joint, figure 7.5(c). Of particular relevance to this study is the varying uplift pressure along the joint accompanying crack opening-sliding.

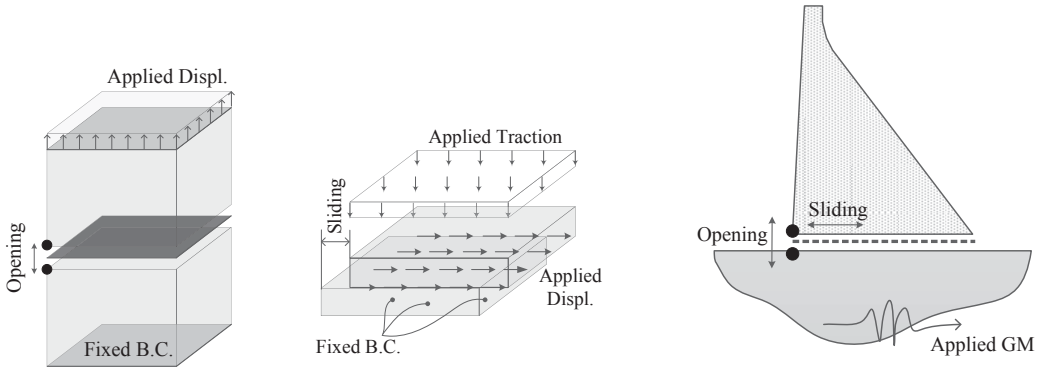

(a) Mode I (b) Mode II (c) Mixed-mode

Figure 7.5: Investigated models

7.3.2 Materials

As earlier stated, only very few of the the parameters in the joint constitutive model can be experimentally measured. Those include the tensile strength f'_t, the cohesion c, the angle of friction ϕ_f, and the fracture energy G_F^I. For the present study, the fracture parameters shown in Table 7.1 are used. To each parameter a mean value and the coefficient of variation (COV) (which is the ratio of standard deviation to mean) is assumed based on engineering judgment. In all the cases, normal distributions are assumed and are truncated to [0.5 mean, 1.5 mean]. Indeed, since many of the joint parameters have to be estimated by the analyst (primarily for reported laboratory tests and subsequent analyses), the purpose of this paper is precisely to assess their impact on the results.

Table 7.1: Parameters defining the zero thickness joint element

Characteristics	Symbol	Unit	Mean	COV	[Lower, Upper]
Tangential stiffness	k_t	GPa	224	0.2	[112, 336]
Normal stiffness	k_n	GPa	224	0.2	[112, 336]
Tensile strength	f_t'	MPa	2.24	0.2	[1.12, 3.36]
Cohesion	c	MPa	1.90	0.2	[0.95, 2.85]
Friction angle	ϕ_f	Deg.	38	0.2	[19, 57]
Dilatancy angle	ϕ_d	Deg.	20	0.2	[10, 30]
Specific mode I fracture energy	G_F^I	N/m	252	0.2	[126, 378]
Specific mode II fracture energy	G_F^{II}	N/m	2520	0.2	[1260, 3780]
Relative irreversible deformation	γ	-	0.3	0.1	[0.15, 0.45]
Max. displacement for dilatancy	$u_{D_{max}}$	m	0.01	0.1	[0.005, 0.015]
Tensile stress at break-point	$s_{1\sigma}$	MPa	0.56	-	-
COD at break-point	$w_{1\sigma}$	m	1.12e-4	-	-
Cohesion at break-point	s_{1c}	MPa	0.475	-	-
CSD at break-point	w_{1c}	m	1.89E-3	-	-

7.4 Results and discussion

7.4.1 Mode I Fracture

For mode I fracture, the incremental displacement is applied at the upper face of the upper element. No in-plan movement is allowed. Figure 7.6 shows the evolution of mode I fracture for the interface joint element. Along the joint opening, both the upper and lower elements show increase in elastic strain in the direction of loading. The final plot shows the separation of the elements and so there is no further stress on the joint element.

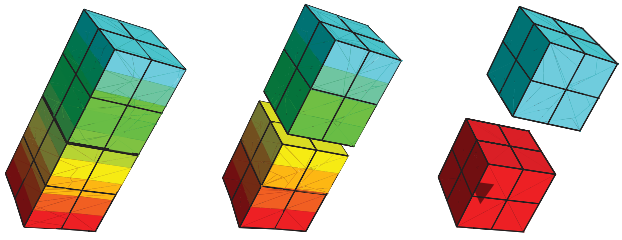

(a) Initiation (b) Softening (c) Fractured

Figure 7.6: Evolution of mode I fracture in the joint element

7.4.1.1 Sensitivity Assessment

In the presence of 14 RVs, 2×14+1=35 displacement control POA are performed. In order to investigate the sensitivity of the results to the variation of the particular RV, two sets of boundary limits are considered (Eq. 7.7). First a low variation $[0.75\eta_{RV_i}, 1.25\eta_{RV_i}]$, and then a high variation $[0.50\eta_{RV_i}, 1.50\eta_{RV_i}]$. Note that η_{RV_i} is the median of the ith RV which is equal to the mean for the normal distributions.

Figure 7.7 shows the capacity curves from the 35 POA for the two models. Response is either bi- or tri-linear. The first change in slope corresponds to fracture initiation and the second to failure. As expected the narrower band, figure 7.7(a), exhibits smaller dispersion than the broader one. The tornado diagram corresponding to these two analyses are shown in figure 7.8. It is worth

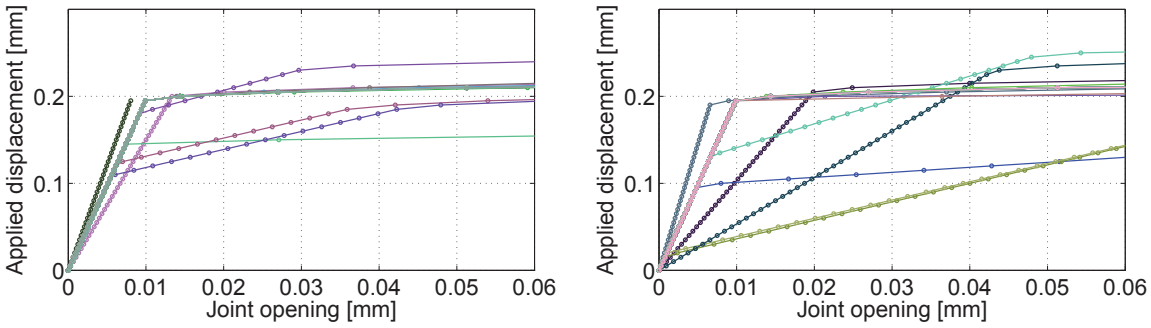

(a) Bounded by $(0.75, 1.25)\eta_{RV_i}$

(b) Bounded by $(0.50, 1.50)\eta_{RV_i}$

Figure 7.7: Capacity curves for mode I fracture through 35 analyses

noting, that though this model has 14 parameters, only about half of them govern the response in mode I. By far, the dominant effect is the tensile strength f_t. This is to be anticipated given the failure envelope in figure 7.1(b). In figure 7.8(b) the bar diagram corresponding to G_F^I indicates sensitivity to increases of the original G_F^I and not to their decrease. Likewise for some of the other eccentric values. Henceforth, in this case about half of the parameters may have to be assumed as variables, the others can be fixed.

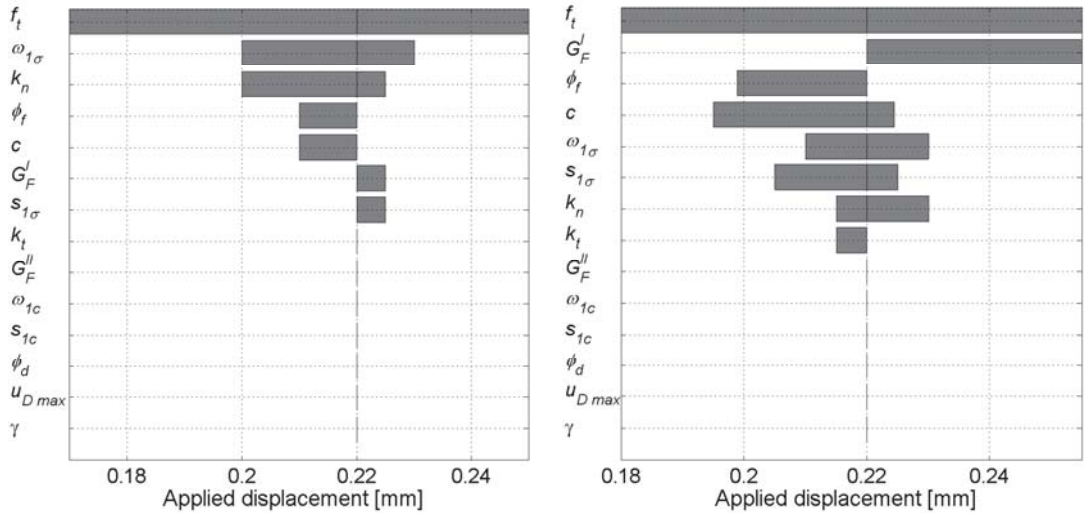

(a) Bounded by $(0.75, 1.25)\eta_{RV_i}$ (b) Bounded by $(0.50, 1.50)\eta_{RV_i}$

Figure 7.8: Tornado diagrams for the mode I fracture

7.4.1.2 Uncertainty Quantification

The sensitivity analysis having identified five most sensitive parameters: f_t, G_F^I, k_n, ϕ_f, and c the uncertainties associated with them should be quantified. A total of $m = 1,000$ analyses are performed for each of the most sensitive parameters. Two cases are considered. First, 13 parameters are kept constant, and the one investigated is drawn randomly through a LHS, Table 7.1. In the second case, in each one of the 1,000 analysis 10 RVs are randomly selected.

Single RV: In this case all RV's are kept constant, and one is randomly sampled. Results are shown in figure 7.9. The first column plots the capacity curves for each of the five most sensitive RVs. The median capacity curve (solid line) and the 16% and 84% fractiles (dashed lines) are shown also. The corresponding dispersion (Eq. 7.10) are shown in the second one, and finally the fragility curves (Eq. 7.9) in the third.

The dispersion of results vary from one RV to the other. For example most of the dispersion for f_t occurs post-fracture (as expected, Eq. 7.1), however the dispersion for k_n occurs in the linear ascending range, and disappears one separation of the surfaces occur.

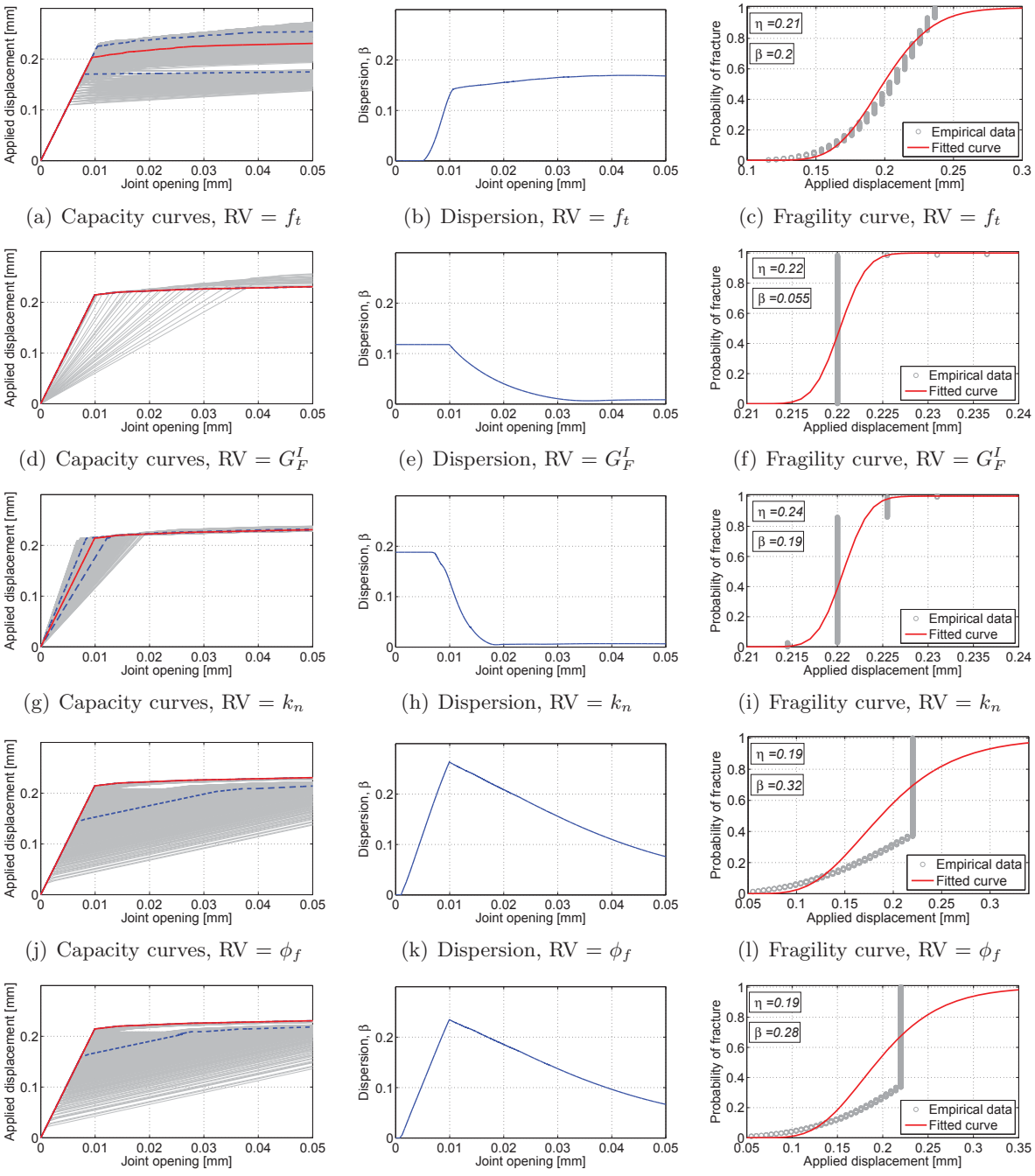

(a) Capacity curves, RV = f_t (b) Dispersion, RV = f_t (c) Fragility curve, RV = f_t

(d) Capacity curves, RV = G_F^I (e) Dispersion, RV = G_F^I (f) Fragility curve, RV = G_F^I

(g) Capacity curves, RV = k_n (h) Dispersion, RV = k_n (i) Fragility curve, RV = k_n

(j) Capacity curves, RV = ϕ_f (k) Dispersion, RV = ϕ_f (l) Fragility curve, RV = ϕ_f

(m) Capacity curves, RV = c (n) Dispersion, RV = c (o) Fragility curve, RV = c

Figure 7.9: Uncertainty quantification for single RVs under the mode I fracture

Each fragility plot includes the empirical data point (from the 1,000 analyses) as well as the fitted log-normal distribution (Eq. 7.9). In some cases, such as for f_t the fitted one follows well the empirical data point over a broad range of applied displacements. On the other

hand, when there is a very small dispersion (G_F^I and k_n) the resulting fragility curve is very narrow. When the dispersion is bi-linear (ϕ_f and c), the fragility curve poorly matches the empirical data points.

Multiple RVs: In this case only 10 of the RV are considered. They are all the material parameters (Table 7.1) except those defining the softening break points. Since multiple RVs are concurrently selected, one can consider either one of two cases: uncorrelated or correlated RVs. The correlation coefficients **C** are given in Table 7.2. It is important to note that these correlation coefficients are arbitrarily assigned based on the physics of the model by the authors. Results of the two sets of sampling (driven by LHS) are expressed in figures

Table 7.2: Correlation among the RVs of zero thickness joint element

	k_t	k_n	f_t'	c	ϕ_f	ϕ_d	G_F^I	G_F^{II}	γ	$u_{D_{max}}$
k_t	**1.0**									
k_n	0.7	**1.0**								
f_t'	0.1	0.1	**1.0**							
c	0.1	0.1	0.7	**1.0**						
ϕ_f	0.3	0.3	0.3	0.7	**1.0**					
ϕ_d	0.1	0.1	0.3	0.3	0.3	**1.0**				
G_F^I	0.1	0.1	0.7	0.5	0.3	0.1	**1.0**			
G_F^{II}	0.1	0.1	0.5	0.7	0.7	0.1	0.8	**1.0**		
γ	0.0	0.0	0.0	0.0	0.0	0.0	0.0	0.0	**1.0**	
$u_{D_{max}}$	0.0	0.0	0.0	0.0	0.0	0.0	0.0	0.0	0.0	**1.0**

7.10(a) and 7.10(b). In the presence of a zero correlation coefficient, the corresponding cell indicates that samples are randomly distributed (disk). The diagonal plots are the histograms of each RV (truncated normal distribution).

Figure 7.11 compares the uncertainty quantification with and without correlations. This is to be contrasted with figure 7.9 where only one RV was randomly assigned. Note that since all RVs are simultaneously randomly assigned, only one set of plots is needed. The capacity functions are noted to be smoother than those in the previous case. Furthermore, the dispersion for correlated RVs is nearly constant. In the un-correlated RVs, it peaks, than descends. In this case the dispersion is nearly twice the one of the correlated RVS.

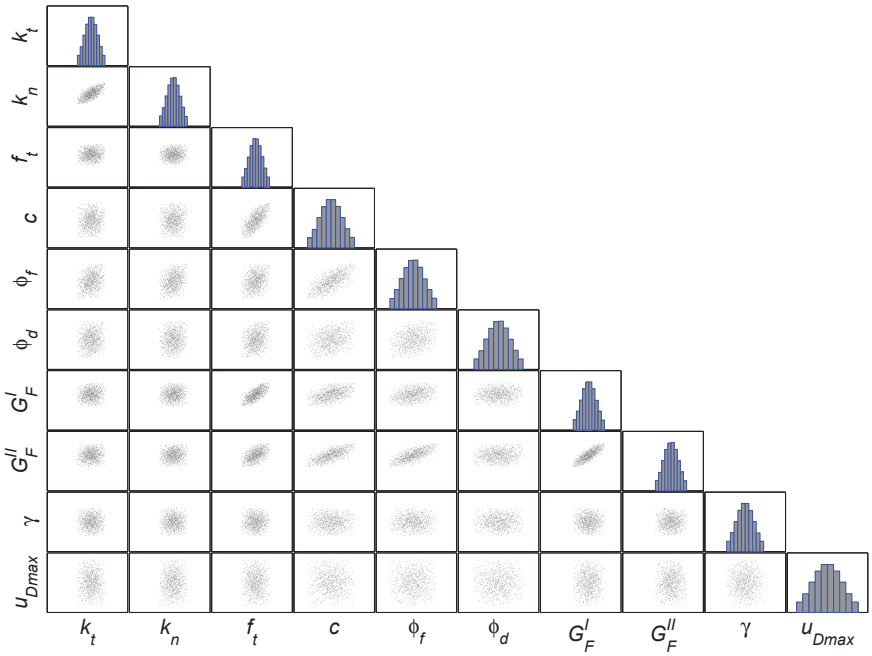

(a) With correlation

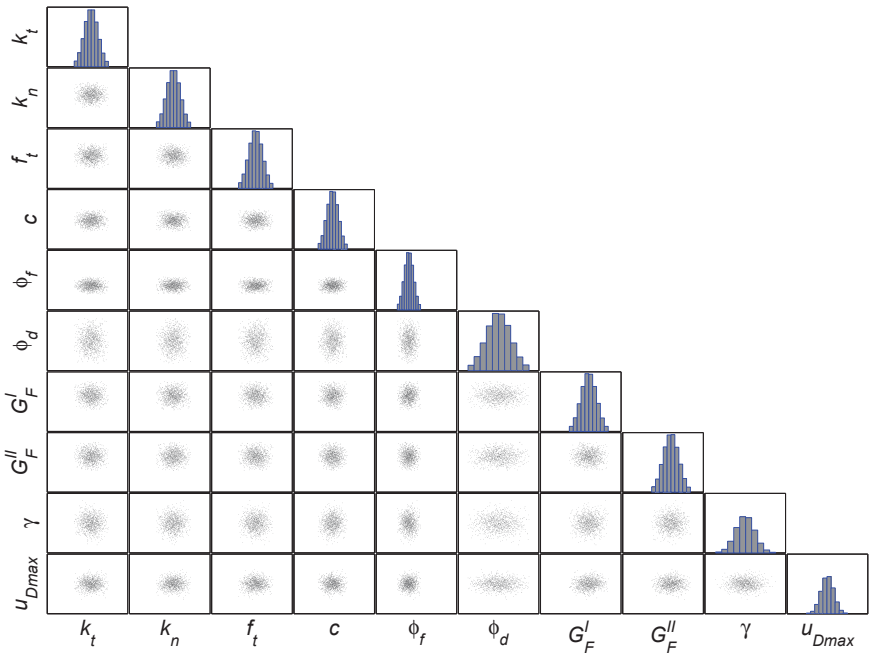

(b) Without correlation

Figure 7.10: Sampling of the RVs for mode I and II fracture mechanics (no scale)

Finally, the fragility curves of the correlated case better match the empirical data points than in the uncorrelated one.

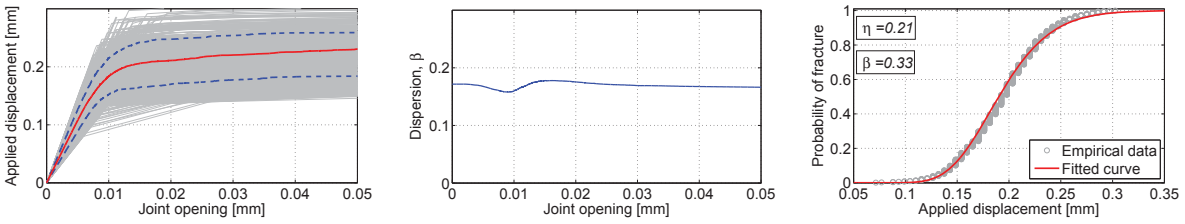

(a) Capacity curves, Correlated RVs (b) Dispersion, Correlated RVs (c) Fragility curve, Correlated RVs

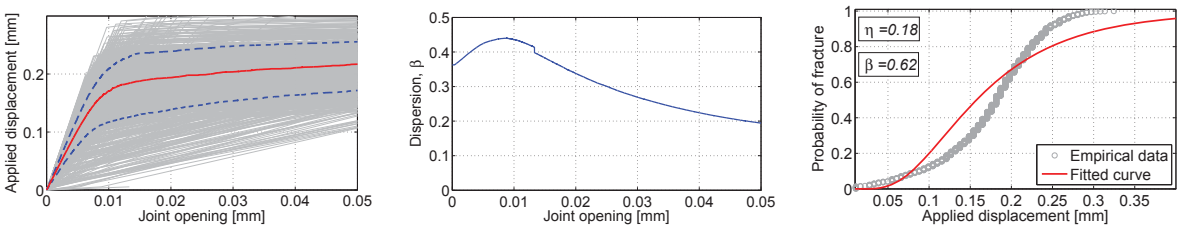

(d) Capacity curves, Uncorrelated RVs (e) Dispersion, Uncorrelated RVs (f) Fragility curve, Uncorrelated RVs

Figure 7.11: Impact of RV correlation on the uncertainty quantification of the mode I fracture

Finally, figure 7.12 compares all the individual, correlated and un-correlated fragility curves for mode I fracture. Considering the uncertainty in all RVs without any correlation leads to the most wide fragility curve. In some cases, correlation decreases the dispersion even less than the one for the individual RV.

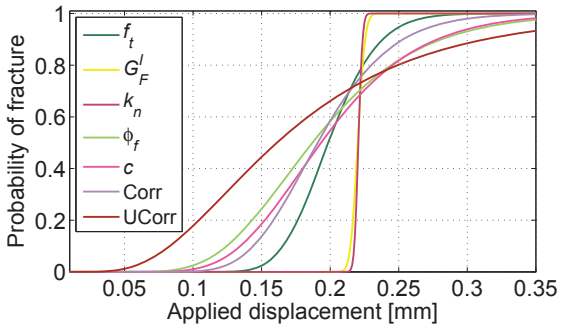

Figure 7.12: Comparison of different fragility curves for mode I fracture

7.4.2 Mode II Fracture

For mode II fracture mechanics, the incremental shear displacement is applied at the lower face of the upper block. Special attention is required to prevent other forms of fracture (mode I

and III). A continuous traction is applied on the top of the upper element to generate the friction between two surfaces under sliding force. Figure 7.13 shows the evolution of mode II fracture for the interface joint element. The lower element does not have any displacement profile. Considering that the two surfaces are not perfectly rigid, there is some finite penetration of the upper element in the lower one due to applied constant force on the top of the upper block. At the time of fracture, there is a full separation between two parts.

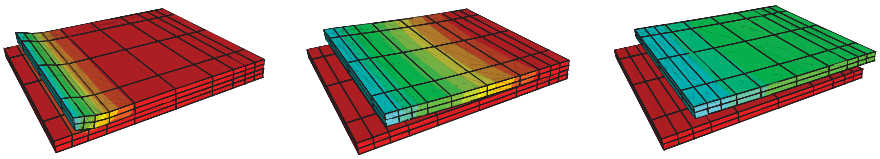

(a) Initiation (b) Softening (c) Fractured

Figure 7.13: Evolution of mode II fracture in the joint element

7.4.2.1 Sensitivity Assessment

With identical material properties as those previously considered for the Mode I case, Table 7.1, N_{sim} =35 (14 variables, 2×14+1) displacement control POA are performed. Two plates are in contact through the zero thickness interface element, a normal compressive traction is applied on the top face, and imposed displacement imposed on the lower surface of the top plate. Again, two sets of boundary limits are considered: a low variation [$0.75\eta_{RV_i}$, $1.25\eta_{RV_i}$], and then a high variation [$0.50\eta_{RV_i}$, $1.50\eta_{RV_i}$]. Figure 7.14 shows the capacity curves resulted from POA for the two bounded models. Contrarily to the Mode I case (figure 7.7) the transition from linear to sliding to failure is much smoother. In the former case, the failure is indeed more brittle, whereas in this case, the presence of friction dampens the response. As before, there is a higher variation in the broad band.

Figure 7.15 shows the associated tornado diagram. Clearly, and as expected, cohesion c and angle of friction ϕ_f are dominant. Surprisingly, in this pure mode II loading, G_F^I and G_F^{II} are similar (but marginal) impact. Contrarily to Mode I, the bounds have no impact on the order of

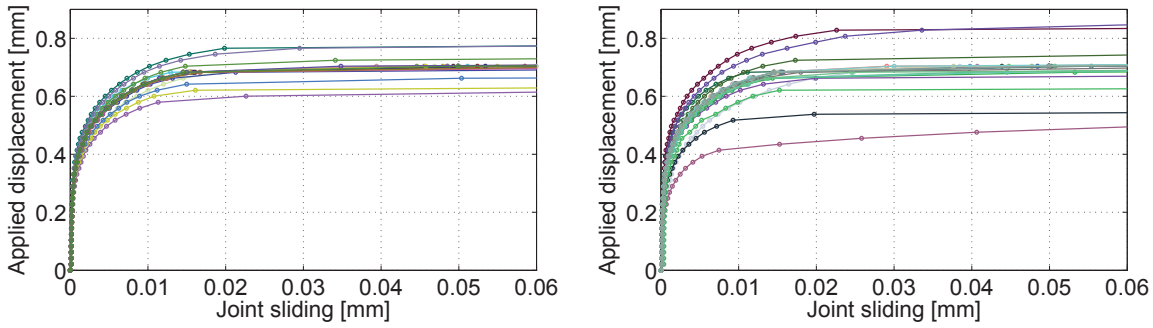

(a) Bounded to $(0.75, 1.25)\eta_{RV_i}$ (b) Bounded to $(0.50, 1.50)\eta_{RV_i}$

Figure 7.14: Capacity curves for the mode II fracture

the most sensitive variables, figure 7.8 *vs.* figure 7.15.

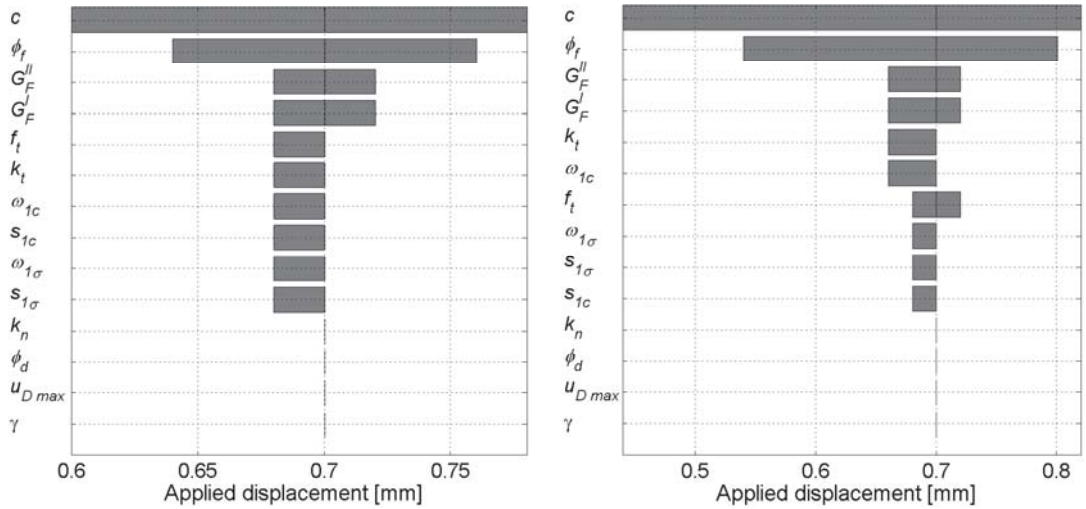

(a) Bounded to $(0.75, 1.25)\eta_{RV_i}$ (b) Bounded to $(0.50, 1.50)\eta_{RV_i}$

Figure 7.15: Tornado diagrams for the mode II fracture

7.4.2.2 Uncertainty Quantification

The sensitivity analysis having identified the three most sensitive parameters: c, ϕ_f and G_F^{II} the uncertainties associated with them will be quantified next. Again, a total of $m = 1,000$ analyses are performed for each one of them. Two cases are considered. First, the 13 parameters are kept constant, and the one investigated is drawn randomly through a LHS, Table 7.1. In the second

case, in each one of the 1,000 analysis 10 RV are randomly selected.

Single RV: Figure 7.16 shows the variability in the capacity curves, and in all three cases the curves are both smooth and nearly identical. The dispersion of the applied shear displacement (here as IM) along the joint opening (as EDP) is nearly constant and approximately 10% at most.

Finally, the fragility curves (probability of fracture for different RVs), where fracture is defined as the point where the slope of the capacity curve is about 2% the initial one. In all thee cases the fragility curves have nearly identical median, $\hat{\eta}$ =0.70; and the dispersion $\hat{\beta}$ are very close [0.08-0.10]. Finally, in all cases, the fitted fragility curve matches well with the empirical data points.

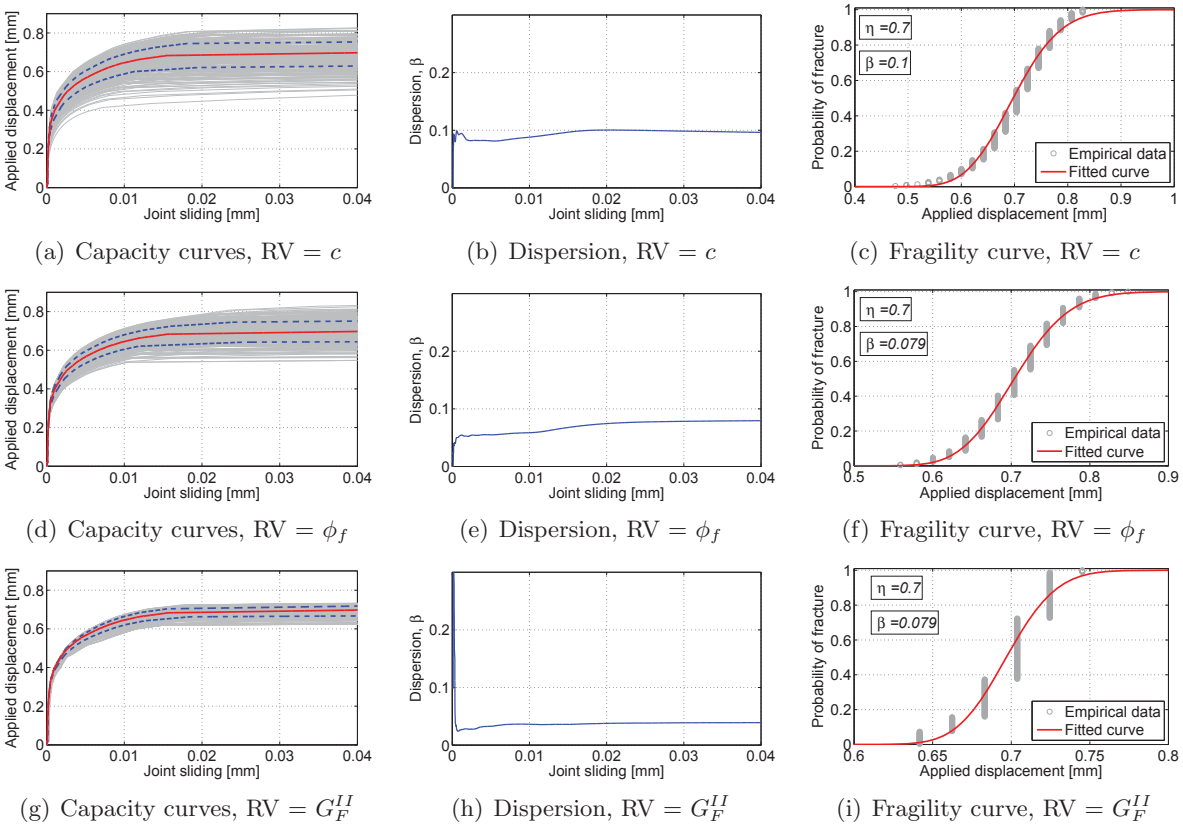

(a) Capacity curves, RV = c (b) Dispersion, RV = c (c) Fragility curve, RV = c

(d) Capacity curves, RV = ϕ_f (e) Dispersion, RV = ϕ_f (f) Fragility curve, RV = ϕ_f

(g) Capacity curves, RV = G_F^{II} (h) Dispersion, RV = G_F^{II} (i) Fragility curve, RV = G_F^{II}

Figure 7.16: Uncertainty quantification for single RVs under the mode II fracture

Multiple RVs: Similar to the mode I, the correlated (Table 7.2) and uncorrelated RVs are inves-

tigated for mode II. Figure 7.17 compares the uncertainty quantification with and without correlation effect. In both cases, the capacity functions are quit similar, while there is a discontinuity in the dispersion curve for the un-correlated condition. The median of the two fragility curves are identical and the dispersion of un-correlated RVs is slightly higher than the other one. This is due to the dominant role of ϕ_f and c in Mode II. Hence, and contrarily to the Mode I case, having correlated RVs does not improve the fragility curve (nearly identical dispersion).

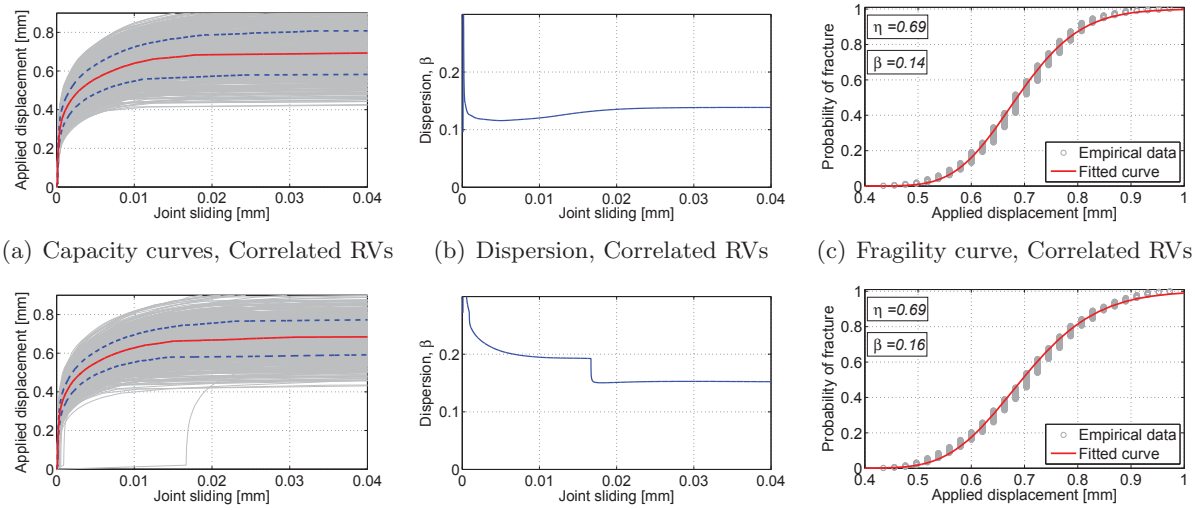

(a) Capacity curves, Correlated RVs (b) Dispersion, Correlated RVs (c) Fragility curve, Correlated RVs

(d) Capacity curves, Uncorrelated RVs (e) Dispersion, Uncorrelated RVs (f) Fragility curve, Uncorrelated RVs

Figure 7.17: Impact of RV correlation on the uncertainty quantification of the mode II fracture

Finally, figure 7.18 compares all the individual, correlated and un-correlated fragility curves for mode II fracture. Considering all the uncertainties together ends up with the wider fragility curve compared to the individual ones. All the fragility curves pass the <∼0.7, ∼0.5> coordinate on the IM - P [FRAC|IM] system.

7.4.3 Mixed-Mode Fracture

Having examined two highly idealized cases, attention is now turned to a mixed mode crack propagation in a real structure: a concrete dam subjected to seismic loading, figure 7.5(c). In this

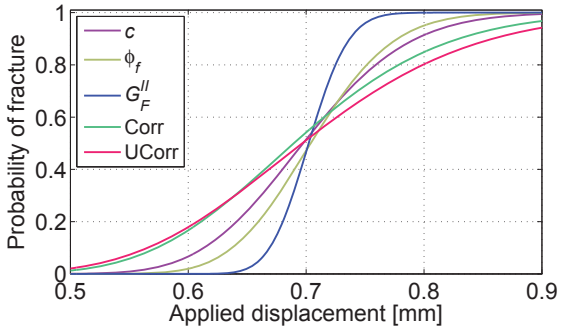

Figure 7.18: Comparison of different fragility curves for mode II fracture

case response is governed by the one of the zero thickness interface elements between the concrete and the rock. Variables associated with the joint have already been reported in Table 7.1 and Table 7.3 shows the RVs associated with concrete and rock. Four of them will be added to the list of 13 RVs: E_c, ν_c, ρ_c, and E_f for a complete assessment.

Table 7.3: Characteristics of concrete and rock

Characteristics	Symbol	Unit	Mean	COV	[Lower, Upper]
Concrete modulus of elasticity	E_c	GPa	22.4	0.15	[15.6, 29.1]
Concrete Poisson's ratio	ν_c	-	0.2	0.15	[0.14, 0.26]
Concrete tensile strength	f'_{t_c}	MPa	2.24	0.20	[1.12, 3.36]
Concrete mass density	ρ_c	kg/m^3	2500	0.10	[2000, 3000]
Foundation modulus of elasticity	E_f	GPa	24.0	0.15	[16.8, 31.2]
Foundation Poisson's ratio	ν_f	-	0.25	0.15	[0.18, 0.32]

7.4.3.1 Sensitivity Assessment

Sensitivity analysis will be performed for 12 RVs for the joint ($u_{D_{max}}$ and γ were left out in light of their limited contribution), and the four elastic proprieties of the concrete and rock. Thus, $2 \times 16 + 1 = 33$ observations are required.

In the spirit of this probabilistic-based fracture mechanics investigation, three separate acceleration functions are considered within the framework of the so-called Endurance Time Analysis (Hariri-Ardebili and Saouma, 2014). This method uses 3 dynamic analyses for each case and then takes the mean response. Hence the original 33 models have to be analyzed three times each

resulting in 99 nonlinear transient analyses. In this case, the boundary limit is $[0.66\eta_{RV_i}, 1.33\eta_{RV_i}]$.

The essence of the ETA procedure starts with the generation of an artificial acceleration function in which the peak ground acceleration (PGA) and spectral acceleration $S_a(T)$ are nearly linearly increasing with time Estekanchi et al. (2007). Hence, analysis proceeds until fracture occurs. Figure 7.19(a) shows the EDP (in this case the crest displacement δ) in terms of the time. Next, the maximum absolute value of the EDP is plotted versus time, resulting in the ETA curve, figure 7.19(b). In the third step the axes are switched, and time is replaced by PGA Hariri-Ardebili et al. (2014b), figure 7.19. Finally, the average of the three capacity curves is adopted.

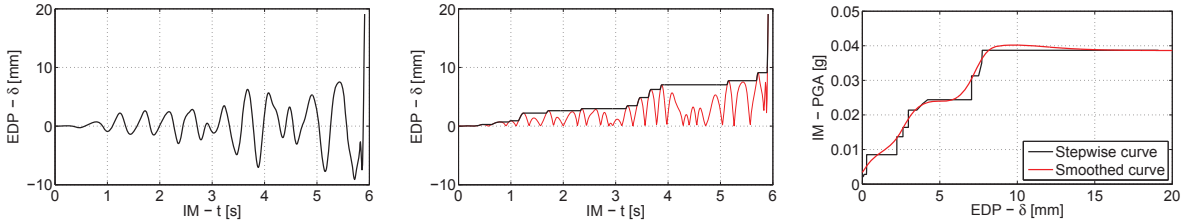

(a) Step 1: Transient analysis (b) Step 2: ETA curve (c) Step 3: Capacity curve

Figure 7.19: Steps toward deriving a continues capacity curve using ETA

Based on the mean response of the three analyses, the tornado diagram is determined in figure 7.20. A major difference with the preceding two tornado diagrams (figure 7.8 and 7.15) nearly all parameters are equally important. This implies that there are no redundant parameters in the examined model.

7.4.3.2 Control the Sensitivity Analysis

The results of the sensitivity analysis are controlled using a real ground motion explicitly. For this purpose single record incremental dynamic analysis technique is used. Analyses are performed in two groups: 1) Constant boundary limitation for RVs, while the intensity of ground motion is increased in 4 increments; 2) Constant ground motion intensity, while the variation of RVs is changed in 3 levels. Each set of sensitivity assessment requires $2 \times N_{RV} + 1$ =33 and thus totally N_{anlz} =198 nonlinear transient analyses. The 1967 Koynanagar earthquake caused significant

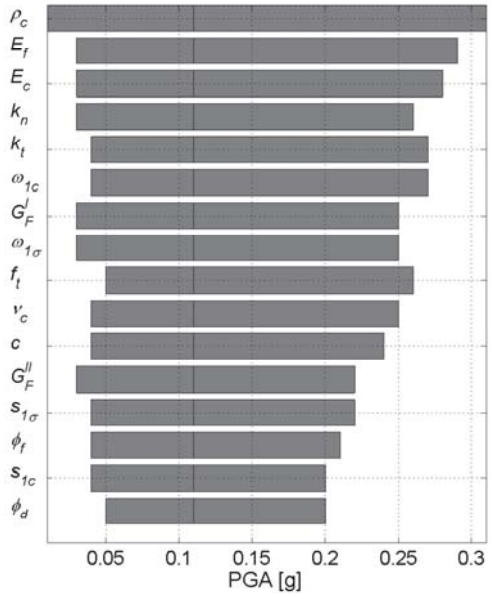

Figure 7.20: Tornado diagram for the mixed-mode fracture

structural damage to the Koyna gravity dam is used to shake the coupled system.

Considering that the system is analyzed in discrete points, the safety or failure of the dam is reported in each scenario, figure 7.21. The 6 studied packs are:

- Pack 1: Material variation $(1 \pm 0.33)\eta_{RV_i}$; ground motion PGA = 0.062 g.
- Pack 2: Material variation $(1 \pm 0.33)\eta_{RV_i}$; ground motion PGA = 0.125 g.
- Pack 3: Material variation $(1 \pm 0.33)\eta_{RV_i}$; ground motion PGA = 0.250 g.
- Pack 4: Material variation $(1 \pm 0.33)\eta_{RV_i}$; ground motion PGA = 0.500 g.
- Pack 5: Material variation $(1 \pm 0.17)\eta_{RV_i}$; ground motion PGA = 0.125 g.
- Pack 6: Material variation $(1 \pm 0.66)\eta_{RV_i}$; ground motion PGA = 0.125 g.

As expected, almost in all cases increasing the intensity of ground motion leads to more failed cases. Also increasing the material variation increase the failure probability. This figure is in good agreement with that reported in figure 7.20.

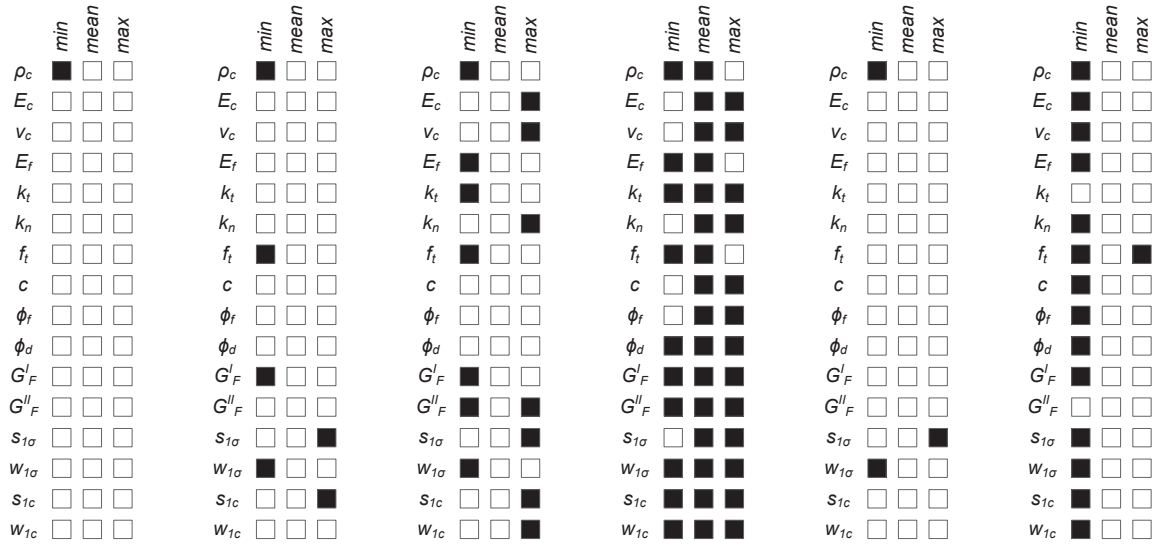

(a) Pack 1 (b) Pack 2 (c) Pack 3 (d) Pack 4 (e) Pack 5 (f) Pack 6

Figure 7.21: Sensitivity of the mixed-mode fracture under deterministic ground motion; B = failed, W = safe

7.4.3.3 Uncertainty Quantification

Since the preceding sensitivity analysis has determined that all RVs are nearly equally relevant, the uncertainty quantification will retain them all. For each set of uncertainty, 100 simulations are performed. The randomness in the target variable is sampled though LHS, Tables 7.1 and 7.3. Contrarily to the sensitivity analysis, the ETA method is limited to a single acceleration function in order to avoid aleatoric uncertainties to be mixed with epistemic ones. Again, two set of analyses will be reported. In the first one RV is sampled at a time, in the second, all the RVs are sampled simultaneously. Furthermore, whereas in the first two cases there was only a single LS which was failure, in the case of a dam, four of them are identified. They correspond to crack length over the total base. Four distinct ones are selected 10%, 30%, 60%, and 99% (Hariri-Ardebili and Saouma, 2014).

Single RV: It was determined that nearly all the fragility curves corresponding to a given LS_i ($i = 1, 2, 3, 4$) are identical. This confirms the results of sensitivity analysis in figure 7.20. To better quantify the results, the median and dispersion are separately shown in figure

7.22. It is noted that the median at LS=0.10 and LS=0.30 are almost identical for all RVs. The median at LS=0.60 and LS=0.99 vary for different RVs yet have the same trend. Another notable observation is that the dispersion of $RV1 = \rho_c$ is about twice the next highest one. This can be explained by the fact that in the context of the seismic analysis, proper evaluation of the mass is essential.

Multiple RV: Correlated and uncorrelated RVs when they are all modified simultaneously is shown in figure 7.23. It is clear that in this process the range of capacity curves go from nearly zero to a maximum. The former is induced by a random selection of unfavorable RVs across the board. Examination of the damage index reveals that higher PGAs are needed to trigger larger limit states. Results for correlated an uncorrelated values are nearly identical. The fragility curves confirm the brittle nature of the problem, where difference between LS=0.10 and 0.30 is small; however the one between 0.30 and 0.60 is substantially larger. Accounting for correlation reduces the dispersion of fragility curves, Table 7.4.

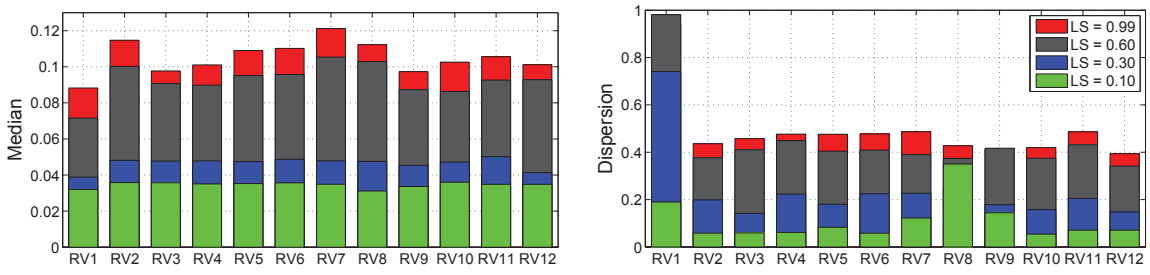

(a) Median (b) Dispersion

Figure 7.22: Comparison of all RVs for four LSs under mixed-mode fracture condition

Table 7.4: Dispersions β of dam analyses

LS	0.10	0.30	0.60	0.99
Correlated	0.78	0.82	1.03	1.06
Un-correlated	0.85	0.91	1.21	1.12

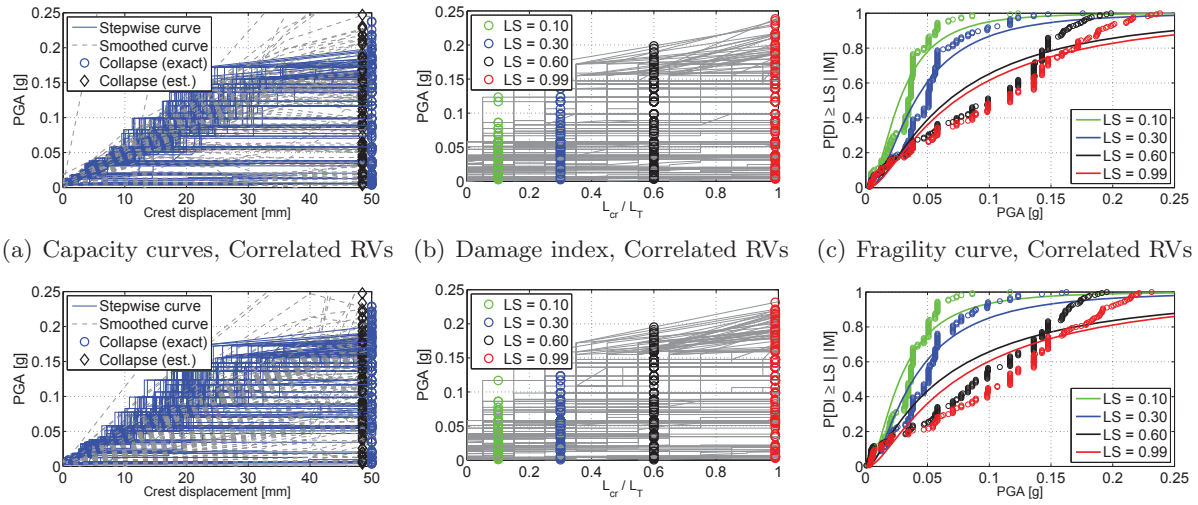

(a) Capacity curves, Correlated RVs (b) Damage index, Correlated RVs (c) Fragility curve, Correlated RVs

(d) Capacity curves, Uncorrelated RVs (e) Damage index, Uncorrelated RVs (f) Fragility curve, Uncorrelated RVs

Figure 7.23: Impact of RV correlation on the uncertainty quantification of the mixed-mode fracture

7.5 Conclusions

This paper was an attempt to elucidate the importance of the fourteen parameters defining a fracture mechanics based zero thickness cohesive crack model. This is achieved within the framework of a rigorous probabilistic approach.

Most of the results confirm what may be intuitively guessed, the procedure quantifies for the first time their importance. Among the other unanticipated conclusions, one can mention:

(1) The bi- and tri-linear form of the capacity curve in mode I fracture *vs.* the smoothed curve for Mode II fracture.

(2) Importance of the boundary variation, $(1-e, 1+e)\eta_{RV_i}$, for Mode I fracture, while it does not affect the tornado diagram in Mode II fracture.

(3) Four completely different form of capacity curves in Mode I, while all curves in Mode II are nearly identical.

(4) There is a discontinuity in dispersion curves of the Mode I, while they are uniform in Mode II.

(5) Better correlation of fitted fragility curve and the empirical data points in Mode II single RVs than Mode I.

(6) Priority in using correlated RVs than to un-correlated one for Mode I and mixed-mode fracture, while its effect is negligible in Mode II.

(7) Determining 5 most sensitive RVs in Mode I and 3 in Mode II; however, in mixed mode all of the RVs are nearly important.

Chapter 8

Probabilistic Seismic Demand Model for Gravity Dams

This chapter is based on:

Hariri-Ardebili, M.A. and Saouma, V.E., (2015), Probabilistic Seismic Demand Model and Optimal Intensity Measure for Concrete Dams (submitted to Structural Safety)

8.1 Introduction

In the context of performance-based earthquake engineering (PBEE) (Porter, 2003) ultimately one seeks to determine the fragility curve (Porter et al., 2007) which is the conditional probability statement of the likelihood that the structural system will exceed a damage state (DS) or even a specified level of engineering demand parameter (EDP) given the intensity measure (IM). The EDP is the outcome of a nonlinear transient finite element analysis performed on the basis of an excitation governed by the IM.

Probabilistic seismic demand model (PSDM) is a conditional probability statement that expresses the probability that a system (dam-foundation coupled system in the present paper) or any of the structural components experiences a certain level of demand (D) for a given IM level, $P[D \geq d|IM]$ (Padgett et al., 2008). A PSDM is a result of probabilistic seismic demand analysis (PSDA), which is the coupling of probabilistic seismic hazard analysis (PSHA) and nonlinear structural analysis (Shome et al., 1998). A PSDA can be summarized in the following steps: 1) selection of a set of ground motion records based on PSHA, 2) determination of the local and global EDPs for

the structure, 3) preparation of nonlinear finite element model, 4) performing nonlinear transient analyses, and 5) establishing a PSDM for the system.

The outcome of PSDA is a seismic fragility curves and selection of optimal IM parameter. PSDA and PSDM supporting theories can be found in Shome (1999), Luco (2002) and Jalayer (2003). Advanced IM and selection of optimal ones have been addressed by a number of researchers Tothong and Luco (2007), Padgett et al. (2008), Baker and Cornell (2008). PSDM in turn has been applied to steel moment-resisting frame (Barroso and Winterstein, 2002), reinforced-concrete frame buildings (Jankovic and Stojadinovic, 2004), (Ramamoorthy et al., 2006), reinforced-concrete shear wall (Tang and Zhang, 2011), highway bridges (Mackie and Stojadinovic, 2001), (Bisadi et al., 2012), curved concrete bridges (Tondini and Stojadinovic, 2012), and un-anchored steel storage tanks (Berahman and Behnamfar, 2009).

In the present paper, a probabilistic seismic demand model is proposed for concrete dams. This approach is performed within the context of a cloud analysis (i.e. a multitude of probabilistically defined input data) (Jalayer, 2003). From such an analysis, optimal IM (in term of efficiency, practicality, proficiency, sufficiency, and hazard compatibility) is selected for Pine Flat gravity dam, and the seismic fragility curves built.

8.2 Theory; Background

Given the importance of a properly defined IM, this will be critically reviewed in this section. Subsequently, the essence of cloud analysis within the context of PSDM will be addressed.

8.2.1 Time-Dependent Function IM

General formulas have been proposed to represent the intensity of a time-dependent function ($f(t)$, $t \subseteq [0, t_{tot}]$ where t_{tot} refers to the total duration of the function Riddell (2007). For the purpose of this study, $f(t)$ is defined to be either: 1) a time-dependent ground motion characteristics (such as acceleration, velocity and displacement), or 2) a frequency-dependent ground motion characteristics (such as acceleration, velocity and displacement response spectra).

The intensity measure relations for a raw function are given by Riddell (2007)

$$\begin{aligned} f_{peak} &= max(|f(t)|) \\ f_{sum} &= \int_{t_1}^{t_2} f(t)dt \\ f_{sum}^{abs} &= \int_{t_1}^{t_2} |f(t)|\, dt \\ f_{avg} &= \frac{1}{t_2 - t_1} \int_{t_1}^{t_2} f(t)dt \end{aligned} \tag{8.1}$$

where t_1 and t_2 refer to specific duration ($t_2 > t_1$).

For oscillatory $f(t)$ we define

$$\begin{aligned} f_{sum}^{sqr} &= \int_{t_1}^{t_2} (f(t))^2 dt \\ f_{avg}^{sqr} &= \frac{1}{t_2 - t_1} \int_{t_1}^{t_2} (f(t))^2 dt \end{aligned} \tag{8.2}$$

When Eqs. 8.1 and 8.2 are integrated from t_0 to t_{tot} they yield a single scalar quantity (this is generally the case when the full ground motion record is used). On the other hand, if integration is carried between t_0 and an arbitrary t_i then a vector results. This is the case when artificial function, e.g. endurance time acceleration function (ETAF) are used (Hariri-Ardebili et al., 2014b), figure 8.1.

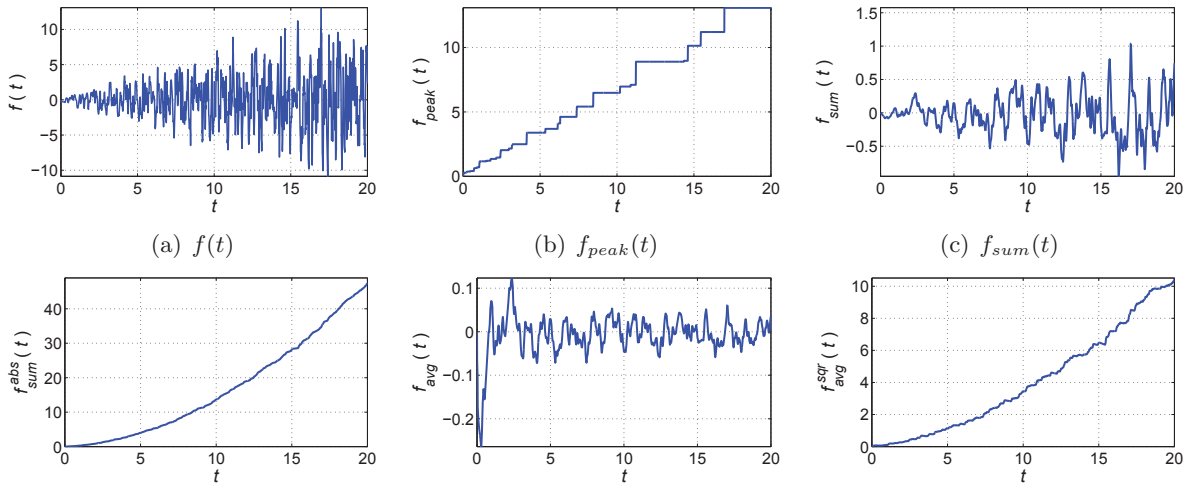

(a) $f(t)$ (b) $f_{peak}(t)$ (c) $f_{sum}(t)$

(d) f_{sum}^{abs} (e) f_{avg} (f) f_{avg}^{sqr}

Figure 8.1: Different time-dependent representation of IM for a sample ETAF based on Eqs. 8.1 and 8.2

8.2.2 Ground Motion Based IM

The first step in PBEE consists in the definition of ground motion IM. Since various authors have proposed a variety of IM (mostly in the context of buildings) this section first reviews the seven most important categories, and then select those most applicable to concrete dams.

8.2.2.1 Category I: Unscalable IMs

In this case, the IMs are independent from both the ground motion scaling methods and the characteristics of the target structure. These are: earthquake magnitude, M, epicentral distance, R_{epi}, hypocentral distance, R_{hypo}, ground motion duration, t_{tot}, and significant duration, t_{sig}. Significant duration is a measure of strong ground motion part and usually refers to a portion of ground motion which includes about 90% of the energy. The most common form for t_{sig} is:

$$t_{sig} = t_{0.95I_A} - t_{0.05I_A} \tag{8.3}$$

where I_A refers to the Arias intensity of the ground motion record. t_{sig} is also shown as D_{5-95}.

Another intensity measure that seismologists often adopt is D_{5-75}. It is similar to Eq. 8.3, as it is assumed that D_{5-75} is a more accurate measure for the most significant part of the ground motion.

8.2.2.2 Category II: Ground Motion Dependent Scalar IMs

Peak Values The most widely used IM is the peak ground acceleration (PGA). Not only is used in hazard maps but attenuation relations are usually available in terms of PGA. Peak ground velocity (PGV) and peak ground displacement (PGD) are other typical single-parameter scalar IMs. Hao et al. (2005) found that PGV correlates to damage better than PGA (of Construction, 2000).

$$\begin{aligned} \text{PGA} &= max\left(|\ddot{u}(t)|\right) \\ \text{PGV} &= max\left(|\dot{u}(t)|\right) \\ \text{PGD} &= max\left(|u(t)|\right) \end{aligned} \tag{8.4}$$

where $\ddot{u}(t)$, $\dot{u}(t)$, and $u(t)$ refer to the acceleration, velocity and displacement time history of the ground motion record, respectively.

Root-mean-square $(.)_{rms}$ of acceleration, a_{RMS}, velocity, v_{RMS}, and displacement, u_{RMS}, are used as a measure of effective $F(t)$ acceleration (or velocity or displacement) of a ground motion time-history

$$(..)_{RMS} = \left(\frac{1}{t_{tot}} \int_0^{t_{tot}} ((.)(t))^2 dt \right)^{1/2} \tag{8.5}$$

A set of intensity measures similar to Eq. 8.5, which do not account for the average values (shown in the denominator of the previous equation) and neglecting the damping ratio was also proposed (Nau and Hall, 1982)

$$\begin{aligned} a_{rs} &= \left(\underbrace{\int_0^{t_{tot}} (\ddot{u}(t))^2 dt}_{E_a} \right)^{1/2} \\ v_{rs} &= \left(\underbrace{\int_0^{t_{tot}} (\dot{u}(t))^2 dt}_{E_v} \right)^{1/2} \\ u_{rs} &= \left(\underbrace{\int_0^{t_{tot}} (u(t))^2 dt}_{E_d} \right)^{1/2} \end{aligned} \tag{8.6}$$

Arias Intensity is a measure of dissipated energy per unit mass in an elasto-plastic system (Arias A., 1970)

$$I_A(\xi) = \frac{\cos^{-1}\xi}{g\sqrt{1-\xi^2}} \int_0^{t_{tot}} (\ddot{u}(t))^2 dt \tag{8.7}$$

where ξ is the damping ratio of a structure and g the gravitational acceleration. In the standardized form, I_A with zero damping yields

$$I_A = \frac{\pi}{2g} \int_0^{t_{tot}} (\ddot{u}(t))^2 dt \tag{8.8}$$

Destructiveness Potential Although the original (and standardized) I_A accounts for the ground motion peak and duration, the frequency characteristics are somehow neglected. Araya

and Saragoni (1984) proposed a factor that measures the destructiveness potential, P_D, or capacity to induce structural damage.

$$P_D = \frac{I_A}{\upsilon_0^2} \tag{8.9}$$

where υ_0 is the number of zero-crossings occurrence of the ground motion record per unit time.

Specific Energy Density, SED, measures the total energy of the ground motion:

$$SED = \int_0^{t_{tot}} (\dot{u}(t))^2 dt \tag{8.10}$$

Since SED is calculated from the velocity time history, the general trend of mean values is not as smooth as the other parameters.

Cumulative Absolute Velocity, CAV, defined as the integral of the absolute value of the acceleration time series (EPRI-NP-5930, 1988)

$$CAV = \int_0^{t_{tot}} |\ddot{u}(t)|\, dt \tag{8.11}$$

CAV is the IM that best correlates with the onset of damage. However it should be noted that CAV does not account for the mismatch of arrival time for different energy phases. This is the case for large velocity pulse (Campbell and Bozorgnia, 2010). The Electrical Power Research Institute (EPRI) introduced a standardized version of CAV_{STD} that prevents contribution of the low-amplitude, non-damaging ground motions (EPRI-1014099, 2006)

$$CAV_{STD} = \sum_{i=1}^{N} \left(H(PGA_i - \ddot{u}_{min}) \int_{i-1}^{i} |a(t)|\, dt \right), \quad H(\delta) = \begin{cases} 0 & \delta < 0 \\ 1 & \delta \geq 0 \end{cases}$$

where N is the number of non-overlapping one-second time intervals, PGA_i is the peak ground acceleration (in term of g) in i^{th} time interval (inclusive of the first and last points), $\ddot{u}_{min}$ is an acceleration threshold (user-defined, but usually taken as $0.025g$) to exclude low amplitude motions contributing to the sum, $H(x)$ is the Heaviside step function.

Cumulative Absolute Displacement, CAD, is defined in a similar way to CAV (Mackie and Stojadinovic, 2003)

$$CAD = \int_0^{t_{tot}} |\dot{u}(t)|\, dt \tag{8.12}$$

Sustained Values The absolute values of highest accelerations that sustained for 3 and 5 cycles in acceleration time history are defined as 3-cycle sustained and 5-cycle sustained maximum accelerations, SMA, respectively. A similar concept is applicable to the velocity time history which results in sustained maximum velocity, SMV (Nuttli, 1979).

8.2.2.3 Category III: Ground Motion Dependent Compound IMs

A generalization of the previously addressed scalar IM, is one which considers the IM to be a vectorial quantity.

$$IM_{com} = C_{com}\,(\mathrm{PGA})^{\beta_1}\,(\mathrm{PGV})^{\beta_2}\,(\mathrm{PGD})^{\beta_3}\,(a_{RMS})^{\beta_4}\,(v_{RMS})^{\beta_5}\,(u_{RMS})^{\beta_6}\,(I_A)^{\beta_7}\,(t_{sig})^{\beta_8} \tag{8.13}$$

where β_i, $i = 1, ..., 8$ are effectively weight coefficients associated with each of the IMs, and C_{com} a pre-multiplying factor.

Some of the most commonly representation for IM_{com} include the following:

Velocity to Acceleration Ratio is probably the most commonly used one and is expressed in terms of PGV and PGA. It is the simplest method to categorize near-fault pulse-like ground motions.

$$\begin{aligned} I_{v/a} &= (PGA)^{-1}\,(PGV)^{+1} \\ I_{v^2/a} &= (PGA)^{-1}\,(PGV)^{+2} \end{aligned} \tag{8.14}$$

Characteristic Intensity, I_C, is defined by Park et al. (1985)

$$I_C = (a_{RMS})^{+3/2}\,(t_{sig})^{+1/2} \tag{8.15}$$

Riddell-Garcia Intensity proposed a set of compound IMs that minimize dispersion of hysteretic energy-dissipation spectra of inelastic systems (Riddell and Garcia, 2001)

$$\begin{aligned} I_a &= (PGA)^{+1}\,(t_{sig})^{+1/3} \\ I_v &= (PGV)^{+2/3}\,(t_{sig})^{+1/3} \\ I_d &= (PGD)^{+1}\,(t_{sig})^{+1/3} \end{aligned} \tag{8.16}$$

Fajfar Intensity is a compound IM that takes into account the damage capacity of medium-period structures (Fajfar et al., 1990)

$$I_F = (PGV)^{+1} (t_{sig})^{+1/4} \tag{8.17}$$

Cosenza-Manfredi Intensity, I_D, accounts for the number of plastic cycles or equivalently the energy content of the earthquake (Cosenza and Manfredi, 1997). This is a dimensionless IM defined by

$$I_D = \frac{2g}{\pi} (PGA)^{-1} (PGV)^{-1} (I_A)^{+1} \tag{8.18}$$

Shaking Intensity Rate, SIR, applicable for liquefaction-induced building settlements (Dashti et al., 2009). It represents the rate of earthquake energy buildup:

$$SIR = \frac{I_{A5-75}}{D_{5-75}} \tag{8.19}$$

where I_{A5-75} is the change in Arias intensity from 5 to 75% of its total value, and D_{5-75} is its corresponding time duration.

8.2.2.4 Category VI: Structure-Independent Spectral IMs

Bounded Spectrum Intensities These IMs are determined from the ground motion response spectra. In some cases, a specific period range is considered. Acceleration, ASI, velocity, VSI, and displacement DSI spectrum intensities are defined by (Bradley, 2011):

$$\begin{aligned} ASI &= \int_{0.1}^{0.5} S_a (T, \xi = 5\%)\, dT \\ VSI &= \int_{0.1}^{2.5} S_v (T, \xi = 5\%)\, dT \\ DSI &= \int_{2.0}^{5.0} S_d (T, \xi = 5\%)\, dT \end{aligned} \tag{8.20}$$

where S_a, S_v and S_d are the acceleration, velocity, and displacement response spectral, T the vibration period and ξ the damping ratio.

Housner Intensity, HI, is similar to VSI; however, the pseudo velocity spectrum, PS_v, is used instead of S_v (Housner, 1975):

$$HI = \int_{0.1}^{2.5} PS_v (T, \xi = 5\%)\, dT \tag{8.21}$$

Effective Peak Values Effective peak acceleration, EPA, and effective peak velocity, EPV first defined in ATC (1978) and modified in Kurama and Farrow (2003) as follows (note that the factor 2.5 is an empirical value):

$$\begin{aligned} EPA = &\quad \frac{1}{2.5} \times \frac{\int_{0.1}^{0.5} S_a\left(T, \xi = 5\%\right) dT}{0.4} \\ EPV = &\quad \frac{1}{2.5} \times \frac{\int_{0.8}^{1.2} S_v\left(T, \xi = 5\%\right) dT}{0.4} \end{aligned} \tag{8.22}$$

Improved Effective Peak Values Since the fixed period range for EPA and EPV does not account for the ground motion frequency content, and since the dominant period, T_P, of a response spectrum implicitly accounts for the frequency characteristics of the ground motions, the following expressions were proposed (Yang et al., 2009a)

$$\begin{aligned} IEPA = &\quad \frac{1}{2.5} \times \frac{\int_{T_P^a-0.2}^{T_P^a+0.2} S_a\left(T, \xi = 5\%\right) dT}{0.4} \\ IEPV = &\quad \frac{1}{2.5} \times \frac{\int_{T_P^v-0.2}^{T_P^v+0.2} S_v\left(T, \xi = 5\%\right) dT}{0.4} \end{aligned} \tag{8.23}$$

where T_P^a and T_P^v are the periods where the spectral acceleration, S_a, and spectral velocity, S_v, reach the maximum value, respectively.

8.2.2.5 Category V: Structure-Dependent Spectral IMs

This set of IM parameters are derived from response spectrum of the ground motion while accounting for the natural periods of the target structure.

Single-Period Intensities are the most commonly used structure-dependent spectral IMs. They are expressed in terms of $S_a(T_1, \xi = 5\%)$, $S_v(T_1, \xi = 5\%)$ and $S_d(T_1, \xi = 5\%)$ in which T_1 is the first-natural period of the structure. Moreover, spectral acceleration of some specific modes are of interest such as: $S_a(T = T_P, \xi = 5\%)$, $S_a(T = 0.2, \xi = 5\%)$ and $S_a(T = 1.0, \xi = 5\%)$. Critical T values are 0.2 and 1.0 s as they are often used in design codes.

Cordova Intensity A limitation of the previous case is the significant variability in the level of structural response in a MDOF system (Shome et al., 1998). $S_a(T_1, \xi = 5\%)$ does not account for the higher-order vibration modes and so is not appropriate for structures sensitive to higher

modes. Hence, an improved two-parameter scalar IM that accounts for the period lengthening is given by (Cordova et al., 2001)

$$S_a^* = \left(S_a\left(T_1, \xi\right)\right)^{1-\alpha} \left(S_a\left(c.T_1, \xi\right)\right)^{\alpha} \tag{8.24}$$

where c and α are two parameters to be calibrated; however, usually taken to be 2.0 and 0.5, respectively.

Vamvatsikos Intensity Vamvatsikos and Cornel (2005) proposed an IM which considers the participation of higher-order vibration modes as:

$$\begin{aligned} \overline{S_a} &= \left(S_a\left(T_a, \xi = 5\%\right)\right)^{1-\alpha} \left(S_a\left(T_b, \xi = 5\%\right)\right)^{\alpha} \\ \overline{\overline{S_a}} &= \left(S_a\left(T_a, \xi = 5\%\right)\right)^{1-\beta-\gamma} \left(S_a\left(T_b, \xi = 5\%\right)\right)^{\beta} \left(S_a\left(T_c, \xi = 5\%\right)\right)^{\gamma} \end{aligned} \tag{8.25}$$

where T_a, T_b and T_c are arbitrary periods and α, β, $\gamma \in [0, 1]$ are obtained by system identification with $\beta + \gamma \leq 1$.

Multiple-Period Intensities is primarily used for high-rise building structures (Zhou et al., 2012) and accounts for both the higher-order modes and the effective mass at each mode. Considering the first two vibration modes, the combined intensity measures can be expressed as:

$$S_a^{1\&2} = \left(S_a\left(T_1, \xi\right)\right)^{\alpha'} \left(S_a\left(T_2, \xi\right)\right)^{\beta'}, \quad \alpha' = \frac{m_1^{eff}}{m_1^{eff} + m_2^{eff}}, \quad \beta' = \frac{m_2^{eff}}{m_1^{eff} + m_2^{eff}} \tag{8.26}$$

where α' and β' are the ratios of effective mass and m_i^{eff}, $i = 1, 2, 3$ is the effective masses for the i^{th} mode.

Hariri-Saouma Intensity (Modified Multiple-period Intensity) In the case that multiple vibration modes contribute in the general vibration behavior of the structural system, the effects of the all those modes can be considered in the combined spectral value-based IM:

$$S_a^{1-to-N} = \sum_{i=1}^{N} \left(S_a\left(T_i, \xi\right)\right)^{\alpha_i}, \quad \alpha_i = \frac{m_i^{eff}}{\sum_{j=1}^{N} m_i^{eff}} \tag{8.27}$$

where N is the number of the effective modes, T_i is the period of the i^{th} mode, and α_i is the ratio of effective masses. Note that in the case that N=1, S_a^{1-to-N} yields to $S_a\left(T_i, \xi\right)$.

8.2.2.6 Category VI: Vector-Based IMs

Vector-based IMs are defined in terms of two or more parameters (Bojorquez et al., 2012).

Vamvatsikos Vector-Based Intensity uses a combination of a scalable and one scaling-independent IM Vamvatsikos and Cornel (2005). The scalable component is $S_a\left(T_1,\xi\right)$, while the spectral ratio, $R_{sa}\left(\kappa,T_1,\xi\right)$, is the non-scalable one.

$$\left\langle S_a\left(T_1,\xi\right),R_{sa}\left(\kappa,T_1,\xi\right)\right\rangle=\left\langle S_a\left(T_1,\xi\right),\frac{S_a\left(\kappa T_1,\xi\right)}{S_a\left(T_1,\xi\right)}\right\rangle \tag{8.28}$$

where κ is a constant factor, usually 1.5.

Baker Intensity has a scalable parameter given by $S_a(T_1)$ and a scaling independent one that is typically the magnitude, M_w, distance, R, or epsilon, ϵ (Baker and Cornell, 2005). It is found that $\left\langle S_a\left(T_1,\xi\right),\epsilon\right\rangle$ is significantly superior to $S_a(T_1)$ alone. ϵ is defined as the number of standard deviations by which an observed logarithmic spectral acceleration, $\ln S_a(T)$, differs from the mean logarithmic spectral acceleration, $\overline{\ln S_a(T)}$, of a ground-motion prediction equation.

Bojorquez Intensity uses a combination of $S_a\left(T_1,\xi\right)$ with other scalar IMs in order to determine the optimal vector IM Bojorquez et al. (2012). $\left\langle S_a\left(T_1,\xi\right),PGA\right\rangle$ and $\left\langle S_a\left(T_1,\xi\right),PGV\right\rangle$ are used as indicators of the peak responses of the structural system. $\left\langle S_a\left(T_1,\xi\right),t_{sig}\right\rangle$ and $\left\langle S_a\left(T_1,\xi\right),I_D\right\rangle$ are used as indicator of combination of peaks and cumulative damage potential of ground motions.

$$\begin{aligned}\left\langle S_a\left(T_1,\xi\right),R_{T_1,T_2}\right\rangle\ ,\quad R_{T_1,T_2}&=\frac{S_a(T_2)}{S_a(T_1)}\\ \left\langle S_a\left(T_1,\xi\right),N_p\right\rangle\ ,\quad N_p&=\frac{S_a\left(\left(\prod_{i=1}^{N}T_i\right)^{1/N},\xi\right)}{S_a(T_1,\xi)}\end{aligned} \tag{8.29}$$

8.2.2.7 Category VII: IM for Multiple-Component Ground Motions

All the scalar or vector-based IMs parameters introduced so far were determined for a single-component ground motion record. In multiple-component ground motions one determines an IM

for each one of them. Subsequently those values are averaged (Kostinakis et al., 2015).

$$\begin{aligned} \mathrm{IM_{art}} = & \quad \frac{1}{2}\sum_{i=1}^{2}\mathrm{IM}_i \\ \mathrm{IM_{geo}} = & \quad \left(\prod_{i=1}^{2}\mathrm{IM}_i\right)^{1/2} \\ \mathrm{IM_{srss}} = & \quad \left(\sum_{i=1}^{2}\mathrm{IM}_i^2\right)^{1/2} \\ \mathrm{IM_{max}} = & \quad max(\mathrm{IM}_i), i = 1, 2 \end{aligned} \tag{8.30}$$

8.2.3 Cloud Analysis

Cloud analysis is a numerical procedure in which first a structure is subjected to a set of (un-scaled or as-recorded) ground motions and is analyzed numerically. Then from the results, EDP *vs.* IM are determined and form the so-called cloud response. Results are usually plotted either on a arithmetic (figure 8.2(a)) or logarithmic (figure 8.2(b)) scale. In the logarithmic scale, scatter data points are usually linear trend implying a power curve in the arithmetic scale.

$$\eta_{\mathrm{EDP|IM}}(\mathrm{IM}) = a.(\mathrm{IM})^b \tag{8.31}$$

$$\ln\left(\eta_{\mathrm{EDP|IM}}(\mathrm{IM})\right) = b.\ln(\mathrm{IM}) + \ln(a) \tag{8.32}$$

where $\ln(a)$ and b are the linear regression constants and $\eta_{\mathrm{EDP|IM}}$ is the median value of EDP given IM.

Cloud analysis results can then be used to develop a PSDM (also known as fragility function) which is a relationship between peak EDP and ground motion IM (Cornell et al., 2002).

$$P\left[\mathrm{EDP} \geq edp|\mathrm{IM}\right] = 1 - \Phi\left(\frac{\ln(edp) - \ln(\eta_{\mathrm{EDP|IM}})}{\beta_{\mathrm{EDP|IM}}}\right) \tag{8.33}$$

where $\Phi(.)$ is the standard normal cumulative distribution function and $\beta_{\mathrm{EDP|IM}}$ the logarithmic standard deviation (also called dispersion) of the EDP conditioned on the IM. This model assumes that the conditional seismic demands has a lognormal distribution.

The logarithmic standard deviation is given by

$$\beta_{\mathrm{EDP|IM}} \cong \sqrt{\frac{\sum\left(\ln\left(edp_i\right) - \ln\left(a.\mathrm{IM}^b\right)\right)^2}{n-2}} \tag{8.34}$$

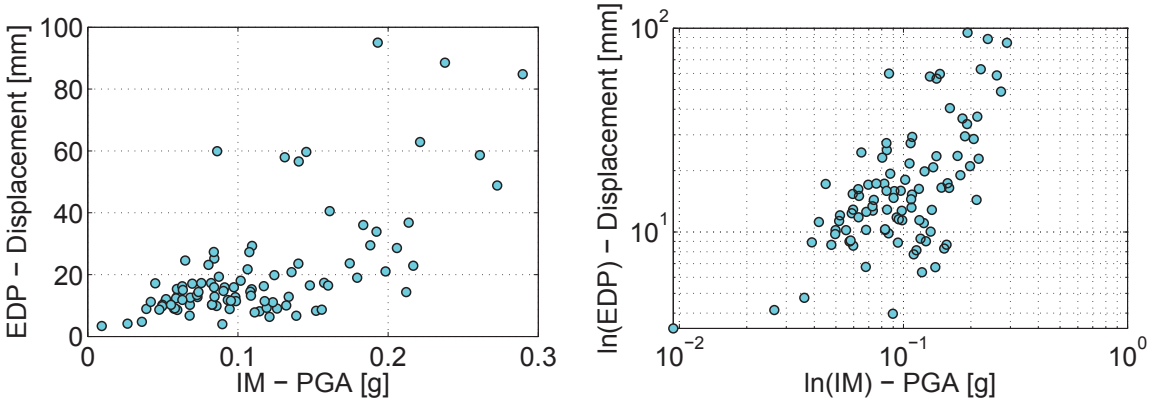

(a) Arithmetic scale (b) Logarithmic scale

Figure 8.2: Results of cloud analysis

and will be subsequently used as a metric for optimal IM selection. n is the number of nonlinear transient analyses resulting in figure 8.2. It should be recalled that

$$\beta_{\mathrm{EDP|IM}} = \sigma_{\ln(\mathrm{EDP})|\mathrm{IM}} \tag{8.35}$$

where the second terms is the corresponding standard deviation in the arithmetic scale.

Substituting Eq. 8.34 into 8.33 and expanding on the definition of Φ, the fragility function can be rewritten as:

$$P\left[\mathrm{EDP} \geq edp|\mathrm{IM}\right] = 1 - \int_0^{edp} \frac{1}{\sqrt{2\pi}\,.\,\beta_{\mathrm{EDP|IM}}\,.\,edp} \exp\left[-\frac{1}{2}\left(\frac{\ln(edp) - \ln(\eta_{\mathrm{EDP|IM}})}{\beta_{\mathrm{EDP|IM}}}\right)^2\right] \mathrm{d}\,edp \tag{8.36}$$

Should there be numerical failures in the set of n analysis, Eq. 8.33 has to be altered and an alternative expression of the fragility function has been suggested (Jalayer et al., 2007).

$$P\left[\mathrm{EDP} \geq edp|\mathrm{IM}\right] = P\left[\mathrm{EDP} \geq edp|\mathrm{IM}, \mathrm{NLg}\right].\left(1 - P\left[\mathrm{Lg}|\mathrm{IM}\right]\right) + P\left[\mathrm{Lg}|\mathrm{IM}\right] \tag{8.37}$$

where $P\left[\mathrm{Lg}|\mathrm{IM}\right]$ is the probability of having "very large" (Lg) EDP (such as about 10 mean) for a given IM. $P\left[\mathrm{EDP} \geq edp|\mathrm{IM}, \mathrm{NLg}\right]$ is the fragility function given "no very large" (NLg) EDP are present:

$$P\left[\mathrm{EDP} \geq edp|\mathrm{IM}, \mathrm{NLg}\right] = 1 - \Phi\left(\frac{\ln(edp) - \ln(\eta_{\mathrm{EDP|IM,NLg}})}{\beta_{\mathrm{EDP|IM,NLg}}}\right) \tag{8.38}$$

where $\eta_{\text{EDP|IM,NLg}}$ and $\beta_{\text{EDP|IM,NLg}}$ are median and logarithmic standard deviation of EDP given IM and NLg.

8.2.4 Criteria for an Optimal IM

Selection of optimal IM parameter for building structures should be based on Padgett et al. (2008), Tothong and Luco (2007):

Efficiency: Efficient IM parameter will reduce the EDP variability for a given IM (Giovenale et al., 2004). In other words, efficiency will simply lower the dispersion, $\beta_{\text{EDP|IM}}$ (Eq. 8.34) with respect to the estimated median for a set of nonlinear transient analyses. It is inversely proportional to efficiency.

Practicality: is an indicator of the correlation between an IM and the EDP (Padgett et al., 2008). Practicality can be measured by b in Eq. 8.32 (high values being indicative of increased practicality).

Proficiency: is a composite measure of efficiency and practicality. A more proficient IM would have lower modified dispersion, ζ (Padgett et al., 2008). Thus, substituting Eq. 8.32 into 8.33:

$$P\left[\text{EDP} \geq edp|\text{IM}\right] = \Phi\left(\frac{\ln(\text{IM}) - \frac{\ln(edp)-\ln(a)}{b}}{\zeta}\right), \quad \zeta = \frac{\beta_{\text{EDP|IM}}}{b} \tag{8.39}$$

Sufficiency: A sufficient IM is one in which the conditional probability distribution of EDP (for a given IM) is independent of seismic hazard parameters such as M_w, R_{rup}, ε and T_p (Tothong and Luco, 2007)

$$P\left[\text{EDP} \geq edp|\text{IM}\right] \cong P\left[\text{EDP} \geq edp|\text{IM}, \varepsilon, M_w, R_{rup}, T_p\right] \tag{8.40}$$

Sufficiency is quantified by the p-value which is the probability of rejecting the null hypothesis and thus proves independency of IM from other seismic hazard characteristics (M_w, R_{rup}, and ε). Higher p-value is a sign of sufficient IM. Numerically p-values are obtained

from linear regression of the residuals, $\epsilon^{\text{EDP}}|\text{IM}$:

$$\begin{aligned} \epsilon^{\text{EDP}}|\text{IM} = \quad & a_M + b_M(M_w) \\ \epsilon^{\text{EDP}}|\text{IM} = \quad & a_R + b_R(R_{rup}) \\ \epsilon^{\text{EDP}}|\text{IM} = \quad & a_\varepsilon + b_\varepsilon(\varepsilon) \end{aligned} \tag{8.41}$$

where a_i and b_i are the linear regression coefficients.

Hazard compatibility : Corresponds to the computational complexity in determining the hazard curve for a candidate IM (Giovenale et al., 2004). Currently, hazard curves are available in terms of PGA or $S_a(T)$, while the other IMs require more effort to be determined.

The first four criteria in PSDA can be holistically represented by figure 8.3.

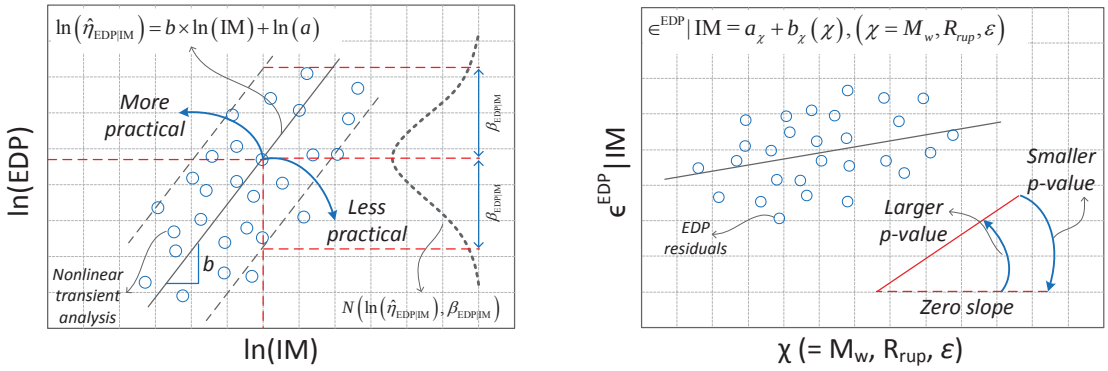

(a) Efficiency, practicality, proficiency (Padgett et al., 2008)

(b) EDP residuals, p-value and sufficiency

Figure 8.3: PSDM and criteria for optimal IM selection

8.3 Model and Ground motions

8.3.1 Dam Finite Element Model

Pine Flat Dam is a concrete gravity dam on the Kings River of central California in the United States. Figure 8.4 shows the cross section of the tallest non-overflow monolith. The finite element code Merlin (Saouma et al., 2010) is used for analysis. 4-node and 3-node plain strain 2D

elements are used for modeling the dam body and the foundation. Nonlinearity stems from the use of zero-thickness interface elements for modeling the discrete joints (Cervenka et al., 1998). Applied loads to the system are: 1) self-weight, 2) hydrostatic pressure, 3) uplift which is automatically updated with crack propagation, and 4) seismic loads. Hydrodynamic pressure is modeled based on Westergaard (Westergaard, 1933) added mass approach on both the dam upstream face and the foundation.

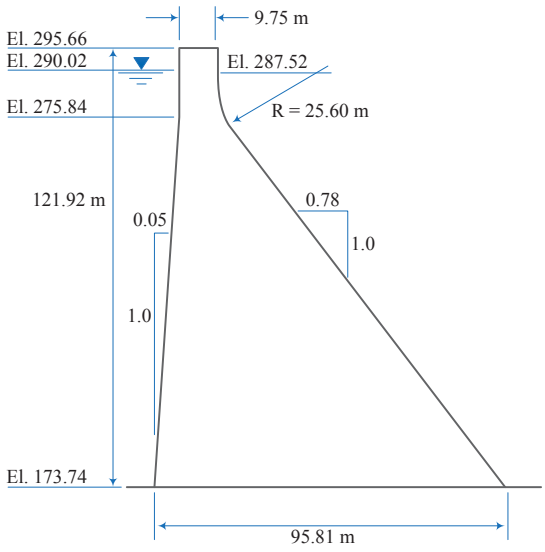

Figure 8.4: Tallest non-overflow monolith of Pine Flat dam (Løkke and Chopra, 2014)

Considering that the dam vibration characteristics are used to determine the structure-dependent IMs (Sec. 8.2.2.5), its natural periods are first extracted, figure 8.5.

8.3.2 Ground motion Characteristics

In order to investigate the seismic IM in concrete gravity dam, a large set of ground motions ($n = 100$) are selected. The unconditional (not dependent on structure natural periods) ground motion selection is adopted Baker and Jayaram (2008) and obtained form a Matlab-based code Jayaram et al. (2011). For smaller n, conditional mode would have been preferable. In the unconditional ground motion selection, the means and covariances are determined based on the

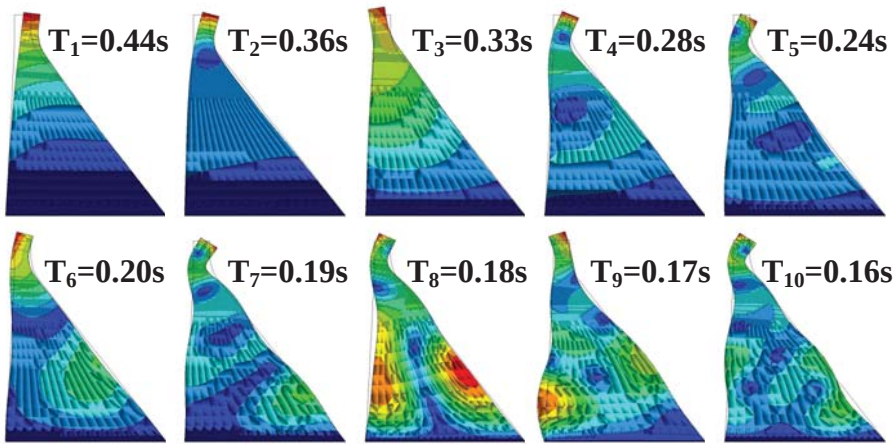

Figure 8.5: Mode shapes and natural period of dam

predefined target spectrum. A probabilistic seismic hazard analysis of Pine Flat Dam give:

- Site-to-source distance, $0 < R < 40$ km
- Magnitude, $5.5 < M_w < 7.0$
- Fault mechanism: Strike-slip
- Shear wave velocity, 360 m/s $< V_{S30} <$ 1500 m/s

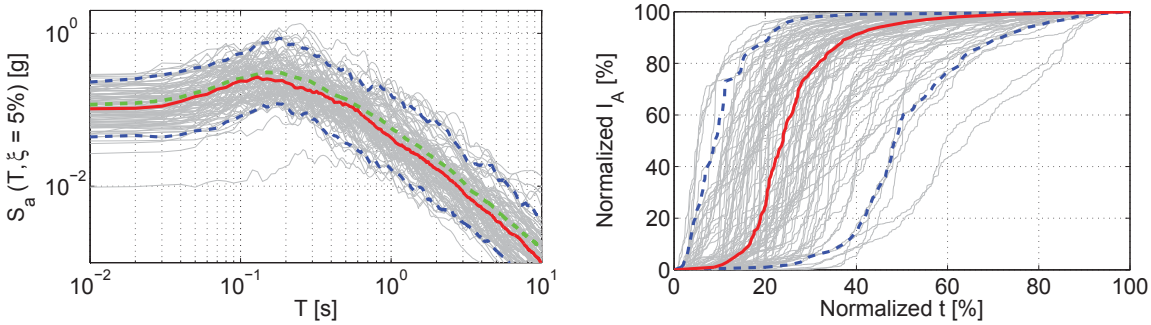

(a) Response spectra

(b) Normalized shape of Arias intensity

Figure 8.6: Time- and frequency-dependent characteristics of the selected ground motions; mean = green solid line, median = red solid line, 95% confidence interval = blue dashed line

Acceleration response spectra of the 100 ground motions, their mean, median and 95% confident intervals are shown in figure 8.6(a). Arias intensity, I_A, is the only IM parameter with the

capability of showing the ground motion intensity time history. Thus, normalized I_A is plotted in terms of normalized time in figure 8.6(b), as well as the median and the 95% confidence intervals. One may extract the exact I_A at any time knowing the final I_A value and the duration of motion. For the sake of completeness, a further characteristic of the selected ground motion is shown in figure 8.7. As in most cases, there is no statistical relationship between V_{S30} and M or R_{hypo}.

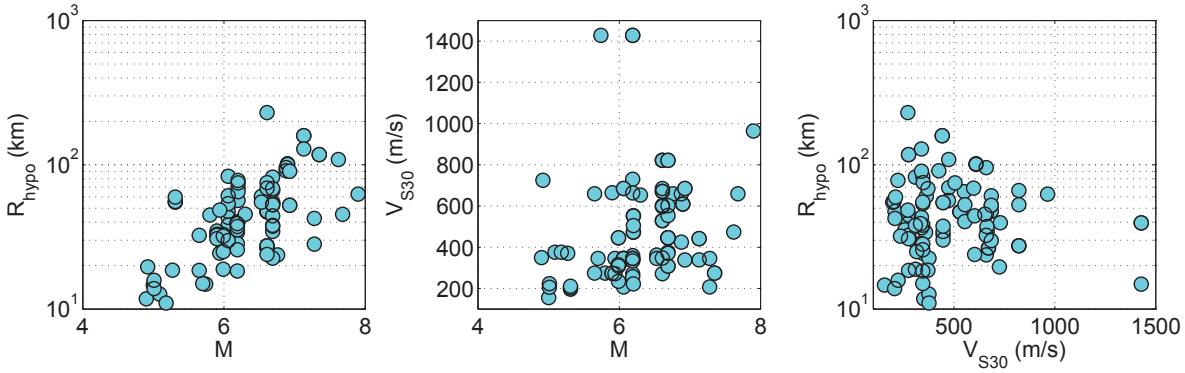

Figure 8.7: Relationship among M, R_{hypo}, V_{S30}

8.4 Results and Discussion

8.4.1 IM Distribution Models for Selected GMs

Sec. 8.2.2 defined seven broad categories of IMs; however, only the first five are considered. This will result in $C_1S_1N_8$, $C_2S_8N_{17}$, $C_3S_6N_9$, $C_4S_4N_7$, $C_5S_5N_{29}$ where C_i, S_j, and N_k refer to the ith category that has defined, j subcategories (italicized previously) and k total cases. This results in a total of 70 IMs being considered for the 100 ground motions selected in Sec. 8.3.2. For each one, a histogram is plotted and the most appropriate distribution model is fitted to the observed/computed data. The data are fitted through one of the following: 1) normal, 2) lognormal, 3) exponential, and 4) Weibull. The Anderson-Darling (AD) test (Anderson and Darling, 1954) is used to determine the most appropriate distribution type in each case. The application of the AD method requires the conversion of the resulting statistic to a uniform variable, p-value $\in$ [0,1) (Marsaglia and Marsaglia, 2004). The larger p-values for a given distribution, the better the fit. In addition to the most proper

distribution model, the second choice is also provided wherever is possible. Table 8.1 summarizes the optimal distributional model for each IM category, in conjunction with figures 8.8 to 8.12.

Table 8.1: Summary of optimal IM distributional models

Cat.	Fig.	Optimal Dist.	Observations
I	8.8	Varying	The normal distribution is found to be the best fit for M, Weibull for D_{5-75}, and lognormal distribution for the others. The pdf for Weibull distribution is (MATLAB, 2013): $y = f(x\|a,b) = ba^{-b}x^{b-1}e^{-\left(\frac{x}{a}\right)^b} I_{(0,\infty)}(x)$
II	8.9	LogN	For some IMs, specially those which are displacement-dependent, the fitting is relatively poor. In such cases, most of the observations are located in a narrow bound. For the rest of the models, normalized standard deviation vary between 0.5 and 0.6.
III	8.10	LogN	The displacement-related compound IMs exhibit a relatively poor fitting. I_d and SIR shows relatively high lognormal standard deviation.
VI	8.11	LogN	In most cases, the standard deviation fluctuates around 0.6. All the IM distribution follow an identical trend.
V	8.12	LogN	Using the spectral acceleration at different periods does not change the standard deviation. The contribution of the higher modes shifts the model from lognormal to normal. Incorporating the effective mass of the higher modes reduces the standard deviation.

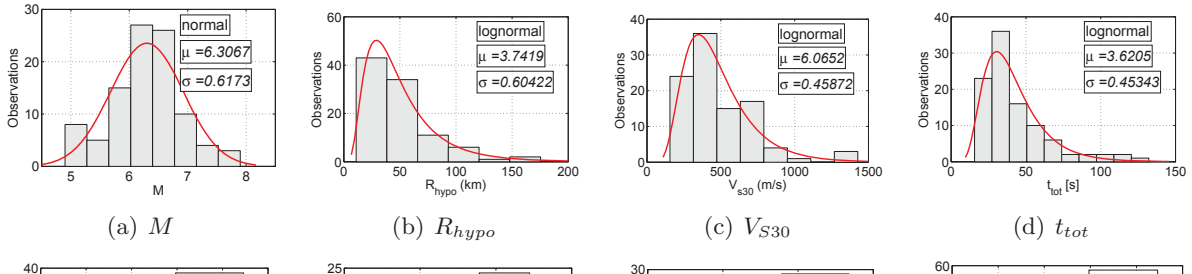

(a) M (b) R_{hypo} (c) V_{S30} (d) t_{tot}

(e) t_{sig} (f) D_{5-75} (g) T_p^{accel} (h) T_p^{vel}

Figure 8.8: Histograms and distributional models for unscalable IMs (Sec. 8.2.2.1)

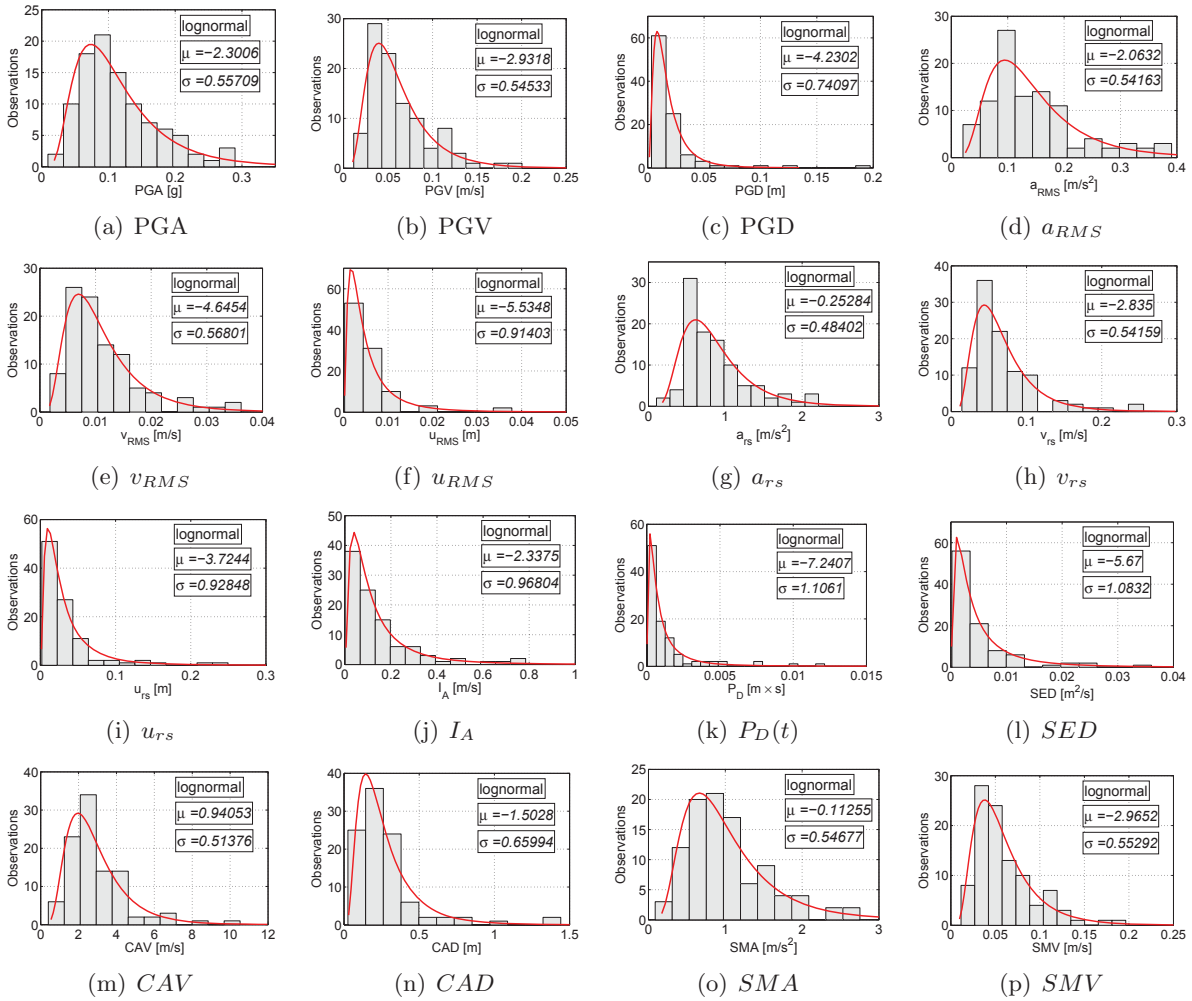

(a) PGA (b) PGV (c) PGD (d) a_{RMS}

(e) v_{RMS} (f) u_{RMS} (g) a_{rs} (h) v_{rs}

(i) u_{rs} (j) I_A (k) $P_D(t)$ (l) SED

(m) CAV (n) CAD (o) SMA (p) SMV

Figure 8.9: Histograms and distributional models for ground motion dependent scalar IMs (Sec. 8.2.2.2)

8.4.2 Cloud Analysis

Out of the 100 analyses, 17 failed through large sliding (resulting from through cracks), and none through overturning. Four EDP were considered: 1) Horizontal crest displacement, 2) Ratio of crack length over total base length; 3) Crack mouth opening and 4) Sliding.

Cloud analysis results are shown in figure 8.13 where failure are shown as vertical lines. For each one of the four considered EDPs, the maximum corresponding value recorded is arbitrarily set as the critical one prior to failure. Those are

- Horizontal displacement: $u_x^{lim} = 35$ mm

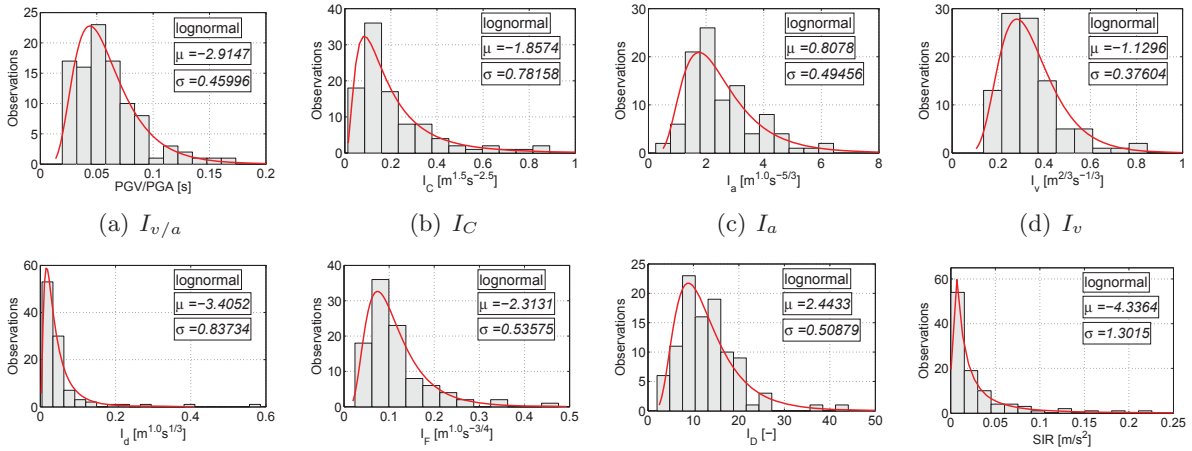

(a) $I_{v/a}$ (b) I_C (c) I_a (d) I_v

(e) I_d (f) I_F (g) I_D (h) SIR

Figure 8.10: Histograms and distributional models for ground motion dependent compound scalar IMs (Sec. 8.2.2.3)

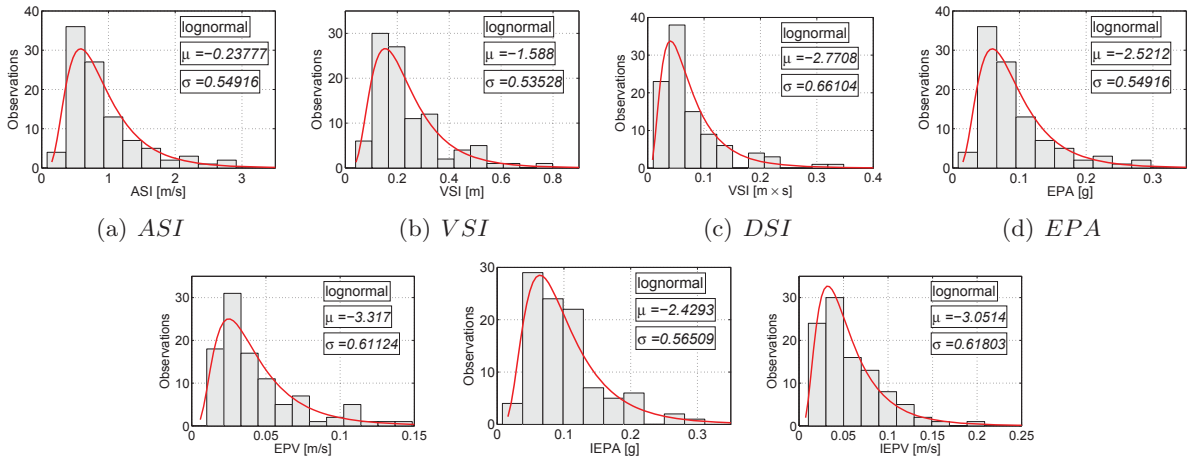

(a) ASI (b) VSI (c) DSI (d) EPA

(e) EPV (f) $IEPA$ (g) $IEPV$

Figure 8.11: Histograms and distributional models for structure-independent spectral IMs (Sec. 8.2.2.4)

- Maximum crack length ratio L_{cr}/L_T=1.0
- Maximum joint opening: $Jn_O^{lim} = 10$ mm
- Maximum joint sliding: $Jn_S^{lim} = 10$ mm

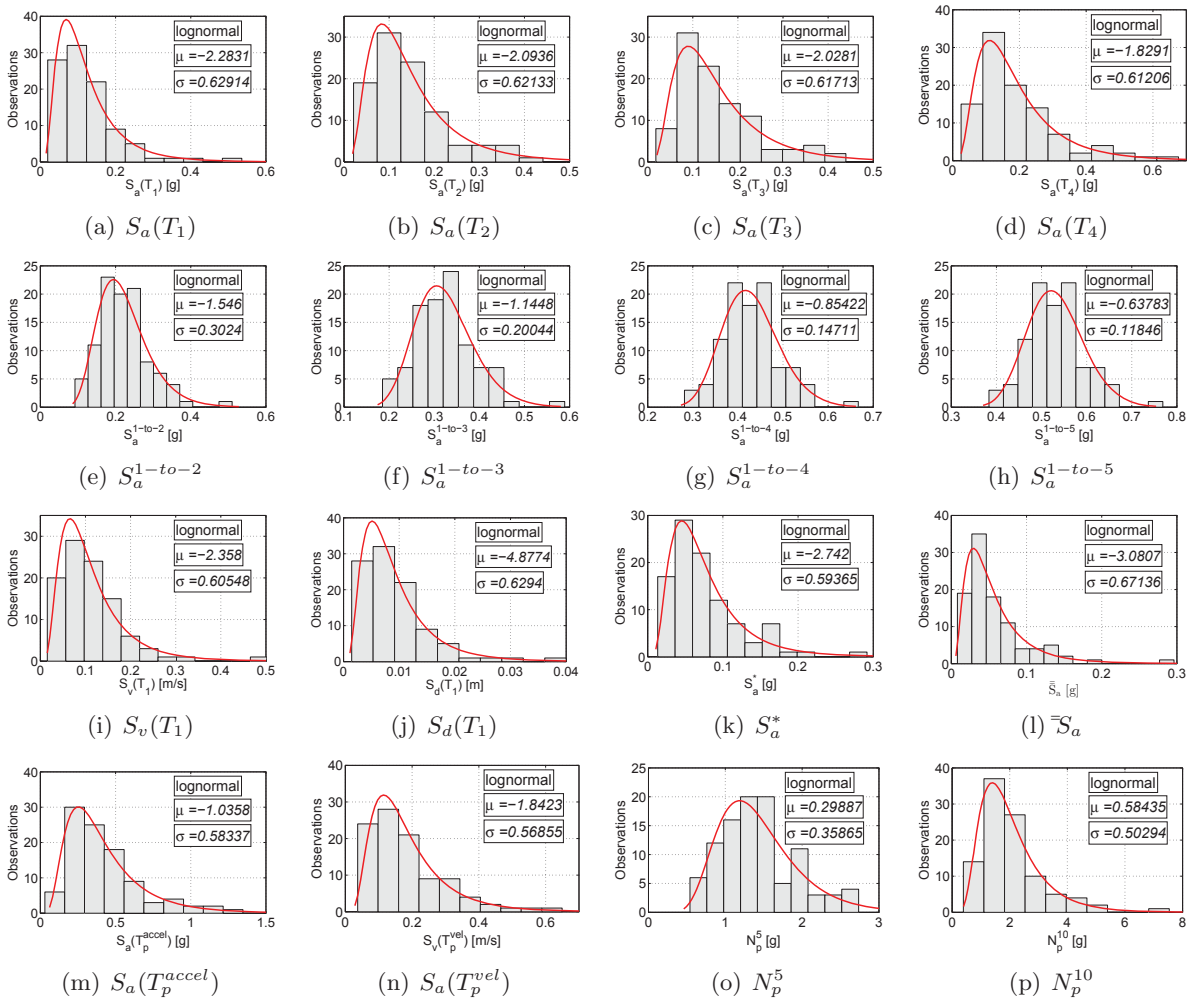

Figure 8.12: Histograms and distributional models for structure-dependent spectral IMs (Sec. 8.2.2.5)

8.4.3 Optimal IM, (EDP = Displacement)

Given the 70 IM, a critical question arises: which is the most representative IM for the selected GM and a given EDP. For argument sake, the displacement EDP is considered. Assessment is made on the basis of the five criteria defined in Sec. 8.2.4. The optimal selection parameters for each IM are tabulated in Table 8.2.

Practicality is assessed from b, Fig. 8.3(a) and Table 8.2.

For category I (unscalled IMs), b is negative for most cases (1 to 8). This is clearly unde-

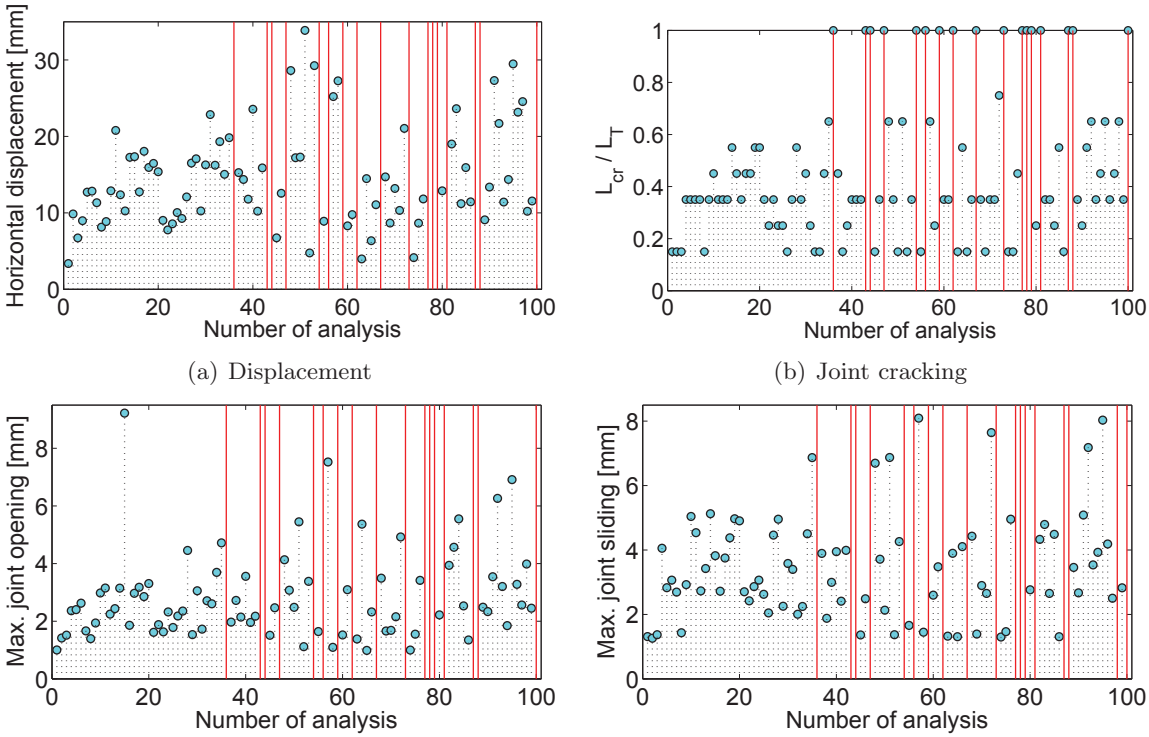

(a) Displacement

(b) Joint cracking

(c) Joint opening

(d) Joint sliding

Figure 8.13: Results of cloud analysis, n =100

sirable as an increase in IM reduces the displacement. Maximum b corresponds to T_p^{accel}.

For category II (ground motion-dependent scalar IMs), PGV, a_{rs} and SMV have the highest b values. v_{RMS}, v_{rs} and CAV have also relatively high slope.

For category III (ground motion-dependent compound IMs), Fajfar IM, I_F, has the highest b value. Cosenza and Manfredi IM, I_D, has negative slope.

For category IV (structure-independent spectral IMs), have nearly identical slopes. together. The highest ones correspond to ASI, VSI and EPA.

For category V (structure-dependent spectral IMs), those IMs related to a specific vibration period of dam (T_i, 42-53) have a slope in the range of 0.55 - 0.85. Furthermore, in this subgroup IM corresponding to spectral velocity at the first-mode (43) has larger slope than the spectral acceleration (42); however, $S_a(T_1)$ and $S_d(T_1)$ are identical. Increasing the period (45-53) reduces the b value. Thus, should one use a sinle period, it should be the

first. For (62-70), corresponding to combined spectral acceleration including the effective mass, b is about ten time greater than those corresponding to single spectral acceleration (42-53). Note that for (60-61) corresponding to N_p^5 and N_p^{10} b is negative.

Figure 8.14(a) shows the ln(IM)-ln(EDP) results for five spectral accelerations (T_1 to T_5). Clearly there is not a distinct separation between the five IM. However, using the combined spectral accelerations (S_a^{1-to-i}) hereby proposed by the authors, data points are much crisper and accounting for higher modes result in a nearly vertical curve (more practicality), figure 8.14(b).

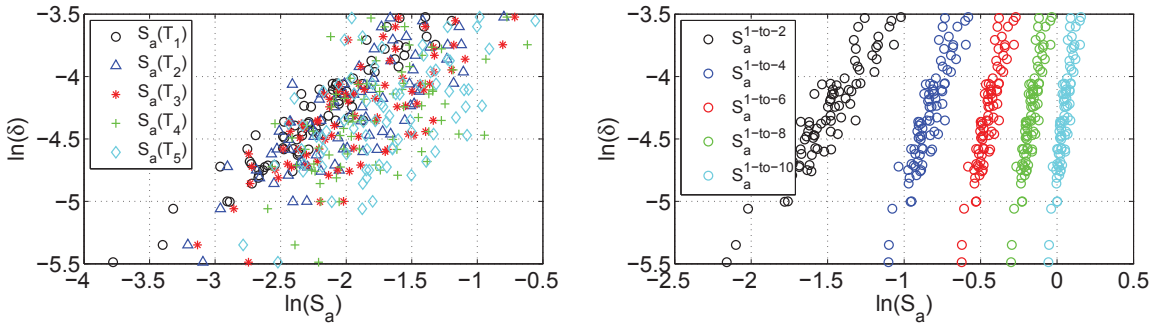

(a) $S_a(T_i)$ (b) S_a^{1-to-i}

Figure 8.14: Comparison the practicality of the IMs from spectral acceleration

Efficiency is gauged by $\beta_{\text{EDP|IM}}$, (the lower, the better).

For category I (unscalable IM) $0.53 \leq \beta_{\text{EDP|IM}} \leq 0.57$.

For category II (ground Motion Dependent Scalar IM) $0.32 \leq \beta_{\text{EDP|IM}} \leq 0.56$. Among all IMs, PGV and SMV have the lowest $\beta_{\text{EDP|IM}}$.

For category III (ground Motion-Dependent Compound IMs) $0.36 \leq \beta_{\text{EDP|IM}} \leq 0.56$. I_F has lowest $\beta_{\text{EDP|IM}}$ parameter.

For category IV (structure Independent Spectral IM) $0.32 \leq \beta_{\text{EDP|IM}} \leq 0.53$.

For category V (structure Dependent Spectral IM) $0.21 \leq \beta_{\text{EDP|IM}} \leq 0.55$. In this category, $S_a(T_1)$ has the lowest dispersion among the other periods. $S_v(T_1)$ and $S_d(T_1)$ have also the

Table 8.2: Demand models and IM comparisons for displacement response

No.	IM	a	b	β	ζ	R^2	p-value (M)	p-value (R_{hypo})
		Eq. 8.32	Eq. 8.32	Eq. 8.34	Eq. 8.39	-	Eq. 8.41	Eq. 8.41
1	M	0.01	0.22	0.57	2.54	0.00	0.89	0.00
2	R_{hypo}	0.06	-0.35	0.53	-1.48	0.14	0.00	0.71
3	V_{S30}	0.03	-0.11	0.57	-4.96	0.01	0.41	0.00
4	t_{tot}	0.02	-0.02	0.57	-24.24	0.00	0.59	0.00
5	t_{sig}	0.03	-0.21	0.55	-2.64	0.05	0.06	0.01
6	D_{5-75}	0.02	-0.15	0.56	-3.75	0.04	0.04	0.01
7	T_p^{accel}	0.03	0.42	0.53	1.26	0.13	0.81	0.00
8	T_p^{vel}	0.02	0.01	0.57	44.74	0.00	0.64	0.00
9	PGA	0.07	0.66	0.43	0.65	0.42	0.00	0.38
10	PGV	0.19	0.85	0.32	0.38	0.67	0.93	0.61
11	PGD	0.05	0.27	0.53	1.94	0.13	0.04	0.00
12	a_{RMS}	0.06	0.68	0.43	0.64	0.42	0.75	0.68
13	v_{RMS}	0.30	0.64	0.43	0.68	0.41	0.01	0.00
14	u_{RMS}	0.03	0.10	0.56	5.60	0.03	0.46	0.00
15	a_{rs}	0.02	0.84	0.39	0.47	0.52	0.84	0.66
16	v_{rs}	0.11	0.70	0.42	0.61	0.44	0.00	0.00
17	u_{rs}	0.02	0.09	0.56	5.96	0.02	0.48	0.00
18	I_A	0.04	0.42	0.39	0.94	0.52	0.84	0.66
19	P_D	0.28	0.40	0.35	0.87	0.62	0.38	0.00
20	SED	0.11	0.35	0.42	1.22	0.44	0.00	0.00
21	CAV	0.01	0.64	0.46	0.72	0.34	0.03	0.00
22	CAV_{STD}	0.01	0.44	0.44	1.01	0.39	0.13	0.04
23	CAD	0.03	0.40	0.50	1.25	0.22	0.02	0.00
24	SMA	0.02	0.70	0.42	0.59	0.46	0.00	0.29
25	SMV	0.18	0.84	0.33	0.39	0.67	0.93	0.42
26	$I_{v/a}$	0.03	0.23	0.56	2.47	0.03	0.83	0.00
27	$I_{v^2/a}$	0.19	0.42	0.44	1.04	0.40	0.15	0.00
28	I_C	0.03	0.43	0.46	1.06	0.36	0.19	0.04
29	I_a	0.01	0.74	0.43	0.58	0.42	0.18	0.83
30	I_v	0.05	1.03	0.41	0.40	0.47	0.01	0.00
31	I_d	0.03	0.18	0.55	3.02	0.07	0.13	0.00
32	I_F	0.10	0.82	0.36	0.44	0.60	0.06	0.01
33	I_D	0.03	-0.25	0.55	-2.20	0.05	0.13	0.00
34	SIR	0.05	0.29	0.43	1.48	0.44	0.00	0.18
35	ASI	0.02	0.84	0.32	0.39	0.67	0.00	0.06
36	VSI	0.06	0.84	0.34	0.41	0.64	0.74	0.48
37	DSI	0.04	0.31	0.53	1.74	0.13	0.10	0.00
38	EPA	0.13	0.84	0.32	0.39	0.67	0.00	0.06
39	EPV	0.14	0.66	0.40	0.60	0.52	0.83	0.01
40	$IEPA$	0.08	0.66	0.43	0.64	0.44	0.00	0.40
41	$IEPV$	0.14	0.72	0.35	0.49	0.62	0.84	0.07
42	$S_a(T_1)$	0.09	0.84	0.21	0.24	0.87	0.93	0.46
43	$S_v(T_1)$	0.12	0.86	0.22	0.26	0.85	0.32	0.77
44	$S_d(T_1)$	1.15	0.84	0.21	0.25	0.87	0.93	0.46
45	$S_a(T_2)$	0.07	0.80	0.29	0.36	0.74	0.13	0.87
46	$S_a(T_3)$	0.06	0.76	0.32	0.42	0.68	0.06	0.79
47	$S_a(T_4)$	0.05	0.67	0.38	0.57	0.55	0.03	0.68
48	$S_a(T_5)$	0.04	0.66	0.37	0.56	0.57	0.02	0.96
49	$S_a(T_6)$	0.04	0.67	0.39	0.58	0.53	0.00	0.59
50	$S_a(T_7)$	0.04	0.68	0.38	0.56	0.55	0.00	0.42
51	$S_a(T_8)$	0.04	0.67	0.38	0.57	0.54	0.00	0.34
52	$S_a(T_9)$	0.04	0.65	0.40	0.61	0.52	0.00	0.37
53	$S_a(T_{10})$	0.04	0.62	0.41	0.65	0.48	0.00	0.49
54	$S_a(T_p^{accel})$	0.03	0.60	0.44	0.74	0.39	0.01	0.81
55	$S_v(T_p^{vel})$	0.07	0.81	0.33	0.40	0.67	0.56	0.21
56	$S_a(T = 0.2s)$	0.04	0.67	0.39	0.58	0.53	0.00	0.59
57	$S_a(T = 1.0s)$	0.08	0.53	0.45	0.85	0.37	0.82	0.00
58	S_a^*	0.12	0.81	0.31	0.38	0.70	0.74	0.01
59	$\bar{S}_a$	0.11	0.70	0.32	0.46	0.67	0.44	0.05
60	N_p^5	0.02	-0.39	0.55	-1.43	0.06	0.99	0.00
61	N_p^{10}	0.02	-0.29	0.55	-1.88	0.05	0.93	0.00
62	S_a^{1-to-2}	0.19	1.74	0.22	0.12	0.85	0.37	0.98
63	S_a^{1-to-3}	0.24	2.56	0.23	0.09	0.84	0.30	0.90
64	S_a^{1-to-4}	0.25	3.46	0.24	0.07	0.83	0.14	0.80
65	S_a^{1-to-5}	0.19	4.23	0.24	0.06	0.82	0.15	0.91
66	S_a^{1-to-6}	0.13	4.99	0.24	0.05	0.82	0.15	0.99
67	S_a^{1-to-7}	0.08	5.86	0.24	0.04	0.82	0.10	0.82
68	S_a^{1-to-8}	0.04	6.63	0.24	0.04	0.82	0.11	0.86
69	S_a^{1-to-9}	0.02	7.43	0.24	0.03	0.81	0.10	0.84
70	$S_a^{1-to-10}$	0.01	8.23	0.25	0.03	0.81	0.09	0.81

same dispersion at $T = T_1$. In the case of contribution of the higher modes with effective mass, there is no meaningful change in the dispersion value (it is almost constant in the

range of [0.22, 0.25]). It means that considering the higher modes does not change the efficiency of the IM parameter. The $\beta_{\text{EDP|IM}}$ parameter for combined spectral accelerations is a bit higher than that observed for $S_a(T_1)$ (which is 0.21); however, this differences are negligible.

Figure 8.15 shows the practicality (in term of b) and efficiency (in term of $\beta_{\text{EDP|IM}}$) for three spectral parameters (i.e. acceleration, velocity, displacement) at different periods. As shown, b is highest and $\beta_{\text{EDP|IM}}$ lowest at $T = 0.44$ s which corresponds to the fundamental period confirming that this is indeed the optimal choice for IM. One also notes that the spectral acceleration and displacement are nearly superimposed over the entire range. On the other hand, the spectral velocity intersects those curves at the fundamental period.

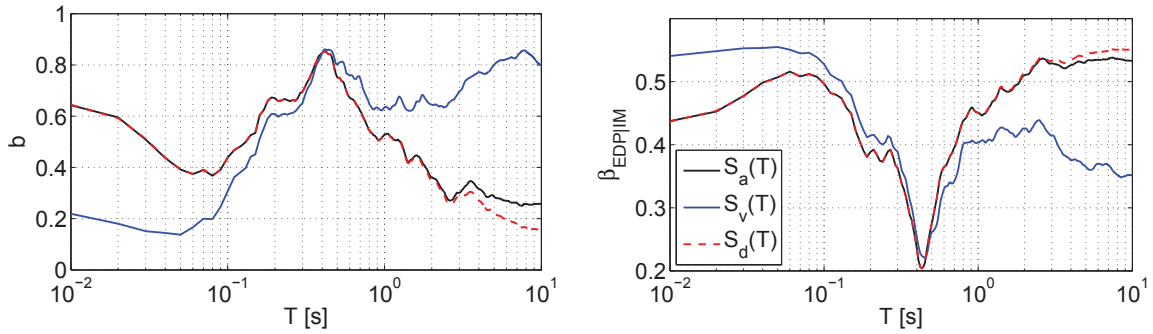

(a) Practicality (b) Efficiency

Figure 8.15: Comparison the efficiency and practicality of the spectral values versus the vibration period

Proficiency As previously mentioned (Eq. 8.39), proficiency is a hybrid indicator in terms of efficiency and practicality where a lower modified dispersion, $\zeta_{\text{EDP|IM}}$, is indicative of higher proficiency.

From Table 8.2, PGV has a lower $\zeta_{\text{EDP|IM}}$ than the one corresponding to PGA and both are lower than PGD. Thus, among the IMs in category II, PGV is the best choose. Among the IMs in category III, I_v has the lowest $\zeta_{\text{EDP|IM}}$. Therefore, the velocity-dependent IMs seems to be a good choice in this study. In category V, the three spectral accelerations at

the first mode have nearly identical $\zeta_{\text{EDP|IM}}$. For acceleration response spectrum, $S_a(T)$, higher modes increase the modified dispersion. Finally, for combined spectral accelerations, S_a^{1-to-N} accounting for higher modes decreases $\zeta_{\text{EDP|IM}}$ and consequently increase proficiency.

Goodness-of-fitting Goodness-of-fitting (GOF) is a well accepted indicator of data fitting. Table 8.2 shows that all IMs in category I have unacceptably small R-squared values [0.0-0.14]. For category II, PGV and SMV have higher R-squared (0.67). In category III, I_F has the highest value (0.60). In category IV, almost all of the IMs have relatively high R-squared [0.44-0.67] except for DSI (0.13). In category V, $S_a(T_1)$, $S_v(T_1)$ and $S_d(T_1)$ have the highest R-squared values [0.85-0.87]. Furthermore, it is noted that increasing the number of modes, decreases the R-squared value. In the case of combined acceleration response spectra, S_a^{1-to-N}, all have nearly same R-squared value [0.81-0.85].

Sufficiency is quantified through the p-value and estimates from linear regression upon the residuals with respect to M_w, R_{rup}, ε, Eq. 8.41. A higher p-value corresponds to a sufficient IM. Whereas different significance levels can be adopted to reject the null hypothesis a 5% significance level is used in this study.

Since most researchers use the PGA as IM, Table 8.2 reports the corresponding p-values based on M_w and R_{rup}. Results confirm what is commonly known that is R_{rup} is preferable over M_w (corresponding p-values being 0.38 and 0.0). As to PGD, p-value is smaller than 0.05 for both magnitude and distance. One can also note that in most cases p-values are greater than 0.05 when R_{hypo} (rather than M) are considered.

When a variable number of modes can be considered (No. 45-53) an increase in number corresponds with a decrease in p-value. This is also the case for the combined spectral accelerations (No. 62-70). Figure 8.16 illustrates the sufficiency dependency of $S_a(T_1)$ and $S_a^{1-to-10}$ on both earthquake magnitude and distance. In figure 8.16(a) $S_a(T_1)$ (p-value=0.93) is more sufficient than $S_a^{1-to-10}$ (p-value=0.09). However, based on figure

8.16(b) it is the other way around (p-values of 0.81 and 0.46).

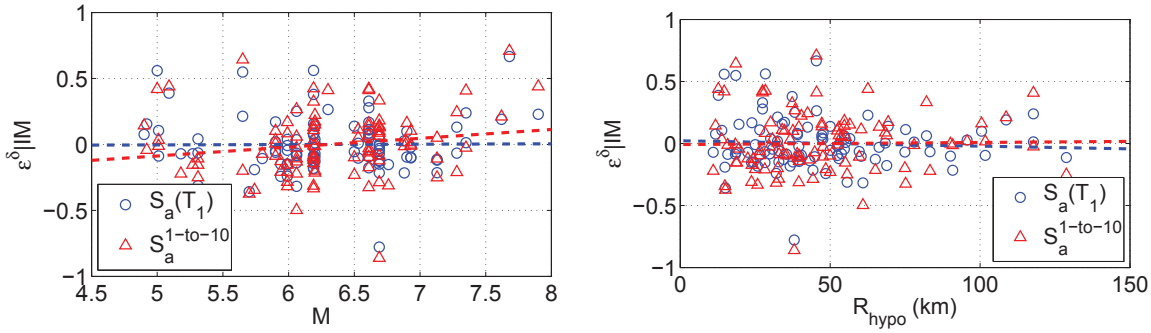

(a) Earthquake magnitude (b) Earthquake hypocentral distance

Figure 8.16: Linear regression of the displacement residuals

Based on the above extensive study, the following major conclusions can be drawn:

- None of the unscalable IMs (Category I) is suitable for probabilistic seismic analyses.
- Among the ground motion dependent scalar IM parameters (Category II), PGV is the best option.
- Among the ground motion dependent compound IMs (Category III), I_F has the efficiency, practicality and proficiency but does not reject the null hypothesis for earthquake distance. Overall, I_F is the most suitable IM for this category.
- Among the structure-independent spectral IMs (Category IV), both the ASI and EPA lead to similar condition.
- Among the structure-dependent spectral IMs (Category V) $S_a(T_1)$, $S_v(T_1)$ and $S_d(T_1)$ lead to nearly identical condition. Among the acceleration response spectra, the fundamental mode is by far better than higher modes. Combined acceleration response spectra, including the effective mass, S_a^{1-to-N}, are the most practical and proficient in whole set.

8.4.4 Optimal IM; Impact of EDP

In so far, the optimal IM was sought for a single EDP (crest displacement). Next, the impact of other EDPs is investigated. For concrete gravity dams, the major contender for an alternative EDP are: crack length ratio 8.13(b), joint opening 8.13(c), and joint sliding 8.13(d). Given the 70 IMs considered in this study, only a selected few will be considered. Those are divided into two groups:

Group 1: includes the optimal IMs determined in the previous section as well as other popularly used ones: PGA, PGV, PGD, I_F, ASI, $S_a(T_1)$, $S_v(T_1)$, $S_d(T_1)$.

Group 2: includes different combined spectral accelerations: S_a^{1-to-N}, $N \in [2, 10]$.

Practicality Nearly identical trends are found in figure 8.17(a). In all cases, crest displacement and joint opening leads to higher b value than crack length ratio and joint sliding. All IMs have nearly identical practicality except PGD (lower). For S_a^{1-to-N} (figure 8.17(b)), increasing the number of modes, increases the practicality in all EDPs. The ratio of different bins corresponding to different responses remains nearly constant.

Efficiency Crest displacement leads to the lowest $\beta_{\text{EDP|IM}}$ (highest efficiency), figure 8.17(c) while again, spectral parameters have higher efficiency. Similar trend is observed in group 2 IMs, figure 8.17(d). The other three EDPs, i.e. crack length ratio, joint opening and joint sliding have nearly identical $\beta_{\text{EDP|IM}}$.

Proficiency Figure 8.17(e) shows the modified dispersion for the first group. It is evident that PGD should not be used, while spectral parameters, i.e. $S_a(T_1)$, $S_v(T_1)$ and $S_d(T_1)$ constitute the best options. In nearly all cases, displacement lead to higher proficiency. As to the second group, figure 8.17(f), an increase in mode contribution decreases $\zeta_{\text{EDP|IM}}$.

Sufficiency is difficult to assess as it is highly dependent on the type of EDP and the selected seismic hazard parameter (M or R_{hypo}). PGA is a sufficient IM based on R_{hypo} for all

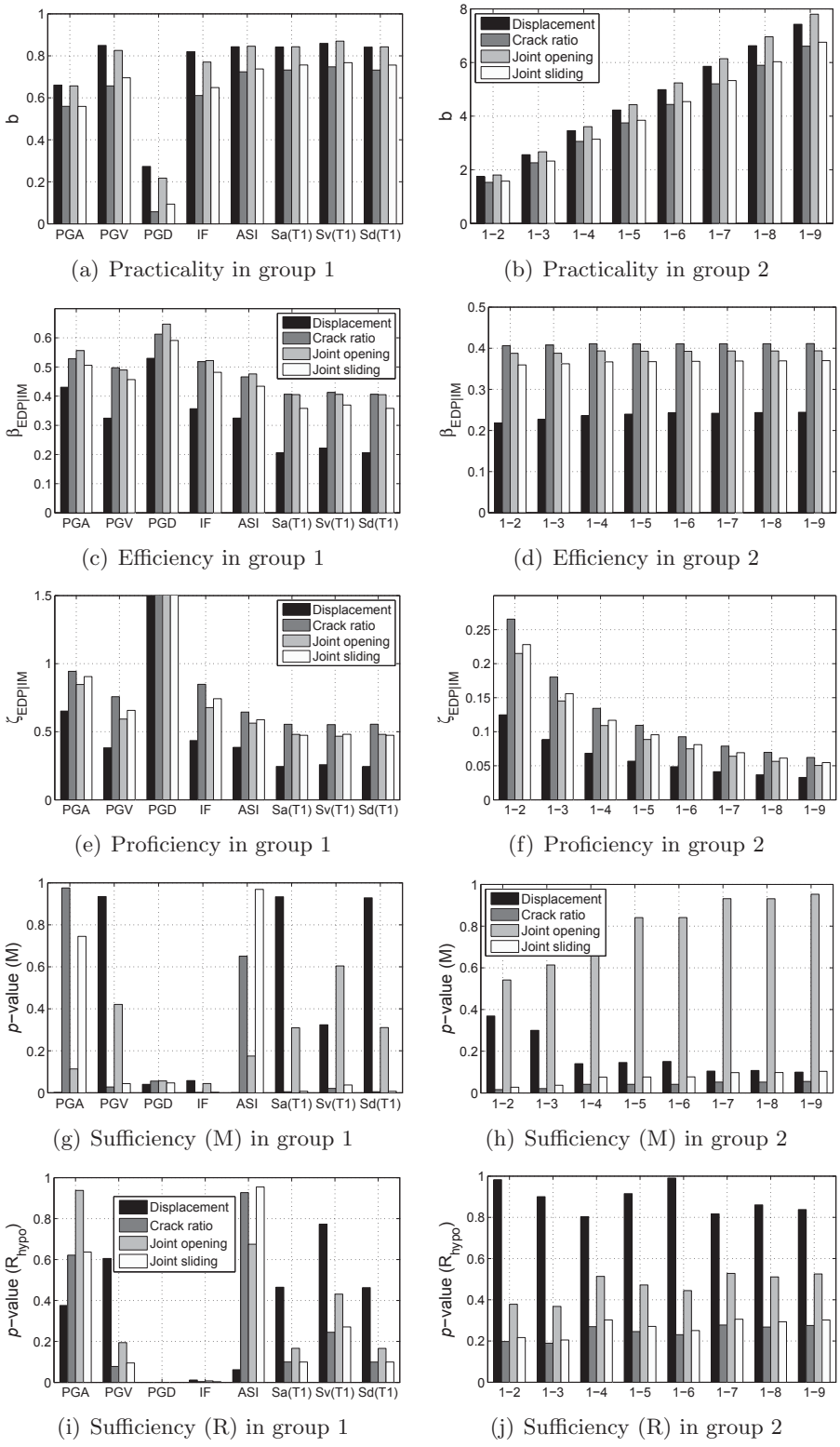

(a) Practicality in group 1

(b) Practicality in group 2

(c) Efficiency in group 1

(d) Efficiency in group 2

(e) Proficiency in group 1

(f) Proficiency in group 2

(g) Sufficiency (M) in group 1

(h) Sufficiency (M) in group 2

(i) Sufficiency (R) in group 1

(j) Sufficiency (R) in group 2

Figure 8.17: Impact of different EDPs on the optimal IM

EDPs; however, it is not qualified based on M and displacement (figures 8.17(g) and 8.17(i)). $S_a(T_1)$ is a sufficient IM based on all EDPs and R_{hypo}; however, based on M, it is valid for displacement and joint opening.

In the second group, all IMs are sufficient based on R_{hypo} (figure 8.17(j)). Displacement having the highest p-value (near unit in most cases) followed by joint opening. Using M for regression analysis of residuals leads to high p-value for the joint opening (figure 8.17(h)). Increasing the contribution of higher modes, results in an increase of p-value for joint opening and a decrease crest displacement.

8.4.5 Cloud-based Fragility Curves

8.4.5.1 Comparing fragility models assumptions

The cloud analysis, Sec. 8.2.3 is next used to determine the PSDM-based fragility curves. The well established equation for the fragility curve is given by Eq. 8.33 which is generalized by Eq. 8.37 to account for very large data point in the EDP (such as collapse or instability in the numerical model) as illustrated by Fig. 8.13. Based on these equations, one can consider four distinct cases ($S_a(T_1)$ is considered as the default IM):

Case 1: Probability of exceedance is determined from the complete data set using Eq. 8.33.

Case 2: The large data points are bounded to a user-defined limit (usually the largest non-collapse data) and the probability of exceedance is determined from all the bounded data points using Eq. 8.33.

Case 3: The large data points are not considered in calculation of the probability of exceedance and Eq. 8.38 is used.

Case 4: Large and not large data points are considered separately using Eq. 8.37.

Figure 8.18 compares the previous four cases for two *edp*: 10 and 25 mm crest displacement (as representatives of low and high limit states - LS). In both analyses, Case 1 results in large

dispersion of IM. In figure 8.18(a), Case 3 and Case 4 lead to similar observations. Thus, P [Lg|IM] does not play a critical role in the total probability of exceedance of the lower LS. On the other hand, Case 4 has lower median than Case 3 for higher LS, figure 8.18(b). Finally, in all cases, comparing Case 1 with Case 4 one notes the importance of the large data points.

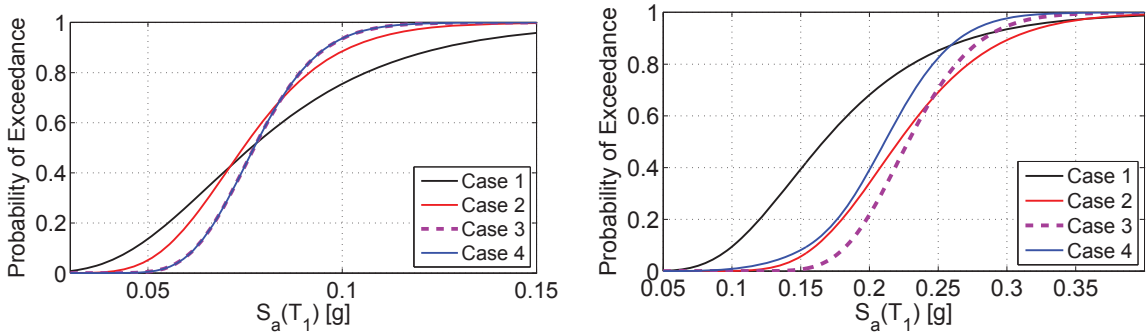

(a) Displacement; $edp = 10$ mm

(b) Displacement; $edp = 25$ mm

Figure 8.18: Comparison of fragility curves based on definitions

8.4.5.2 Impact of IM

Based on the results of PSDM (figure 8.13) and optimal IM (Table 8.2), the impact of other IMs on fragility curve is examined next and results are shown in figure 8.19(a). In all cases, crest displacement is the EDP and the limit value arbitrarily set to $edp = 20$ mm. Both PGA and $S_a(T_2)$ generates wider curves than $S_a(T_1)$. In addition, S_a^{1-to-2} is similar to the $S_a(T_1)$ shifted by about 0.1 g. Figure 8.19(b) shows the contribution of the higher modes and the effective mass on the fragility curves. Again, based on Table 8.2, $S_a^{1-to-10}$ was the most practical and proficient IM parameter, on the other hand there is no considerable differences among the fragility curves. Thus, the contribution of higher modes, appear to result in a simple shift of the curve. Finally, the fragility curves based on S_a^{1-to-N} are narrower than those based on other IM, thus dispersion is limited.

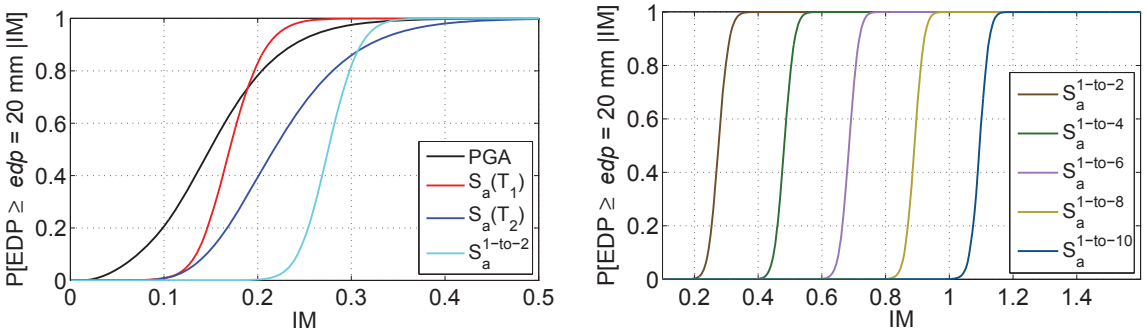

(a) Selective IM parameters (b) S_a^{1-to-N}-based IMs

Figure 8.19: Comparison of fragility curves based on IM parameter

8.4.5.3 Single-IM fragility surface

In so far all results were shown for a specific EDP. The effect of the later along with the IM on the $P\left[\text{EDP} \geq edp|\text{IM}\right]$, is shown in figure 8.20. This figure clearly shows as the the *edp* increases, the effective range of IM increases too.

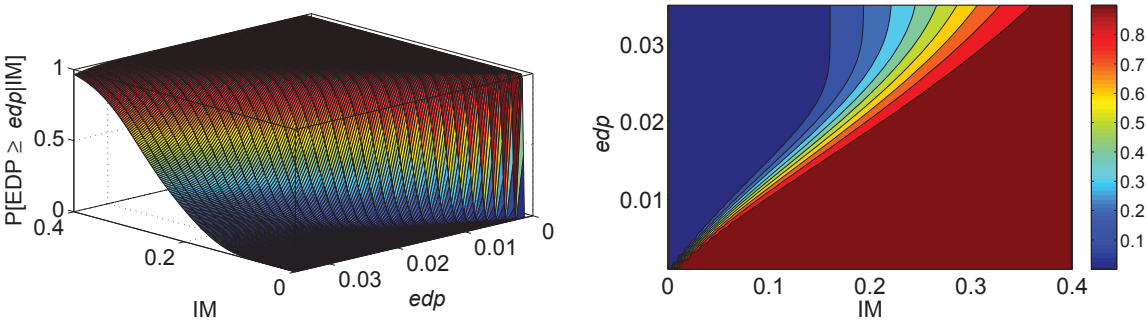

(a) 3D plot (b) Contour plot

Figure 8.20: Fragility surface for varying *edp*

8.4.5.4 Impact of EDP

From figure 8.17, crest displacement was determined to be the adequate EDP in most cases. However, other EDPs could be used for fragility curves. For example, if the objective is to assess the dam-foundation interface, joint opening/sliding should be used as EDP. An example of such relevance is the effect of joint displacements on the conditions of the water-stops in arch dams.

Figure 8.21 shows the fragility curves based on joint opening and sliding at the dam-rock interface. Three different LS are considered: a) 2 mm: initiation of opening/sliding, b) 5 mm: propagation of the opening/sliding, and c) 8 mm: near collapse condition. In all cases, joint sliding has the highest probability of exceedance. However, the difference between crack opening and crack sliding is reduced by increasing the LS.

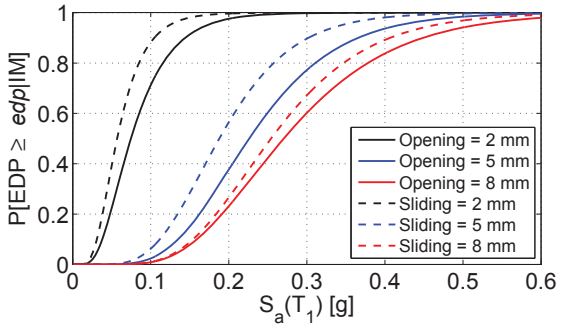

Figure 8.21: Comparison of fragility curves based on IM parameter

8.4.5.5 Fragility curves for damage index

One can define fragility curves in a more generic way in terms of damage index (DI). Those were proposed for gravity dams (Hariri-Ardebili and Saouma, 2014) in terms of crack length L^C, dissipated energy E_H, and maximum drift u_{max}. However, in the present study, only crack length ratio is considered.

$$\mathrm{DI} = f\left(L^C, E_H, u_{max}\right) \tag{8.42}$$

A fragility curve based on DI and a specific LS is:

$$P\left[\mathrm{DI} \geq \mathrm{LS}|\mathrm{IM}\right] = 1 - \Phi\left(\frac{\ln(\mathrm{LS}) - \ln(\eta_{\mathrm{DI}|\mathrm{IM}})}{\beta_{\mathrm{DI}|\mathrm{IM}}}\right) \tag{8.43}$$

where $\eta_{\mathrm{DI}|\mathrm{IM}}$ is the median value of DI given IM and $\beta_{\mathrm{DI}|\mathrm{IM}}$ is the logarithmic standard deviation of the DI conditioned on the IM.

Table 10.2 shows different proposed damage states (DS) for concrete dams. In the present analysis, damage can only occurs at the dam-foundation joint. Figure 8.22(a) shows the fragility

curves of the concrete dam in terms of the LS. The last curve (LS = 0.99) corresponds to the the probability of failure (collapse). If the LS are not discrete values, the fragility contour is shown in figure 8.22(b).

Table 8.3: Definition of the damage states for gravity dams (Hariri-Ardebili and Saouma, 2014)

Symbol	DS	DI range
DS1	Intact	$\overline{\overline{DI}} = 0.00$
DS2	Slight	$0.00 < \overline{\overline{DI}} \leq \mathbf{0.10}$
DS3	Moderate	$0.10 < \overline{\overline{DI}} \leq \mathbf{0.30}$
DS4	Severe	$0.30 < \overline{\overline{DI}} \leq \mathbf{0.60}$
DS5	Near collapse	$0.60 < \overline{\overline{DI}} \leq \mathbf{0.99}$
DS6	Collapse	$\overline{\overline{DI}} = 1.00$

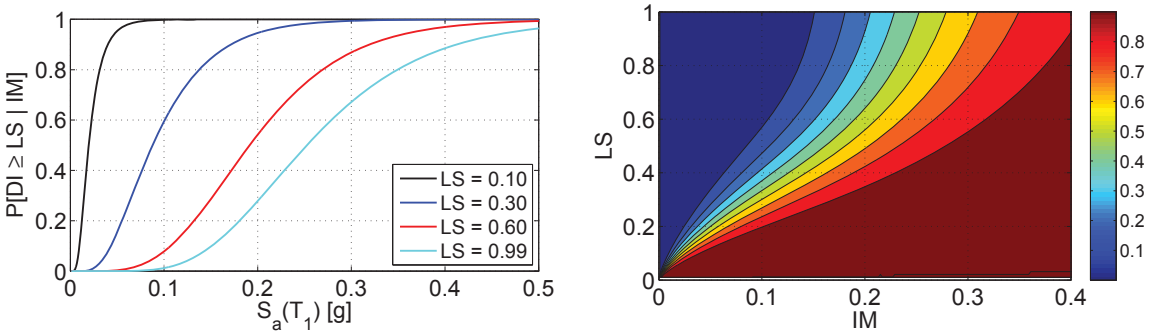

(a) Selective LS for gravity dams

(b) Contour plot over $0 < LS < 1$

Figure 8.22: Comparison of fragility curves based on DI concept

8.5 Conclusions

PSDM in general and IM in particular are well established parameters used in the context of PBEE as applied to buildings. This paper is a first attempt to extend the definition of those terms to concrete dams toward a subsequent PBEE analysis.

First, over 70 scalar intensity measure parameters are mathematically identified (along with a newly proposed one), then the optimal one (in term of efficiency, practicality, proficiency, sufficiency, and hazard compatibility) is selected for Pine Flat dam.

Then, in the context of PSDM, different fragility curves and surfaces are determined for the

dam. Aside from Ellingwood and Tekie (2001) and Tekie and Ellingwood (2003) this is probably the first use of probabilistic seismic safety assessment of concrete dams.

Chapter 9

Collapse Fragility Curves for Gravity Dams

This chapter is based on:

Hariri-Ardebili, M.A. and Saouma, V.E., (2015), Collapse Fragility Curves for Concrete Dams: A Comprehensive Study (submitted to Structural Engineering - ASCE)

9.1 Introduction

9.1.1 Probabilistic Safety Assessment of Dams

Dams are critical components of a nation's infrastructure. Yet, many dams are aging and most were designed at a time with limited seismic field data, or technical knowledge. Taking a simple binary approach Safe/Fail, as commonly done presently through a deterministic application of safety codes (USACE, 2007; CDA, 2007) is not only unrealistic but could yield very expensive rehabilitation program. Probabilistic methods on the other hand have been early on used for buildings (Cornell, 1968) and subsequently to nuclear power plants (Kennedy et al., 1980). More recently, performance based earthquake engineering (PBEE) has been introduced for buildings (Porter, 2003; Gunay and Mosalam, 2013). As to dams, the accepted procedure is based on the so-called potential failure mode (PFM) identification (FERC-PFMA, 2005).

Inspired by the PBEE model some researchers selectively focused on one of its components and applied it to concrete dam analysis. Those studies can be grouped as follows:

Advanced Structural Analysis: Single-record incremental dynamic analysis (SR-IDA), also known as capacity curve, of an arch dam by Pan et al. (2015); multiple-record incremental dynamic analysis (MR-IDA) of gravity and arch dams by Alembagheri and Ghaemian (2013b); endurance time analysis (ETA) of a gravity dam by Hariri-Ardebili and Saouma (2014); and multiple-strip analysis (MSA) of an arch dam by Hariri-Ardebili et al. (2015).

Seismic Fragility Analysis: Seismic fragility curves for gravity dams based on different limit states (LS) by Ellingwood and Tekie (2001) and Tekie and Ellingwood (2003); fragility curves incorporating the structural uncertainty in the form of series and parallel components by Lupoi and Callari (2012); and cloud-based probabilistic seismic demand analysis (PSDA) by Hariri-Ardebili and Saouma (2015a).

9.1.2 Vertical Ground Acceleration

Effects of vertical (V) ground motion component have been addressed either from 1) seismological point of view, and/or 2) Structural one.

Seismological Aspects: Vertical components of a ground acceleration are associated with P-waves, while the horizontal (H) with the S-waves. Thus, the vertical component includes higher frequencies. In addition, the arrival time interval, t_{V-H}, (between PGA^V and PGA^H where PGA stands for peak ground acceleration) affects the interaction between the ground motion components (Collier and Elnashai, 2001). The interaction between the components is maximum when t_{H-V} is less than 0.5 s and it is zero when t_{H-V} is more than 4.0 s. The relative characteristics of the ground motion components is usually presented by V/H ratio. Based on Lee and Mosalam (2014), it is a strong function of natural period, local site condition, and source-to-site distance, and a relatively poor function of magnitude, and fault mechanism.

Structural Aspects: Most of the research focused on the effects of ground motion's vertical component on reinforced concrete columns of highway bridges, Papazoglou and Elnashai (1996),

Kim et al. (2011), and Button et al. (2002). It was concluded that the vertical component has a major impact on the axial force demand of columns. The only accessible research on impact of the vertical component on fragility curves is the work of Wang et al. (2013b). They analyzed a representative model of multi-span continuous steel girder bridge with liquefiable soil layers. Both the fragility curves and surfaces are derived. It was determined that using scalar intensity measure (IM) from horizontal motion, peak ground velocity (PGV) will be the optimal one. However, for engineering demand parameters (EDP) that are mostly influenced by vertical components, the square-root-of-the-sum-of-squares of vertical spectral accelerations at the first and second vertical modes is the optimal one. They stated that the fragility curves that neglect the vertical component effect underestimate the failure probability of the certain components.

9.2 PEER PBEE Background Theory

9.2.1 General Concepts of PBEE

The general framework for pacific earthquake engineering research center (PEER) PBEE (also known as PBEE-2) has been laid by (Porter, 2003). It breaks the seismic performance assessment into four primary steps: 1) ground motion hazard characterization, 2) structural response analysis, 3) damage analysis, and 4) loss assessment. The results of each of these steps are represented as generalized variables, IM, EDP, damage measure (DM), and decision variable (DV). This process can be expressed in terms of a triple integral that is an application of the total probability theorem:

$$g\left[\mathrm{DV}|\mathrm{D}\right] = \int\int\int p\left[\mathrm{DV}|\mathrm{DM,D}\right] p\left[\mathrm{DM}|\mathrm{EDP,D}\right] p\left[\mathrm{EDP}|\mathrm{IM,D}\right] g\left[\mathrm{IM}|\mathrm{D}\right] d\mathrm{IM}.d\mathrm{EDP}.d\mathrm{DM} \quad (9.1)$$

where $p\left[\mathrm{X}|\mathrm{Y}\right]$ denotes the complementary cumulative distribution function of X conditioned on Y, $g\left[\mathrm{X}|\mathrm{Y}\right]$ denotes the mean annual occurrence rate of X given Y, and D denotes facility location, structural, non-structural, and other features. The first three steps will be applied in the subseuquent study of Pine Flat dam.

9.2.2 Analytical Collapse Fragility Functions

A fragility function quantifies the probability of exceeding a particular level of damage (LS, or structural collapse in the end) as a function of ground motion IM (Baker, 2014). It can be categorized into three main groups (Lallemant et al., 2015): 1) empirical fragility curves derived from post-earthquake damage data (Sabetta et al., 1998), 2) analytical fragility curves derived from transient structural analysis (Shinozuka et al., 2000), and 3) heuristic fragility curves using the expert opinion (Porter et al., 2007).

A lognormal cumulative distribution function (CDF) is usually used to quantify a fragility function (Shinozuka et al., 2000). The collapse fragility curve is then defined as:

$$p\left[\mathrm{C}|\mathrm{IM}=im\right]=\Phi\left(\frac{\ln(im)-\ln(\eta)}{\beta}\right) \tag{9.2}$$

where $\Phi(.)$ is the standard normal cumulative distribution function and β the logarithmic standard deviation (also called dispersion), and η median of the fragility function.

Note that the global collapse is treated separately in PEER PBEE framework (in spite of the terms introduced in Eq. 9.1) since its probability does not change from a damageable group to another (Gunay and Mosalam, 2013).

Application of Eq. 9.2 in structural analysis, requires calibration of the η and β parameters. Fitting the fragility function to the analytical data point leads to estimation of $\hat{\eta}$ and $\hat{\beta}$. Among the different models for fragility curve fitting (Lallemant et al., 2015) (Baker, 2014), three methods are used in this paper: 1) method of moments (MM), 2) sum of squared error (SSE), and 3) maximum likelihood estimation (MLE).

MM seeks $\hat{\eta}$ and $\hat{\beta}$ in a way that the resulting distribution (log-normal in this paper) has the same moments (mean and standard deviation) as the data points:

$$\hat{\eta}=\exp\left(\frac{1}{n}\sum_{i=1}^{n}\ln(\mathrm{IM}_i^c)\right),\quad \hat{\beta}=\sqrt{\frac{\sum_{i=1}^{n}\left(\ln\left(\mathrm{IM}_i^c\right)-\ln\left(\hat{\eta}\right)\right)^2}{n-1}} \tag{9.3}$$

where n is number of ground motions and superscript c refers to the onset of collapse. This method is simple to implement, however, it has a major shortcoming: It requires a full scale IDA

Vamvatsikos and Cornel (2002) and cannot be used for truncated IDA (Baker, 2014).

SSE seeks $\hat{\eta}$ and $\hat{\beta}$ in a way to minimize the sum of squared error between the observed fractions of collapsed data and probabilities predicted by the fragility function (Baker, 2014):

$$\left\{\hat{\eta}, \hat{\beta}\right\} = \underset{\hat{\eta},\hat{\beta}}{\operatorname{argmin}} \sum_{i=1}^{m} \left(\frac{n_i^c}{n_i} - \Phi\left(\frac{\ln(im_i) - \ln(\eta)}{\beta} \right) \right)^2 \tag{9.4}$$

where n_i^c and n_i are number of collapsed data and ground motions at level IM $= im_i$, and m is the number of IM levels. Note that $\frac{n_i^c}{n_i}$ is the observed probability of collapse at level IM $= im_i$.

MLE seeks $\hat{\eta}$ and $\hat{\beta}$ in a way to maximize a "likelihood" function which assumes the observation of each ground motion is either collapsed or safe and also is independent of the other ground motions. The equivalent formula to be maximized is proposed by (Baker, 2014):

$$\left\{\hat{\eta}, \hat{\beta}\right\} = \underset{\hat{\eta},\hat{\beta}}{\operatorname{argmax}} \sum_{i=1}^{m} \left(n_i^c \ln\left(\Phi\left(\frac{\ln(im_i)-\ln(\eta)}{\beta} \right) \right) + (n_i - n_i^c) \ln\left(1 - \Phi\left(\frac{\ln(im_i)-\ln(\eta)}{\beta} \right) \right) \right) \tag{9.5}$$

9.3 Ground Motion Hazard Characterization

Probabilistic seismic hazard analysis (PSHA) is used for ground motion selection (horizontal and vertical components). PEER ground motion database (PEER, 2014) is used in this study. It considers fault mechanism, earthquake magnitude, site-to-source distance and local geological site condition. Twenty one ground motion records listed in Table 9.1 are selected based on the following conditions:

- Site-to-source distance, $1 < R_{rup} < 100$ km
- Magnitude, $5.5 < M_w < 7.5$
- Fault mechanism: Strike-slip
- Shear wave velocity, 600 m/s $< V_{S30} <$ 1500 m/s; preferably $V_{S30} \approx 760 m/s$
- No pulse-like record

In this study shear wave velocity range is selected such that it accounts for the site class B, $760 m/s < V_{S30} < 1500 m/s$, and site class C, $360 m/s < V_{S30} < 760 m/s$, of NEHRP site

classification (Council, 2003). The unconditional ground motion selection methodology is used in this study Baker (2010) in order to examine different IM parameters and select the optimal one. This type of evaluation is refereed to scenario-based performance assessment (SBPA) (ATC-58, 2012) where only the intensity is uncertain while the ground motion magnitude and distance are known. It is noteworthy that conditional selection of ground motions at the fundamental period (T_1) may reduce the dispersion in $S_a(T_1)$; however the objective of this study is to compare all the possible IMs in a even-handed condition.

Table 9.1: List of the selected ground motion records

No.	Earthquake Name	Year	Station Name	M	R_{rup} (km)	V_{S30} (m/s)	t_{sig} (s)
1	Coyote Lake	1979	Gilroy Array #1	5.74	10.67	1428.14	6.8
2	Livermore-01	1980	Tracy - Sewage Treatm Plant	5.8	53.82	650.05	20.2
3	Morgan Hill	1984	Gilroy - Gavilan Coll.	6.19	14.84	729.65	8.6
4	Morgan Hill	1984	Gilroy Array #1	6.19	14.91	1428.14	9.5
5	Morgan Hill	1984	UCSC Lick Observatory	6.19	45.47	713.59	9.1
6	Landers	1992	Silent Valley - Poppet Flat	7.28	50.85	659.09	31.7
7	Landers	1992	Twentynine Palms	7.28	41.43	635.01	30.9
8	Big Bear-01	1992	Pear Blossom - Pallet Creek	6.46	95.94	624.01	27.1
9	Big Bear-01	1992	Silent Valley - Poppet Flat	6.46	35.41	659.09	13.3
10	Kobe	1995	Chihaya	6.9	49.91	609	12
11	Kobe	1995	Kobe University	6.9	0.92	1043	7
12	Kobe	1995	MZH	6.9	70.26	609	24.8
13	Kobe	1995	Nishi-Akashi	6.9	7.08	609	11.2
14	Kobe	1995	OKA	6.9	86.94	609	23
15	Kobe	1995	TOT	6.9	119.64	609	27.4
16	Duzce	1999	Lamont 1060	7.14	25.88	782	18.6
17	Duzce	1999	Lamont 531	7.14	8.03	638.39	14.9
18	Upland	1990	Ocean Floor SEMS III	5.63	71.73	659.6	47.7
19	Manjil	1990	Abbar	7.37	12.55	723.95	29.1
20	Hector Mine	1999	Anza - Pinyon Flat	7.13	89.98	724.89	23.3
21	Hector Mine	1999	Banning - Twin Pines Road	7.13	83.43	667.42	27.1

Figure 9.1 shows the horizontal and vertical components of 21 un-scaled acceleration response spectra. The arithmetic and geometric mean are also shown. In addition, figure 9.1(c) shows the V/H ratio as a function of period. As seen, the mean ratio is less than unit. For T = 0.1 s the V/H ratio is close to unit; however, for T $\simeq$ [0.2, 0.8] this ratio decreases to about 0.6. On the other hand, some of the individual ground motions shows a V/H ratio up to 3.0.

Table 9.2 lists 37 IM parameters taken from the 70 reported in (Hariri-Ardebili and Saouma, 2015a). It should be noted that IM corresponding to 33-37 have been proposed by the authors.

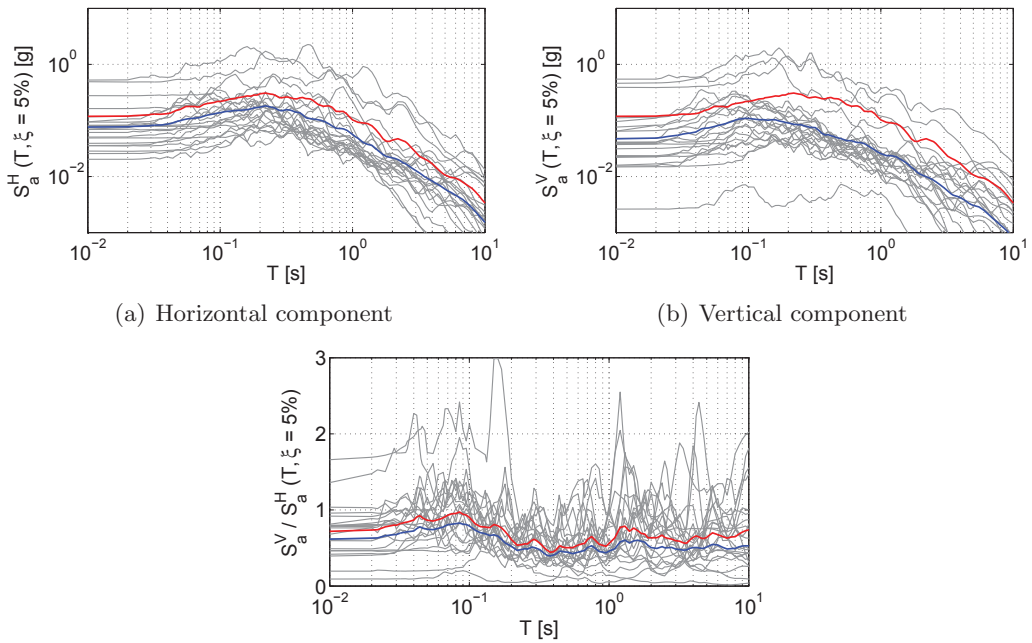

(a) Horizontal component

(b) Vertical component

(c) V/H ratio

Figure 9.1: Response spectra for 21 un-scaled ground motions (Gray: individual ground motions, red: arithmetic mean, blue: geometric mean)

The V/H ratio of IMs are extracted for the ground motions listed in Table 9.1, and the mean, median, [min, max], and [16%, 84%] fractiles are reported. In most cases, the V/H ratio for both mean and median is less than one (30 out of 37 IMs in mean and 34 out of 37 IMs in median). However, in most cases, the maximum V/H ratio or the 84% fractile exceeds unity, indicating the predominance of the vertical component.

PGA and $S_a(T_1)$ are the two most widely used IMs. On the other hand, PGV and $S_v(T_1)$ are two potential alternatives in multiple-component seismic analysis (Wang et al., 2013b). Figure 9.2(a) illustrates the V/H ratio of all 21 ground motions. Indeed, PGA has the highest mean and median V/H ratio followed by PGV. On the other hand, $S_a(T_1)$ and $S_v(T_1)$ are nearly identical. 4 out of 21 ground motions have at least one IM with V/H ratio more than one (strong vertical component).

Hariri-Ardebili and Saouma (2015a) have shown that combined spectral acceleration with the higher modes and effective mass, S_a^{1-to-N} is the optimal IMs for PSDA. Thus, the V/H ratio is

examined for this family of IMs, figure 9.2(b). Contribution of higher modes pushes the V/H ratio towards unity. For example, for S_a^{1-to-6} the mean and median are both 0.95 and the [min, max] is bracketed by [0.85, 1.10]. Thus, these IMs are likely to reduce the dispersion of the structural analyses (as will be shown below).

Table 9.2: Processing the V/H ratio of selected IM parameters

No.	Description	IM	Mathematical definition	mean	[min, max]	median	[16%, 84%]
1	Significant duration	t_{sig}	$t_{0.95I_A} - t_{0.05I_A}$	1.10	[0.73, 1.81]	1.11	[0.87, 1.31]
2	Seismological duration	D_{5-75}	$t_{0.75I_A} - t_{0.05I_A}$	1.20	[0.52, 2.71]	1.11	[0.92, 1.51]
3	Predominant period (acceleration)	T_p^{accel}	-	0.68	[0.12, 1.61]	0.63	[0.34, 1.03]
4	Predominant period (velocity)	T_p^{vel}	-	3.10	[0.39, 14.0]	1.61	[0.60, 5.81]
5	Peak ground acceleration	PGA	$max\left(\lvert\ddot{u}(t)\rvert\right)$	0.72	[0.13, 1.62]	0.76	[0.41, 0.99]
6	Peak ground velocity	PGV	$max\left(\lvert\dot{u}(t)\rvert\right)$	0.61	[0.10, 1.21]	0.53	[0.41, 0.91]
7	Peak ground displacement	PGD	$max\left(\lvert u(t)\rvert\right)$	1.70	[0.1, 15.0]	0.72	[0.35, 1.80]
8	Root-mean-square of acceleration	a_{RMS}	$\sqrt{\frac{1}{t_{tot}}\int_0^{t_{tot}}(\ddot{u}(t))^2 dt}$	0.67	[0.18, 1.02]	0.70	[0.45, 0.89]
9	Root-mean-square of velocity	v_{RMS}	$\sqrt{\frac{1}{t_{tot}}\int_0^{t_{tot}}(\dot{u}(t))^2 dt}$	0.62	[0.18, 0.99]	0.63	[0.42, 0.78]
10	Root-mean-square of displacement	u_{RMS}	$\sqrt{\frac{1}{t_{tot}}\int_0^{t_{tot}}(u(t))^2 dt}$	1.81	[0.09, 16]	0.67	[0.36, 2.01]
11	Arias intensity	I_A	$\frac{\pi}{2g}\int_0^{t_{tot}}(\ddot{u}(t))^2 dt$	0.49	[0.03, 1.01]	0.49	[0.21, 0.78]
12	Specific energy density	SED	$\int_0^{t_{tot}}(\dot{u}(t))^2 dt$	0.42	[0.03, 0.99]	0.40	[0.18, 0.62]
13	Cumulative absolute velocity	CAV	$\int_0^{t_{tot}}\lvert\ddot{u}(t)\rvert\, dt$	0.67	[0.20, 1.02]	0.68	[0.46, 90]
14	Cumulative absolute displacement	CAD	$\int_0^{t_{tot}}\lvert\dot{u}(t)\rvert\, dt$	0.66	[0.25, 1.12]	0.67	[0.42, 0.87]
15	Peak velocity to acceleration ratio	$I_{v/a}$	$(PGA)^{-1}\,(PGV)^{+1}$	0.98	[0.23, 2.11]	0.94	[0.58, 1.21]
16	Characteristics intensity	I_C	$(a_{RMS})^{+3/2}\left(t_{sig}\right)^{+1/2}$	0.58	[0.09, 1.00]	0.54	[0.34, 0.86]
17	Riddell Garcia acceleration index	I_a	$(PGA)^{+1}\left(t_{sig}\right)^{+1/3}$	0.73	[0.14, 1.53]	0.76	[0.43, 0.99]
18	Riddell Garcia velocity index	I_v	$(PGV)^{+2/3}\left(t_{sig}\right)^{+1/3}$	0.72	[0.25, 1.11]	0.73	[0.55, 0.92]
19	Riddell Garcia displacement index	I_d	$(PGD)^{+1}\left(t_{sig}\right)^{+1/3}$	1.71	[0.1, 14.0]	0.75	[0.38, 1.82]
20	Fajfar index	I_F	$(PGV)^{+1}\left(t_{sig}\right)^{+1/4}$	0.62	[0.11, 1.12]	0.57	[0.41, 0.89]
21	Cosenza index	I_D	$\frac{2g}{\pi}\,(PGA)^{-1}\,(PGV)^{-1}\,(I_A)^{+1}$	1.32	[0.43, 2.72]	0.96	[0.75, 2.21]
22	Shaking intensity rate	SIR	$(I_{A5-75})(D_{5-75})^{-1}$	0.47	[0.015, 0.94]	0.44	[0.11, 0.87]
23	Acceleration spectrum intensity	ASI	$\int_{0.1}^{0.5} S_a\,(T, \xi = 5\%)\, dT$	0.57	[0.16, 0.94]	0.55	[0.39, 0.76]
24	Velocity spectrum intensity	VSI	$\int_{0.1}^{2.5} S_v\,(T, \xi = 5\%)\, dT$	0.59	[0.09, 0.92]	0.56	[0.38, 0.83]
25	Displacement spectrum intensity	DSI	$\int_{2.0}^{5.0} S_d\,(T, \xi = 5\%)\, dT$	0.65	[0.29, 1.31]	0.57	[0.36, 0.94]
26	Effective peak acceleration	EPA	$\frac{1}{2.5\times 0.4}\times\int_{0.1}^{0.5} S_a\,(T, \xi = 5\%)\, dT$	0.57	[0.16, 0.94]	0.55	[0.39, 0.76]
27	Effective peak velocity	EPV	$\frac{1}{2.5\times 0.4}\times\int_{0.8}^{1.2} S_v\,(T, \xi = 5\%)\, dT$	0.59	[0.05, 1.12]	0.54	[0.38, 0.93]
28	First-mode spectral acceleration	$S_a(T_1)$	$S_a(T_1, \xi = 5\%)$	0.54	[0.11, 1.31]	0.49	[0.31, 0.78]
29	First-mode spectral velocity	$S_v(T_1)$	$S_v(T_1, \xi = 5\%)$	0.52	[0.13, 1.02]	0.49	[0.29, 0.79]
30	First-mode spectral displacement	$S_d(T_1)$	$S_d(T_1, \xi = 5\%)$	0.54	[0.11, 1.31]	0.50	[0.30, 0.77]
31	Spectral acceleration at predominant period	$S_a(T_p^{accel})$	-	0.65	[0.14, 1.31]	0.71	[0.34, 0.91]
32	Spectral velocity at predominant period	$S_v(T_p^{vel})$	-	0.54	[0.06, 0.95]	0.53	[0.31, 0.76]
33	Combined (mode 1 to 2) spectral acceleration	S_a^{1-to-2}	$\sum_{i=1}^{2}\left(S_a\left(T_i, \xi\right)\right)^{\alpha_i},\ \alpha_i = \frac{m_i^{\text{eff}}}{\sum_1^2 m_i^{\text{eff}}}$	0.72	[0.38, 1.01]	0.68	[0.58, 0.90]
34	Combined (mode 1 to 3) spectral acceleration	S_a^{1-to-3}	$\sum_{i=1}^{3}\left(S_a\left(T_i, \xi\right)\right)^{\alpha_i},\ \alpha_i = \frac{m_i^{\text{eff}}}{\sum_1^3 m_i^{\text{eff}}}$	0.97	[0.80, 1.30]	0.95	[0.84, 1.10]
35	Combined (mode 1 to 4) spectral acceleration	S_a^{1-to-4}	$\sum_{i=1}^{4}\left(S_a\left(T_i, \xi\right)\right)^{\alpha_i},\ \alpha_i = \frac{m_i^{\text{eff}}}{\sum_1^4 m_i^{\text{eff}}}$	0.95	[0.82, 1.10]	0.95	[0.86, 1.10]
36	Combined (mode 1 to 5) spectral acceleration	S_a^{1-to-5}	$\sum_{i=1}^{5}\left(S_a\left(T_i, \xi\right)\right)^{\alpha_i},\ \alpha_i = \frac{m_i^{\text{eff}}}{\sum_1^5 m_i^{\text{eff}}}$	0.96	[0.86, 1.10]	0.96	[0.89, 1.10]
37	Combined (mode 1 to 6) spectral acceleration	S_a^{1-to-6}	$\sum_{i=1}^{6}\left(S_a\left(T_i, \xi\right)\right)^{\alpha_i},\ \alpha_i = \frac{m_i^{\text{eff}}}{\sum_1^6 m_i^{\text{eff}}}$	0.95	[0.85, 1.10]	0.95	[0.90, 1.02]

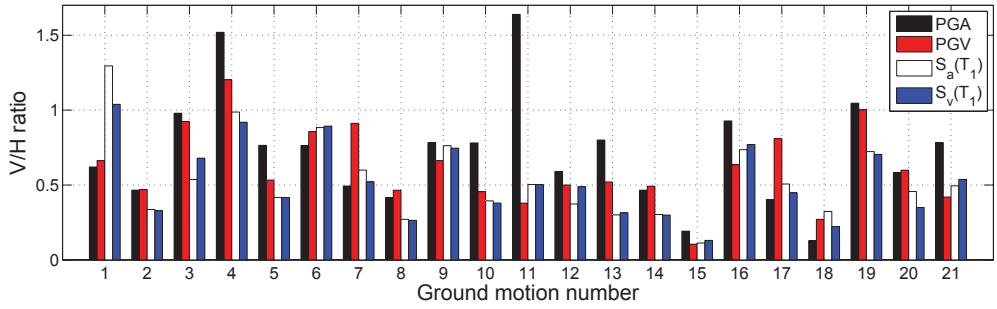

(a) Acceleration and velocity dependent IMs

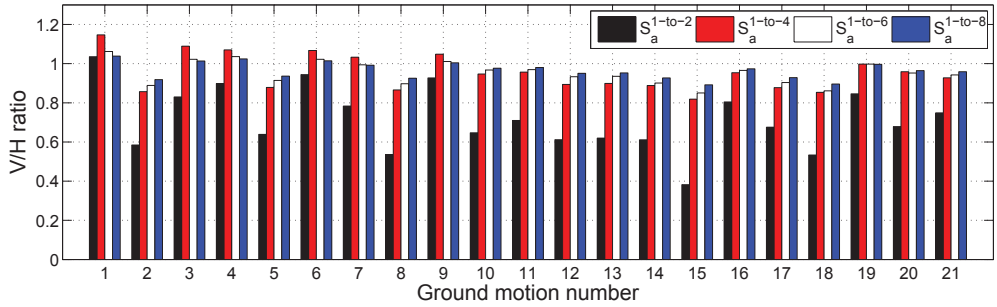

(b) Proposed combined spectral accelerations

Figure 9.2: Detailed V/H ratio in the single ground motions

9.4 Transient Structural Analysis

As previously indicated the second step of the PBEE method is the structural analysis. This will be performed for the 122 m high Pine Flat gravity dam. The finite element code Merlin (Saouma et al., 2010) is used for analysis. 4-node and 3-node plain strain 2D elements are used for modeling the dam body and the foundation. Nonlinearity stems from the use of zero-thickness interface elements for modeling the discrete joints (Cervenka et al., 1998). Also smeared crack model is used for simulation of concrete cracking. Applied loads are: 1) self-weight, 2) hydrostatic pressure, 3) uplift which is automatically updated with crack propagation, and 4) seismic loads.

There are four analyses possibilities in the context of this study, those are shown in the IM-EDP space in figure 9.3. First the single deterministic analysis (SDA) is performed for one ground motion and one intensity level. Then the same ground motion can be extended to different seismic intensities until failure occurs in the last point, single-record incremental dynamic analysis (SR-IDA). Then the effect of multiple ground motions at a given seismic intensity are performed

in the context of single strip analysis (SSA), and failure may or may not occur along any point (depending on the selected IM magnitude). Finally, the effect of multiple ground motions at multiple intensities is performed by an MR-IDA. Those analysis (with exception of the SSA) will be reported sequentially below.

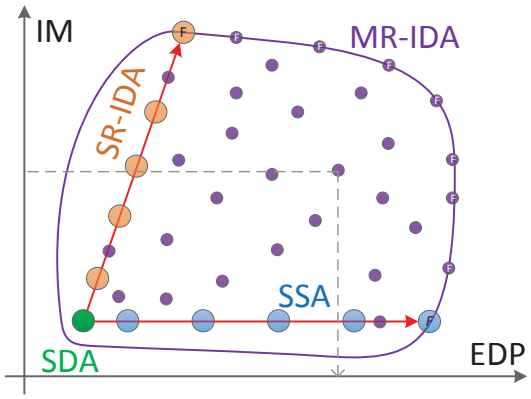

Figure 9.3: Interaction among Analyses techniques

9.4.1 Single Deterministic Analysis

Impact of vertical ground motion on the dynamic response of Pine Flat is first assessed through a single deterministic analysis. In this study, all the nonlinearity stems from the zero-thickness interface joint. Ground motion record 1 from Table 9.1 is selected and the corresponding $\frac{PGA^V}{PGA^H}$, $\frac{PGV^V}{PGV^H}$, and $\frac{PGD^V}{PGD^H}$ are equal to 0.62, 0.66, and 0.59 respectively. PGA^H and PGA^V are reached at t = 3.68 and 3.06 s respectively. Thus, t_{V-H} is 0.62 s. I_A of the horizontal component is nearly twice the vertical one, however, in the time interval [1, 3] s, the vertical component has higher intensities. $\frac{S_a^V(T_i)}{S_a^H(T_i)}$ ratio for the first five vibration periods of the system are 1.29, 0.79, 1.02, 0.88, and 0.73. Thus, at the fundamental period (T = 0.44 s) the vertical component has higher spectral value.

Figures 9.4(a) and 9.4(b) show the displacement time histories at the index point (crest). As can be noted, the vertical component of the ground acceleration has dramatically increased the

displacement in both horizontal (+ 60%) and vertical (+ 50%) directions. It is noteworthy that peak displacement due to "H only" and "H + V" occur at different times.

Figures 9.4(c) and 9.4(d) show the principal stresses. Again the combined "H + V" results in higher stress than for "H only". Accounting for the vertical component increased the (tensile) S11 at crest by nearly 85%; however, the mean value of stress increases in the body is only 7%. On the other hand, the S11 at the heel increased from 0.57 to 0.60 MPa due to vertical component effect.

Figure 9.4(e) shows the normalized base crack length at the dam-foundation interface. In this case the vertical component had no impact, however, inclusion of the vertical component leads to an earlier joint fracture. Figures 9.4(f) and 9.4(g) show the total horizontal and vertical forces acting on the interface joint. In both cases, including the vertical component increases the forces; however, and as expected, the vertical component drastically increased the total normal force (by nearly doubling it). Figures 9.4(h) and 9.4(i) show the time history of joint opening and sliding at the heel. Again in both cases "H + V" lead to higher responses. Comparing these two figures with figure 9.4(e) reveals that the joint opening/sliding starts at about 0.5-1.0 s after the second major cracking at the base.

9.4.2 Single Record Incremental Dynamic Analyses

9.4.2.1 Anatomy of SR-IDA

One of the main challenges in a probabilistic based analysis, is the determination of the LS or the performance level (PL) of a structure. This can be indeed achieved through a SR-IDA. This paradigm starts with an initial record and its IM (both horizontal and vertical components). It is first normalized such that the PGA is equal to one, and then multiple analyses are performed by gradually scaling the record by a scale factor until failure occurs.

The SR-IDA of a steel frame (IM vs inter-story drift) is reported to have anyone of four forms (Vamvatsikos and Cornel, 2002), figure 9.5(a): 1) Softening response, 2) limited hardening,

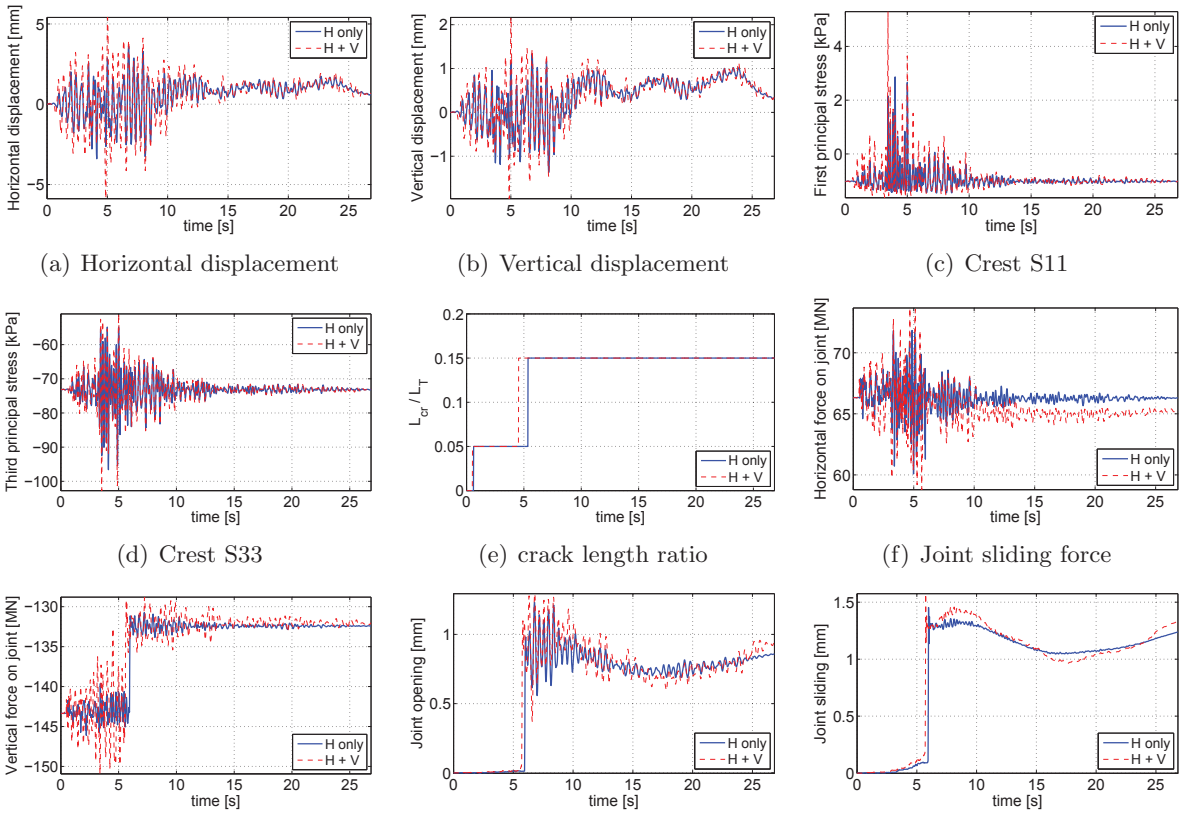

(a) Horizontal displacement (b) Vertical displacement (c) Crest S11

(d) Crest S33 (e) crack length ratio (f) Joint sliding force

(g) Joint normal force (h) Joint opening at heel (i) Joint sliding at heel

Figure 9.4: Time history response of a deterministic analysis

3) severe hardening, and 4) wavy response.

In an attempt to determine the SR-IDA curves for gravity dams, all 21 records of Table 9.1 were subjected to the SR-IDA, and three forms were identified for the IM in terms of the EDP (crest displacement) and four types for IM in terms of damage index - DI (crack ratio), figure 9.5(b) and 9.5(c), respectively.

Whereas the softening response of the concrete dam is expected, the hardening one is enigmatic. This is attributed to the fact that two scaled ground accelerations at a given time t may result in damages in two different locations Vamvatsikos and Cornel (2002). In gravity dam, cracking tend to initiate at the heel, and depending on the ground motion amplitude different cracking patters may follow.

From the IDA curve, one can extract any desired LS or PL using the following rules:

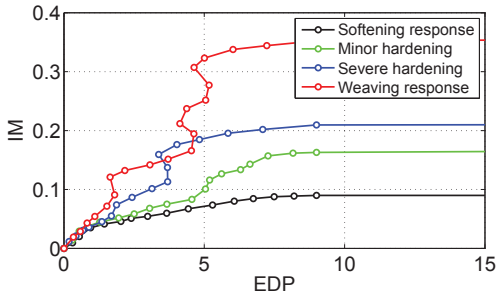

(a) Framed structure, adapted from Vamvatsikos and Cornel (2002)

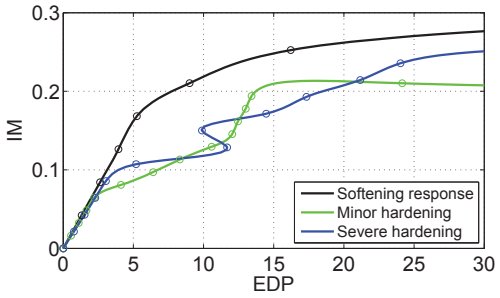

(b) Concrete gravity dam, (EDP)

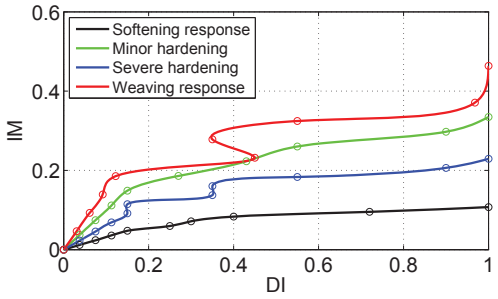

(c) Concrete gravity dam (DI)

Figure 9.5: SR-IDA curves

EDP-based rule: (such as imposing a limitation on the crest displacement) starts by selecting the EDP capacity, C_{EDP} on the basis of experiments, theory, or engineering judgment, figure 9.6. The lowest corresponding IM is to be selected as the failure one.

IM-based rule: is where one seeks to determine the IM which will cause complete failure of the structure. It is to be selected along the highest asymptotic value in the curve. Other intermediary horizontal segments are indicative of localized failure, Fig. 9.6.

9.4.2.2 Multiple Component SR-IDA

In Sec. 9.4.1, differences between analysis with single and multiple components were addressed within the context of a SDA, figure 9.4. In this section, the differences caused by multiple over single component in the context of SR-IDA figure 9.6 indicate that inclusion of the vertical component reduces the IM failure capacity, C_{IM}. Furthermore, for a given IM, the vertical displacement is smaller than the horizontal one for both "H only" and "H + V", and finally, "H + V"

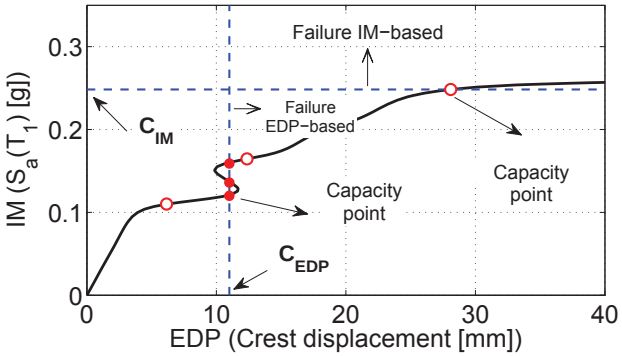

Figure 9.6: Determination of capacity points on an IDA curve

results in larger displacements.

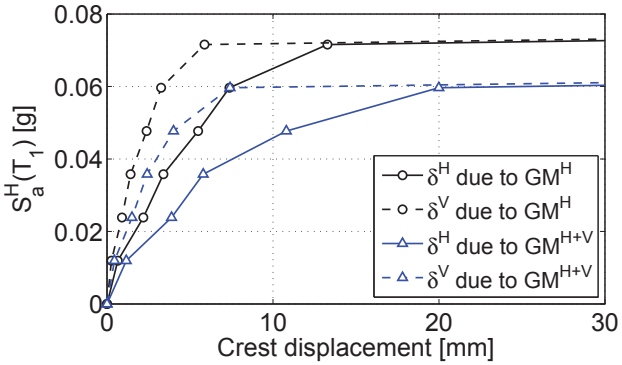

Figure 9.7: SR-IDA curves for multiple-component signals

In the classical PBEE literature associated with buildings, it is shown that in an IDA a first failure triggered by an IM_j may be followed by a non-failure at IM_{j+1} and failure again at IM_{j+2}. The transition from j to $j+1$ has been labeled as "resurrection" (Vamvatsikos and Cornel, 2002). It was determined that to capture such a phenomena in concrete dams one must model the concrete nonlineariy (using smeared cracks) in addition to the discrete nonlinear rock/concrete interface. This is shown in figure 9.8 and resurrection occurs only for "H + V" between IM 4 and 6 (9.8(p), 9.8(q) and 9.8(r)). Moreover, the overall failure is at lower amplitude in "H + V" than "H only".

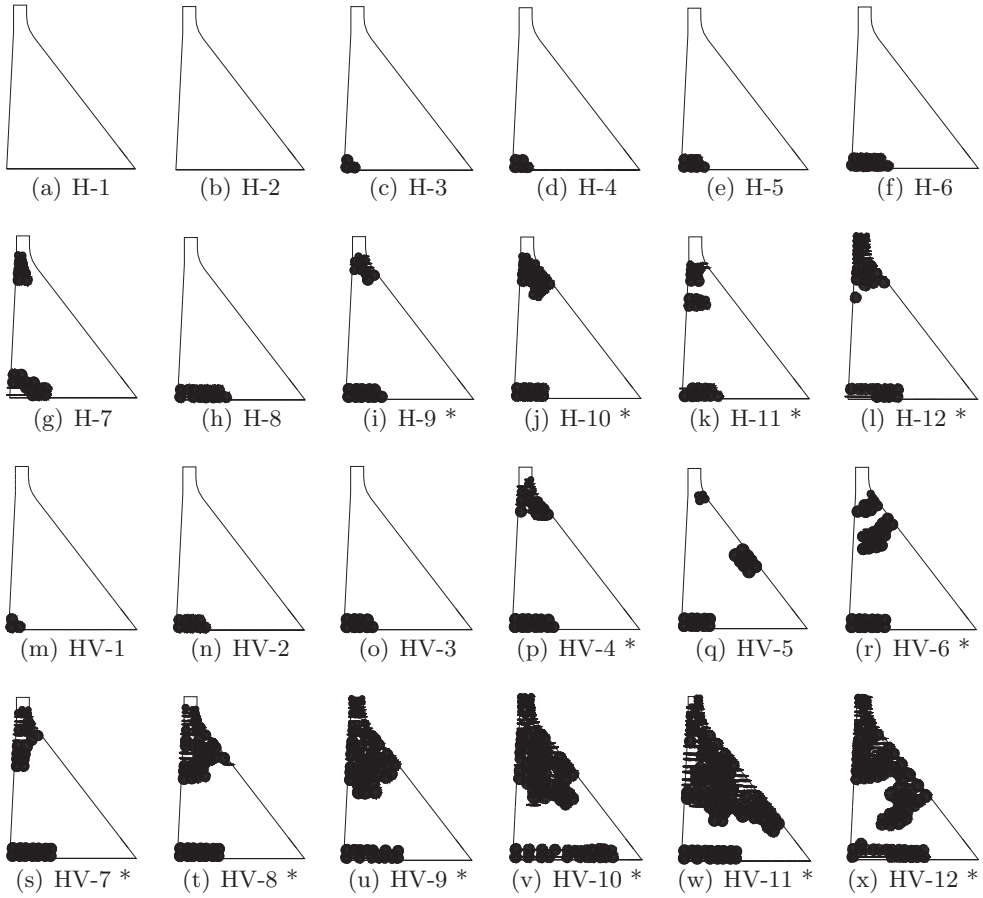

Figure 9.8: Progressive failure under SR-IDA considering multiple-component effects (* means failure)

9.4.3 Multiple Record Incremental Dynamic Analysis

With reference to figure 9.3 this last procedure relies on all 21 records tabulated in Table 9.1 and each one of them scaled incrementally.

Results are shown in figure 9.9(a) for both cases "H only" and "H + V" where the EDP corresponds to the crest horizontal displacement and the IM to $S_a(T_1)$. Both the discrete data points and a fitting spline are shown. Each one of the curves corresponding to a SR-IDA (as investigated in the previous section) can not be used directly in a PBEE analysis. However, having performed 21 analyses, one can determine the median, 16% and 84% fractiles, figure 9.9(b). As expected "H + V" yield smaller IM capacities. Finally, figure 9.9(c) shows the dispersion of $S_a(T_1)$

given δ^H. For nearly all ranges of δ^H, "H + V" result in higher dispersion, i.e. spread between the resulting SR-IDAs.

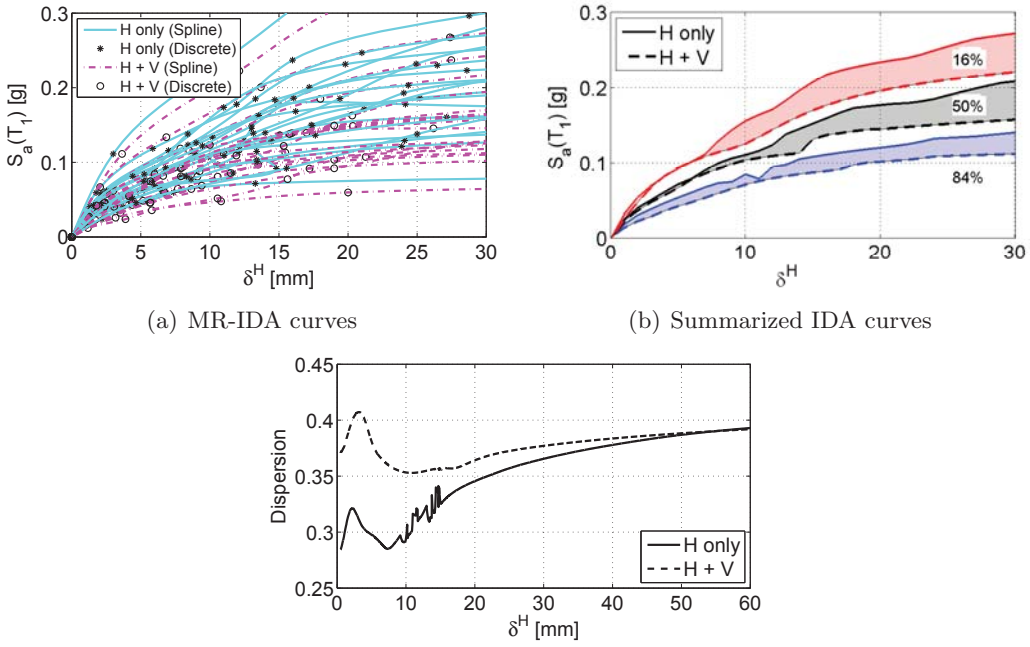

(a) MR-IDA curves

(b) Summarized IDA curves

(c) Dispersion given δ^H

Figure 9.9: MR-IDA curves for IM Corresponding to Spectral Acceleration

Whereas figure 9.9 had the IM corresponding to $S_a(T_1)$, it is important to assess the impact of alternative IMs. Results of such investigation are shown in figure 9.10 for IM equal to the PGA, ASI and S_a^{1-to-2}, while the EDP is the horizontal crest displacement. Again, in all cases, the "H + V" still has a lower IM capacity than "H only", the dispersion for S_a^{1-to-2} is smaller than the other two (a desirable effect). For investigation of the other IMs listed in Table 9.2 results are shown in Table 9.3. The following conclusions can be drawn:

- In most IM parameters, "H + V" leads to equal or higher dispersion than "H only".
- Displacement-related IMs result in higher dispersion.
- In most cases, acceleration-related IMs are better than velocity-based ones.
- Spectral-related IMs lead to the lowest dispersion.

- Lowest dispersion is achieved through combined spectral acceleration (33-37 in Table 9.2).
- Increasing the contribution of modes in the combined spectral accelerations result in a reduction of the dispersion for "H only", and a stable one for the "H + V" case. This can be attributed to the predominantly horizontal vibration modes.

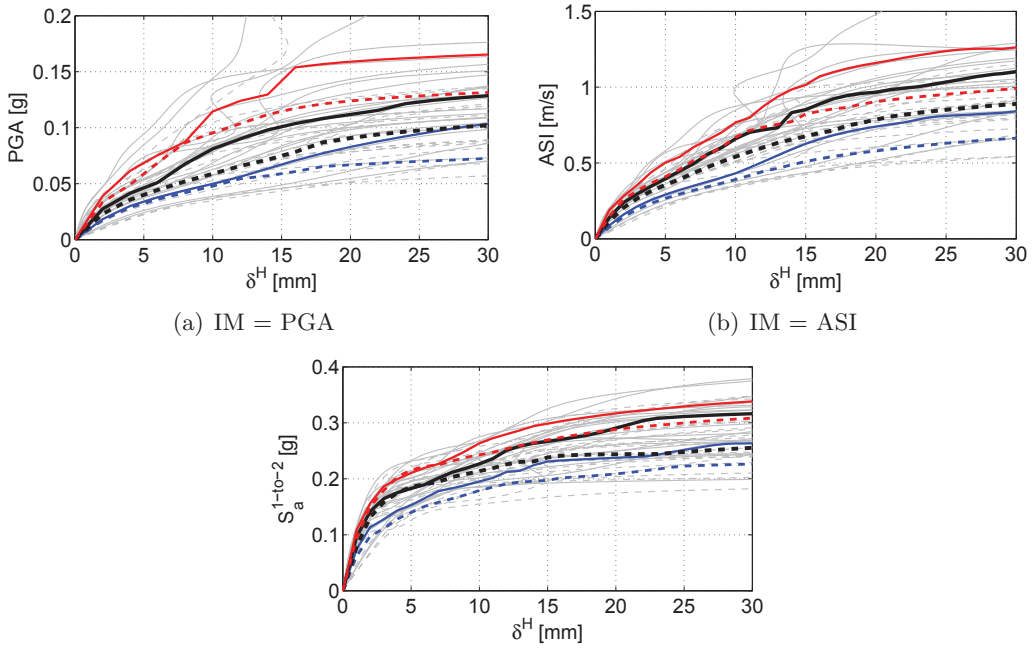

(a) IM = PGA

(b) IM = ASI

(c) IM = S_a^{1-to-2}

Figure 9.10: Impact of IM on the MR-IDA curves and their summary

Table 9.3: Dispersion of MR-IDAs with different IMs given EDP collapse

IM	"H only"	"H + V"	IM	"H only"	"H + V"	IM	"H only"	"H + V"
PGA	0.26	0.27	PGV	0.57	0.55	PGD	1.13	1.13
a_{RMS}	0.38	0.39	v_{RMS}	0.72	0.72	u_{RMS}	1.31	1.32
I_A	0.45	0.45	SED	1.36	1.34	CAV	0.32	0.33
CAD	0.72	0.72	$I_{v/a}$	0.69	0.68	I_C	0.56	0.59
I_a	0.26	0.29	I_v	0.43	0.43	I_d	1.12	1.13
I_F	0.59	0.59	I_D	0.50	0.60	SIR	0.70	0.71
ASI	0.19	0.19	VSI	0.47	0.46	DSI	0.89	0.89
EPA	0.19	0.19	EPV	0.52	0.52	$S_a(T_1)$	0.39	0.39
$S_v(T_1)$	0.34	0.35	$S_d(T_1)$	0.39	0.39	$S_a(T_p^{accel})$	0.27	0.27
$S_v(T_p^{vel})$	0.65	0.63	S_a^{1-to-2}	0.17	0.18	S_a^{1-to-3}	0.12	0.15
S_a^{1-to-4}	0.08	0.15	S_a^{1-to-5}	0.07	0.15	S_a^{1-to-6}	0.06	0.15

The impact of IM was previously addressed on a single EDP (crest horizontal displacement).

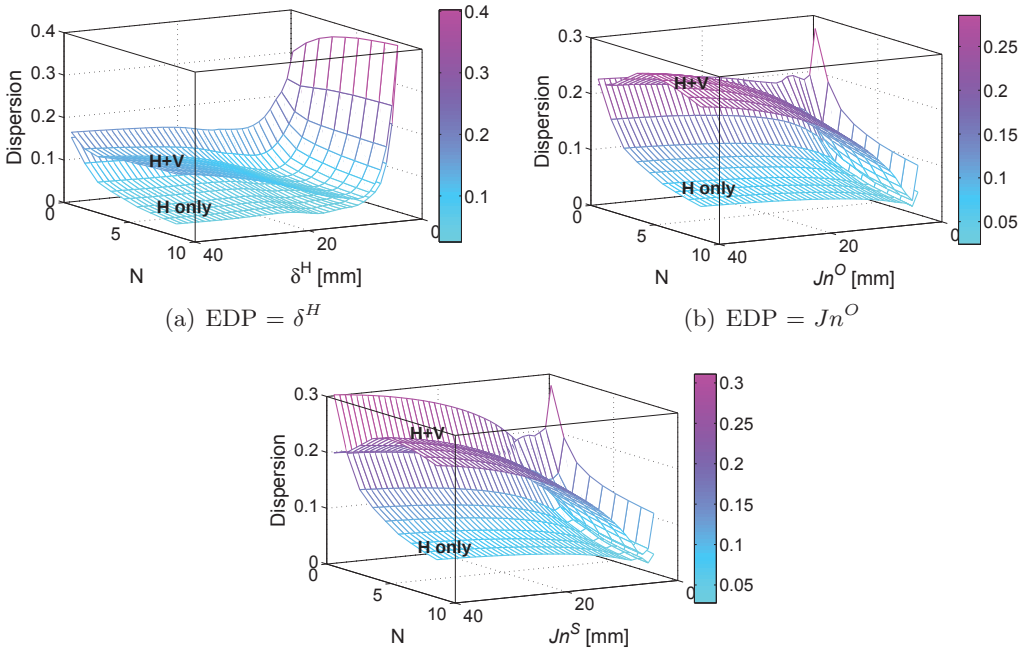

(a) EDP = δ^H

(b) EDP = Jn^O

(c) EDP = Jn^S

Figure 9.11: Dispersion of S_a^{1-to-N}, given different EDPs

Next the impact of the EDP is considered for the maximum joint opening at the base, Jn^O, and maximum joint sliding at the base, Jn^S. Figure 9.11 shows the magnitude of dispersion in terms of the combined spectral acceleration, S_a^{1-to-N} and range of selected EDP. Again, "H only" leads to lower dispersion in all three EDPs and as in the previous study, increase in N decreases the dispersion for "H only".

9.5 Collapse Fragility Curves

Having determined the MR-IDA it is now possible to determine the collapse fragility curves. With reference to figure 9.12, first the asymptotic value of the IM is tagged as the failure one. Then a probability distribution function (PDF) is fitted through this data points (typically a log-normal one), and the corresponding cumulative distribution function (CDF) determined (Eq. 9.2). To determine the corresponding β and η all three previously mentioned methods (MM, SSE, and MLE) are examined (Eqs. 9.3, 9.4 and 9.5). Finally, the fragility curves are plotted, figure 9.13

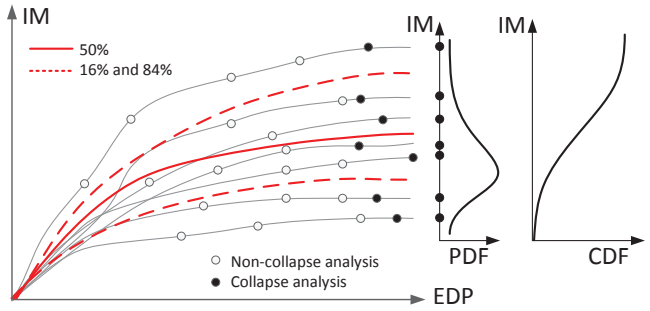

Figure 9.12: Determination of collapse fragility curve from MR-IDA

(showing two different IMs). The worst fit was achieved through the simplest method (MM) as it underestimated the probability of collapse for both IMs. This is consistent with the essence of this simplified method which seeks to match the central parameters (median and standard deviation) rather than the entire distribution as also determined in Lallemant et al. (2015).

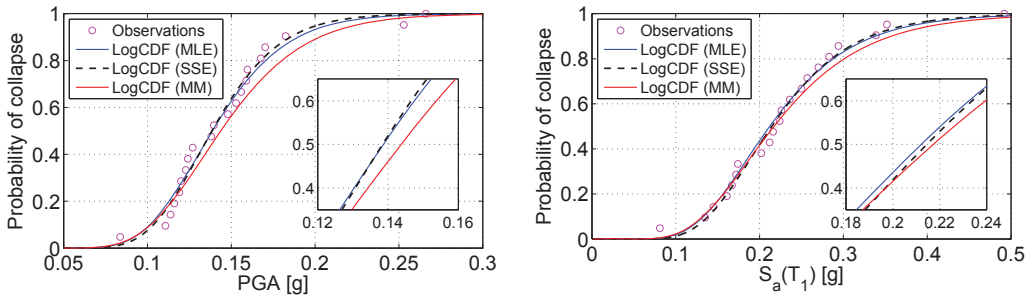

(a) IM = PGA

(b) IM = $S_a(T_1)$

Figure 9.13: Comparison of different methods for collapse fragility curves

Figure 9.14 shows the impact of vertical ground motion component on the fragility curves. Three IMs are used: $S_a(T_1)$, S_a^{1-to-2} and S_a^{1-to-4}. In all cases, accounting for the vertical component reduces the median of the probability of collapse by 22%, 13% and 8%. Also, as shown in the tabulation of the dispersion for various IM (Table 9.3), $S_a(T_1)$ does not affects the dispersion; however, incorporating the higher modes increases the dispersion of "H + V" with respect to "H only". Note that incorporating the higher modes, reduces the goodness-of-fit of log-normal distribution to

the data points.

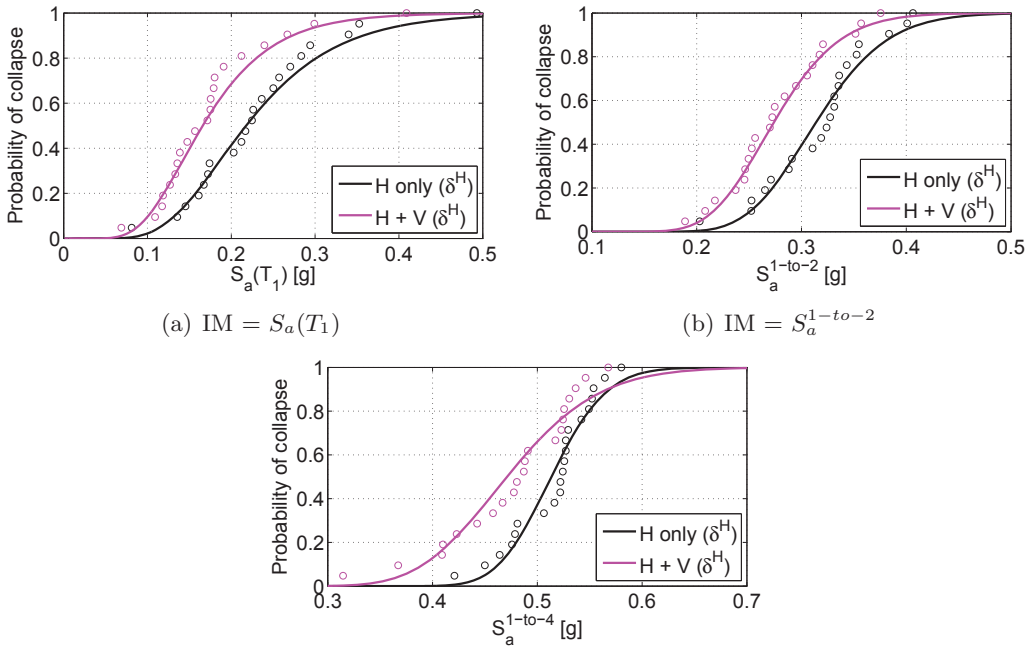

(a) IM = $S_a(T_1)$

(b) IM = S_a^{1-to-2}

(c) IM = S_a^{1-to-4}

Figure 9.14: Vertical component effect on the collapse fragility curve with respect to IM

9.6 Discussion

9.6.1 Epistemic and Aleatory Uncertainties

In so far, the only variability was the record-to-record (aleatory uncertainty) while the material properties were deemed to be deterministic. On the other hand, one could account for both uncertainties (aleatory and epistimic) (Liel et al., 2009), (Vamvatsikos and Fragiadakis, 2010), (Celik and Ellingwood, 2010), and (Celarec and Dolsek, 2013).

Figure 9.15(a) shows results of an uncertainty analysis under ETA (Hariri-Ardebili and Saouma, 2015b) for the same Pine Flat dam. It shows the dispersion, β_U, of capacity curves at collapse for 12 single random variables (RV) and a correlated model. The twelve RVs are: RV1 = concrete mass density, RV2 = concrete modulus of elasticity, RV3 = concrete Poisson's ratio, RV4 = rock modulus of elasticity, RV5 = joint tangential stiffness, RV6 = joint normal stiffness,

RV7 = joint tensile strength, RV8 = joint cohesion, RV9 = joint friction angle, RV10 = joint dilatancy angle, RV11 = joint specific mode I fracture energy, RV12 = joint specific mode II fracture energy, Corr = uncertainty in all RVs with correlation.

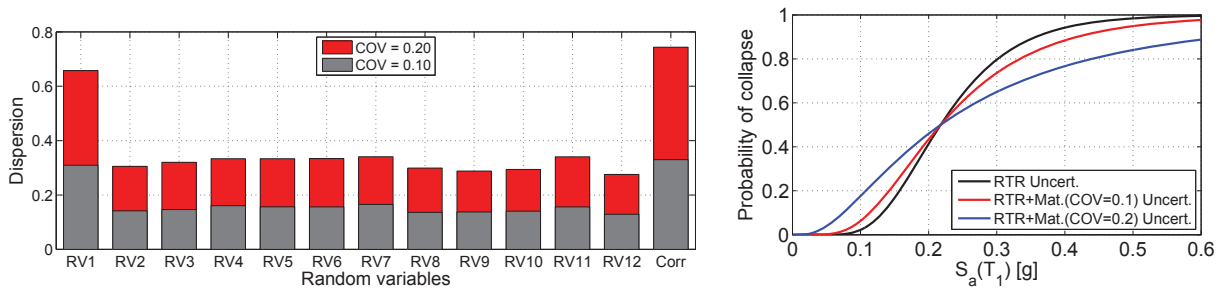

(a) Material uncertainty

(b) Combined curves

Figure 9.15: Impact of aleatory and epistimic uncertainty on collapse fragility curves

Ideally one would perform Monte Carlo simulation with direct sampling which accounts for both uncertainties (Celarec and Dolsek, 2013), however this can be very computer intensive for the nonlinear analysis of dams. An alternative and simplified method combines analytically the two uncertainties through (Cornell et al., 2002):

$$\beta_{RU} = \sqrt{\beta_R^2 + \beta_U^2} \tag{9.6}$$

where β_R is the uncertainty associated with the record-to-record aleatory randomness (and previously determined in this paper). Hence, the originally determined fragility curves in terms of β_R are replaced with β_{RU}. Major underlying assumptions in Eq. 9.6 are: 1) The two sources of uncertainties are independent, and 2) Median values remain constant while the dispersion is altered. Finally, it should be noted that some recent studies have shown that the epistemic uncertainty not only increases dispersion but also affects the median response (Liel et al., 2009), (Vamvatsikos and Fragiadakis, 2010) and (Dolšek, 2012).

The resulting collapse fragility curves with both uncertainties is shown in figure 9.15(b). Two curves associated with two levels of material variation (COV = 0.1 and 0.2) are presented. As seen, epistemic uncertainty increase the total dispersion and makes the curves wider. Note that the results are presented only for horizontal excitation.

9.6.2 Impact of Reservoir Elevation

Impact of reservoir elevation is assessed next. First, ten natural periods of dam, dam plus foundation, and dam plus foundation plus water are determined, figure9.16(a). Then, the corresponding fragility curves for the full and empty dams are computed, figure 9.16(b). For this dam, $\frac{\eta^{\text{Full}}}{\eta^{\text{Empty}}}$ is 0.75 and 0.78 for "H only" and "H + V" cases, respectively. $\frac{\beta^{\text{Full}}}{\beta^{\text{Empty}}}$ is 1.08 in both cases, i.e. the dispersion is not affected. Note that PGA is used as IM to avoid dependency to the vibration period.

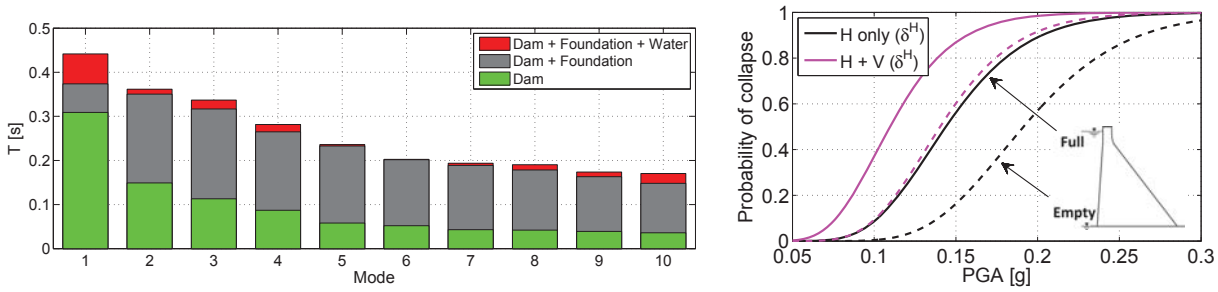

(a) Vibration period of the system

(b) Combined curves

Figure 9.16: Impact of water level on collapse fragility curves

9.6.3 IDA *vs.* PSDA

MR-IDA is based on ground motion scaling to capture the structural behavior from linear to collapse. The nature of scaled ground motion has been questioned if a larger scale factor is used (Vamvatsikos and Cornel, 2002). On the other hand, probabilistic seismic demand analysis (PSDA) uses a set of un-scaled ground motions to derive fragility curves Jalayer (2003). Hence, it is important to compare those two approaches for dams.

Figure 9.17(a) shows a cloud-based PSDA using 100 un-scaled ground motions and the linear regression (Hariri-Ardebili and Saouma, 2015a). These data are used to derive the median and dispersion of fragility curves. Then, figure 9.17(b) compares the PSDA and MR-IDA at four LS (corresponding to 10%, 30%, 60% and 99% of the crack ratio at base). At the collapse level (LS = 0.99%) PSDA has higher median than IDA whereas at LS = 0.60% they are almost identical, and

for LS = 0.30% and 0.10% IDA has higher median. Increasing crack limit state in PSDA increases the dispersion; however, this is less sensitive for the IDA. These findings are consistent with those reported by (Zhang and Huo, 2009) and (Jalayer et al., 2014).

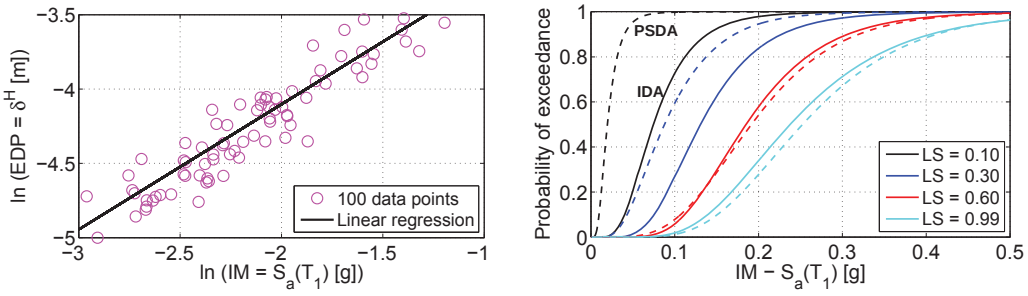

(a) Cloud-based PSDA (b) Comparison of fragility curves

Figure 9.17: Impact of ground motion scaling on the fragility curve

9.7 Conclusions

The probabilistic seismic response of an gravity dam is explored in the context of performance based earthquake engineering. The effect of intensity measure was first addressed to determine the optimal one. Then transient nonlinear analyses were performed through three methods of increasing complexity culminating with the multiple record incremental dynamic analysis. Results of which were subsequently used to determine the collapse fragility curves in which both aleatoric and epistemic uncertainties were accounted for. Throughout the analyses, importance of the vertical component of the ground motion was emphasized.

Chapter 10

Hybrid Damage Index for Gravity Dams

This chapter is based on:

Hariri-Ardebili, M.A. and Saouma, V.E., (2015), Quantitative failure metric for gravity dams, Earthquake Engineering and Structural Dynamics, 44(3): 461-480.

10.1 Introduction

Dams are critical components of a nation's infrastructure. They provide energy, flood protection, water storage for domestic, industrial, agricultural use and recreation. Yet, many dams are aging and most were designed at a time with limited seismic field data, or technical knowledge. Taking a simple binary approach Safe/Fail, as commonly done presently through a deterministic application of safety codes (FERC-PFMA, 2005; USACE, 2007; CDA, 2007) is not only unrealistic but could yield very expensive rehabilitation program. On the other hand, Performance Based Earthquake Engineering (PBEE) (Gunay and Mosalam, 2013; Porter, 2003), by now widely embraced for buildings, does provide a new paradigm for dams, one where nonlinear time history analysis is performed and quantitative failure assessment is necessary.

Indeed dams have historically provided a framework of applications for innovative numerical methods, such as the finite difference one (Richardson, 1911) or the finite element method (Clough and Wilson, 1962). Whereas linear elastic analysis prevailed for a long time (Basu, 2009) due to limited computational capabilities, new advances in hardware has lead to innovative nonlinear

transient analysis models (Omidi and Lotfi, 2013; Zhang et al., 2013a; Nayak and Maity, 2013). Dam-foundation interaction and also modeling the far-end boundaries of the semi-infinite medium were investigated by other researchers (Basu and Chopra, 2004; Saouma et al., 2011; Hariri-Ardebili and Mirzabozorg, 2013).

Damage analysis is one of the four steps which is used in PEER (Pacific Earthquake Engineering Research) PBEE. The relationship between these steps is shown in Fig. 10.1. During the dynamic analysis, the structure undergo certain damage characteristics that are associated with significant changes in its strength and behavior. Damage can be described qualitatively (Damage State- DS) and quantitatively (Damage Index- DI). Various researchers proposed damage indices with different applications for framed structures. Cumulative local damage indices such as: normalized cumulative rotation (Banon and Veneziano, 1982), low cycle fatigue (Stephens, 1985), damage index (Park and AH-S., 1985), and energy-based damage index (Kratzig et al., 1989). Non-cumulative local damage indices such as: ductility ratio (Newmark, N.M. and Rosenblueth, E., 1971), interstorey drift (Roufaiel and Meyer, 1981), slope ratio (Toussi and Yao, 1982), flexural damage ratio (Roufaiel and Meyer, 1981), stiffness damage index (Ghobarah et al., 1999). Global damage indices such as: maximum and final softening (Dipasquale and Cakmak, 1988). Finally, damage spectra concept instead of the conventional damage index have been proposed (Bozorgnia and Bertero, 2003).

Although much has been reported in terms of analytical procedures for concrete dams, little attention has been given to result interpretations. Damage estimation methodology were first introduced Ghanaat (2004) and later adopted in the USACE guideline (USACE, 2007). It proposes a systematic method based on linear time history results in terms of local and global performance indices. It uses several criteria such as Demand Capacity Ratio (DCR), cumulative inelastic duration and the percentage of the overstressed area on dam body for evaluation of the seismic performance. Considering that the cracking behavior of mass concrete is governed by the strain components, the previously proposed stress-based methodology by USACE was expanded in term of the strain-based methodology (Hariri-Ardebili et al., 2013). Displacement-based and energy-based damage

indices for seismic assessment of gravity dams through a static pushover analysis and Incremental Dynamic Analysis (IDA) have been proposed (Alembagheri and Ghaemian, 2013b) and criteria for assessment of the accumulated damage in gravity dams in local and global space (Zhang et al., 2013a). The seismic vulnerability of an arch dam using Endurance Time Analysis (ETA) technique by comparing predicted crack profile from a nonlinear analysis with the overstressed area estimated by a linear elastic one has also been investigated (Hariri-Ardebili and Mirzabozorg, 2014). The capacity of the dam at different seismic intensity levels was quantitatively estimated as shown in Fig. 10.2. This figure represents the percentage of the overstressed area on upstream face of an arch dam as a function of DCR and Peak Ground Acceleration (PGA) of the applied excitation. Spatial distribution of the overstressed are also shown for the case with DCR=1.0 and different PGAs. As seen, the most vulnerable part of the dam is the upper central sections in vicinity of the crest. Results of linear analyses were subsequently validated with nonlinear models.

Within the context of PBEE, Damage Measure (DM) refer to physically observable damage states which can be subsequently related to repairs. Hence, the propensity for potential failure modes of concrete dams should be quantified.

In the present paper, the nonlinear seismic behavior of a concrete gravity dam is evaluated quantitatively using a multi-scale approach with different damage indices. The nonlinear behavior of mass concrete is formulated through damage plastic model, while the Drucker-Prager elasto-plastic model is adopted for crack simulation in the foundation rock. Potential failure modes for a gravity dam under dynamic excitation are detected and the appropriate criteria introduced for interpretation of the result.

10.2 Potential Failure Modes

10.2.1 Qualitative Observations

In the present study, three major potential failure modes of gravity dams are identified: a) overstressing, b) sliding along cracks inside the dam or planes of weakness within the foundation,

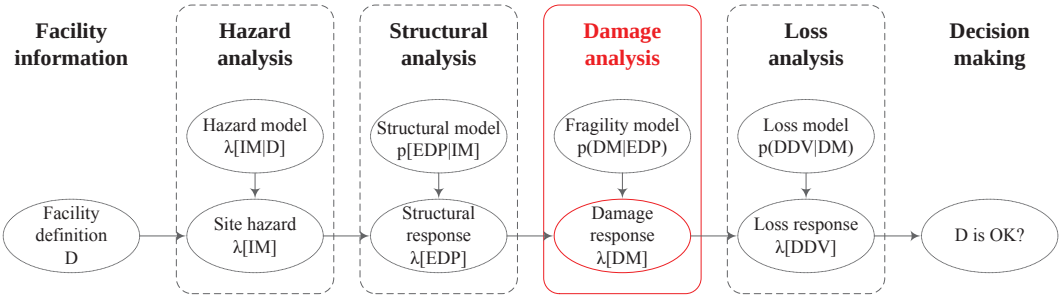

Figure 10.1: Framework of PEER PBEE methodology (Haselton et al., 2008)

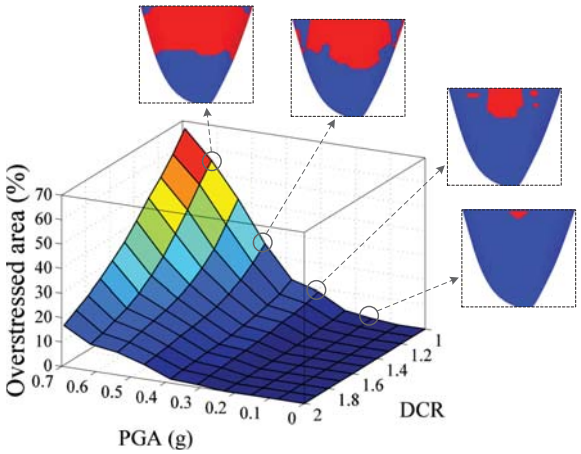

Figure 10.2: Quantitative seismic assessment of an arch dam (Hariri-Ardebili and Mirzabozorg, 2014)

and c) sliding accompanied by overturning. Many studies have shown that under severe ground shaking a typical gravity dam section may suffer tensile cracks at the base and/or near the upper downstream face discontinuity (Pan et al., 2011; Zhang et al., 2013a; Alembagheri and Ghaemian, 2013b). The upper cracks usually initiate from the upstream or downstream face of the dam and propagate horizontally or at an angle toward the opposite face. The consequence of cracking, if extended through the dam section, may lead to sliding or rotational instability of the separated block (Ghanaat, 2004). For earthquake motion in the upstream direction, the potential cracking usually occurs at the heel of the dam at the maximum expected water levels. For earthquake motion

in the downstream direction, the potential cracking usually occurs at the slope discontinuity under the minimum expected water level conditions and near the toe of the dam. As earthquake motion cycles swing toward the upstream direction, the potential cracking shifts to the upper part and the base of the dam (USACE, 2007).

Figure 10.3 shows failure mechanism of concrete gravity dams under increasing intensity of earthquake ground motions adapted from Leger (2007). As seen, under normal water level and imposed ground motion, there are some critical locations in dam where cracking may start at these locations. They are: (A) neck area at the change of downstream face slope; (B) along lift joints at various elevations; (C) along dam-foundation interface at the toe and heel of dam; and (D) horizontal, vertical or inclined cracking at the foundation in near-field of the dam. It should be emphasized the main source of nonlinearity stems from the rock-concrete interface. Hence, in practice there is no need to consider the far-field of the foundation in potential failure mode analysis of dam body.

In the context of PBEE, it is essential that damage indices be defined for that interface. Since brittle material (such as concrete and rock) are particularly sensitive to both the intensity and duration of the dynamic loading (Zhang et al., 2013a), the damage level will be evaluated within the dam through a cumulative damage index and for the dam-foundation system through both the damaged area on dam body and near-field foundation rock.

10.2.2 Quantitative Analysis Techniques

Failure analysis of a structure under seismic excitation is inherently nonlinear, and one seeks to determine the seismic excitation(s) which indeed trigger failure.

In its simplest form, such an analysis is deterministic. A ground motion is first selected (and scaled) based on the response spectrum of dam site and is applied to the coupled dam-reservoir-foundation system. This will provide a discrete damage index values (one DI corresponding to a single analysis). Hence, determination of the exact value for onset of the nonlinear behavior which precedes failure would require many analysis and results are highly ground motion-dependent.

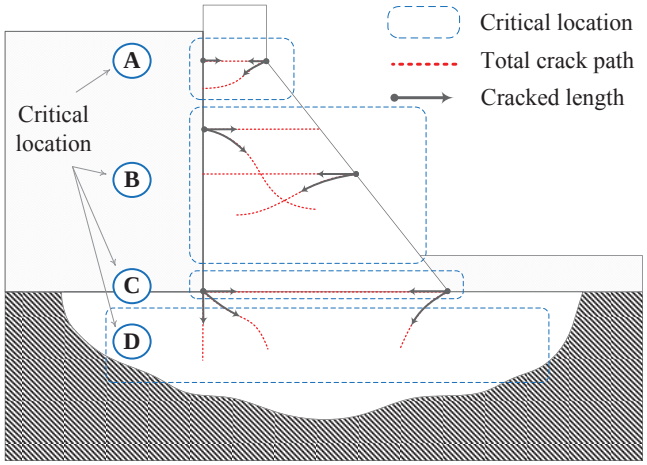

Figure 10.3: Potential failure mechanism of a typical gravity dam, critical locations and crack paths

Alternatively, a stochastic approach can be embraced. In this approach a set of p ground motions are selected based on a hazard analysis of the dam site. Then, each of these ground motions is incrementally scaled to q levels, thus a total of $p \times q$ nonlinear analyses are required to capture the seismic response of the coupled system at different intensity levels and under various ground motions (Vamvatsikos and Cornel, 2002). This method is refereed to incremental dynamic analysis. Application of IDA method to concrete dams (Alembagheri and Ghaemian, 2013b). Although this method provides a comprehensive assessment on the progressive failure analysis of concrete dam, the large number of analyses precludes it as it is computationally expensive and nearly impossible to undertake in practice.

Finally, an ETA can be undertaken. This method hinges on a set of e intensifying acceleration function to be generated. These artificial seismic excitation, called endurance time acceleration functions (ETAF) (Estekanchi et al., 2007) are generated such that their peak zero-period acceleration (PZA) and acceleration response spectrum remain linearly proportional to time. Hence, adoption of ETAFs for the transient analysis of gravity dams will result in a continuous response from linear elastic to the onset of nonlinear response, to crack initiation, to crack propagation, and finally to dam failure. Therefore, the progressive failure analysis can be captured through a single

analysis. Finally, because the artificial ground motions are generated through random numbers, it is best to average analysis results obtained from at least three ETAFs ($e = 3$) (Hariri-Ardebili and Mirzabozorg, 2014; Hariri-Ardebili et al., 2014a).

10.3 Damage Index in Reinforced Concrete Framed Structures

Given the lead taken by the building industry in spearheading PBEE (Porter, 2003; Gunay and Mosalam, 2013), this section will start by reviewing work done in this field.

10.3.1 Damage Index vs. Damage Variable

In general, damage in concrete or reinforcement concrete can be attributed to irrecoverable (inelastic) deformations. First one differentiates between *damage variable* (DV) and *damage index*. Any structural response that can be used as an indicator of damage is designated DV. Examples include: plastic deformation, energy dissipation, low cycle fatigue of element, and changes in vibrational parameter of structure. On the other hand, damage index, is a quantity set to zero in the absence of any damage and unity when failure or collapse occurs. A DI can be combination of one or several DVs (Kappos, 1997). Figure 10.4(a) illustrates the DI as a function of only one DV. DI is 0 at $DV \leq DV_0$ and its value is one at $DV = DV_u$ where the structure is failed. In fact, DV_0 and DV_u are the lower and upper boundaries (threshold) of the damage variable. Once the initial and the end points are determined, an appropriate function should be derived between the damage index and damage variable. The shape of this function should be defined based on experimental tests. The general format of this function can be (Kappos, 1997):

$$DI = \left(\frac{DV - DV_0}{DV - DV_u} \right)^{\kappa} \tag{10.1}$$

where κ is an exponent related to the rate of the changes in damage index at different stages of the damage variable.

If the DI is a function of more than one DV, e.g. two variables as DV^1 and DV^2, it can be

shown that the DI function will be given by:

$$DI = \left(\frac{DV^1 - DV_0^1}{DV^1 - DV_u^1}\right)^{\kappa_1} \times \left(\frac{DV^2 - DV_0^2}{DV^2 - DV_u^2}\right)^{\kappa_2} \tag{10.2}$$

where κ_1 and κ_2 are the exponents associated with the rate of the changes of the respective damage indices. Figures 10.4(b) and 10.4(c) show the relationship between the DI and two DVs where κ_1 and κ_2 are both larger than one or both smaller than one.

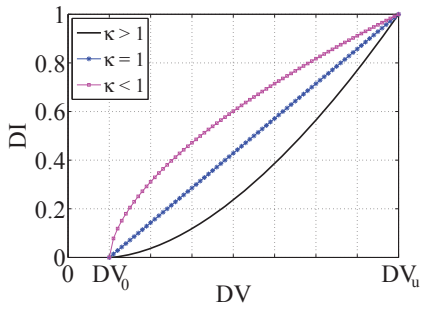

(a) $DI = f(DV)$

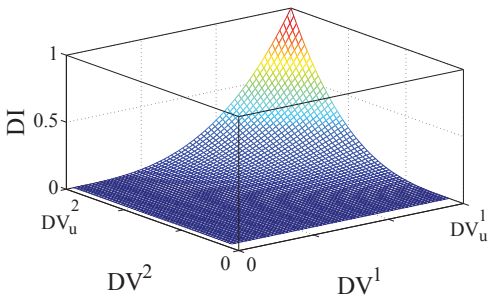

(b) $DI = f(DV^1, DV^2)$, κ_1, $\kappa_2 > 1$

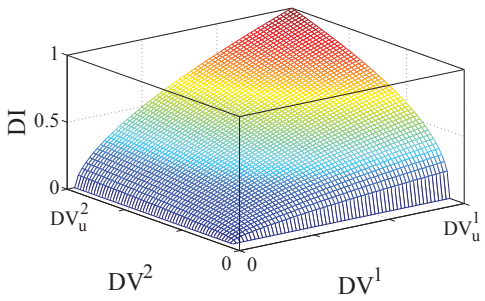

(c) $DI = f(DV^1, DV^2)$, κ_1, $\kappa_2 < 1$

Figure 10.4: Relationship between damage variable and damage index

10.3.2 Classification of Damage Index

As earlier stated, it is helpful to review and summarize the damage indices previously introduced for reinforced concrete framed structures as they may inspire those to be adopted for dams. Based on the summary shown in Table 10.1.

Table 10.1: Summary of the most important damage indices

ID	Category	Formula	Explanations
1	Deformation-based, non-cumulative, local Powell and Allahabadi (1988)	$DI_{\mu} = \frac{\Delta_{max}-\Delta_y}{\Delta_{mon}-\Delta_y} = \frac{\mu-1}{\mu_{mon}-1}$	Δ_{max} = maimum deformation Δ_y = yield deformation Δ_{mon} = maximum deformation under monotonically increasing lateral deformation $\mu = \Delta_{max}/\Delta_y$ $\mu_{mon} = \Delta_{mon}/\Delta_y$
2	Drift-based, non-cumulative, global	$DI_{\Delta} = \frac{\Delta^t_{max}}{H^t}$	Δ^t_{max} = maximum drift at the target point H^t = corresponding structural height
3	Displacement-based, cumulative Banon and Veneziano (1982)	$DI_{NCR} = \frac{\sum_{i=1}^{n}\lvert(\theta_{max})_i-\theta_y\rvert}{\theta_y}$	$(\theta_{max})_i$ = maximum rotation in cycle i θ_y = yield value n = number of cycles
4	Force-based, cumulative Wang and Shah (1987)	$DI_D = 1 - \frac{F_y}{F_{max}}$	F_y = failure force during a loading cycles F_{max} = maximum force during previous cycle
5	Hysteretic energy-based Cosenza and Manfredi (2000)	$DI_{E_H} = \frac{E_H}{E_{H\,mon}}$	E_H = non-recoverable dissipated hysteretic energy $E_{H\,mon}$ = hysteretic energy capacity of the structure obtained from pushover analysis
6	Multi-variable Park-Ang Park and AH-S. (1985)	$DI_{P-A} = \frac{\Delta_{max}}{\Delta_{mon}} + \beta\frac{E_H}{F_y\Delta_{mon}}$	F_y = yield strength $\beta \geq 0$ is a constant depends on the structural characteristics and history of inelastic response and is obtained by experimental test
7	Multi-variable modified Park-Ang Kunnath et al. (1992)	$DI^{modified}_{P-A} = \frac{\varphi_{max}-\varphi_y}{\varphi_u-\varphi_y} + \beta\frac{\int dE}{M_y\varphi_u}$	φ_u = ultimate curvature φ_y = curvature at failure point φ_{max} = curvature corresponding to the maximum bending moment M_y = bending moment at failure dE = incremental dissipated hysteretic energy
8	Global, based on the modal parameters of the structure Dipasquale and Cakmak (1988), Dipasquale and Cakmak (1989)	$\begin{cases} DI_{max} = 1 - \frac{T_{UD}}{T_{max}} & \text{maximum softening} \\ DI_{pl} = 1 - \frac{T^2_D}{T^2_{max}} & \text{plastic softening} \\ DI_F = 1 - \frac{T^2_{UD}}{T^2_D} & \text{final softening} \end{cases}$	T_{UD} = period of the undamaged structure T_D = period of the damaged structure T_{max} = natural period corresponding to the maximum softening
9	Damage spectra Bozorgnia and Bertero (2003)	$\begin{cases} DI^1_{B-B} = \left[\frac{(1-\alpha_1)(\mu-\mu_e)}{(\mu_{mon}-1)}\right] + \alpha_1\left(\frac{E_H}{E_{H\,mon}}\right) \\ DI^2_{B-B} = \left[\frac{(1-\alpha_2)(\mu-\mu_e)}{(\mu_{mon}-1)}\right] + \alpha_2\sqrt{\left(\frac{E_H}{E_{H\,mon}}\right)} \end{cases}$	$\mu_e = \Delta_{elastic}/\Delta_y$ = elastic ductility $\mu_e = 1$ for inelastic behavior $\mu_e = \mu$ if the response remains elastic $0 \leq \alpha_1 \leq 1$ and $0 \leq \alpha_2 \leq 1$ are two constant coefficients

Following is the summary of different classifications:

Local vs. Global: Local DI is an indicator of damage in an element, member, or limited part of the structure. The global DI on the other hand captures damage state in an entire. The global DI can be computed by weighted summation of the local DIs.

Single-variable vs. Multi-variable: As shown in Figure 10.4 the DI can be computed either from a single variable or from a combination of several ones. Usually combined DI takes into account different parameters and provides a more comprehensive indicator of the damage progress.

Cumulative vs. Non-cumulative: A cumulative DI is capable of capturing the accumulation of the damage during the transient analysis, whereas a non-cumulative one can only capture the end state.

Deterministic vs. Stochastic: As all materials are heterogeneous, the DI may or may not capture this heterogeneity through stochastic or deterministic expressions.

Damage index vs. Damage spectrum: Damage spectrum represents variation of the damage index versus the structural period for a series of single-degree-of-freedom systems subjected to a ground motion record (Bozorgnia and Bertero, 2003).

Structural vs. Economical: Structural DI captures the damage in terms of structural parameters. On the other hand, an economical DI would introduce concepts of cost such as the ratio of repair cost to corresponding replacement cost.

10.4 Quantitative Failure Metric for Dams

10.4.1 Proposed Damage Index for Gravity Dams

Based on the summary of the damage indices reviewed in the previous section, a cumulative multi-variable damage index is introduced for concrete gravity dams. This DI will handle local,

intermediate, and global states. The controlling variables in the proposed damage index are crack length L^C, dissipated energy E_H, and maximum drift u_{max}.

$$DI = f\left(L^C, E_H, u_{max}\right) \tag{10.3}$$

The dam structural integrity will be assumed to reach unity (critical) when a thorough crack (connecting upstream and downstream faces) occurs. Hence, a micro damage index for each of the critical locations shown in Figure 10.3 is defined as the weighed ratio of cracked length over the estimated total crack path:

$$DI_i^j = \beta_\Delta \times \frac{L_i^C}{L_i^T} \tag{10.4}$$

where $DI_i^j \in [0,1]$ is a micro damage index where i and j refer to the i^{th} crack path in the j^{th} critical location and $j = A, B, C, D$ shown in Fig. 10.3. L^C and L^T are the cracked and total lengths, respectively. β_Δ is the controlling coefficient which is computed based on the index point's displacement.

It is noteworthy that the DI is a post-analysis quantity which is determined from the controlling damage variables obtained from nonlinear analysis. Definition of the L^T deserves special attention. There are two possibilities, i.e. either the thorough crack pre-exists or the section is initially partially cracked. In the former case, the length of L^T is deterministic as it can be accurately quantified. In the later, it is estimated based on Fig. 10.3 and accounting for the fact that a crack will always propagate such that there is minimum energy dissipation. In those cases where the crack abruptly changes its path, then Eq. 10.4 would lead to conservative results.

The case of a thorough crack across the concrete dam deserves special attention. Whereas at first one may conclude that a thorough crack (upstream-downstream) is indeed synonymous with failure, this is not necessarily the case. Indeed a thorough crack where the upper segment did not overturn is indicative of severe damage but not failure. Conceptually, this is akin of a dam resting on concrete foundation with a contact surface providing shear resistance through friction exclusively. For example, the 109 m high Sefid-rud concrete buttress dam suffered thorough crack during the devastating 1990 Manjil earthquake, and the dam was subsequently repaired and strengthened using

epoxy grouting and post-tensioned anchors (Ghaemmaghami and Ghaemian, 2009). Examples of seismic analysis of a dam with concrete thorough crack include (Ghaemmaghami and Ghaemian, 2008; Malla and Wieland, 1999). In both cases analysis starts with a fully developed crack from upstream to downstream. Accordingly, a dam may have a thorough crack ($\frac{L^C}{L^T} = 1$), yet there is no (or minimal) sliding, u_{max}, compared to what may be perceived as an unacceptable one u_{ult}, which is selected based on the location of the index point and the type of the predicted failure. This is addressed through the coefficient β_Δ,

$$\beta_\Delta = \begin{cases} \Gamma & |DR| < DR_{limit} \\ 1.00 & |DR| \geq DR_{limit} \end{cases} \tag{10.5}$$

where $0.9 < \Gamma < 1.0$ is the reduction factor, and the drift ratio (DR) is simply defined as

$$DR = \frac{u_{max}}{H_{dam}} \times 100\% \tag{10.6}$$

In reinforced concrete frames, the limit drift ratio is usually around 5% (ASCE/SEI 7, 2010). Based on the authors experience it is estimated that for gravity dam this ratio should not exceed $\simeq 0.1\%$ (DR of 0.188% and 0.088% have been reported by Ellingwood and Tekie (2001) and Zhong et al. (2011) respectively). It is determined by simply substracting the linear response from the nonlinear one under near-collapse intensity earthquake.

Next, this DI is expanded based on the dissipated energy at the system during the damage process. The dissipated energy due to inelastic action and damage, E_H, can be evaluated (Uang and Bertero, 1990):

$$E_H = E_I - E_K - E_D - E_E \tag{10.7}$$

where E_I is the energy imparted to the system by the dynamic motion of the ground, E_K the stored kinetic energy, E_D the energy dissipated by damping, and E_E elastic strain energy. Those

are given by

$$E_I = \int \mathbf{U}_t^T \cdot \mathbf{M} \cdot d\mathbf{U}_g + \int \mathbf{S} \cdot \mathbf{P} \cdot d\mathbf{U} + \int \mathbf{f}_{ext}^T \cdot d\mathbf{U} \tag{10.8}$$

$$E_K = \frac{1}{2}\dot{\mathbf{U}}_t^T \cdot \mathbf{M} \cdot \dot{\mathbf{U}}_t \tag{10.9}$$

$$E_D = \int \dot{\mathbf{U}}_t^T \cdot \mathbf{C} \cdot d\mathbf{U} \tag{10.10}$$

$$E_E = \frac{1}{2}\mathbf{U}_t^T \cdot \mathbf{K}_e \cdot \mathbf{U}_t \tag{10.11}$$

where $\mathbf{M}$, $\mathbf{K}_e$ and $\mathbf{C}$ are mass, elastic stiffness and damping matrices of the structure, respectively. $\mathbf{P}$ and $\mathbf{U}$ are the vectors of hydraulic pressure and displacement. The subscripts t and g refer to total and ground displacements, respectively. $\mathbf{S}$ is the coupling matrix of fluid-structure. $\mathbf{f}_{ext}$ is vector of body forces.

The ratio of dissipated energy along a crack path with respect to total dissipated energy is:

$$\zeta_i^j = \frac{(E_H)_i}{E_H} \tag{10.12}$$

where $(E_H)_i$ is the dissipated energy along the discrete joint elements (if discrete cohesive cracks are used) or inside surrounding solid elements (if a smeared crack model is adopted).

The previously defined micro DI and the dissipated energy can then be combined to define a meta DI, corresponding to each critical location in Figure 10.3

$$\overline{DI}^j = \sum_{i=1}^{n} DI_i^j \times \zeta_i^j \tag{10.13}$$

where n is the total number of cracks.

Finally, one can define a macro DI for the entire dam or the dam-foundation coupled system as:

$$\overline{\overline{DI}} = \sum_{j=A}^{D} \overline{DI}^j \tag{10.14}$$

where m is the identifier of critical locations. The coupled system can be divided into four main locations as shown in Figure 10.3 (for instance the dam would correspond to $m = A, B, C$, while the foundation to $m = D$).

Usually concrete dams are designed with relatively high safety factor against seismic excitation; hence their performance is expected to be in the serviceability range. The performance of a concrete gravity dam under the earthquake excitation can be categorized as one of six possibilities (as shown also in Figure 10.5):

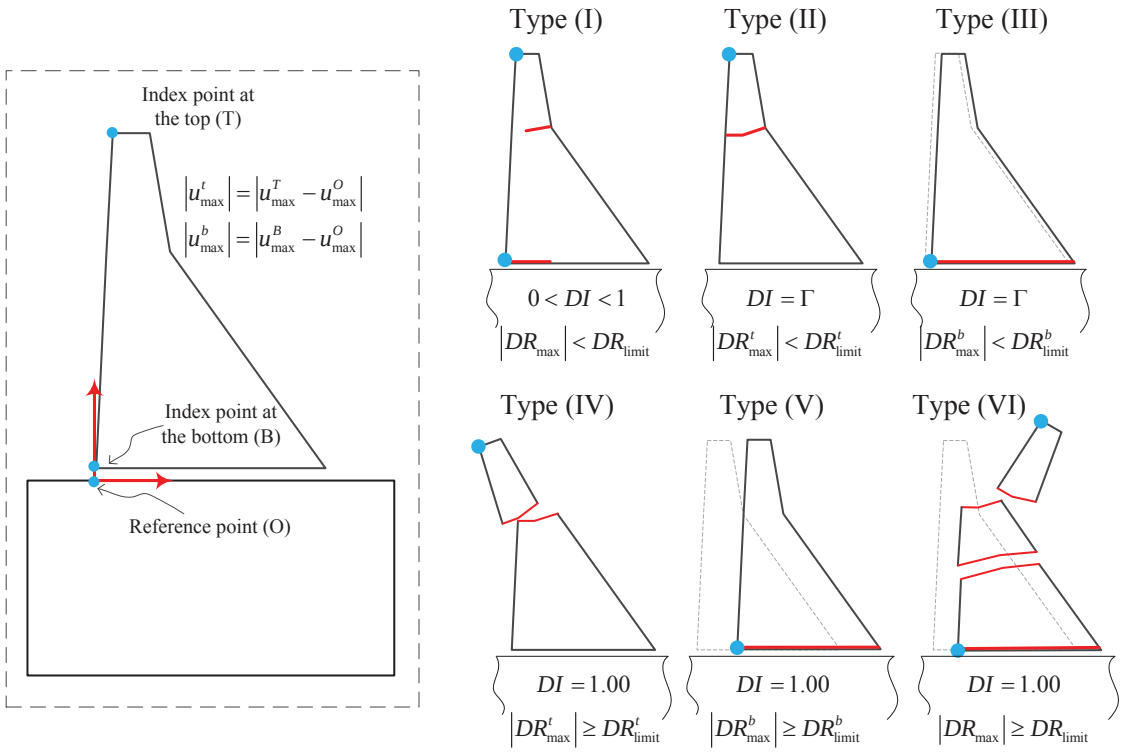

Figure 10.5: Different cracking scenarios for gravity dams under earthquake excitation

Type (I): There is no thorough crack between the upstream and downstream faces. In this case the micro, meta and macro DIs are computed from Eqs. 10.4, 10.13 and 10.14.

Type (II): There is one thorough crack at the critical locations A or B (Figure 10.3) but the upper segment does not overturn. Maximum displacement of the index point (shown as a circle) is less than the ultimate displacement (or $|DR| < DR_{limit}$). DI will be assigned a value of Γ, and the dam will be considered to be damaged but not failed.

Type (III): There is one thorough crack at the critical locations C or D but the dam body has

no or limited displacement. Maximum displacement of the index point is less than the ultimate displacement. Here, DI= Γ. The dam is considered to be severely damaged but not failed. Damage type (III) is worse than type (II), as it may lead to larger flood in downstream should there be full failure.

Type (IV): There is one thorough crack at critical locations A or B and the upper segment slides or overturns freely with respect to the lower stable part. Maximum displacement of the index point is excessive and so the instability coefficient is set to unit. Under this scenario $DI = 1.00$. The dam is assumed to have failed (reach to limit).

Type (V): There is one thorough crack at critical locations C or D and the dam body slides excessively. Maximum drift or rotation of the index point is excessive and hence DI= 1.00. The dam is assumed to have failed (reach to limit).

Type (VI): There is more than one thorough crack and the cracked segments slide and overturn with respect to each other. Maximum drift or rotation of the index point are excessive. DI= 1.00 with catastrophic failure.

In summary, performance of a gravity dam can be quantitatively evaluated using those proposed micro, meta and macro damage indices prior to full damage. Finally, damage severity and judgment on failure can be assessed from the location of cracking and magnitude of the cracked segment movement. It should be noted that the proposed DI is independent of the seismic analysis model for crack propagation. The effects of hydrodynamic pressure, pore water pressure and ... are implicitly taken into account and the dam stability during seismic analysis is controlled by Fig. 10.5. However, post-seismic stability of dam (in terms of stable or unstable crack) is not the subject of this paper.

10.4.2 Proposed Progressive Failure Assessment Methodology

As stated in Section 10.2.2, the ETA subjects the dam to multiple equivalent acceleration functions through the minimal number of analysis (Hariri-Ardebili et al., 2014b). Hence, this

section will propose a methodology which combines ETA with the DI previously defined. The ETAF generation methodology is succinctly described in Fig. 10.6 and the six steps proposed methodology for progressive failure assessment in Fig. 10.7.

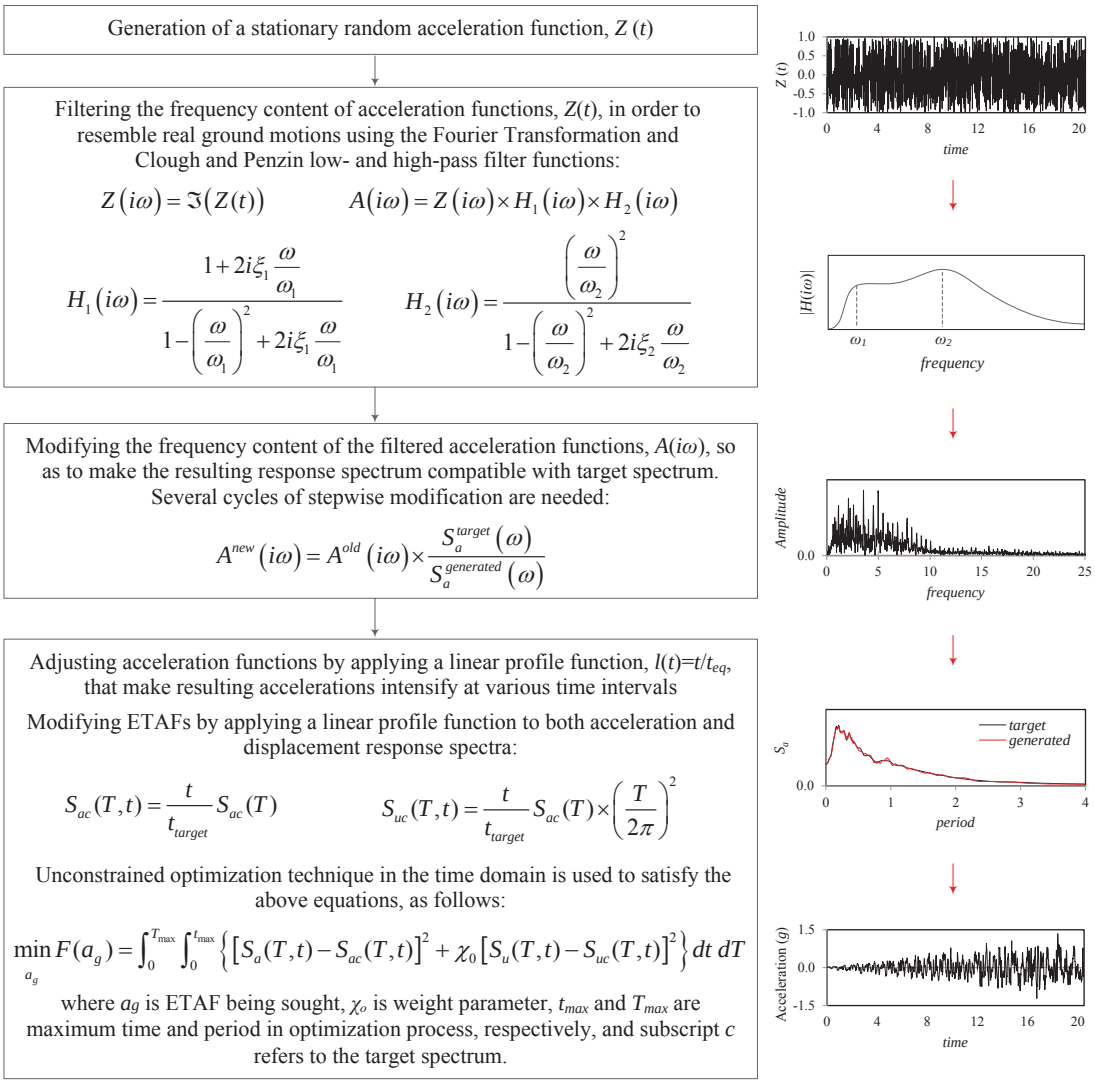

Figure 10.6: Algorithm for ETAF generation

- **Step 1:** Generate a set of artificial acceleration functions with increased intensities where the peak increases linearly with time. At any given time, we have

$$S_{a_j}(T) \simeq \frac{t_j}{t_i} S_{a_i}(T) \tag{10.15}$$

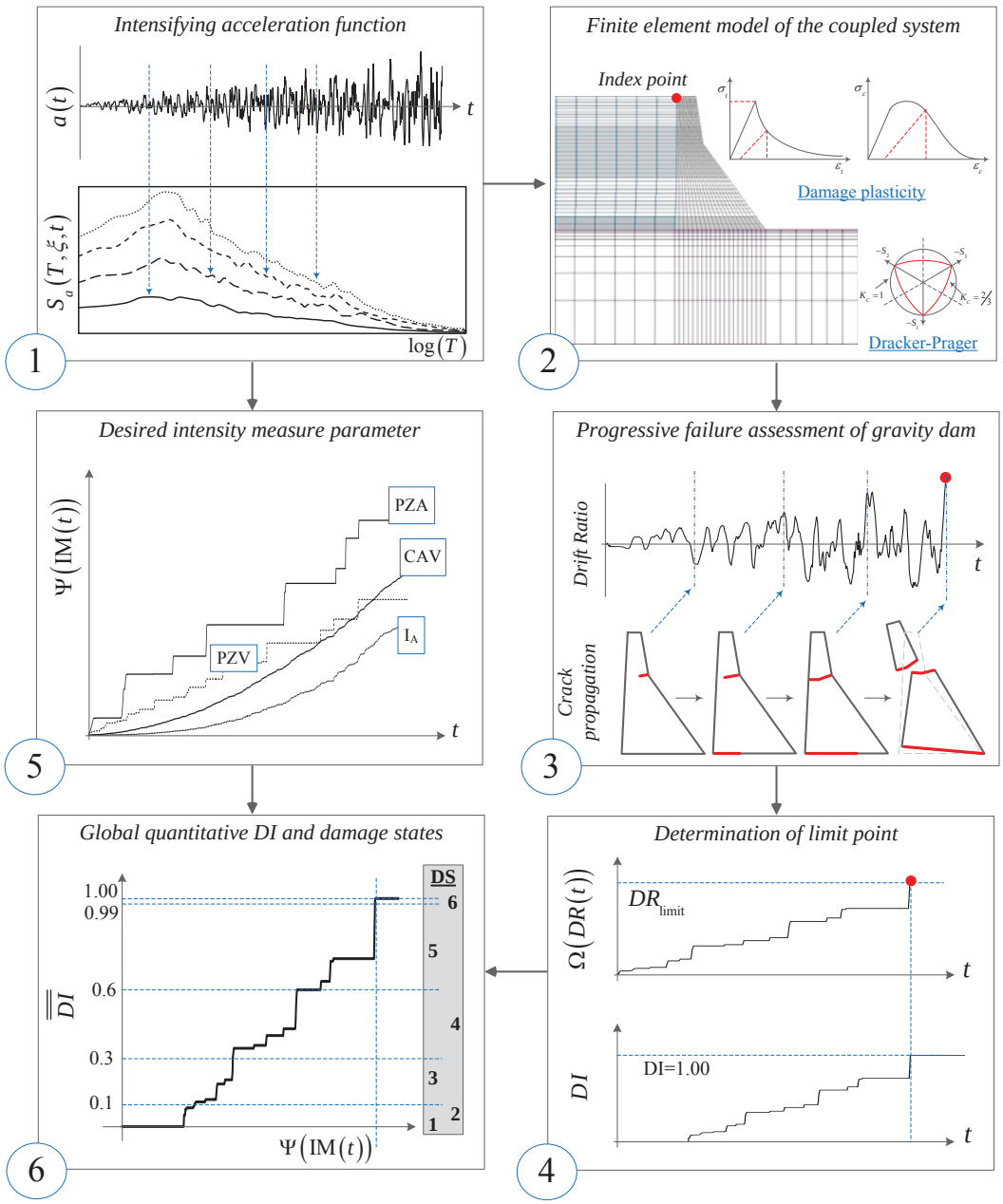

Figure 10.7: Proposed methodology for progressive failure assessment of concrete gravity dams

- **Step 2:** Prepare the finite element model for a nonlinear analysis. At a minimum, the model should account for fluid-structure interaction (Zangar, 1953), rock-structure interaction (Saouma et al., 2011), material nonlinearities in concrete (Lee and Fenves, 1998), and

joint models (Cervenka et al., 1998). In addition, it may be desirable to account for both rock nonlinearity and fluid-fracture interaction (Slowik and Saouma, 2000b).

- **Step 3:** Perform the nonlinear transient analysis until failure. From the analysis, extract index point displacements, dissipated energies (Eq. 10.7), and crack profiles.

- **Step 4:** Plot the maximum drift ratios at index points in terms of time from

$$\Omega\left(DR(t)\right) = \max\left\{\mathrm{Abs}\left(DR(\tau) : \tau \in [0,t]\right)\right\} \tag{10.16}$$

and the corresponding DI from Eq. 10.3. $t_{failure}$ occurs when the drift ratio has exceeded the ultimate one, and thus the corresponding damage index is one.

- **Step 5:** So far, the damage index has been expressed solely in terms of time. Yet, within a context of PBEE, it may be desirable to express the DI in terms of more "palpable" engineering quantities generically referred to as intensity measures (IM). The following IM's are related to transient results through the following equation

$$\Psi\left(\mathrm{IM}(t)\right) = \max\left\{\mathrm{IM}(\tau) : \tau \in [0,t]\right\} \tag{10.17}$$

where the IM are defined as follows

$$\mathrm{IM}(t) = \begin{cases} \text{Peak zero-period acceleration} & PZA(t) = \max\left(\,|\,a\big(t\big)\,|\,\right) \\ \text{Peak zero-period velocity} & PZV(t) = \max\left(\,|\,v\big(t\big)\,|\,\right) \\ \text{Peak zero-period displacement} & PZD(t) = \max\left(\,|\,u\big(t\big)\,|\,\right) \\ \text{Arias intensity} & I_A(t) = \frac{\pi}{2g}\int_0^{t_{tot}} a^2\big(t\big)dt \\ \text{Cumulative absolute velocity} & CAV(t) = \int_0^{t_{tot}} |a\big(t\big)|dt \\ \text{First mode spectral acceleration} & S_a(T_1,\xi,t) \end{cases} \tag{10.18}$$

where $a\big(t\big)$, $v\big(t\big)$, $u\big(t\big)$ are acceleration, velocity and displacement time histories, respectively. t_{tot} total duration of ground motion, T_1 fundamental period of the system, and ξ the critical damping ratio.

- **Step 6:** In the final step, we first combine the results of steps 4 and 5 to generate a curve of the damage index in terms of the selected intensity measure parameter. Incidentally, one could generate a plot of the damage index in terms of two or more IM. Then, for final qualitative assessment and decision making it is desirable to identify a damage state. Following a similar approach to the one espoused by the reinforced concrete seismic design community (Ang, 1988) the damage states shown in Table 10.2 are proposed. The quantitative numbers are based on the expert opinions of the authors who have extensive experience in testing and analysis.

Table 10.2: Definition of the proposed damage states for gravity dams

Symbol	Damage State	Damage index range
DS1	Intact	$\overline{\overline{DI}} = 0.00$
DS2	Slight	$0.00 < \overline{\overline{DI}} \leq 0.10$
DS3	Moderate	$0.10 < \overline{\overline{DI}} \leq 0.30$
DS4	Severe	$0.30 < \overline{\overline{DI}} \leq 0.60$
DS5	Near collapse	$0.60 < \overline{\overline{DI}} \leq 0.99$
DS6	Collapse	$\overline{\overline{DI}} = 1.00$

10.5 Application to a Gravity Dam

10.5.1 Dam description

As a vehicle for the proposed method, Koyna dam (Figure 10.8(a)) is selected. Completed in 1963, made of rubble concrete, this gravity dam is 853 m long and 103 m high, its thickness at the base and the crest are the 70.2 m and 12.1 m, respectively for the central non-overflow monoliths. The dam has 56 monoliths 15.24 m wide on average. While it is customary to model gravity dams as 2D plane structures, for the sake of this investigation a 3D model (Figure 10.8(b)) of the non-overflow section is adopted and results are compared with the middle section of block 2D.

Table 10.3 summarizes the mechanical properties of concrete and rock. It should be noted that the dynamic properties of mass concrete are different from the static ones due to rate dependence

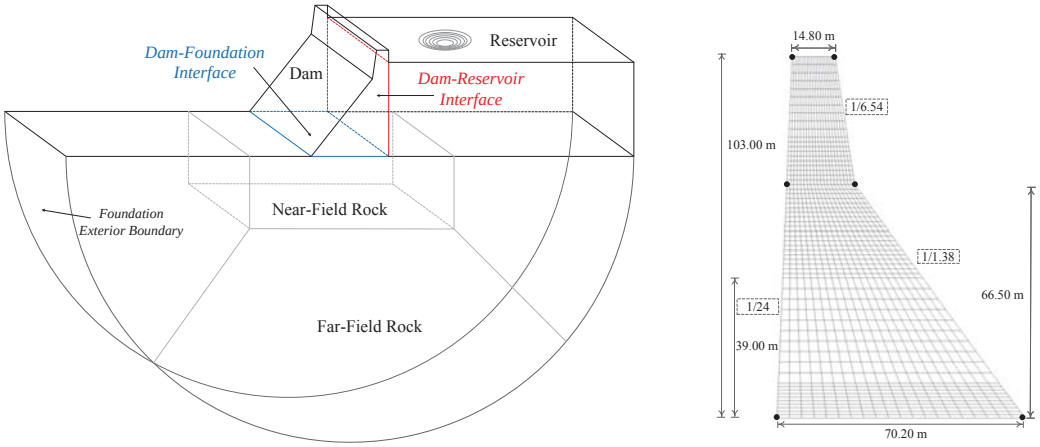

(a) 3D graphical overview (b) 2D finite element model

Figure 10.8: Koyna concrete gravity dam

of mechanical and strength properties of material (USACE, 2007). Loading consists of gravity, hydrostatic pressure and seismic excitation. Newmark-β method is adopted (contrarily to the Hilber-Hughes-α method there is no numerical damping likely to affect the energy computation) for the time integration, where the M_b=7.0 1967 recorded Koyna earthquake is considered. PGA of the horizontal and vertical components are 0.47 g and 0.31 g, respectively. Furthermore, a set of three ETAFs (Hariri-Ardebili and Mirzabozorg, 2014) is adopted to consider response of the coupled system under low to high dynamic loading.

In the nonlinear analyses, plastic damage model originally developed by Fenves and Lee (Lee and Fenves, 1998) is adopted for concrete, and the Drucker-Prager elasto-plastic model (Drucker and Prager, 1952) is adopted for crack simulation in the foundation rock. This criterion is extensively used for intact rocks and its application in the nonlinear foundation analysis of gravity dams was investigated (**?**Chen et al., 2008; Wang et al., 2013a; Hariri-Ardebili, 2014). Fluid-structure dynamic interaction is modeled based on the Eulerian-Lagrangian approach and the staggered solution is used to solve the coupled equations of motion at each load step of the transient analysis. Massed foundation model is used for rock medium while the infinite elements are implemented on the foundation exterior surface to prevent wave reflection at the artificial boundaries. The application

and accuracy of the used fluid-structure and rock-structure interaction models has been studied before (Hariri-Ardebili and Mirzabozorg, 2013).

Analysis was performed with the ABAQUS finite element software (ABAQUS, 2007) and displacement was adopted as a convergence criterion. The detached segment at the failure time is capable of overturning. Thus, the convergence criterion is not necessarily achieved for the port-failure crack analysis. Finite element model of the dam was compared with small scale shaking table test performed by the US Army Corps of Engineers (Wilcoski et al., 2001). In both small scale testing and numerical models, the crack initiates downstream on the sharp corner and propagates diagonally down more or less orthogonally to the average downstream slope. This primary crack is essentially horizontal (thus again orthogonal to) the upstream face. Following propagation of the primary crack, secondary cracks propagated and the concrete spalls at different location of the downstream and upstream faces.

Table 10.3: Mechanical properties of mass concrete and foundation rock

Characteristics	Symbol	Static value	Dynamic value
Modulus of elasticity (concrete)	E_c (GPA)	31.03	35.68
Mass density (concrete)	ρ_c (kg/m^3)	2,643	2,643
Poisson's ratio (concrete)	ν_c	0.20	0.14
Tensile strength (concrete)	f_t (MPa)	2.4	3.6
Compressive strength (concrete)	f_c (MPa)	24.0	36.0
Fracture energy (concrete)	G_f (N/m)	-	200
Modulus of elasticity (rock)	E_r (GPA)	16.86	16.86
Mass density (rock)	ρ_r (kg/m^3)	2,700	2,700
Poisson's ratio (rock)	ν_r	0.18	0.18
Cohesion (rock)	c (MPa)	0.6	0.6
Angle of fraction (rock)	ϕ $(deg.)$	41	41

10.5.2 Results and Discussion

The damage response of a gravity dam is first investigated through scaled real ground motion. Different discrete damage indices are computed and the seismic intensity level's impact on DI are investigated. Then, an endurance time analysis will be performed. Two finite element models are considered:

- **Model (1)**: where both concrete and rock are assumed to be linear elastic. This model is needed for reference.

- **Model (2)**: where both concrete and rock are assumed nonlinear. The former is modeled with the damage plastic approach, and the later using a simple Drucker-Prager elasto-plastic model.

10.5.2.1 Scaled Time History Analysis

A static analysis including gravity and hydrostatic is first performed, and then through a restart the dynamic analysis is performed with modified properties. The dam-reservoir-foundation system is excited by a combination of the horizontal and vertical components. Time history of crest displacements along stream direction is shown in Figure 10.9. The responses of the nonlinear models prior to crack initiation at $t = 2.62$ s coincide with those obtained from the linear elastic analysis suggesting that both the tensile and compressive stresses of the concrete and rock were below their elastic limits. Cracking leads to the discontinuity of the curves among each other. Nonlinear model fails at $t = 3.98$ s with the failure type (IV) because there is one thorough crack at the neck area (Figure 10.10) and the upper cracked segment overturns freely because the displacement of the index point (which is crest point in this case) approaches to very high values (Figure 10.9).

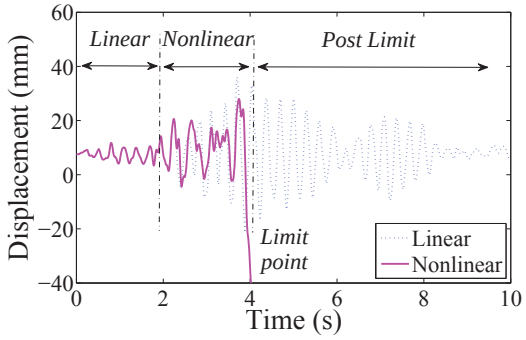

Figure 10.9: Dam response under scaled ground motion

Figure 10.10 illustrates the crack propagation for nonlinear analysis. As expected, cracks initiate at the point of slope discontinuity on the downstream face and extends across the width

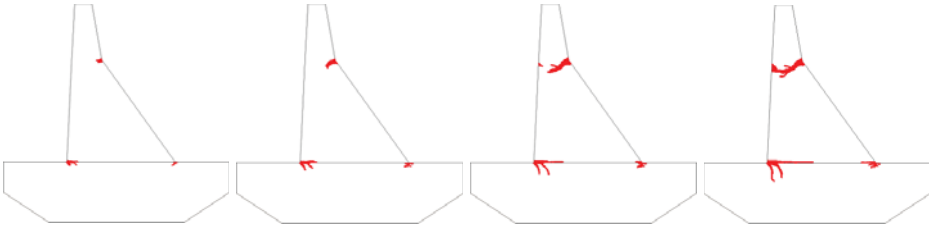

Figure 10.10: Crack propagation within the dam-foundation system under scaled ground motion

of the neck. Subsequently an upstream crack initiates at the neck and propagates horizontally to eventually coalesce with the downstream one. Cracks also nucleate at the dam-foundation interface and propagate from heel to toe. The final cracked length of the base is longer in nonlinear rock model than in the linear one. Also assuming the elasto-plastic model for the rock leads to cracking of the foundation near both the heel and the toe of the dam. Cracks propagate diagonally downward and eventually become vertical. This is consistent with laboratory observations (Slowik et al., 1998). The micro damage indices for the two critical locations at the end of failure are computed as: $DI_1^A = 1.00$ and $DI_2^C = 0.55$.

Considering that there is at least one thorough crack in the dam and the cracked segment overturns, the dam is considered to have failed. There is no need to compute the meta and macro damage indices because they are assumed to be unity under this condition. Since the dam has failed from the neck, flood damage should be separately assessed.

The analyses are repeated for lower seismic intensities by scaling the ground excitation by a scalar scale factor, SF. The scaled ground motions are then applied to the coupled system and the corresponding damage indices are computed as reported in Table 10.4. Except for the case with SF=1.0, none of the models failed. Applying the ground motion with SF=0.7, reduce the macro damage index to about 37%. The model remains fully in the elastic range when the ground motion is applied with the scale factor of SF=0.3. Finally, the dam experiences a small damage index under the ground motion with SF=0.5. Based on the numerical analyses and engineering judgment, the onset of the nonlinear behavior can be assumed to occur at an intensity equal to

40% of the original motion.

Table 10.4: Impact of seismic intensity level on the damage index

SF	DI	$\overline{DI}$	$\overline{\overline{DI}}$	DS
1.0	$DI_1^A = 1.00,\ DI_2^C = 0.55$	$\overline{DI} = 1.00$	$\overline{\overline{DI}} = 1.00$	Collapse
0.7	$DI_1^A = 0.68,\ DI_2^C = 0.26$	$\overline{DI}^A = 0.17,\ \overline{DI}^C = 0.20$	$\overline{\overline{DI}} = 0.37$	Severe
0.5	$DI_1^A = 0.14,\ DI_2^C = 0.06$	$\overline{DI}^A = 0.04,\ \overline{DI}^C = 0.05$	$\overline{\overline{DI}} = 0.08$	Slight
0.3	$DI = 0.00$	$\overline{DI} = 0.00$	$\overline{\overline{DI}} = 0.00$	Intact

10.5.2.2 Endurance Time Analysis

Next, results of the three ($e = 3$) endurance time analyses (section 10.4.2) are presented. First, index point displacements *vs* time are shown for both linear and nonlinear analyses, Fig. 10.11(a)-10.11(b). Identical responses are obtained between those two models up to $t = 2.5$ s, $t = 1.7$ s, and $t = 2.2$ s for ETAF-1, ETAF-2, and ETAF-3, respectively. On the other hand, all three nonlinear models reached its acceptable capacity (as defined above) at nearly the same time, $t_{failure} \simeq 4.0$ s. It should be noted that numerically, this may not necessarily correspond to failure (typically a result of numerical instability). In all cases, limit acceptable capacities were caused by excessive crest drift ratios $\Omega(DR(t))$ exceeds DR_{limit}. In this example, DR_{limit} was taken as 0.1%, Fig. 10.11(c).

Figure 10.12 illustrates the crack propagation for each of the three ETAFs. In all cases, limits (as previously defined in Section 10.4.1) were triggered by first thorough crack. Again, these limits were arbitrarily set to define what is acceptable, they may result in localized but not necessarily in overall dam failure. Actual dam failure may subsequently occur should there be aftershocks (failure type VI).

Figure 10.13 illustrates time history of the micro and macro damage indices as a result of increased ETAF. From Figure 10.13(a) and 10.13(b) it is clear that nonlinearity (caused by racking) starts around $t = 2$ s, that the micro DI at the neck first reaches the limit value, while the corresponding one at the base is around 0.33. Also corresponding to a micro DI of 0.5 at the neck,

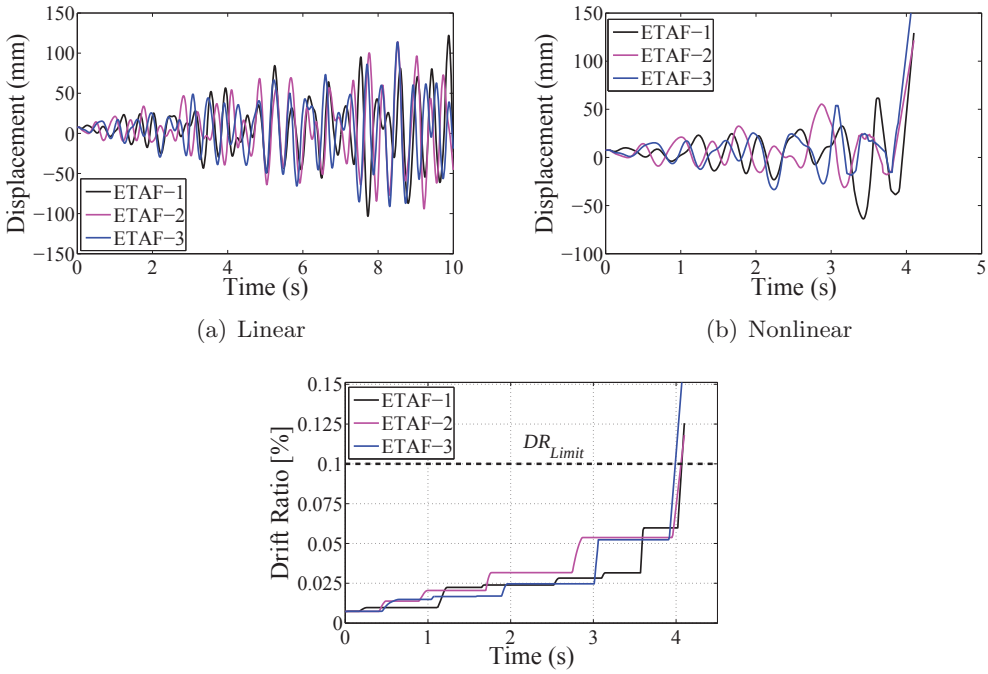

(a) Linear

(b) Nonlinear

(c) Maximum absolute displacements in nonlinear analysis

Figure 10.11: Dam response under ETAF

there is a sharp discontinuity in the response caused by an increased compliance due to cracking. Finally, Fig. 10.13(c) illustrates the evolution of the macro DI (defined by Eq. 10.13 and 10.14). A Macro DI of 0.53 corresponds to the neck failure at $t = 4 - \varepsilon$ s. Then at $t = 4$ s the ultimate limit load is reached, and there is a corresponding sudden increase of the macro DI to 1.0.

Furthermore, and with reference to Fig. 10.7 one can convert the time to selected intensity measure parameters (step 5) and then plot the damage index in terms of them (step 6). This conversion and plot for the current analysis (for the neck area) is shown in Fig. 10.14. For clarity, the damage index values are projected into two planes corresponding to intensity measure parameters. The dam reaches its ultimate damage index values for a PZA $\sim$ 0.26 g and $S_a(T_1)$ $\sim$ 0.68 g. Finally, it should be emphasized that given a different ground motion, one could use the average of these curves to estimate the damage index without the need to perform another structural analysis.

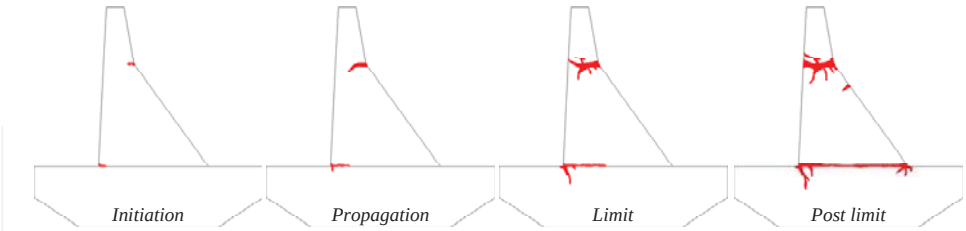

(a) ETAF-1

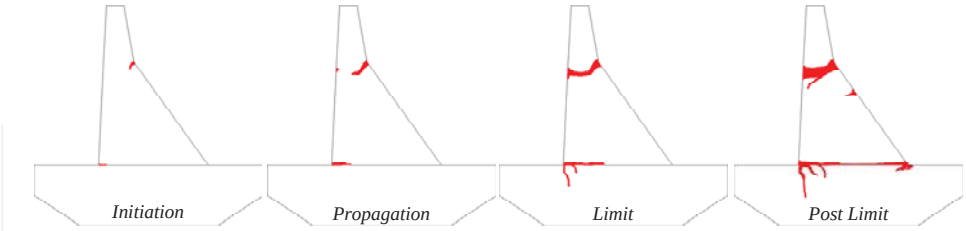

(b) ETAF-2

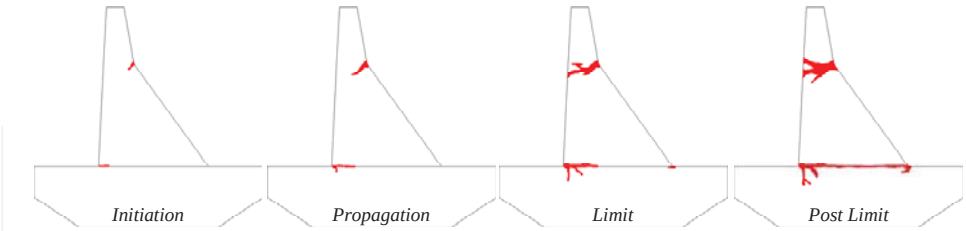

(c) ETAF-3

Figure 10.12: Progressive failure analysis of Koyna dam under the intensifying acceleration functions

10.6 Conclusions

This paper proposed a metric to assess the damage in concrete gravity dams. The assessment starts by qualitatively identifying the possible failure modes, and then proposes a multi-variable cumulative damage index. The proposed damage index being multi-scale, starts with micro damage to ultimately result in a single macro parameter.

A six steps methodology to perform such a study within the context of endurance time analysis for progressive failure assessment of the dam is proposed.

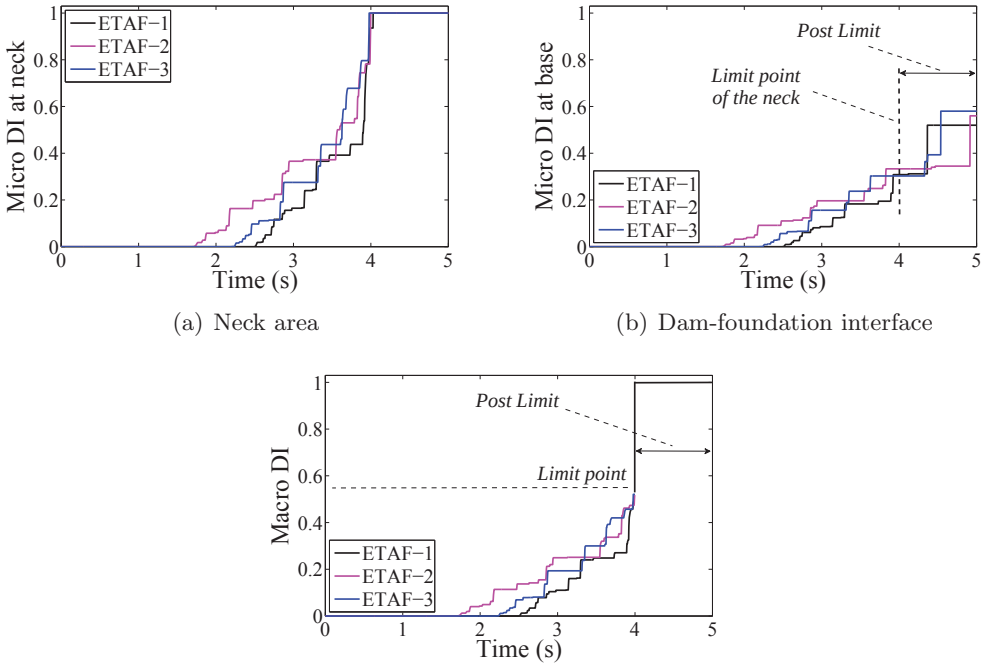

(a) Neck area

(b) Dam-foundation interface

(c) Macro damage index

Figure 10.13: Time history of the computed damage indices

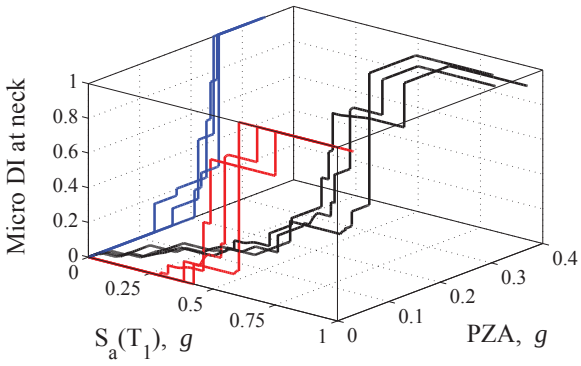

Figure 10.14: Variation of the micro damage index at neck with respect to PZA and $S_a(T_1)$

A case study is presented, and plots of damage index versus intensity measures are produced.

Finally, it should be pointed out that the proposed methodology fits squarely within the paradigm of performance based earthquake engineering.

Chapter 11

Conclusions and Future Research Needs

11.1 Summary and Conclusions

The overarching objective of this study was to quantitatively safety assessment of concrete dams using the elements provided by performance-based earthquake engineering (PBEE) and potential failure mode analysis (PFMA). This is a thesis in the field of earthquake engineering heavily borrowing the concepts of structural mechanics for nonlinear transient analysis of coupled dam-reservoir-foundation system. This research addressed many important issues as summarized in the following list:

- Proposing the concept of capacity function for concrete dams and a comprehensive review on all the mechanics-, hydrologic- and seismic-based approaches to derive this function (Chapter 3).
- Develop a Matlab-based computational tool for probabilistic performance assessment of concrete dams (Chapter 4).
- A detailed nonlinear transient analysis of concrete gravity dams (Chapter 5).
- Develop an extended and quantitative version of PFMA for concrete dams (Chapter 6).
- Perform the sensitivity analysis on dam-foundation system, quantify the material (epistemic) uncertainties, determine tornado diagram, capacity and fragility curves (Chapter 7).

- Develop a probabilistic seismic demand model for concrete dams considering the global failure (Chapter 8).
- Propose an optimal intensity measure parameter for concrete dams (Chapter 8).
- Determine the collapse fragility curves of concrete dams though multiple-record incremental dynamic analysis (Chapter 9).
- Perform different structural analysis techniques on concrete dams. In particular: cloud analysis, multiple strip analysis, incremental dynamic analysis, and endurance time analysis (Chapters 6, 8, 9 and 10).
- Propose a multi-scale damage index for gravity dams as a function of crest displacement, crack ratio, and dissipated energy (Chapter 10).
- Propose a computationally simple but effective methodology for progressive failure analysis of dams (Chapter 10).

Following is the detailed conclusions for each chapter:

Chapter 3 proposed the concept of capacity functions for concrete dams and tried to presents a simple mathematical model for it. Capacity function was defined as a relationship between the response and stressors (in terms of an external one such as hydraulic or seismic or an internal one such as alkali silica reaction). Then, all the existing numerical methods for progressive failure analysis of concrete dams were reviewed and revisited. Whenever it was possible, the differences of these method, their advantageous and disadvantageous were presented. Finally, a combined and extended capacity functions were explained for concrete dams.

Chapter 4 presented the computational tools developed and used during this research for probabilistic performance assessment of concrete dams (PPACD). This includes a group of Matlab-based scripts and functions which were used also Merlin finite element code for processing the models. The interaction of all these scripts and their application in PBEE were explained.

Chapter 6 compared different potential failure modes for all three types of concrete dams, i.e. gravity, arch, and buttress. First, the qualitative approach was reviewed and then the extended quantitative version proposed for both the linear and nonlinear systems. For the linear analyses, different indices introduced and their limit states quantified.

Multiple strip analysis method used for assessment of a case study arch dam. A large set of simulated engineering demand parameters generated for the dam and the optimal scalar and vectorized intensity measure parameter quantified. Finally, the results of linear and nonlinear system correlated.

Chapter 7 quantified the sensitivity and uncertainty in dam-foundation system. First, the theory of an advanced fracture mechanics based zero-thickness interface joint element studied. Then, it was applied for analysis of three problems: mode I and II fracture mechanics of idealized blocks subjected to displacement control pushover analysis, and mixed-mode fracture analysis of a real gravity dam-foundation system. For each case, the most sensitive random variables (RV) determined and the associated tornado diagram plotted. Monte Carlo simulation with Latin Hypercube Sampling used for uncertainty quantification of the sensitive RVs. The impact of correlation among the RVs studied also. Finally, the capacity curves plotted for each case and the associated fragility curve derived. It was found that using the correlated RVs than to un-correlated ones for Mode I and mixed-mode fracture is in priority, while its effect is negligible in Mode II.

Chapter 8 proposed a probabilistic seismic demand model for gravity dams. First, all the existing intensity measure parameters for structural systems summarized in seven categories and a new one proposed for dams. Then, a cloud-based probabilistic seismic demand analysis performed using 100 un-scaled ground motions. Using these ground motions, an appropriate distributional model proposed for each intensity measure. The most optimal intensity measure parameter determined considering the parameters such as sufficiency, efficiency, proficiency, practicality, and hazard compatibility. Finally, the fragility curves derived for the dam and the impact of different intensity measure and engineering demand parameters investigated.

Chapter 9 presented collapse fragility curves for gravity dams. First, different methods for fitting a lognormal cumulative distribution function to the empirical data points reviewed. Transient analyses were performed based on incremental dynamic analysis (IDA) methodology. The Anatomy of a single-record IDA was studied in detail and contrasted with framed structures. The optimal intensity measure parameter selected based on the minimum dispersion of multiple-record IDA curves. Finally, the collapse fragility curves derived for the dam.

The importance of the ground motion vertical component on the IDA curves and the resulted collapse fragility curves investigated. It was found that vertical component decreases the IM capacity of IDA curves. In addition, in most of the IM parameters, incorporating the vertical component leads to equal or higher dispersion than horizontal component only.

Dispersion due to material uncertainty was added to the record-to-record variability and the extended collapse fragility curves plotted. It was found that considering the epistemic uncertainty increases total dispersion of the fragility curves.

Moreover, the impact of reservoir water level was studied on probability of collapse. It was found that emptying the reservoir decreases the probability of collapse.

Chapter 10 proposed a multi-scale damage index (DI) for gravity dams. The new DI is based on maximum crest displacement, energy dissipation in system and the ratio of the cracked segments. Then, a computationally simple but effective method proposed for systematic progressive failure assessment of gravity dams based on endurance time analysis. This method provides continuous performance of the dam in terms of DI and the desired intensity measure parameter.

11.2 Future Research Needs

Following is the summary of future research need based on the findings of this thesis:

- This thesis only investigates the major potential failure modes of concrete dams; however, for practical purposes, all the failure modes should be considered simultaneously. The impact of correlation among the failure modes should be considered. Safety assessment can

be performed for component-level and system-level separately.

- Performance base assessment of concrete dam-reservoir-foundation system is computationally expensive. Especially for three-dimensional finite element models it is practically impossible to perform nonlinear transient analyses in conjunction with Latin Hypercube sampling. To solve this problem, it is recommended to develop a mathematical equivalent model for the dam-reservoir-foundation system (a multi-degree-of-freedom system) to estimate the collapse response of the dam.

- In this thesis, the material uncertainty is quantified using an innovative method through the endurance time analysis technique. It is recommended to compare this method with the extended incremental dynamic analysis.

- Application, advantageous and disadvantageous of different uncertainty quantification techniques, e.g. first-order second moment (FOSM) compared to Monte Calro simulation. In addition, reliability analysis can be performed for parametric models of concrete dams and the reliability index can be derived for different failure modes.

- The probabilistic seismic demand model proposed in this thesis was a two-dimensional model and consequently the scalar optimal intensity measure parameter was introduced. This can be extended for vectorized intensity measure parameters (linear or quadratic).

- Application of synthetic ground motions which are specifically generated to be used within the context of the PBEE should be compared with respect to real ground motions.

- The IDA-based fragility curves studied in this thesis were collapse fragility curves; however, to be used within the context of PBEE, the conditional probability of a specific damage state should be presented with respect to engineering demand parameters.

- Loss analysis in terms of loss of money, loss of life and downtime should be performed for concrete dams. This requires a comprehensive research on loss models for dams. Not only

the main dam body but also the spillways, powerhouse and all other equipments should be considered.

Bibliography

ABAQUS (2007). Abaqus Theory Manual. ABAQUS, Inc., Providence, RI, USA, version6.7 edition.

Abrahamson, N. and Silva, W. (2008). Summary of the abrahamson & silva nga ground-motion relations. Earthquake Spectra, 24(1):67–97.

Ahmadi, M., Khoshrang, G., Mokhtarzadeh, A., and Jalalzadeh, A. (1992). Behavior of a large concrete dam to an actual maximum credible earthquake. In Proceeding of the 10th World Conferance on Earthquake Engineering, volume 7, pages 3995–4000.

Alembagheri, M. and Ghaemian, M. (2013a). Damage assessment of a concrete arch dam through nonlinear incremental dynamic analysis. Soil Dynamics and Earthquake Engineering, 44:127–137.

Alembagheri, M. and Ghaemian, M. (2013b). Seismic assessment of concrete gravity dams using capacity estimation and damage indexes. Earthquake Engineering and Structural Dynamics, 42:123–144.

Allen, T. and Wald, D. (2007). Topographic slope as a proxy for seismic site conditions (vs30) and amplification around the globe. Technical report, U.S. Geological Survey.

American Society of Civil Engineers (2013). 2013 report card for america's infrastructure; dams. `http://www.infrastructurereportcard.org/a/\#p/dams/overview`. Last viewed March 2014.

ANCOLD (2003). Guidelines on risk assessment, ancold. Technical report, Australian National Committee on Large Dams, Sydney, New South Wales, Australia.

Anderson, T. and Darling, D. (1954). A test of goodness of fit. Journal of the American Statistical Association, 49:765–769.

Ang, A. (1988). Seismic damage assessment and basis for damage-limiting design. Probabilistic Engineering Mechanics, 3:146–150.

ANSYS (2007). Ansys software reference manuals, release notes, mechanical apdl, elements reference, commands reference and theory reference, version release 11.

Antoniou, S. and Pinho, R. (2004a). Advantages and limitations of adaptive and non-adaptive force-based pushover procedures. Journal of Earthquake Engineering, 8:497–522.

Antoniou, S. and Pinho, R. (2004b). Development and verification of a displacement-based adaptive pushover procedure. Journal of Earthquake Engineering, 8:643–661.

Applied Technology Council (2012). Seismic performance assessment of buildings volume 1 methodology. Technical Report FEMA P-58-1, Federal Emergency Management Agency.

Araya, R. and Saragoni, R. (1984). Earthquake accelerogram destructiveness potential factor. In Proceedings of the 8th World Conference of Earthquake Engineering, pages 835–841, San Francisco, USA.

Arias A. (1970). A measure of earthquake intensity, Seismic Design for Nuclear Power Plants. MIT Press, Cambridge, UK.

Army Corps of Engineers (1992). Reliability assessment of navigation structures. ETL 1110-2-532, Department of the Army, US Army Corps of Engineers, Washington, D.C.

ASCE/SEI 7 (2010). Minimum design loads for buildings and other structures. Technical report, American Society of Civil Engineers.

ASCE/SEI4106 (2007). Seismic rehabilitation of existing building. Technical report, American Society of Civil Engineers.

ASDSO (2011). State and federal oversight of dam safety must be improved. Magazine of ASDOS.

Aslani, H. and Miranda, E. (2005). Probabilistic earthquake loss estimation and loss disaggregation in buildings. PhD thesis, Stanford University, Stanford.

ATC (1978). Tentative provisions for the development of seismic regulations for buildings, report no. atc 3-06. Technical report, Applied Technology Council, Palo Alto, CA.

ATC-13 (1985). Earthquake damage evaluation data for california. report no.atc-13. Technical report, Applied Technology Council, Redwood City, CA.

ATC-14 (1987). Evaluating the seismic resistance of existing buildings. report no.atc-14. Technical report, Applied Technology Council, Redwood City, CA.

ATC-40 (1996). Seismic evaluation and retrofit of concrete buildings. report no.atc-40. Technical report, Applied Technology Council, Redwood City, CA.

ATC-58 (2012). Seismic performance assessment of buildings, volume 1: Methodology atc-58-1. Technical report, Federal Emergency Management Agency, Redwood City, CA.

Azarbakht, A. and Dolsek, M. (2007). Prediction of the median ida curve by employing a limited number of ground motion records. Earthquake Engineering and Structural Dynamics, 36:2401–2421.

Azarbakht, A. and Dolsek, M. (2011). Progressive incremental dynamic analysis for first-mode dominated structures. Journal of Structural Engineering, 137:445–455.

Baker, J. (2014). Efficient analytical fragility function fitting using dynamic structural analysis. Earthquake Spectra.

Baker, J. and Cornell, C. (2005). A vector-valued ground motion intensity measure consisting of spectral acceleration and epsilon. Earthquake Engineering and Structural Dynamics, 34:1193–1217.

Baker, J. and Cornell, C. (2008). Vector-valued intensity measures incorporating spectral shape for prediction of structural response. Journal of Earthquake Engineering, 12:534–554.

Baker, J. and Jayaram, N. (2008). Correlation of spectral acceleration values from nga ground motion models. Earthquake Spectra, 24:299–317.

Baker, J. W. (2010). Conditional mean spectrum: Tool for ground-motion selection. Journal of Structural Engineering, 137(3):322–331.

Banon, H. and Veneziano, D. (1982). Seismic safety of reinforced members and structures. Earthquake Engineering and Structural Dynamics, 10:179–193.

Barbato, M., Petrini, F., Unnikrishnan, V., and Ciampoli, M. (2013). Performance-based hurricane engineering (pbhe) framework. Structural Safety, 45:24–35.

Barpi, F. and Valente, S. (2008). Modeling water penetration at dam-foundation joint. Engineering Fracture Mechanics, 75:629–642.

Barroso, L. and Winterstein, S. (2002). Probabilistic seismic demand analysis of controlled steel moment-resisting frame structures. Earthquake Engineering and Structural Dynamics, 31:2049–2066.

Basu, U. (2009). Explicit finite element perfectly matched layer for transient three-dimensional elastic waves. International Journal for Numerical Methods in Engineering, 77:151–176.

Basu, U. and Chopra, A. (2004). Perfectly matched layers for transient elastodynamics of unbounded domains. International Journal for Numerical Methods in Engineering, 59:1039–1074.

Bazant, Z. and Lin, F. (1988). Nonlocal smeared cracking model for concrete fracture. ASCE Structural Engineering, 114:2493–2510.

Bazant, Z.P. (1988). Mathematical modeling of creep and shrinkage of concrete. John Wiley and Sons, New York.

Berahman, F. and Behnamfar, F. (2009). Probabilistic seismic demand model and fragility estimates for critical failure modes of un-anchored steel storage tanks in petroleum complexes. Probabilistic Engineering Mechanics, 24:527–536.

Bertero, R. and Bertero, V. (2002). Performance-based seismic engineering: the need for a reliable conceptual comprehensive approach. Earthquake Engineering and Structural Dynamics, 31:627–652.

Bertero, R. and V.V., B. (2000). Application of a comprehensive approach for the performance-based earthquake-resistant design of buildings. In Proceeding of the 12th World Conferance on Earthquake Engineering.

Bhattacharjee, S. and Leger, P. (1993). Seismic cracking and energy dissipation in concrete gravity dams. Earthquake Engineering and Structural Dynamics, 22:991–1007.

Bisadi, V., Gardoni, P., and Head, M. (2012). Probabilistic demand models and fragility estimates for bridges elevated with steel pedestals. Journal of Structural Engineering, 139:1515–1528.

Bojorquez, E., Iervolino, I., Reyes-Salazar, A., and Ruiz, S. (2012). Comparing vector-valued intensity measures for fragility analysis of steel frames in the case of narrow-band ground motions. Engineering Structures, 45:472–480.

Bouaanani, N. and Lu, F. (2009). Assessment of potential-based fluid finite elements for seismic analysis of dam-reservoir systems. Computers and Structures, 87:206–224.

Bouaanani, N., Paultre, P., and Proulx, J. (2009). Two-dimensional modelling of ice cover effects for the dynamic analysis of concrete gravity dams. Earthquake Engineering and Structural Dynamics, 31:2083–2102.

Bowles, D. and McClelland, D. (2000). Event tree analysis. Technical report, Working paper prepared for the Canadian Electricity Association Dam Safety Interest Group. Institute for Dam Safety Risk Management, Utah State University, Logan, Utah.

Boyer, D. (2006). Geologic factors influencing dam foundation failure modes. In Proceedings of the 26th Annual USSD Conference, San Antonio, Texas, USA.

Bozorgnia, Y. and Bertero, V. (2003). Damage spectra: characteristics and applications to seismic risk reduction. Structural Engineering, ASCE, 129:1330–1340.

Bradley, B. (2010). Site-specific and spatially distributed ground-motion prediction of acceleration spectrum intensity. Bulletin of the Seismological Society of America, 100:792–801.

Bradley, B. (2011). Empirical equations for the prediction of displacement spectrum intensity and its correlation with other intensity measures. Soil Dynamics and Earthquake Engineering, 31:1182–1191.

Button, M., Cronin, C., and Mayes, R. (2002). Effect of vertical motions on seismic response of highway bridges. Journal of structural engineering, 128:1551–1564.

California Division of Mines and Geology (1966). Geologic map of california. Fresno Sheet, 1:250,000. Fourth printing 1991.

Campbell, K. and Bozorgnia, Y. (2008). Nga ground motion model for the geometric mean horizontal component of pga, pgv, pgd and 5ranging from 0.01 to 10s. Earthquake Spectra, 24:139–171.

Campbell, K. and Bozorgnia, Y. (2010). A ground motion prediction equation for the horizontal component of cumulative absolute velocity (cav) based on the peer-nga strong motion database. Earthquake Spectra, 26(3):635–650.

Carol, I., Bažant, Z. P., and Prat, P. C. (1992). Microplane type constitutive models for distributed damage and localized cracking in concrete structures. In Bažant, Z. P., editor, Proc. Fracture Mechanics of Concrete Structures, pages 299–304. Elsevier.

Carol, I., Prat, P., and Lopez, C. (1997). Normal/shear cracking model: Application to discrete crack analysis. ASCE Journal of Engineering Mechanics, 123(8).

Casarotti, C. and Pinho, R. (2007). An adaptive capacity spectrum method for assessment of bridges subjected to earthquake action. Bulletin of Earthquake Engineering, 5:377–390.

CDA (2007). Dam safety guidelines. Technical report, Canadian Dam Association, Edmonton, Alberta, Canada.

Celarec, D. and Dolsek, M. (2013). The impact of modelling uncertainties on the seismic performance assessment of reinforced concrete frame buildings. Engineering Structures, 52:340–354.

Celik, O. and Ellingwood, B. (2010). Seismic fragilities for non-ductile reinforced concrete framesrole of aleatoric and epistemic uncertainties. Structural Safety, 32:1–12.

Cervenka, J., Chandra, J., and Saouma, V. (1998). Mixed mode fracture of cementitious bimaterial interfaces; part ii: Numerical simulation. Engineering Fracture Mechanics, 60(1):95–107.

Cervenka, J. and Papanikolaou, V. (2008). Three dimensional combined fracture-plastic material model for concrete. International Journal of Plasticity, 24(12):2192–2220.

Chandler, A. and Lam, N. (2001). Performance-based design in earthquake engineering: A multidisciplinary review. Engineering Structures, 23:1525–1543.

Chen, S., Qiang, S., Shahrour, I., and Egger, P. (2008). Composite element analysis of gravity dam on a complicated rock foundation. International Journal of Geomechanics, 8:275–284.

Chen W.F. (1982). Plasticity in reinforced concrete. McGraw-Hill Book Company, New York.

Cheung, P., Pauley, T., and Park, R. (1991). New zealand tests on full-scale reinforced concrete beam-column-slab sub-assemblages designed for earthquake resistance. In ACI Special Publication SP-123, Design of Beam-Column Joints for Seismic Resistance, pages 1–37, Detroit, MI, USA.

Chopra, A. and Chakrabarti, P. (1973). The koyna earthquake and the damage to koyna dam. Bulletin of the Seismological Society of America, 63(2):381–397.

Chopra, A. and Goel, R. (1999). Capacity-demand-diagram methods based on inelastic design spectrum. Earthquake Spectra, 15:637–656.

Chopra, A. and Goel, R. (2002). A modal pushover analysis procedure for estimating seismic demands for buildings. Earthquake Engineering and Structural Dynamics, 31:561–582.

Chopra, A. and Wang, J. (2010). Earthquake response of arch dams to spatially varying ground motion. Earthquake Engineering and Structural Dynamics, 39:887–906.

Ciampoli, M., Petrini, F., and Augusti, G. (2011). Performance-based wind engineering: towards a general procedure. Structural Safety, 33(6):367–378.

Cirak, F., Ortiz, M., and Pandolfi, A. (2005). A cohesive approach to thin-shell fracture and fragmentation. Computer Methods in Applied Mechanics and Engineering, 194(21):2604–2618.

Clark, P., Frank, K., Krawinkler, H., and Shaw, R. (1997). Protocol for fabrication, inspection, testing and documentation of beam-column connection and other experimental specimens. Technical Report SAC/BD-97/02, SAC Joint Venture, Sacramento, CA, USA.

Clough, R. and Wilson, E. (1962). Stress analysis of a gravity dam by the finite element method. In Proceedings of the symposium on use of computers in civil engineering, Lisbon, Portugal.

Clough, R.W. and Penzien, J. (1993). Dynamics of Structures. McGraw-Hill Inc., London, UK.

Cocchetti, G., Maier, G., and Shen, X. (2002). Piecewise linear models for interfaces and mixed mode cohesive cracks. 3:279–298.

Collier, C. and Elnashai, A. (2001). A procedure for combining vertical and horizontal seismic action effects. Journal of Earthquake Engineering, 5:521–539.

Comi, C., Fedele, R., and Perego, U. (2009). A chemo-thermo-damage model for the analysis of concrete dams affected by alkali-silica reaction. Mechanics of Materials, 41:210–230.

Conover, W.J. (1980). Practical nonparametric statistics, 2nd ed. Wiley, New York.

Cordova, P., Mehanny, S., Deierlein, G., and Cornell, C. (2001). Development of a two-parameter seismic intensity measure and probabilistic assessment procedure. In Proceedings of the 2nd US-Japan workshop on performance-based earthquake engineering methodology for RC building structures, pages 187–206, Japan.

Cornell, A. and Jalayer, F. (2002). Factored nonlinear displacement demand estimation methods for probability-based safety assessment. In Annual Meeting Research Digest No. 2002-7, A publication of the Pacific Earthquake Engineering Research Center.

Cornell, A., Jalayer, F., and Hamburger, R. (2002). Probabilistic basis for 2000 sac federal emergency management agency steel moment frame guidelines. Journal of Structural Engineering, 128:526–532.

Cornell, C. (1968). Engineering seismic risk analysis. Bulletin of the Seismological Society of America, 58:1583–1606.

Cornell, C. and Krawinkler, H. (2000). Progress and challenges in seismic performance assessment. http://peer.berkeley.edu/news/2000spring/index.html.

Cosenza, E. and Manfredi, G. (1997). The improvement of the seismic-resistant design for existing and new structures using damage criteria. In Fajfar, P. and Krawinkler, H., editors, Seismic design methodologies for the next generation of codes, pages 119–130, Roterdam. Balkema.

Cosenza, E. and Manfredi, G. (2000). Damage indices and damage measures. Progress in Structural Engineering and Materials, 2:50–59.

Council, A. T. (1992). Guidelines for cyclic seismic testing of components for steel structures. Technical report, Applied Technology Council, Redwood City, CA, USA.

Council, B. S. S. (2003). Nehrp recommended provisions for seismic regulations for new buildings and other structures, part1: Provisions, fema 368. Technical report, Federal Emergency Management Agency, Washington, DC.

Czarnecki, R. (1973). Earthquake damage to tall buildings, Optimum Seismic Protection and Building Damage Statistics, Report No. 5. PhD thesis, Massachusetts Institute of Technology, Cambridge, Departement of Civil Engineering.

Dahlblom, O. and Ottosen, N. S. (1990). Smeared crack analysis using a generalized fictitious crack model. Journal of Engineering Mechanics, 116(1):55–76.

DAmbrisi, A. and Mezzi, M. (2014). An energy-based approach for nonlinear static analysis of structures. Bulletin of Earthquake Engineering.

Dashti, S., Bray, J., Pestana, J., Riemer, M., and Wilson, D. (2009). Centrifuge testing to evaluate and mitigate liquefaction-induced building settlement mechanisms. Journal of geotechnical and geoenvironmental engineering, 136:918–929.

de Arajo, J. and Awruch, A. (1998). Cracking safety evaluation on gravity concrete dams during the construction phase. Computers and Structures, 66:93–104.

Deaggregation, U. (2003). Psha interactive deaggregation tool, u.s. geological survey.

deArajo, J. and Awruch, A. (1998). Probabilistic finite element analysis of concrete gravity dams. Advances in Engineering Software, 29:97–104.

del Consiglio dei Ministri, P. (2001). Guidelines for seismic safety reassessment of existing dams in italy. Technical report, Dipartimento per I Servizi Tecnici Nazionali, Italy.

Der-Kiureghian, A. and Ditlevsen, O. (2009). Aleatory or epistemic? does it matter? Structural Safety, 31:105–112.

Dewals, B., Erpicum, S., Detrembleur, S., Archambeau, P., and Pirotton, M. (2011). Failure of dams arranged in series or in complex. Natural Hazards, 56:917–939.

Dipasquale, E. and Cakmak, A. (1988). Identification of the serviceability limit state and detection of seismic structural damage, report nceer-88-0022. Technical report, National Center for Earthquake Engineering Research, State University of New York, Buffalo NY.

Dipasquale, E. and Cakmak, A. (1989). On the relation between local and global damage indices, technical report nceer-89-0034. Technical report, National Center for Earthquake Engineering Research, State University of New York, Buffalo NY.

Dolsek, M. (2009). Incremental dynamic analysis with consideration of modeling uncertainties. Earthquake Engineering and Structural Dynamics, 38:805–825.

Dolsek, M. (2011). Estimation of seismic response parameters through extended incremental dynamic analysis. In Papadrakakis, M., Fragiadakis, M., and Lagaros, N. D., editors, Computational Methods in Earthquake Engineering, volume 21 of Computational Methods in Applied Sciences, pages 285–304. Springer Netherlands.

Dolšek, M. (2012). Simplified method for seismic risk assessment of buildings with consideration of aleatory and epistemic uncertainty. Structure and infrastructure engineering, 8:939–953.

Dong, Y., Frangopol, D., and Saydam, D. (2013). Time-variant sustainability assessment of seismically vulnerable bridges subjected to multiple hazards. Earthquake Engineering and Structural Dynamics, 42:1451–1467.

Drucker, D. and Prager, W. (1952). Soil mechanics and plastic analysis or limit design. Quarterly of Applied Mathematics, 10:157–165.

Ellingwood, B. and Tekie, P. (2001). Fragility analysis of concrete gravity dams. Journal of Infrastructure Systems, ASCE, 7:41–48.

EPRI-1014099 (2006). Program on technology innovation: Use of cumulative absolute velocity (cav) in determining effects of small magnitude earthquakes on seismic hazard analyses. Technical report, Electrical Power Research Institute (EPRI), Palo Alto, CA.

EPRI-NP-5930 (1988). A criterion for determining exceedance of the operating basis earthquake. Technical report, Electrical Power Research Institute (EPRI), Palo Alto, CA.

Estekanchi, H., Vafai, A., and Sadeghazar, M. (2004). Endurance time method for seismic analysis and design of structures. Scientia Iranica, 11:361–370.

Estekanchi, H., Valamanesh, V., and Vafai, A. (2007). Application of endurance time method in linear seismic analysis. Engineering Structures, 29(10):2551–2562.

Fajfar, P. (2000). A nonlinear analysis method for performance based seismic design. Earthquake Spectra, 16:573–592.

Fajfar, P., Vidic, T., and Fischinger, M. (1990). A measure of earthquake motion capacity to damage medium-period structures. Soil Dynamics and Earthquake Engineering, 9:236–242.

Fanelli, M. and Lombardi, G. (1997). On the lombardi slenderness coefficient for assessing the cracking potential of arch dams. In Proceedings of the International Symposium on Arch Dams, Nanjing, China.

FEMA (1997a). Nehrp commentary on the guidelines for seismic rehabilitation of buildings. Technical report, Federal Emergency Management Agency, Washington, DC.

FEMA (1997b). Nehrp guidelines for seismic rehabilitation of buildings. Technical report, Federal Emergency Management Agency, Washington, DC.

FEMA (2000). Prestandard and commentary for the seismic rehabilitation of buildings. Technical report, Federal Emergency Management Agency, Washington, DC.

FEMA-PFM (2011). Selecting analytic tools for concrete dams to address key events along potential failure mode paths. Technical report, Federal Emergency Management Agency, Denver, Colorado.

Feng, J., Wei, H., Pan, J., Jian, Y., Wang, J., and Zhang, C. (2011). Comparative study procedure for the safety evaluation of high arch dams. Computers and Geotechnics, 38:306–317.

Fenves, G. and Chopra, A. (1984). Earthquake analysis of concrete gravity dams including reservoir bottom absorption and dam-water-foundation rock interaction. Earthquake Engineering and Structural Dynamics, 12:663–680.

Fenves, G. and Chopra, A. (1987). Simplified earthquake analysis of concrete gravity dams. Journal of Structural Engineering, 113:1688–1708.

FERC-Arch (1999). Engineering guidelines for the evaluation of hydraopower projects: Chapter 11: Arch dams. Technical report, Federal Energy Regulatory Commission, Washington, DC, USA.

FERC-PFMA (2005). Ferc guidance document: Poteintial failure mode analysis, draft version. Technical report, Federal Emergency Regulatory Committee.

Field, E., Jordan, T., and Cornel, C. (2003). Opensha: A developing community-modeling environment for seismic hazard analysis. Seismological Research Letters, 74:406–419.

Filiatrault, A., Wanitkorkul, A., and Constantinou, M. (2008). Development and appraisal of a numerical cyclic loading protocol for quantifying building system performance. Technical Report MCEER-08-0013, University at Buffalo, State University of New York.

Freeman, S. (1978). Prediction of response of concrete buildings to severe earthquake motion. In Institute, A. C., editor, Proceedings of Douglas McHenry international symposium on concrete and concrete structures, Detroit, MI, USA.

Freeman, S. (1998). The capacity spectrum method. In Proceedings of the 11th European conference on earthquake engineering, Paris, France.

Ghaemian, M. and Ghobarah, A. (1998). Staggered solution schemes for dam-reservoir interaction. Fluids and Structures, 12:933–948.

Ghaemmaghami, A. and Ghaemian, M. (2008). Experimental seismic investigation of sefid-rud concrete buttress dam model on shaking table. Earthquake Engineering and Structural Dynamics, 37:809–823.

Ghaemmaghami, A. and Ghaemian, M. (2009). Shaking table test on small-scale retrofitted model of sefid-rud concrete buttress dam. Earthquake Engineering and Structural Dynamics, 39:109–118.

Ghanaat, Y. (2004). Failure modes approach to safety evaluation of dams. In Proceedings of the 13th World Conference on Earthquake Engineering, Vancouver, BC, Canada.

Ghanaat, Y., Hashimoto, P., Zuchuat, O., and Kennedy, R. (2011). Seismic fragility of mhleberg dam using nonlinear analysis with latin hypercube simulation. In Proceeding of the 2011 USSD Annual Conference, pages 1197–1212.

Ghanaat, Y., Patev, R., and Chudgar, A. (2012). Seismic fragility analysis of concrete gravity dams. In Proceedings of the 15th World Conference on Earthquake Engineering, Lisbon, Portugal.

Ghanaat, Y., Patev, R., and Chudgar, A. (2015). Seismic fragility for risk assessment of concrete gravity dams. In Proceeding of the 2015 USSD Annual Conference, pages 645–660.

Ghobarah, A. (2001). Performance-based design in earthquake engineering: State of development. Engineering Structures, 23:878–884.

Ghobarah, A. and Ghaemian, M. (1998). Experimental study of small scale dam models. Journal of Engineering Mechanics - ASCE, 124:1241–1248.

Ghobarah, H., Abou-Elfath, H., and Biddah, A. (1999). Response-based damage assessment of structures. Earthquake Engineering and Structural Dynamics, 28:79–104.

Ghosh, J. and Padgett, J. (2010). Aging considerations in the development of time-dependent seismic fragility curves. Journal of Structural Engineering, 136:1497–1511.

Giorgi, P. and Scotta, R. (2013). Validation and improvement of {N1} method for pushover analysis. Soil Dynamics and Earthquake Engineering, 55:140–147.

Giovenale, P., Cornell, A., and Esteva, L. (2004). Comparing the adequacy of alternative ground motion intensity measures for the estimation of structural responses. Earthquake Engineering and Structural Dynamics, 33:951–979.

Goodman, R.E. and Taylor, R.C. and Brekke, T.C. (1968). A Model for the Mechanics of Jointed Rocks. J. of the Soil Mechanics and FOundations Division ASCE, 94:637–659.

Google (2013). Google maps. https://www.google.com/maps/place/Pine+Flat+Dam,+Sanger,+CA+93657/@36.8325771,-119.3258813,745m/data=!3m2!1e3!4b1!4m2!3m1!1s0x8095aa27e5eea299:0xe8b1f3cbaceda401. Last viewed October 2013.

Gosschalk, E., Severn, R., Charles, J., and Hinks, J. (1994). An engineering guide to seismic risk to dams in the united kingdom, and its international relevance. Soil Dynamics and Earthquake Engineering, 13:163–179.

Gunay, S. and Mosalam, K. (2013). Peer performance-based earthquake engineering methodology, revisited. Journal of Earthquake Engineering, 17(6):829–858.

Guo, A., Yuan, W., Lan, C., Guan, X., and Li, H. (2015). Time-dependent seismic demand and fragility of deteriorating bridges for their residual service life. Bulletin of Earthquake Engineering, pages 1–21.

Hamburger, R., Rojahn, C., Moehle, J., Bachman, R., Comartin, C., and Whittaker, A. (2004). The atc-58 project: Development of next-generation reformance-based earthquake engineering design criteria for buildings. In Proceeding of the 13th World Conferance on Earthquake Engineering, Vancouver, Canada.

Hao, M., Xie, L., and Xu, L. (2005). Some considerations on the physical measure of seismic intensity. Acta Seismologica Sinica, 27:230–234.

Hariri-Ardebili, M. (2014). Impact of foundation nonlinearity on the crack propagation of high concrete dams. Soil Mechanics and Foundation Engineering, 51:72–82.

Hariri-Ardebili, M. and Kianoush, M. (2014). Integrative seismic safety evaluation of a high concrete arch dam. Soil Dynamics and Earthquake Engineering, 67:85–101.

Hariri-Ardebili, M. and Kianoush, M. (2015). Seismic analysis of a coupled dam-reservoirfoundation system considering pressure effects at opened joints. Structure and Infrastructure Engineering, 11:833–850.

Hariri-Ardebili, M. and Mirzabozorg, H. (2013). A comparative study of the seismic stability of coupled arch dam-foundation-reservoir systems using infinite elements and viscous boundary models. International Journal of Structural Stability and Dynamic, 13.

Hariri-Ardebili, M. and Mirzabozorg, H. (2014). Estimation of probable damages in arch dams subjected to strong ground motions using endurance time acceleration functions. KSCE Journal of Civil Engineering, 18:574–586.

Hariri-Ardebili, M., Mirzabozorg, H., and Ghasemi, A. (2013). Strain-based seismic failure evaluation of coupled dam-reservoir-foundation system. Coupled Systems Mechanics, 2(1):85–110.

Hariri-Ardebili, M., Rahmani-Samani, H., and Mirtaheri, M. (2014a). Seismic stability assessment of a high-rise concrete tower utilizing endurance time analysis. International Journal of Structural Stability and Dynamics, 14.

Hariri-Ardebili, M. and Saouma, V. (2014). Quantitative failure metric for gravity dams. Earthquake Engineering and Structural Dynamics.

Hariri-Ardebili, M. and Saouma, V. (2015a). Probabilistic seismic demand model and optimal intensity measure for concrete dams. Structural Safety (under review).

Hariri-Ardebili, M. and Saouma, V. (2015b). Sensitivity and uncertainty quantification of the cohesive crack model. Engineering Fracture Mechanics (under review).

Hariri-Ardebili, M., Saouma, V., and Porter, K. (2015). Quantification of seismic potential failure modes in concrete dams. Earthquake Engineering and Structural Dynamics.

Hariri-Ardebili, M., Sattar, S., and Estekanchi, H. (2014b). Performance-based seismic assessment of steel frames using endurance time analysis. Engineering Structures, 69:216–234.

Hartford, D. and Baecher, G. (2004). Risk and uncertainty in dam safety. Technical report, Thomas Telford, Ltd, London, UK.

Haselton, C., Goulet, C., Mitrani-Reiser, J., Beck, J., Deierlein, G., Porter, K., Stewart, J., and Taciroglu, E. (2008). An assessment to benchmark the seismic performance of a code-conforming reinforced concrete moment-frame building, peer report 2007/12. Technical report, Pacific Earthquake Engineering Research Center, University of California, Berkeley, Califprnia.

Hastie, T.J. and Tibshirani, R.J. (1990). Generalized Additive Models. Chapman and Hall: New York.

Hernandez-Montes, E., Kwon, O., and Aschheim, M. (2004). An energy-based formulation for first-and multiple-mode nonlinear static (pushover) analyses. Journal of Earthquake Engineering, 8:69–88.

Hillerborg, A., Modéer, M., and Petersson, P. (1976). Analysis of crack formation and crack growth in concrete by means of fracture mechanics and finite elements. Cement and Concrete Research, 6(6):773–782.

Housner, G. (1975). Measures of severity of earthquake ground shaking. In Proceedings of the U.S. National Conference on Earthquake Engineering, pages 25–33, Ann Arbor, MI.

HSE (2001). Reducing risks, protecting people: Hses decisionmaking process, risk assessment policy unit. Technical report, Health and Safety Executive (HSE), London, England.

Huaizhi, S., Jiang, H., and Wen, Z. (2013). Service life predicting of dam systems with correlated failure modes. ASCE Journal of Performance of Constructed Facilities, 27:252–269.

ICOLD (1974). Lessons from dam incidents, complete edition. Technical report, International Commission on Large Dams, Paris, France.

ICOLD (1989). Selecting seismic parameters for large dams, bulletin 72. Technical report, International Commission on Large Dams, Paris, France.

ICOLD (2010). Selecting seismic parameters for large dams, guidelines, revision of bulletin 72. Technical report, International Commission on Large Dams, Paris, France.

Iman, R. and Conover, W. (1982). A distribution-free approach to inducing rank correlation among input variables. Communications in Statistics-Simulation and Computation, B11:311–334.

Jalayer, F. (2003). Direct probabilistic seismic analysis: implementing non-linear dynamic assessments. PhD thesis, Stanford University, Stanford.

Jalayer, F., De Risi, R., and Manfredi, G. (2014). Bayesian cloud analysis: efficient structural fragility assessment using linear regression. Bulletin of Earthquake Engineering, pages 1–21.

Jalayer, F., Franchin, P., and Pinto, P. (2007). A scalar damage measure for seismic reliability analysis of rc frames. Earthquake Engineering and Structural Dynamics, 36:2059–2079.

Jankovic, S. and Stojadinovic, B. (2004). Probabilistic performance-based seismic demand model for {R/C} frame buildings. In Proceeding of the 13th World Conferance on Earthquake Engineering, Vancouver, B.C., Canada.

Jayaram, N., Lin, T., and Baker, J. (2011). A computationally efficient ground-motion selection algorithm for matching a target response spectrum mean and variance. Earthquake Spectra, 27:797–815.

Kappos, A. (1997). Seismic damage indices for rc buildings: evaluation of concepts and procedures. Progress in Structural Engineering and Materials, 1:78–87.

Karacabeyli, E. (1998). Lateral resistance of nailed shear walls subjected to static and cyclic displacements. In Research Report, FPS 49th Annual Meeting, Portland, OR, USA.

Kazantzi, A., Vamvatsikos, D., and Lignos, D. (2014). Seismic performance of a steel moment-resisting frame subject to strength and ductility uncertainty. Engineering Structures, 78:69–77.

Kennedy, R., Cornell, C., Campbell, R., Kaplan, S., and Perla, H. (1980). Probabilistic seismic safety study of an existing nuclear power plant. Nuclear Engineering and Design, 59:315–338.

Kim, S., Holub, C., and Elnashai, A. (2011). Analytical assessment of the effect of vertical earthquake motion on rc bridge piers. Journal of Structural Engineering, 137:252–260.

Kostinakis, A., Athanatopoulou, A., and Morfidis, K. (2015). Correlation between ground motion intensity measures and seismic damage of 3d r/c buildings. Engineering Structures, 82:151–167.

Koutromanos, I., Stavridis, A., Shing, P., and Willam, K. (2011). Numerical modeling of masonry-infilled rc frames subjected to seismic loads. Computers and Structures, 89:1026–1037.

Kratzig, W., Meyer, I., and Meskouris, K. (1989). Damage evolution in reinforced concrete members under cyclic loading. In Proceedings of Fifth International Conference on Structural Safety and Reliability, San Francisco, CA.

Krawinkler, H. (1999). Chanllenges and progress in performance-based earthquake engineering. In International Seminar on Seismic Engineering for Tomorrow, Tokyo, Japan.

Kunnath, S., Reinhorn, A., and Lobo, R. (1992). Idarc version 3: A program for the inelastic damage analysis of rc structures, technical report nceer-92-0022. Technical report, National Center for Earthquake Engineering Research, State University of New York, Buffalo NY.

Kupfer, H., Hilsdorf, H., and Rusch, H. (1969). Behavior of concrete under biaxial stresses. ACI, 66:656–666.

Kurama, Y. and Farrow, K. (2003). Ground motion scaling methods for different site conditions and structure characteristics. Earthquake Engineering and Structural Dynamics, 32:2425–2450.

Kustu, O., Miller, D., and Broken, S. (1982). Development of damage functions for high-rise building. Technical report, URS/John A. Blume and Associates, Engineers, San Francisco, CA.

Lallemant, D., Kiremidjian, A., and Burton, H. (2015). Statistical procedures for developing earthquake damage fragility curves. Earthquake Engineering and Structural Dynamics.

Larive, C. (1997). Apports combinés de l'expérimentation et de la modélisation à la compréhension de l'alcali-réaction et de ses effets mécaniques. PhD thesis, Ecole nationale des ponts et chaussees.

Lee, H. and Mosalam, K. (2014). Effect of vertical acceleration on shear strength of reinforced concrete columns. Technical report, Pacific Earthquake Engineering Research Center, College of Engineering, University of California, Berkeley, Berkeley, CA.

Lee, J. and Fenves, G. L. (1998). A plastic-damage concrete model for earthquake analysis of dams. Earthquake Engineering and Structural Dynamics, 27:937–956.

Leger, P. (2007). Reducing the earthquake induced damage and risk in monumental structures: Experience at ecole polytechnique de montreal for large concrete dams supported by hydro-quebec and alcan. In Extreme Man-Made and Natural Hazards in Dynamics of Structures, A. Ibrahimbegovic and I. Kozar (eds.), Springer, pages 285–309.

Li, Q. and Ren, Q. (2013). Research on determining solid structure critical load and failure mode. Engineering Failure Analysis, 32:113–123.

Liel, A., Haselton, C., Deierlein, G., and Baker, J. (2009). Incorporating modeling uncertainties in the assessment of seismic collapse risk of buildings. Structural Safety, 31:197–211.

Lin, T. (2012). Advancement of Hazard-Consistent Ground Motion Selection Methodology through Conditional Spectrum and Adaptive Incremental Dynamic Analysis. PhD thesis, PhD Thesis, Department of Civil and Environmental Engineering, Stanford University, Stanford, California.

Liu, J., Feng, X., Ding, X., Zhang, J., and Yue, D. (2003). Stability assessment of the three-gorges dam foundation, china, using physical and numerical modeling - part i: physical model tests. International Journal of Rock Mechanics and Mining Sciences, 40:609–631.

Løkke, A. and Chopra, A. (2013). Response spectrum analysis of concrete gravity dams including dam-water-foundation interaction. Technical report, Pacific Earthquake Engineering Research Center Headquarters at the University of California, Berkeley, Berkeley, CA.

Løkke, A. and Chopra, A. (2014). Response spectrum analysis of concrete gravity dams including dam-water-foundation interaction. Journal of Structural Engineering.

Lopez, C., Carol, I., and Aguado, A. (2008). Meso-structural study of concrete fracture using interface elements. i: Numerical model and tensile behavior. Materials and Structures, 41:583–599.

Lotfi, H. and Shing, P. (1994). Interface model applied to fracture masonry structures. ASCE J. of Engineering Mechanics, 120(1):63–79.

Luco, N. (2002). Probabilistic seismic demand analysis, SMRF connection fractures, and near-source effects. PhD thesis, Stanford University, Stanford.

Lupoi, A. and Callari, C. (2011). The role of probabilistic methods in evaluating the seismic risk of concrete dams. In Dolek, M., editor, Protection of Built Environment Against Earthquakes, pages 309–329.

Lupoi, A. and Callari, C. (2012). A probabilistic method for the seismic assessment of existing concrete gravity dams. Structure and Infrastructure Engineering, 8:985–998.

Mackie, K. and Stojadinovic, B. (2001). Probabilistic seismic demand model for california highway bridges. Journal of Bridge Engineering, 132:468–481.

Mackie, K. and Stojadinovic, B. (2003). Seismic demands for performance-based design of bridges. Technical report, Pacific Earthquake Engineering Research Center, University of California Berkeley, CA, US.

Mackie, K. and Stojadinovic, B. (2005). Comparison of incremental dynamic, cloud, and stripe methods for computing probabilistic seismic demand models. In Proceedings of the 2005 Structures Congress and the 2005 Forensic Engineering Symposium, New York, NY.

Malla, S. (2013). Earthquake safety assessment of arch dams based on nonlinear dynamic analyses. In Proceedings of the 12th INTERNATIONAL BENCHMARK WORKSHOP ON NUMERICAL ANALYSIS OF DAMS, GRAZ, AUSTRIA.

Malla, S. and Wieland, M. (1999). Analysis of an arch gravity dam with a horizontal crack. Computers and Structures, 72:267–278.

Mander, J., Dhakal, R., Mashiko, N., and Solberg, K. (2007). Incremental dynamic analysis applied to seismic financial risk assessment of bridges. Engineering Structures, 29:2662–2672.

Marsaglia, G. and Marsaglia, J. (2004). Evaluating the anderson-darling distribution. Journal of Statistical Software, 9:1–5.

Mashayekhi, M. and Estekanchi, H. (2013). Investigation of strong-motion duration consistency in endurance time excitation functions. Scientia Iranica, 20:1085–1093.

MATLAB (2013). version 8.2 (R2013b). The MathWorks Inc., Natick, Massachusetts.

McGuire, R. (1995). Probabilistic seismic hazard analysis and design earthquakes: Closing the loop. Bulletin of the Seismological Society of America, 85:1275–1284.

Mills-Bria, B., Nuss, L., Dixon, L., Powell, C., Harris, D., and O'Connell, D. (2006). State-of-practice for the nonlinear structural analysis of dams at the bureau of reclamation. Technical report, U.S. Dept. of the Interior, Bureau of Reclamation.

Mirzabozorg, H., Akbari, M., and Hariri-Ardebili, M. (2012). Wave passage and incoherency effects on seismic response of high arch dams. Earthquake Engineering and Engineering Vibration, 11:567–578.

Mirzabozorg, H., Hariri-Ardebili, M., Shirkhan, M., and Seyed-Kolbadi, S. (2014). Mathematical modeling and numerical analysis of thermal distribution in arch dams considering solar radiation effect. The Scientific World Journal, 2014.

Mitrani-Reiser, J. (2007). An ounce of prevention: probabilistic loss estimation for performance-based earthquake engineering. PhD thesis, California Institute of Technology.

Moehle, J. and Deierlein, G. (2004). A framework methodology for performance-based earthquake engineering. In Proceeding of the 13th World Conferance on Earthquake Engineering, Vancouver, Canada.

Mwafy, A. and Elnashai, A. (2001). Static pushover versus dynamic collapse analysis of rc buildings. Engineering Structures, pages 407–424.

MWH-Global (2003). Upper san joaquin river basin storage investigation, raise pine flat dam. Technical report, A Joint Study by: Bureau of Reclamation, California Department of Water Resources, The California Bay-Delta Authority.

Naeim, F. and Lew, M. (1995). On the use of design spectrum compatible time histories. Earthquake Spectra, 11:111–127.

Nau, J. and Hall, W. (1982). An evaluation of scaling methods for earthquake response spectra. Technical report, Department of Civil Engineering, University of Illinois, Urbana, IL.

Nayak, P. and Maity, D. (2013). Seismic damage analysis of aged concrete gravity dams. International Journal for Computational Methods in Engineering Science and Mechanics, 14:424–439.

Newmark, N.M. and Rosenblueth, E. (1971). Fundamentals of Earthquake Engineering. Prentice-Hall, Englewood Cliffs, NJ.

Nozari, A. and Estekanchi, H. (2011). Optimization of endurance time acceleration functions for seismic assessment of structures. International Journal of Optimization in Civil Engineering, 1:257–277.

NSW (2006). Risk management policy framework for dam safety. Technical report, New South Wales Government Dams Safety Committee, New South Wales, Australia.

Nuss, L., Matsumoto, N., and Hansen, K. (2012). Shaken, but not stirred - earthquake performance of concrete dams. In Proceedings of the 32nd USSD Annual Meeting and Conference: Innovative Dam and Levee Design and Construction for Sustainable Water Management, New Orleans, Louisiana.

Nuttli, O. (1979). The relation of sustained maximum ground acceleration and velocity to earthquake intensity and magnitude. Technical report, U.S. Army Corps of Engineers, Waterways Experiment Station, Vicksburg, Mississippi.

of Construction, J.-M. (2000). Japanese building code. Technical report, Japanese Ministry of Construction, Japan.

Omidi, O. and Lotfi, V. (2013). Earthquake response of concrete arch dams: a plastic-damage approach. Earthquake Engineering and Structural Dynamics, 42:2129–2149.

on California Earthquake Probabilities, . W. G. (2008). The uniform california earthquake rupture forecast, version 2 (ucerf 2). Technical report, U.S. Geological Survey Open-File Report 2007-1437 and California Geological Survey Special Report 203.

Padgett, J. and DesRoches, R. (2007). Sensitivity of seismic response and fragility to parameter uncertainty. Journal of Structural Engineering, 133:1710–1718.

Padgett, J., Nielson, B., and DesRoches, R. (2008). Selection of optimal intensity measures in probabilistic seismic demand models of highway bridge portfolios. Earthquake Engineering and Structural Dynamics, 37:711–725.

Pan, J., Feng, Y., Jin, F., Zhang, C., and Owen, D. (2014). Comparison of different fracture modelling approaches to gravity dam failure. Engineering Computations, 31:18–32.

Pan, J., Xu, Y., and Jin, F. (2015). Seismic performance assessment of arch dams using incremental nonlinear dynamic analysis. European Journal of Environmental and Civil Engineering, pages 1–22.

Pan, J., Zhang, C., Xu, Y., and Jin, F. (2011). A comparative study of the different procedures for seismic cracking analysis of concrete dams. Soil Dynamics and Earthquake Engineering, 31:1594–1606.

Panyakapo, P. (2014). Cyclic pushover analysis procedure to estimate seismic demands for buildings. Engineering Structures, 66:10–23.

Papanikolaou, V. and Elnashai, A. (2005). Evaluation of conventional and adaptive pushover analysis i: Methodology. Journal of Earthquake Engineering, 9:923–941.

Papazoglou, A. and Elnashai, A. (1996). Analytical and field evidence of the damaging effect of vertical earthquake ground motion. Earthquake Engineering and Structural Dynamics, 25:1109–1137.

Park, Y. and AH-S., A. (1985). Mechanistic seismic damage model for reinforced concrete. Journal of Structural Division, ASCE, 111:722–739.

Park, Y., AH-S., A., and Wen, Y. (1985). Seismic damage analysis of reinforced concrete buildings. Journal of Structural Engineering, 111:740–757.

PEER (2014). Ground motion database. `http://ngawest2.berkeley.edu/`. Last viewed November 2014.

Pitilakis, K., Karapetrou, S., and Fotopoulou, S. (2014). Consideration of aging and ssi effects on seismic vulnerability assessment of rc buildings. Bulletin of Earthquake Engineering, 12:1755–1776.

Porter, K. (2000). Assembly-Based Vulnerability of Buildings and its Uses in Seismic Performance Evaluation and Risk-Management Decision-Making. PhD thesis, Stanford University, Stanford.

Porter, K. (2003). An overview of peers performance-based earthquake engineering methodology. In Proceedings of the 9th International Conference on Applications of Statistics and Probability in Civil Engineering (ICASP9), San Francisco, CA.

Porter, K., Kennedy, R., and Bachman, R. (2007). Creating fragility functions for performance-based earthquake engineering. Earthquake Spectra, 23:471–489.

Powell, G. and Allahabadi, R. (1988). Seismic damage prediction by deterministic methods: Concepts and procedures. Earthquake Engineering and Structural Dynamics, 16:719–734.

Pujades, L., Vargas-Alzate, Y., Barbat, A., and Gonzalez-Drigo, J. (2014). Parametric model for capacity curves. Bulletin of Earthquake Engineering.

Puntel, E., Bolzon, G., and Saouma, V. (2006). A fracture mechanics based model for joints under cyclic loading. ASCE Engineering Mechanics, 132:1151–1159.

Ramamoorthy, S., Gardoni, P., and Bracci, J. (2006). Probabilistic demand models and fragility curves for reinforced concrete frames. Journal of Structural Engineering, 132:1563–1572.

Raphael, J. (1984). Tensile strength of concrete. ACI Journal, pages 158–165.

Richardson, L. (1911). The approximate arithmetical solution by finite differences of physical problems involving differential equations, with an application to the stresses in a masonry dam. Philosophical Transactions of the Royal Society, Series A., 210:307–357.

Riddell, R. (2007). On ground motion intensity indices. Earthquake Spectra, 23:147–173.

Riddell, R. and Garcia, J. (2001). Hysteretic energy spectrum and damage control. Earthquake Engineering and Structural Dynamics, 30:1791–1816.

Rosenblueth, E. (1956). Some applicacion of probability theory in aseismic desing.

Roufaiel, M. and Meyer, C. (1981). Analysis of damaged concrete frame buildings, technical report no. nsf-cee-81-21359-1. Technical report, Columbia University, New York, NY.

Sabetta, F., Goretti, A., and Lucantoni, A. (1998). Empirical fragility curves from damage surveys and estimated strong ground motion. In Proceedings of the 11th European Conference on Earthquake Engineering.

Saouma, V. (2015). Applications of fracture mechanics to cementitious materials; a personal perspective. In Cusatis, G., editor, ACI SP-300 Fracture Mechanics Applications in Concrete. American Concrete Institute.

Saouma, V., Martin, R., Hariri-Ardebili, M., and Katayama, T. (2015). A mathematical model for the kinetics of the alkalisilica chemical reaction. Cement and Concrete Research, 68:184–195.

Saouma, V., Miura, F., Lebon, G., and Yagome, Y. (2011). A simplified 3d model for soil-structure interaction with radiation damping and free field input. Bulletin of Earthquake Engineering, 9:1387–1402.

Saouma, V., Perotti, L., and Shimpo, T. (2007). Stress analysis of concrete structures subjected to alkali-aggregate reactions. ACI Structural Journal, 104:532–541.

Saouma, V., Červenka, J., and Reich, R. (2010). Merlin finite element user's manual. `http://civil.colorado.edu/~saouma/pdf/users.pdf`.

Saouma, V. (2014). Numerical Modeling of AAR. CRC Press.

SEAOC (1995). Performance-based seismic engineerin, seaoc vision 2000 committee. Technical report, Structural Engineers Association of California, Sacramento, CA.

Serra, C., Batista, A., and Tavares-de Castro, A. (2012). Creep of dam concrete evaluated from laboratory and in situ tests. Strain, 48:241–255.

Shen, C., Chen, H., Chang, C., Huang, L., Zi, T., Yang, C., Wang, T., and Lo, H. (1974). Earthquake induced by reservoir impounding and their effect on hsinfengkiang dam. Scientia Sinica, 17(2):239–272.

Shinozuka, M., Feng, M., Lee, J., and Naganuma, T. (2000). Statistical analysis of fragility curves. Journal of Engineering Mechanics, 126:1224–1231.

Shome, N. (1999). Probabilistic Seismic Demand Analysis of Nonlinear structures. PhD thesis, Stanford University, Stanford.

Shome, N., Cornell, C., Bazzurro, P., and Carballo, J. (1998). Earthquakes, records, and nonlinear responses. Earthquake Spectra, 14(3):469–500.

Slowik, V., Kishen, C., and Saouma, V. (1998). Mixed mode fracture of cementitious bi-material interfaces, part i: Experimental results. Engineering Fracture Mechanics, 60:83–94.

Slowik, V. and Saouma, V. (2000a). Water pressure in propagating concrete cracks. ASCE Structural Engineering, 126:235–242.

Slowik, V. and Saouma, V. (2000b). Water pressure in propagating cracks. ASCE J. of Structural Engineering, 126(2):235–242.

Stephens, J. (1985). A damage function using structural response measurements. Structural Safety, 5:22–39.

Stephens, M. (1974). Edf statistics for goodness of fit and some comparisons. Journal of the American Statistical Association, 69:730–737.

Su, H., Hu, J., and Wen, Z. (2013). Service life predicting of dam systems with correlated failure modes. Journal of Performance of Constructed Facilities, ASCE, 27:252–269.

Swain, R., England, J., Bullard, K., and Raff, D. (2004). Hydrologic hazard curve estimating procedures. Technical report, U.S. Department of the Interior Bureau of Reclamation.

Tang, Y. and Zhang, J. (2011). Probabilistic seismic demand analysis of a slender {RC} shear wall considering soilstructure interaction effects. Engineering Structures, 33:218–229.

Tekie, P. and Ellingwood, B. (2002). Fragility analysis of concrete gravity dams. Technical report, Georgia Institute of Technology, Prepared for U.S. Army Corps of Engineers, Washington, DC.

Tekie, P. and Ellingwood, B. (2003). Seismic fragility assessment of concrete gravity dams. Earthquake Engineering and Structural Dynamics, 32:2221–2240.

Tondini, N. and Stojadinovic, B. (2012). Probabilistic seismic demand model for curved reinforced concrete bridges. Bulletin of Earthquake Engineering, 10:1455–1479.

Tothong, P. and Luco, N. (2007). Probabilistic seismic demand analysis using advanced ground motion intensity measures. Earthquake Engineering and Structural Dynamics, 36:1837–1860.

Toussi, S. and Yao, J. (1982). Hysteresis identification of existing structures. Journal of Engineering Mechanics, ASCE, 109:1189–1203.

Uang, C.-M. and Bertero, V. (1990). Evaluation of seismic energy in structures. Earthquake Engineering and Structural Dynamics, 19:77–90.

USACE (2007). Em 1110-2-6053: Earthquake design and evaluation of concrete hydraulic structures. Technical report, Department of the Army, U.S. Army Corps of Engineers, Washington D.C., USA.

USBR-manual (2011). Dam safety risk analyaia, best practices training manual, version 2.2. Technical report, U.S. Department of the Interior Bureau of Reclamation in coorporation with the U.S. Army Corps of Engineers, Denver, Colorado.

Valliappan, S. and Chee, C. (2009). Ageing degradation of concrete dams based on damage mechanics concepts. In Yuan, Y., Cui, J., and Mang, H., editors, Computational Structural Engineering, pages 21–35. Springer Netherlands.

Vamvatsikos, D. and Cornel, C. (2002). Incremental dynamic analysis. Earthquake Engineering and Structural Dynamics, 31:491–514.

Vamvatsikos, D. and Cornel, C. (2005). Developing efficient scalar and vector intensity measures for ida capacity estimation by incorporating elastic spectral shape information. Earthquake Engineering and Structural Dynamics, 34(13):1573–1600.

Vamvatsikos, D. and Cornell, C. (2004). Applied incremental dynamic analysis. Earthquake Spectra, 20:523–553.

Vamvatsikos, D. and Fragiadakis, M. (2010). Incremental dynamic analysis for estimating seismic performance sensitivity and uncertainty. Earthquake Engineering and Structural Dynamics, 39:141–163.

Vanmarcke, E. (1977). Seismic safety assessment. In Parkus, H., editor, Random Excitation of Structures by Earthquakes and Atmospheric Turbulence, volume 225 of International Centre for Mechanical Sciences, pages 1–76. Springer Vienna.

Voechovsk, M. and Novk, D. (2009). Correlation control in small-sample monte carlo type simulations i: A simulated annealing approach. Probabilistic Engineering Mechanics, 24:452–462.

Wang, M. and Shah, S. (1987). Reinforced concrete hysteresis model based on the damage concept. Earthquake Engineering and Structural Dynamics, 15:993–1003.

Wang, T. and Hsu, T. (2001). Nonlinear finite element analysis of concrete structures using new constitutive models. Computers and Structures, 79:2781–2791.

Wang, W., Gu, C., and Bao, T. (2013a). Safety monitoring index of high concrete gravity dam based on failure mechanism of instability. Mathematical Problems in Engineering, 2013:1–14.

Wang, Y., Burgess, I., Wald, F., and Gillie, M. (2012). Performance-based fire engineering of structures. CRC Press.

Wang, Z., Padgett, J., and Dueñas-Osorio, L. (2013b). Influence of vertical ground motions on the seismic fragility modeling of a bridge-soil-foundation system. Earthquake Spectra, 29:937–962.

Wei, Z., Xiaolin, C., Chuangbing, Z., and Xinghong, L. (2008). Failure analysis of high-concrete gravity dam based on strength reserve factor method. Computers and Geotechnics, 35:627–636.

Westergaard, H. (1933). Water pressures on dams during earthquakes. Transactions of the American Society of Civil Engineers, 98:418–433.

Whittaker, A., Hamburger, R., and Mahoney, A. (2003). Performance-based engineering of buildings for extreme events. In Proc., Steel Building Symp. Blast and Progressive Collapse Resistance, pages 55–66.

wikipedia (2015). Pine flat dam. `http://en.wikipedia.org/wiki/Pine_Flat_Dam`. Last viewed January 2015.

Wilcoski, J., Robert, R., Matheu, E., Gambill, J., and Chowdhury, M. (2001). Seismic testing of a 1/20 scale model of koyna dam, report no. erdc tr-01-17. Technical report, U.S. Army Corps of Engineers, Engineering Research and Development Center, Washington, USA.

Yang, D., Pan, J., and Li, G. (2009a). Non-structure-specific intensity measure parameters and characteristic period of near-fault ground motions. Earthquake Engineering and Structural Dynamics, 38:1257–1280.

Yang, T., Moehle, J., and Stojadinovic, B. (2009b). Performance evaluation of innovative steel braced frames, peer report 2009/103. Technical report, Pacific Earthquake Engineering Research Center, College of Engineering, University of California, Berkeley, Berkeley, CA.

Yang, T., Moehle, J., Stojadinovic, B., and DerKiureghian, A. (2009c). Seismic performance evaluation of facilities: Methodology and implementation. ASCE Structural Engineering, 135:1146–1154.

Zangar, C. (1953). Hydrodynamic pressures on dams due to horizontal earthquakes. Proceedings of Society of Experimental Stress Analysis, 10:93–102.

Zareian, F. and Krawinkler, H. (2009). Simplified performance based earthquake engineering, report no. 169. Technical report, Department of Civil and Environmental Engineering, Stanford University.

Zhang, J. and Huo, Y. (2009). Evaluating effectiveness and optimum design of isolation devices for highway bridges using the fragility function method. Engineering Structures, 31:1648–1660.

Zhang, S. and Wang, G. (2013). Effects of near-fault and far-fault ground motions on nonlinear dynamic response and seismic damage of concrete gravity dams. Soil Dynamics and Earthquake Engineering, 53:217–229.

Zhang, S., Wang, G., Pang, B., and Du, C. (2013a). The effects of strong motion duration on the dynamic response and accumulated damage of concrete gravity dams. Soil Dynamics and Earthquake Engineering, 45:112–124.

Zhang, S., Wang, G., and Sa, W. (2013b). Damage evaluation of concrete gravity dams under mainshockaftershock seismic sequences. Soil Dynamics and Earthquake Engineering, 50:16–27.

Zhong, H., Lin, G., Li, X., and Li, J. (2011). Seismic failure modeling of concrete dams considering heterogeneity of concrete. Soil Dynamics and Earthquake Engineering, 31:1678–1689.

Zhou, Y., Su, N., and Lu, X. (2012). An elastic spectral value-based intensity measure for the incremental dynamic analysis of tall buildings. In Proceedings of the 5th Kwang-Hua Forum on Innovations and Implementations in Earthquake Engineering Research, Shanghai, China.

Zhu, H., Yin, J., Dong, J., and Zhang, L. (2010). Physical modelling of sliding failure of concrete gravity dam under overloading condition. Geomechanics and Engineering, 2:89–106.